Doctoral Thesis

博士論文

Numerical Assessment of Multi-hazard Vulnerability in Tokyo Bay Using an Integrated Coastal Ocean and Drainage Pipe Model

（沿岸海洋・排水管統合モデルを用いた沿岸複合災害による東京湾沿岸の脆弱性評価）

劉　非

Doctoral Thesis

博士論文

Numerical Assessment of Multi-hazard Vulnerability in Tokyo Bay Using an Integrated Coastal Ocean and Drainage Pipe Model

（沿岸海洋・排水管統合モデルを用いた沿岸複合災害による東京湾沿岸の脆弱性評価）

劉　非

Graduate School of Frontier Sciences

The University of Tokyo

ABSTRACT

In the world, many bays are threatened by coastal hazards such as storm surge, river flood and tsunami. Since most of the existing studies have been focused on one or two of them, joint effects of the three hazards have not been investigated. Thus, in this study, the assessment of inundation vulnerability caused by the three hazards is the research target.

Inundation simulation is a widely used and straightforward way in coastal vulnerability assessments. However, it is computationally expensive, and considering an increase in the number of cases in the multiple hazard analysis, it is necessary to develop an efficient method to identify overall vulnerability and to screen representative scenarios for detailed analysis. For this purpose, an efficient method was proposed using an estimated overflow volume without computing inundation, which was validated by comparing with inundation simulation. It shows that the performance of this method is similar to inundation simulation approach. When free dike overflow is dominant, this method is consistent with inundation simulation approach, while if the overflow becomes submerged type, this approach is not applicable.

Although inundation period is one of the most important parameters for the vulnerability assessment, drainage through drainage pipes has often been ignored. To consider the drainage, a drainage pipe model was implemented in FVCOM for the first time. The integrated model was validated using a tsunami induced pipe-overflow event in Kisarazu Port during the 2011 Tohoku earthquake tsunami. The integrated model performs better than the original one for reproducing overflow inundation from the drainage pipe system in coastal areas.

In addition, a practical method combining atmospheric reanalysis data and a parametric typhoon formula was proposed to create accurate wind and atmospheric pressure fields since only few studies sought their optimum combination to enhance the accuracy of storm surge computation. Its performance was demonstrated by storm surge hindcasting in Tokyo Bay, and this method could be used in areas where accurate reanalysis data is lacking.

Using Tokyo Bay as a study area, the efficient method was then applied to multi-hazard vulnerability assessment. A series of assumed typhoon courses (T7920 course, Taisho 6th year Typhoon course, Isebay Typhoon course, and 1949 Typhoon Kitty course), river discharge scenario (50-year return period), and tsunami scenarios (ToKai-ToNankai type and Kanto type) were prepared based on government reports. Results show that compared to single hazard like only tsunami, in multi-hazard case, e.g., concurrent tsunami and storm surge, the tsunami shoaling process is changed because the anomaly difference of superposing case and concurrent case varies. In most coastal areas, the anomaly of superposing case is greater than that of concurrent case, but in some places, concurrent case results in larger anomalies than superposing case, which demonstrates the interaction between storm surge and tsunami. The anomaly difference of superposing case and concurrent case is basically larger in ports and river channels than in other coastal areas. Worst storm surge would cause larger anomalies than moderate multiple hazards, in which the return period of these two types of hazards is basically identical. Superposing method is an acceptable way for analyzing multi-hazard risks compared to concurrent computation.

Finally, the role of drainage system in local coastal flood was investigated using the integrated model, which showed that the drainage pipe system could help drain the inundation so that the total inundation volume and water logging period can be reduced significantly.

Based on the research, for better disaster prevention, upgrading the dike heights in areas where superposing method underestimates the multi-hazard anomalies may need to be considered. The function of floodgates should also be re-evaluated considering the effect of multiple hazards. The current early-warning and hazard prediction system in the study region may not be able to directly provide the multi-hazard flood information, and for more detailed flood warning, incorporation of drainage system is needed, otherwise, it may cause large inaccuracy. Thus, the capability of multi-hazard computation combining drainage systems is necessary to provide more accurate hazard information.

ACKNOWLEDGEMENTS

First of all, I would like to express my deepest gratitude to my academic supervisor Professor Jun Sasaki for his continuous support and guidance throughout my whole study period in Japan. Without his encouragement and guidance, it would be difficult for me to finish this dissertation work.

I am also indebted to the former lab researcher Dr. O HaeChong for helping me a lot in my life and study during my first year in Japan. I am grateful to the former lab researcher Dr. Mangala Amunugama who always gave me motivation and took time to discuss with me when I needed.

I would also extend my gratitude to Mr. Masanori Endo, who was my tutor during my first year study. Endo-san helped me a lot for the setup of my life and study in Japan.

I am thankful to Mr. Ratnayakage Sameera Maduranga Samarasekara, Mr. Md Abdur Rakib and Mr. Wang Yulong from GPSS-GLI for their motivation.

It is also a good chance to convey my gratitude to all the members of Sasaki Lab for providing me endless help and sharing me enjoyable study environment.

Many thanks go to the thesis examination committee, Professor Mino Takashi, Associate Professor Hiroyasu Sato, Associate Professor Tetsuya Sakuma, and Associate Professor Takenori Shimozono for their valuable comments.

Other than the people mentioned above, I appreciate that there are many others who have helped me in multiple ways. I thank all of them, too.

I would also like to acknowledge the Chinese Scholarship Council for providing me the financial support. Without the scholarship, it would be impossible for me to have such a valuable experience.

Last but not least, I wish to express special thanks to my parents for their unconditional and endless support.

Table of Contents

LIST OF FIGURES

LIST OF TABLES

LIST OF ABBREVIATIONS

ADCIRC: Advanced Circulation Model
BKI: Blumberg and Khanta Implicit radiation boundary condition
CCMP: Cross-Calibrated Multi-Platform Meteorological product
CDMC: Central Disaster Management Council of Japan
CDPC: Central Disaster Prevention Council of Japan
CFL: Courant-Friedrichs-Lewy condition
DBC: Downstream boundary condition
DEM: Digital Elevation Model
DHI: Danish Hydraulic Institute
DR3M-QUAL: Distributed Routing Rainfall-Runoff model
ECMWF: European Center for Medium-Range Weather Forecasts
ECOM-si: Semi-Implicit Estuarine and Coastal Ocean Model
ERA-Interim: a global atmospheric reanalysis from 1979 and continuously be extended forward in time until 31 August 2019
ERA-I: Abbreviation of ERA-Interim
ESL: Extreme Sea Level
FVCOM: Finite Volume Coastal Ocean Model
GFS: Global Forecast System
GMSL: Global Meal Sea Level
GSHHG: Global Self-consistent, Hierarchical, High-resolution Geography Database
GVF: Gradually varied flow
HPC: High Performance Computing
HSPF: Hydrological Simulation Program Fortran
IPCC: Intergovernmental Panel on Climate Change
JCG: Japan Coast Guard
JMA: Japan Meteorological Agency
JODC: Japan Oceanographic Data Center
JRA: Japanese Reanalysis Meteorological data
M–F: Mitsuta and Fujii wind model
MSL: Mean Sea Level
NCEP: National Centers for Environmental Prediction
NetCDF: Network Common Data Form
POM: Princeton Ocean Model
PTVA: Papathoma Tsunami Vulnerability Assessment
RCP: Representative Concentration Pathway
RMSE: Root Mean Square Errors
ROM: Regional Ocean Model
SMS: Surface Water Modeling System
SRES: Special Report on Emission Scenarios

SWMM: Storm Water Management Model
TMG: Tokyo Metropolitan Government
USEPA: United States Environmental Protection Agency

LIST OF SYMBOLS

x, *y*, *z*	East, north, and vertical axis in Cartesian coordinate system
$u,\ v,\ w$	*x*, *y*, *z* velocity components, m/s
T	Temperature, ℃
S	Salinity, PSU
ρ	Density, $\mathrm{kg/m^3}$
P	Pressure, Pa
f	Coriolis parameter, $\mathrm{s^{-1}}$
g	Gravitational acceleration, $\mathrm{m/s^2}$
$F_\mathrm{u},\ F_\mathrm{v},\ F_\mathrm{T},\ F_\mathrm{S}$	Horizontal momentum, thermal, and salt diffusion terms
$K_\mathrm{m},\ K_\mathrm{h}$	Vertical eddy diffusion coefficient; thermal vertical eddy diffusion coefficient
ρ_0	Water density, $\mathrm{kg/m^3}$
$\tau_\mathrm{bx},\ \tau_\mathrm{by}$	Bottom stress, $\mathrm{kg\cdot m^{-1}\cdot s^{-2}}$
C_db	Bottom drag coefficient
$C_\mathrm{db\_min}$	The minimum value of C_db
k	Von Karman constant
z_0	Bottom roughness parameter
$\tau_\mathrm{sx},\ \tau_\mathrm{sy}$	Surface wind stress, $\mathrm{kg\cdot m^{-1}\cdot s^{-2}}$
$w_\mathrm{x},\ w_\mathrm{y}$	*x* and *y* component of the wind velocity
ρ_a	Air density, $\mathrm{kg/m^3}$
C_ds	Drag coefficient
U_{10}	Wind speed in 10 m height above mean sea level, m/s
D_min	Thickness of the viscous layer specified at the bottom, m
D	Bathymetry in FVCOM wet-dry treatment, m
h_B	Land elevation, m
H	Water depth in the ocean, m
H_m	Bathymetric height on the land, m
ζ	Water elevation, m
$\hat{\imath}, \hat{\jmath}, \hat{k}$	Integer numbers to identify the three nodes of a triangle cell.
$D_1,\ D_2$	Applicable range parameter of ERA-Interim wind data, m
$D_3,\ D_4$	Applicable range parameter of Mitsuta–Fujii wind model, m
$P(r)$	Pressure at a radial distance r from the typhoon center, hPa
P_c	Typhoon central pressure, hPa
P_0	Ambient or environmental pressure ($= 1013.25$ hPa)
r	Distance from mesh node to the typhoon center, m
r_max	Maximum wind speed radius, m
U_w	Total wind vector
U_w1	Wind vector induced by the rotating component
U_w2	Moving component
$C_1,\ C_2$	Dimensionless coefficients ranging from 0.6 to 0.75

V_{T}	Typhoon forward speed, m/s
F_{B}	Hybrid wind velocity or atmospheric pressure
F_{ERA}	Wind or atmospheric pressure of ERA-Interim reanalysis data
$F_{\mathrm{M-F}}$	Wind or atmospheric pressure of Mitsuta–Fujii wind model
$L_{\max}$	Maximum searching length, m
Δr	Searching increment, m
R_{b}	Distance from the typhoon center to the searching band, m
n	Maximum integer number, $(n-1)\Delta r = L_{\max} - W_{\mathrm{b}}$
m	Integer number, $1 \le m \le n$
W_{b}	Searching bandwidth
$F_{\mathrm{hb-I,i}}$	Wind or atmospheric pressure at the (*i*)th time step in hybrid method I
$F_{\mathrm{JODC,i}}$	Measured wind or atmospheric pressure
N_{T}	Total number of typhoon time steps
M_{w}, M	Earthquake moment magnitude
M_0	Seismic moment, dyne/cm, 1 dyne-cm = 10^{-7} N-m
L_{F}	Length of tsunami fault area, m
W_{F}	Width of tsunami fault area, m
Y_0	Latitude, °
X_0	Longitude, °
d_{c}	Top depth, m
θ	Strike, °
δ	Dip, °
λ	Rake angle, °
U_{s}	Net slip, m
Q	Flow discharge in the pipe, m^3/s
t	Time, s
A	Flow cross section area, m^2
y_{s}	Water depth in the pipe, m
α	Angle of the pipe with respect to horizontal, °
S_0	Slope of the drainage
S_{f}	Friction slope
β	Momentum flux correction coefficient
K	Piezometric correction coefficient
K'	Ambient piezometric pressure correction coefficient
T_{s}	Force due to internal stresses acting normal to the pipe flow cross section *A*, N
γ	Specific weight of the liquid, $\mathrm{N/m}^3$
q_{L}	Lateral flow rate per unit length of *x*, m^3/s
U_{x}	*x* component of the lateral flow velocity, m/s
C_{s}	Surge celerity, m/s
b_{slot}	Slot width, m
R	Hydraulic radius, m
P_{w}	Wetted perimeter, m

n_{m}	Manning roughness
N_{p}	Number of computational nodes in a pipe
Δx_{s}	Space step in pipe system, m
Δt_{s}	Temporal step in pipe system, s
θ_{s}	Finite difference weighting factor
n_{s}	Number of temporal steps
h_{out}	Water level at outfall of pipe system, m
m_{s}	Number of branches from upstream
Δs	Change of manhole storage within a Δt_{s} time, m^3
Q_{in}	Surface inflow to the manhole, m^3/s
Q_{w}	Flow entering or leaving the manhole, m^3/s
$\vec{F}$	Entire vector of functions
$\vec{x}$	Entire vector of unknown variables
$\vec{J}$	Jacobian matrix
$\vec{x}_{new}$	Updated solution in next iteration
$\vec{x}_{old}$	Solution in last iteration
h_{m}	Water depth in the manhole, m
h	Ground surface elevation above the pipe bottom, m
h_{s}	Elevation of surface inundation above the pipe bottom, m
V_{gw}	Discharge exchange between manhole and ground, m^3/s
Δt_{p}	Time step of pipe module in integrated model, s
Δt_{E}	Time step of external mode of FVCOM, s
ΔL	Shortest edge length of the unstructured mesh, m
D_{max}	Maximum bathymetry depth, m
N_{ext}	External running step number in one internal step of FVCOM
N_{int}	Internal mode running step
Δt_{out}	FVCOM output time interval
T_{F}	FVCOM model time
N_{gw}	External mode running steps
d_{s}	Circular pipe diameter, m
r_{s}	Circular pipe radius, m
P_1, P_2	Atmospheric pressure, hPa
v_1	Vertically averaged horizontal velocity in section 1-1, m/s
H_1	Water surface elevation at section 1-1, m
v_{c}	Overflow velocity in section 2-2, m/s
H_2	Height of sea dike or river bank on the coastline, m
h_{c}	Overflow depth above the sea dike or river bank, m
F_{r}	Froude number
$\bar{v}$	Average flow velocity of flow cross section, m/s
$\bar{h}$	Flow depth of flow cross section, m
V_{nodal}	Nodal overflow volume at a certain coastline node, m^2
V_{dike}	Total overflow volume of the coastline, m^2

N_{out}	Total output time steps
m_{c}	Total number of the coastline nodes
L_{s}	Pipe length, m
ε	Finite difference convergence parameter
A_{c}	Area of one triangle mesh cell
$A_1,\ A_2,\ A_3$	Sub-areas of one mesh cell divided by median lines, m^2
$\alpha_1,\ \alpha_2,\ \alpha_3$	Percentage of $A_1,\ A_2,\ A_3$ in one triangle mesh cell
$Z_1,\ Z_2,\ Z_3$	Inundation height at three vertex of one mesh cell, m
Z	Inundation height at center of the mesh cell, m
$a_s,\ b_s,\ c_s$	Three side lengths of one triangle mesh cell, m
S_{c}	$(a_s + b_s + c_s)/2$, m
$V_{\mathrm{inundation}}$	Inundation volume at this triangle mesh cell, m^3
N	Number of possible scenarios for a given earthquake
$N_{\mathrm{L_F}},\ N_{\mathrm{W_F}}$	Total numbers of meshes covering the length and width of the maximum fault area
$N_{\mathrm{L}},\ N_{\mathrm{W}}$	Total numbers of sub-faults covering the length L and width W
Q_{Ara}	Discharge of Arakawa River, m^3/s
Q_{Edo}	Discharge of Edogawa River, m^3/s
Z_{bank}	Elevation of the river bank, m
H_{r}	Bathymetry of the river, m
D_{r}	Water depth of the river, m
Q_{r}	Rain flow, m^3/s
C_{L}	Land surface runoff coefficient
I	Rainfall intensity, mm/h
A_{r}	Area of the study zone, m^2

1. Introduction

1.1 Background

Tokyo is one of the largest cities in the world, which has a population of over 13 million and an area of 2,188 km^2. Tokyo Bay, which is to the south of Tokyo's central business district, plays an essential role as being the major political and economic center in Japan. Regions along the coastlines of Tokyo Bay, which spans the coastal areas of Tokyo Metropolitan, Kanagawa Prefecture, and Chiba Prefecture, is the most populated and industrialized area in Japan and are exposed to all types of coastal hazards, such as typhoon induced storm surge[1-4], river flood caused by heavy rainfall, and earthquake tsunamis[5-8].

Tropical cyclone, also known as typhoon or hurricane, is an intense circular storm that originates over warm tropical ocean surface, and is characterized by low pressure system, high wind and heavy rain. Normally, an ocean temperature of 26.5 ℃ spanning through a depth at least 50 meters is considered the minimum condition for tropical cyclone formation. Since 1951, more than 1,750 typhoons happened in the Northwest Pacific Ocean area, have been recorded by the Japan Meteorological Agency (JMA)[9], as shown in Figure 1.1 (left panel), and typhoons that passed through the Tokyo Bay area are also screened out and shown in Figure 1.1 (right panel).

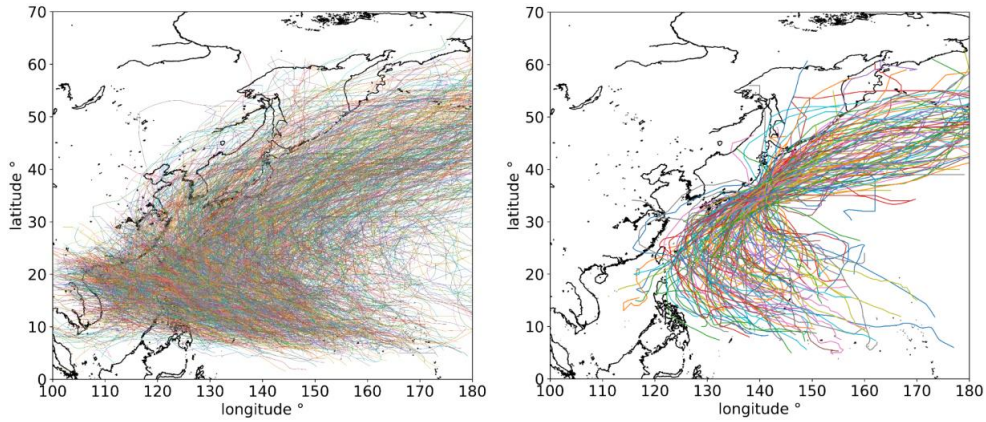

Figure 1.1 Typhoon tracks in the Northwest Pacific Ocean since 1951 (left panel) and those passing through Tokyo Bay (right panel)

Storm surge is defined as the abnormal change in sea level that may accompany either extratropical or tropical storms[10]. In addition to the tides, the magnitude of storm surge is dependent on the wind speed, the typhoon size, the typhoon moving track, the speed of forward translation, the typhoon central pressure, the width and slope of the adjacent continental shelf and the local land topography. Storm surges have a hazardous impact on coastal regions, which may threaten the infrastructures, ecosystems, and even human lives. In the recent history, Typhoon Jebi, which formed on August 28th, 2018, struck Japan on September 4th, 2018, and caused serious damage including 13 people deaths and 741 people injured, and the storm surge inundated many areas of Kobe and Osaka[11]. Typhoon Faxai passed through Tokyo Bay on September 9th, 2019, and caused at least 1 deaths and about 40 injured. Among the historical storm

surge events happened in Tokyo Bay, the typhoon in the 6th year of the Taisho era (1917) caused one of the largest historical storm surge, resulting in overflow beyond the coastal defense infrastructure and leading to extensive damage to properties and a loss of more than 1,300 lives[1].

Storm surge has been regarded as a priority in the disaster mitigation in Tokyo Bay area, and 1917 Taisho Typhoon and its storm surge has played an important role in the development of disaster prevention such as the determination of the height of sea walls[4]. The target sea level departure for the coastal dike in the closed-off section of the bay has been increased from 2.0 m to 3.0 m. Moreover, a study on the potential loss caused by the storm surge in the future has been carried out using the Taisho Typhoon[2]. After the 1917 Taisho Typhoon, in Tokyo Bay, there was no devastating storm surge floods since Typhoon Kitty in the year of 1949. Typhoon Vera, which was also known as Ise-wan Typhoon in Japan made landfall near Ise Bay on September 30, 1959, it generated a 3.5 m catastrophic storm surge that breached the poorly constructed dikes in the area, inundated the low-lying lands, and caused the worst storm surge disaster ever recorded in history of Japan[3]. Since then, Ise-wan Typhoon is often used as a basic case in numerical simulations, combining with Tokyo Bay's geographical features, to derive estimations of potential storm surge levels.

Since 2000, severe storm surge disasters caused by powerful typhoons have been observed in many places over the world, the typical cases include Hurricane Katrina in 2005, Cyclone Nargis in 2008, Hurricane Sandy in 2012 and Typhoon Yolanda (Haiyan) in 2013. Climate scientists have suggested that the intensity of tropical cyclones is likely to be strengthened in the near future, on account of the increased sea surface temperature caused by greenhouse warming[12]. Thus, super typhoons are expected to increase both in number and intensity[13].

Tsunami is a series of waves in the ocean or in a large lake caused by the displacement of a large water volume. The potential tsunami sources include great earthquakes in the ocean, volcanic eruptions in the ocean islands and underwater explosions, all of them have the ability to generate a tsunami.

Japan is an earthquake-prone nation as it is located on and near the plate boundaries of the North American plate, Eurasian plate, Philippine Sea Plate and Pacific plate[14]. The Sagami Trough is located in the Kanto region of central Japan. In the recent history, several catastrophic earthquake tsunamis happened and caused devastating losses, for example, in the 1923 Taisho Kanto earthquake, more than 105,000 people lost their lives in Tokyo[15], and this earthquake caused an approximately 1.5 m coastal uplift at the southern part of the Miura and Boso Peninsulas. The earthquake also produced large tsunami with heights of more than 5 m along the coast around Sagami Bay. Another example is the 1703 Genroku Kanto earthquake which resulted in about 10,000 casualties. The coastal uplift at the Miura Peninsulas and the resultant tsunamis around Sagami Bay were similar to those caused by the 1923 Taisho Kanto earthquake. The source areas of these two events also overlapped, and they are both within and around the Sagami Bay, but tsunamis due to the 1703 Genroku earthquake propagated off the Boso Peninsula since it had a larger rupture area. Past Kanto earthquakes can be divided into two types, one is the Taisho type and the other is the Genroku type. Taisho type earthquakes are thought to happen in a more frequent manner with an occurrence of 400 years on average compared to Genroku type earthquakes, and after several occurrences, e.g., around 2,000 to 2,700 years' time interval, a Genroku type earthquake would take place[16].

Tsunami behavior in Tokyo Bay has also been studied, and most of the previous studies focused on the description and analysis of the major historical tsunamis that attacked Tokyo Bay, such as the 1703 Genroku Kanto earthquake tsunami, the 1854 Ansei Tokai earthquake tsunami, the 1923 Taisho Kanto earthquake tsunami, and the 1960 Chilean earthquake tsunami[7]. Hino and Hino[17] found that the predominant resonant periodicity of the tsunami wave in Tokyo Bay is approximately 60 min to 90 min by performing a numerical experiment on the response characteristics of Tokyo Bay to long waves. Takayama et al.[18] performed a numerical analysis on the behavior of the tsunami caused by the 1923 Taisho Kanto earthquake, including the characteristics in ports and harbors of Tokyo Bay. Hiraishi and Yasuda[19,20] also carried out numerical research on the 1923 Taisho Kanto earthquake tsunami and the 1703 Genroku Kanto earthquake tsunami. During the 2011 Tohoku earthquake tsunami, the tsunami wave also traveled to Tokyo Bay, and caused damage in some parts of the bay. Sasaki et al.[7] studied the effect of 2011 Tohoku earthquake tsunami on Tokyo Bay and the damage of seaweed farming using a field survey and numerical approach.

River flood happens usually due to the large discharge occurring in the upstream of the river, which could be caused by heavy rainfall in a short period. In recent years, river flood has become one of the major natural disasters that occurs during the monsoon season or typhoon weather in Japan. According to the Disaster Management Report[14] proposed by the Cabinet Office of Japanese Government, there is a rising trend of heavy downpours in recent years; thus, there is a strong need to fortify the measures for rapid, effective prediction, evacuation and relief, in anticipation of large scale flood disasters. The Central Disaster Management Council (CDMC) has published a series of disaster scenarios in 2008, which may provide details about the anticipated damage loss in a number of possible cases, for example in Arakawa River and Tonegawa River. Arakawa River and Edogawa River are two large rivers that pass through Tokyo, and flow into Tokyo Bay. Arakawa River passes through Koto ward of Tokyo, where the altitude is below the mean sea level (0 m). Therefore, it has risks of suffering flood in case typhoon brings a large amount of rain that increases the river discharge in a short time period, and high water level caused by storm surge at the river mouth may also elevate the water level in the river mouth, which can deteriorate the flood in the upstream. The possible scenarios described in the CDMC reports include the possible destruction of the strengthened weirs along the river banks of Tonegawa River and Arakawa River in Tokyo metropolitan area which may be caused by the heavy downpours, and in a worst case, such a disaster could lead to 2,600 deaths and another 1.1 million people stranded. To minimize the damage in such an event, the CDMC has formulated the basic policies for large scale water hazard in the metropolitan area, and multiple measures have been promoted so that prompt evacuation can be effected.

Since joint impacts of the three hazards (storm surge, tsunami, and river flood) have not been investigated, in this study, the assessment of inundation vulnerability caused by them is the research target. Inundation simulation is a widely used and straightforward way in coastal vulnerability assessments. However, it is computationally expensive, and considering an increase in the number of cases in the multiple hazard analysis, it is necessary to develop an efficient method to identify overall vulnerability and to screen representative scenarios for detailed analysis. For this purpose, an efficient method was proposed using an estimated overflow volume without computing inundation, which was validated by comparing with inundation simulation. In addition, although inundation period is one of the most important parameters

for the vulnerability assessment, drainage through drainage pipes has often been ignored. To consider this drainage, a drainage pipe model was implemented in FVCOM for the first time. The efficient method was then applied to multi-hazard vulnerability assessment. The worst multi-hazard case and the resultant vulnerability was identified. The difference between single hazard and multi-hazard vulnerabilities including moderate multiple hazards and worst single hazard was also discussed. The role of drainage system in local coastal flood was investigated using the integrated model. Finally, some lessons for better disaster prevention and prediction were extracted. The framework of this research is shown in Figure 1.2.

1.2 Objectives

The main objective of this study is to investigate the multi-hazard vulnerability of Tokyo Bay. To achieve this objective, the followings can be regarded as specific goals:

- Extend the functions of FVCOM by embedding a drainage pipe model for multi-hazard computation
- Demonstrate the applicability of overflow volume approach for multi-hazard vulnerability assessment
- Investigate the vulnerability of Tokyo Bay to multiple coastal hazards
- Clarify the importance of drainage pipe system in local inundation events
- Propose a practical way to enhance the accuracy of storm surge hindcasting

The reason why selecting FVCOM is explained in Section 2.1.1. The significance of the overall objective and specific goals is also discussed in Chapter 2.

1.3 Outline of the dissertation

This dissertation is organized in seven chapters. The content of each chapter is given as:

Chapter 1 contains the background and objectives of this research.

Chapter 2 provides a literature review regarding the numerical models and software, and vulnerability study methods.

Chapter 3 introduces the methods including the adopted numerical model, the developed model, and the vulnerability measurement method.

Chapter 4 describes the model validation including storm surge model, drainage pipe model, the integrated model and the vulnerability measurement method.

Chapter 5 presents the investigation of multi-hazard vulnerability in Tokyo Bay using the integrated coastal ocean model.

Chapter 6 is the discussion part.

Chapter 7 summarizes the conclusions and recommendations.

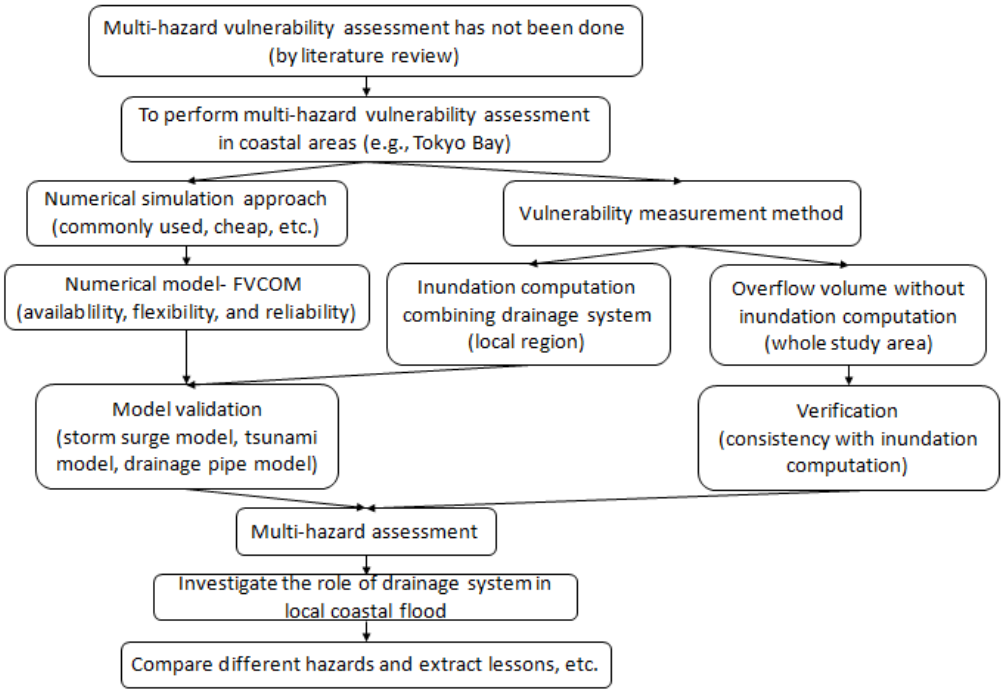

Figure 1.2 Logical flow of this research

2. Literature Review

This chapter reviews the numerical models including the commonly used numerical methods in coastal ocean modeling communities, discusses the advantages and limitations of different numerical methods that are used in these coastal ocean models, based on which the coastal ocean model that will be used in this work is selected. By reviewing the progress of tsunami induced pipe overflow model and multi-hazard vulnerability studies, the significance of the study objectives in this work is highlighted.

2.1 Numerical models and software

2.1.1 Coastal ocean model

The challenging issue in coastal modeling includes resolving the irregular coastal geometry and ensuring conservation of momentum, mass, and heat. In the recent twenty years, finite difference and finite element methods have been widely used in the coastal modeling. The most popular finite difference and finite element coastal ocean models are the Princeton Ocean Model (POM)[23], the semi-implicit Estuarine and Coastal Ocean Model (ECOM-si)[24], the Regional Ocean Model (ROM)[25]. The finite difference method has its advantage in simple code structure and computational efficiency. However, it is difficult in fitting complex coastline geometry accurately. The advantage of the finite element method can overcome this limitation by using unstructured meshes. However, the finite element method usually involves a large size matrix calculation at every time step, which is at the cost of computational efficiency. In addition, as the governing equations are numerically solved by a least square variation method, the finite element method may not be able to provide an explicit way to check the mass conservation in each cells[26].

Moreover, from the perspective of economy, free open source model is often preferable. The Finite Volume Coastal Ocean Model[21] (FVCOM), is one of the commonly used free hydrodynamic model featured by unstructured grid. Unlike differential forms used in a finite difference model, FVCOM discretizes the integral form of the governing equations, and since these integral formulas could be solved by flux calculation used in the finite difference method over arbitrary unstructured meshes, the finite volume approach is better at guaranteeing mass conservation in both individual control volumes and the entire computational domain. Thus, in view of technology, FVCOM combines the advantages of finite difference methods for simple discrete efficiency and finite element methods for fitting coastal geometry in a flexible way[26]. Other commonly used coastal ocean numerical models include Telemac-2d/3d[22], Delft-3d[27], ADCIRC[28], MIKE21[29], etc.

Based on the above discussion on the advantages and limitations among different coastal ocean models, in this study, FVCOM is adopted as the coastal ocean model considering the availability, flexibility and reliability. The introduction and discussion about FVCOM model can be found in Chapter 3.1.1.

2.1.2 Drainage pipe model

Many models have been developed for the simulation of flow in a drainage pipe network. Storm

Water Management Model (SWMM)[30] developed by United States Environmental Protection Agency (USEPA), InfoWorks CS[31] developed UK Wallingford Hydraulic Research Institute, and MIKE-URBAN[32] developed by Danish Hydraulic Institute (DHI) are widely used in the urban flood research community. Also, there are other models such as Hydrological Simulation Program Fortran[33] (HSPF), Distributed Routing Rainfall-Runoff model (DR3M-QUAL)[34], etc. However, these models are mostly focused on rainfall induced urban flood, and lack of the capability of simulating multiple coastal hazards.

Mizuhashi et al.[35] developed an integrated numerical model for computations of tsunami inundation especially focusing on the penetration through underground pipelines, and the model was validated and applied to the tsunami inundation observed around Nakoso in Fukushima during 2011 Tohoku earthquake tsunami. However, their focusing point in that work was to demonstrate the reliability of the model, they did not show more details regarding the importance of underground pipelines in inundation events. Ito et al.[36] verified a three dimensional two-phase numerical model by conducting physical experiments. It was pointed out that the tsunami induced pipe overflow should be considered as an important event, and due to the large volume of inundation from the overflow, part of evacuation routs have risks of being lost during tsunami attack. However, as they told, their model has a high performance to evaluate tsunami induced pipe overflow problem, but the large computational load is one of the main disadvantage. Therefore, a simple and practical simulation method, e.g., one dimension simulation method would be better from engineering point of view. Takabatake et al.[37-39] improved Ito's model, and it combines a one dimensional pipe network flow model and two dimensional inundation model. The model was verified through hydraulic experiments. Then, this model was applied to investigate the risks of tsunami inundation via pipelines. It shows that the influence of the tsunami inundation via the pipelines on coastal areas is not small and it is likely to influence the initial phase of evacuation. However, the function of pipeline in draining inundation has not been clarified, and also they only applied their model in tsunami inundation case, which means the applicability of their model under multiple coastal hazards is still unknown.

Based on the above, in this work, the drainage pipe network model is developed and firstly embedded in FVCOM program. The integrated model has advantages including efficient computation (one dimensional drainage pipe model and possibility of running in parallel in supercomputer), capability of simulating multiple coastal hazards such as storm surge, tsunami, and river flood simultaneously. The unsteady flow theory and the development of drainage pipe model are introduced in Chapter 3.4.

2.2 Overview of vulnerability studies on coastal disasters

The concept of vulnerability is originally defined as the susceptibility to damage or injury by the United Nations Disaster Relief Organization[40]. However, over the years, it has been widely recognized as the degree of susceptibility or fragility of communities, systems, or groups to risks, which may also include their own capacity to adapt to the hazardous conditions[41].

Measuring vulnerability is difficult especially in quantitative hazard studies, and it is often largely dependent on the selection of indicators according to the data. In addition, current vulnerability

assessment studies would usually not take into account all the possible pressures that are related to the diminished capacity and decreased resilience of the communities[42].

In this section, vulnerability studies of tsunami and storm surge, multi-hazard vulnerability studies, and the vulnerability studies of Tokyo Bay are reviewed and discussed including their methods and limitations.

2.2.1 Vulnerability studies on tsunami and storm surge

After the 2004 Indian Ocean tsunami, many studies and much effort have been made to develop vulnerability assessment models for different kinds of exposure in the tsunami, most of the works are dedicated to investigate the vulnerability of buildings. The method that is commonly used in these studies is empirical fragility functions and damage curves[43]. However, data collected during post-tsunami field surveys were crucial to establish the relationship between the observed damage level and tsunami flow depth or current velocity.

Dias et al.[44], Koshimura et al.[45] and Leone et al.[46] collected data during post-tsunami field surveys and established the mathematical relation between observed damage level and tsunami flow depth in the 2004 Indian Ocean tsunami. Suppasri et al.[47-49] used the damage dataset, and developed the fragility functions considering different types of buildings. They calculated the cumulative probability of damage occurrence using the statistical method described in Koshimura et al.[45], and they demonstrated that the damage of different buildings classified by the construction materials and the number of storeys is a function of the inundation depth, which may have a great importance to support the construction of tsunami-resistant buildings in the future. Furthermore, Valencia et al.[50] developed a new approach to assess the tsunami vulnerability by means of deriving fragility functions and damage curves for the European Mediterranean coastal buildings in a European Union project, and the method was also used to investigate the expected tsunami-induced buildings' damage in their test-sites.

Alternatively, approaches based on ranking and weighting of the damage controlling factors are becoming popular in the evaluation of buildings' vulnerability to tsunami impact[43,44]. These approaches can be used to estimate the vulnerability levels for coastal areas where no available data of the building damage could be obtained.

Also, the Papathoma tsunami vulnerability assessment (PTVA) method[51,52] is developed and applied to assess the vulnerability level through calculation of a vulnerability index for each building among the inundation area. It considers multiple vulnerability factors such as number of storeys, building construction materials, moveable objects, etc. However, the PTVA approach has its limitations because when evaluating the building vulnerability, the PTVA model does not take into account any physical parameters of tsunami propagation such as flow depth or current velocity, and it requires a large number of input data which makes its application difficult in large areas with various types of buildings[53]. In the study conducted by Omira et al.[54], they overcame the PTVA limitation by detailed tsunami inundation simulation on the flow depths.

In addition, Shimozono et al.[55] explored the dike breach processes using a high resolution flood model with shock-capturing property. It showed that the levee vulnerability can be identified by the local flow parameters based on high resolution model. They also clarified that due to the neglecting of

non-hydrostatic pressure, the modeled overflow discharge is slightly underestimated compared to that calculated using empirical formulas. However, their method is based on inundation simulation which is commonly thought to be computationally expensive, and they did not investigate the agreement between the dike overflow volume computed using empirical formula and the inundation volume using inundation simulation approach.

In storm surge vulnerability studies, Valchev et al.[56] assessed the magnitude of storm-induced flooding along Varna regional coast and identified the susceptible coastal sectors by employing an European Union coastal risk assessment framework. Rana et al.[57] identified the cyclone associated hazards through questionnaire survey and participatory rural appraisal method in Paikgacha Upazilla of Khulna District. Vulnerability assessment has been done to identify the most vulnerable sector by the impacts of multi-hazard using weighted index method. The collected data reveals that salinity, water logging, embankment erosion, tidal surge and storm surge are the major cyclonic hazards and have adverse effects on agriculture, structure, occupational pattern, consumption pattern and service facilities of the study area. Sajjad et al.[58] developed a coupling approach by integration of ecosystems and tradeoffs model, which was based on seven different biogeophysical variables. Their study highlighted the criticality of the restoration of natural habitats. Park and Lee[59] applied the Naive-Bayes classifier model and implemented the coastal multi-hazard risk analysis along the South Korean coast. The vulnerable areas that could be damaged by typhoon and heavy rainfall was identified. Rao et al.[60] assessed the vulnerability of Andhra Pradesh state in India to the storm surge inundation considering the impact of global warming via scenario-based numerical simulations. Lapidez et al.[61] identified the vulnerable areas of Philippines using simulation of Typhoon Haiyan induced storm surge. They calculated the maximum probable storm surge height for every coastal locality by running simulations of Haiyan-type conditions but with tracks of tropical cyclones from 1948-2013. Lee et al.[62] evaluated the vulnerability of Korea peninsula to typhoons by using a framework that involved society and economy factors. Yuan et al.[63] proposed a method to aggregate different weighting techniques and quantify vulnerability to storm surges using social, economy, and environmental indicators. Kunte et al.[64] developed a coastal vulnerability index (CVI) for the state of Goa. The vulnerability of different administrative units of the state to flooding and inundation was identified.

By reviewing the existing studies regarding tsunami and storm surge vulnerability, the applicability and limitations of using overflow volume as an indicator for inundation vulnerability assessment has not been clarified in the past.

2.2.2 Multi-hazard vulnerability studies

Many studies have been conducted on multi-hazard vulnerability in the world, which are not only associated with earthquake tsunami or typhoon storm surge, but also include heavy rainfall, fire, water quality, etc.

Rahman et al.[65] performed the vulnerability assessment case study on multiple hazards including fire, earthquake, and water-logging in one ward of Dhaka city corporation area. The Geographic Information System was applied to survey the study area. Their findings denote that there are a certain number of structures in very risk position which should receive immediate hazard mitigation measures.

Vivek et al.[66] carried out a multi-hazard vulnerability assessment for the Visakhapatnam coast using five parameters as inputs, i.e., the probability of coastal erosion, coastal slope, coastal elevation, sea level change rate and tsunami arrival height. Multi-hazard maps were made by overlaying the multi-hazards which are affecting the coastal zones. Islam et al.[67] developed a coastal vulnerability index (CVI) by using seven physical parameters including geomorphology, coastal slope, shoreline change rate, rate of sea level change, mean tide range, bathymetry and storm surge height. These variables are considered as relative risk parameters and integrated through geospatial techniques, and then ranked to estimate the degree of coastline vulnerability to sea level rise. Depietri et al.[68] assessed vulnerabilities and risks of New York city to three climate-related hazards, i.e., heat waves, inland flooding, and coastal flooding, by using socioeconomic indicators. The analysis incorporates local experts' opinions to identify sources of multi-hazard risk and weight indicators in the assessment. Clarke and Obrien[69] considered the spatio-temporal processes associated with multi-hazard and cascading extreme events, e.g., earthquakes, floods, landslides, and their impacts on road and rail transport infrastructure networks. Mulyani et al.[70] developed a multi-hazard risk assessment framework for earthquake and tsunami, and used this framework in the city of Padang. They concluded that the building risk associated with tsunami in Padang is considerably lower than that of earthquake, due to the infrequent occurrence of tsunamis in the area. Appelquist et al.[71, 72] developed a coastal hazard wheel framework for hazard assessment and management, which can be used in areas with limited geophysical data availability and institutional capacity. This method provides information on the hazards of ecosystem disruption, gradual inundation, salt water intrusion, erosion and flooding, and has been applied to the state of Djibouti and Karnataka, India. Sahoo and Bhaskaran[73] evaluated the coastal vulnerability for the Odisha coast associated with landfalling tropical cyclones. They estimated the coastal vulnerability index (CVI) from the combined effects due to storm surge and onshore inundation, and further combined it with social, economic, and environmental vulnerability, which provided an integrated overview on the vulnerabilities for the Odisha coast. Mahendra et al.[74] generated the multi-hazard vulnerability map using the historical storm surge heights, future sea level, future shoreline and high resolution topography, which became vital tools for the coastal disaster management in Nellore district, east India. Eshrati et al.[75] presented the casualty model and analyzed the applicability of casualty model for the assessment of multi-hazards vulnerability of building and human with a GIS-based approach. Kumar et al.[76] developed a coastal vulnerability index (CVI) for the maritime state of Orissa using eight relative risk variables, which can be used by the state and district administration involved in the disaster mitigation and management plan. Wiley and Gianotti[77] generated four indices that could reflect several components of risk perception using surveyed data and predicted the holistic risk perception through multivariate regression analysis. Their findings focused on how people perceive and respond to risk in a multi-hazard environment. Furlan et al.[78] developed a multi-hazard assessment method and applied it to the Adriatic sea. The relative risk scenarios induced by endogenic and exogenic pressures over vulnerable marine targets are evaluated. They found that the higher relative hazard scores are linked to exogenic pressures, e.g., sea surface temperature variation, while the lower ones resulted from endogenic and more localized stressors, e.g., abrasion, nutrient input. Mukhtar[79] reviewed the national multi-hazard early warning system plan of Pakistan. The gaps and shortcomings of the prevailing practice are identified. Furthermore, this research also proposed practical

solutions and recommendations for improvement and better alignment of the early warning system. Haigh et al.[80] developed a capacity analysis framework for multi-hazard early warning through the processes of consultation, which covers a range of dimensions, such as legislative, planning, infrastructure, technical and scientific, and institutional partnerships. Gallina et al.[81] presents a review of existing multi-hazard assessment concepts and tools applied by organizations and projects in a climate change perspective. The overall results of the review show that multi-hazard approaches do not consider the effects of climate change and mostly rely on the analysis of static vulnerability. Johnson et al.[82] presents the results of a GIS-based assessment of present risks to socio-natural hazards in two districts of Hong Kong by utilizing indicators to describe the hazards and vulnerabilities. Borg et al.[83] presents insights regarding the assessment of vulnerability and overall system resilience with reference to multi-hazard events in the context of Venice lagoons and territories in the North Adriatic region. Ahammed and Pandey[84] carried out the coastal multi-hazard vulnerability mapping along the Krishna-Godavari deltaic plain, eastern coast of India. The study revealed that the use of multi-layer information combined with geospatial tools is more reliable and cost effective for disaster preparedness and adaptation. Maryam et al.[85] identified a critical center of hazards and areas which are mostly vulnerable to hazards associated with desertification, tectonic, cycles of aridity and surface processes of water and wind. Younus and Sharna[86] explored the perceptions of coastal communities with regard to vulnerability and adaptation strategies in four different areas of Bangladesh by a weighted matrix index approach.

By reviewing these studies, multi-hazard vulnerability (storm surge, tsunami, and river flood) in coastal areas has not been studied in history.

2.2.3 Vulnerability studies of Tokyo Bay to coastal hazard

A few studies have been carried out regarding the vulnerability of Tokyo Bay.

Matsuda[87] verified the vulnerability of Tokyo to natural disasters. The artificial changes of natural conditions including river courses, withdrawal of ground water continue to affect natural disasters and countermeasures in the Tokyo lowland. Takabatake and Shibayama[88] clarified the risk of storm surge and tsunami in Tokyo port by using three different numerical simulations, a storm surge simulation, a tsunami simulation and an overland inundation simulation. As a result, the maximum storm surge height in Tokyo Port was 1.8 m and the typhoon course was clarified. In the tsunami simulation, tsunami behavior in Tokyo Bay is calculated using three types of earthquakes. Among them, the earthquake which causes the highest tsunami in Tokyo Port is the Keicho earthquake, and the tsunami height around Tokyo Port is about 1.5 m.

Tatekoji et al.[89] investigated the vulnerability of Tokyo Bay to storm surge under the impact of bathymetry changes due to urbanization. They found that the highly vulnerable area affected by storm surges has been shifted from mudflat shallow area in the inner bay to the below-sea-level inland area because of the continuous landfill and urbanization activities. Hirano et al.[90] investigated the maximum possible typhoon conditions according to the Intergovernmental Panel on Climate Change (IPCC) Special Report on Emission Scenarios (SRES) A1B using an atmospheric-ocean-wave coupled model. Then, the storm surge level in a closed-off section of Tokyo Bay was numerically assessed from the perspective of risk assessment and disaster management. Their study shows the sea-land interaction and river flows may

significantly affect the depth and increase of inland inundation extent. Ishikawa and Akoh[91] numerically assessed the river flood risk in lowland Tokyo areas in the seventeenth century. A series of numerical flow simulations were conducted to elucidate the hydraulic function of the Nihon levee system, in which levee overtopping and inundation front motion were incorporated. Besides, the government of Tokyo Metropolitan[92, 93] and Chiba Prefecture[94] made efforts for prediction of maximum inundation induced by expected worst typhoon storm surge.

Based on the above summary of the existing works, no studies have been conducted regarding the joint impact of storm surge, river flood and tsunami. Thus, in this thesis work, the assessment of inundation vulnerability caused by them is the research target.

3. Methodology and Data

In this chapter, the vulnerability measurement method used in this research and the numerical models, including the parametric typhoon model, a hybrid method combining the parametric typhoon model and reanalysis meteorological data, the method for tsunami simulation using FVCOM, development of the unsteady flow drainage pipe network model and its coupling with FVCOM are introduced.

3.1 Numerical model-FVCOM

FVCOM was initially developed by a team effort at the University of Georgia with support from Georgia Sea Grant College Program in 1999. The model development team was led by C. Chen and R. C. Beardsley (the Woods Hole Oceanographic Institution), and H. Liu, T. Wang are the members, they contributed to the completion of the original FVCOM code structure. A series of validation experiments were conducted to demonstrate the model capability. The conversion of FVCOM to Fortran 90/95 was carried out, the coding structure was modularized and the capability for parallel computation was added with team led by G. Cowles[95]. The first version of FVCOM user manual was published in 2004 (FVCOM 2.4), and then the second one was published in 2006 (FVCOM 2.6). In the present study, FVCOM 4.3 is utilized for performing simulations.

FVCOM has been tested against other well-established models and is being widely used in studies of coastal ocean circulation[96,97]. FVCOM uses a “terrain following” sigma coordinate transformation in vertical to accommodate irregular bathymetry, and a non-overlapping unstructured triangular grid in horizontal to resolve dynamics in regions with complex shorelines.

3.1.1 Governing equations

The original version of FVCOM consists of momentum, continuity, temperature, salinity, and density equations using the modified Mellor and Yamada “level 2.5” turbulent closure scheme for vertical mixing, and Smagorinsky eddy parameterization for horizontal dissipation and diffusion. The model uses a flux calculation method integrated over each model grid control volume to solve the primitive equations, and a mode-splitting method with external and internal mode time steps is used to accommodate the faster and slower barotropic and baroclinic responses. Two-D external mode is numerically integrated using a modified fourth order Runge-Kutta time-stepping scheme, and three-D internal mode is integrated using the second order Runge-Kutta time-stepping scheme. The advantage of using FVCOM can be mainly attributed to the triangular grids, which suits the complex coastline geometry well especially for the study areas where there are densely distributed river networks and artificial drainage channels, and also the finite volume approach can ensure good mass conservation of the model. The point wetting-drying treatment technique is included to predict the water covering and uncovering process in the tidal zone or inundation area. The governing equations consist of the following momentum, continuity, temperature, salinity, and density equations:

$$\frac{\partial u}{\partial t}+u\frac{\partial u}{\partial x}+v\frac{\partial u}{\partial y}+w\frac{\partial u}{\partial z}-fv=-\frac{1}{\rho_0}\frac{\partial P}{\partial x}+\frac{\partial}{\partial z}\left(K_m\frac{\partial u}{\partial z}\right)+F_u, \tag{3-1}$$

$$\frac{\partial v}{\partial t}+u\frac{\partial v}{\partial x}+v\frac{\partial v}{\partial y}+w\frac{\partial v}{\partial z}+fu=-\frac{1}{\rho_0}\frac{\partial P}{\partial y}+\frac{\partial}{\partial z}\left(K_m\frac{\partial v}{\partial z}\right)+F_v, \tag{3-2}$$

$$\frac{\partial P}{\partial z}=-\rho g, \tag{3-3}$$

$$\frac{\partial u}{\partial x}+\frac{\partial v}{\partial x}+\frac{\partial w}{\partial x}=0, \tag{3-4}$$

$$\frac{\partial T}{\partial t}+u\frac{\partial T}{\partial x}+v\frac{\partial T}{\partial y}+w\frac{\partial T}{\partial z}=\frac{\partial}{\partial z}\left(K_h\frac{\partial T}{\partial z}\right)+F_T, \tag{3-5}$$

$$\frac{\partial S}{\partial t}+u\frac{\partial S}{\partial x}+v\frac{\partial S}{\partial y}+w\frac{\partial S}{\partial z}=\frac{\partial}{\partial z}\left(K_h\frac{\partial S}{\partial z}\right)+F_S, \tag{3-6}$$

$$\rho=\rho(T,S) \tag{3-7}$$

where x, y, z are the east, north, and vertical axis in the Cartesian coordinate system; u, v, w are the x, y, z velocity components; T is the temperature; S is the salinity; ρ is the density; P is the pressure; f is the Coriolis parameter; g is the gravitational acceleration; F_{u}, F_{v}, F_{T}, and F_{S} represent the horizontal momentum, thermal, and salt diffusion terms; K_{m} and K_{h} are the vertical eddy diffusion coefficient and the thermal vertical eddy diffusion coefficient.

The bottom stress is computed according to the quadratic law:

$$\left(\tau_{\mathrm{bx}},\tau_{\mathrm{by}}\right)=C_{\mathrm{db}}\rho_0\sqrt{u^2+v^2}(u,v) \tag{3-8}$$

where ρ_0 is the water density, (u,v) are the x and y component of the water velocity, the bottom drag coefficient, C_{db} , is determined by matching a logarithmic bottom layer to the model at a height z_{ab} above the bottom, i.e.,

$$C_{\mathrm{db}}=\max\left[\frac{k^2}{\ln\left({}^{z_{\mathrm{ab}}}/_{z_0}\right)^2},C_{\mathrm{db\_min}}\right] \tag{3-9}$$

where $k=0.4$ is the von Karman constant, and z_0 is the bottom roughness parameter, and $C_{\mathrm{db\_min}}$ is the minimum value of C_{db}, which typically varies between 0.002 and 0.004, and in FVCOM, the default value is 0.0025. In this study, the default value is selected.

The surface wind stress is computed by

$$\left(\tau_{\mathrm{sx}},\tau_{\mathrm{sy}}\right)=C_{\mathrm{ds}}\rho_{\mathrm{a}}\sqrt{w_{\mathrm{x}}^2+w_{\mathrm{y}}^2}(w_{\mathrm{x}},w_{\mathrm{y}}) \tag{3-10}$$

where $(w_{\mathrm{x}},w_{\mathrm{y}})$ are the x and y component of the wind velocity, respectively, ρ_{a} is the air density, the drag coefficient, C_{ds} is dependent on the wind speed, and in FVCOM source code, Large and Pond[98] scheme is used:

When $U_{10}<11\,\mathrm{m/s}$,

$$C_{\mathrm{ds}}=1.2\times10^{-3} \tag{3-11}$$

When $11\,\mathrm{m/s}\le U_{10}<25\,\mathrm{m/s}$,

$$C_{\mathrm{ds}}=(0.49+0.065\times U_{10})\times10^{-3} \tag{3-12}$$

When $U_{10}\ge25\,\mathrm{m/s}$,

$$C_{\mathrm{ds}}=(0.49+0.065\times25)\times10^{-3} \tag{3-13}$$

3.1.2 Development of unstructured mesh system

In Tokyo Bay, there are many reclamation lands and river channels. The way of dealing with them in mesh generation may impact the numerical simulation results. Also, in the tsunami simulation or inundation simulation, nesting mesh system is usually common because mesh systems with different sizes are needed for the sake of accuracy, and the typical mesh size varies significantly in the tsunami source area and the inundation land area. In tsunami simulation, the mesh resolution in tsunami source areas is 1 km, and in inundation simulation, the mesh resolution in the land area is around 5 m or less. Therefore, nesting grid that connects tsunami source area and other parts, or connects inundation areas and other parts is often necessary. One major advantage of using FVCOM is that the model uses unstructured grids, which provides the possibility of connecting two or several mesh systems with different resolutions properly. Major steps for the generation of an unstructured grid mesh are introduced as follows.

The first step is the pre-process, including the handling of the coastline data and bathymetry data that covers the computational domain. The coastline data from the Global Self-consistent, Hierarchical, High-resolution Geography Database (GSHHG) was utilized for the region except for Tokyo Bay part which was extracted from the Google Earth. Bathymetry data is a combination of the ETOPO-1 Global Relief model and J-EEG500 of Japan Oceanographic Data Center (a 500 meter resolution mesh dataset). Bathymetry data of 1 arc-minute resolution provided by ETOPO was used for the whole domain except for the area around Tokyo Bay and inner Tokyo Bay area. 500-meter-resolution bathymetry data was used for the area that is around Tokyo Bay, and 50-meter-resolution bathymetry data was interpolated to the whole Tokyo Bay area mesh. The coastline data and bathymetry data are converted to Cartesian coordinate, and then the coastline data file is converted to *.cst format so as to be used in the Surface Water Modeling System (SMS) 11.1 (Aquaveo).

The second step is to develop the mesh system in SMS software. Coastline could be a solid boundary in the mesh system, while open boundary is created to make the target area to be an enclosed domain. Smooth open boundary plays an important role in simulations, for example, it can make the simulation more stable than the steep one when performing tide reproducing simulation. The original coastline data usually contains many isolated segments, which should be handled in a proper manner. Also, the overlapped or unconnected segments should be avoided. The usual way to handle it is by zooming in every parts of the coastline segments and then checking whether there are overlapped or unconnected ones.

The mesh development method includes the following contents:

1) Coastline process: import the coastline data, and manually adjust the shape of coastline, and make sure that no overlapped or unconnected segments exist.

2) Create open boundary: create the open boundary line so that the domain is enclosed.

3) Build mesh: build the mesh for enclosed domain that is surrounded by coastline and open boundary.

4) Mesh quality control: this step is important because FVCOM has requirements on the attributes of the mesh triangle elements. The concrete requirements can be found in FVCOM user manual.

5) Bathymetry interpolation: after the mesh is developed successfully, the bathymetry data could be interpolated into the mesh using the scatter module in SMS software.

In inundation simulation or tsunami simulation, a nesting mesh grid is often needed. In tsunami

simulation, the global mesh covers the tsunami propagation area, while the source area mesh only covers the fault area. In inundation simulation, the nesting mesh grid can be divided into two parts. One is the global mesh grid that includes the ocean part, the other is the inundation area that is the land area. To generate a nesting mesh grid, the following steps are needed:

1) Generate a global mesh grid and preset the inundation area or tsunami fault area place (the local mesh)

2) Prepare the global node-string which is used to connect the global mesh and local mesh

3) Use the global node-string as coastline data, and generate the local mesh

4) Prepare the global node-string in local mesh, the node number in the node-string should be the same as that in global mesh

5) Combine the global mesh and local mesh

3.1.3 FVCOM input files

In order to conduct simulations using FVCOM, proper input files should be prepared cautiously, the fvcom-toolbox which is coded in Matlab language can be easily found in Github on the Internet, but in this work, a suite of Python code has been developed to generate the FVCOM inputs from the SMS mesh file. The following input files are necessary for the applications in this study using FVCOM 4.3:

1) CASENAME_COR.dat: Latitudes of mesh nodes which are used to calculate the Coriolis parameter. It is a data array with three columns (*x*, *y*, latitudes). The first two columns *x* and *y* are the location, and the third column is the latitude of each individual mesh node on triangular meshes. The number of rows is equal to the number of nodes.

2) CASENAME_DEP.dat: It is an array with three columns (*x*, *y*, and bathymetry) where *x* and *y* are the location and bathymetry is the water depth or land elevation of the nodes. The number of rows is equal to the number of nodes. The bathymetry value is specified at mesh nodes.

3) CASENAME_GRD.dat: The first part of this file contains the node numbers that identify the triangle cells, the second part contains the *x* and *y* coordinates of all mesh nodes, also the bathymetry is included in the second part.

4) CASENAME_OBC.dat: The information of the open boundary nodes. The number at the last column is regarding the open boundary type, e.g., "7" means the BKI (Blumberg and Khanta Implicit) radiation open boundary[99]. The detailed information can be found in the FVCOM user manual.

5) CASENAME_SPG.dat: Parameter values for a sponge layer at the open boundary

6) CASENAME_SIGMA.dat: Parameter settings for sigma coordinates

7) CASENAME_WIND.nc: Wind field values, mainly including wind velocity and atmospheric pressure.

8) CASENAME_RIVER.nc: River flow discharge, temperature, and salinity data.

9) RIVER_NAMELIST.nml: The river names in the NetCDF format river input file. The location of the river source is usually specified on the triangle elements, and the river inflow location is the type of "edge".

10) CASENAME_GW.nc: The groundwater flux, temperature and salinity values, which are specified at the mesh nodes.

11) CASENAME_HOTSTART.nc: Hotstart file, with which the model starts from the model output as a selected time.

3.1.4 Wet/Dry Treatment

As in the study, applications of inundation analysis using FVCOM is included. Thus, the wet and dry function of the model is needed. The wet and dry point treatment method is available in FVCOM. This method has been validated in a series of tidal simulations using an idealized semi-enclosed estuary which has an inter-tidal zone. The rule used in validation is mass conservation, which is a prerequisite condition for an objective evaluation of the wet and dry point treatment technique in estuaries and coastal regions where inundation occurs.

The Wet/Dry criteria is:

By defining

$$D = H_{\mathrm{m}} + \zeta \tag{3-14}$$

where $H_{\mathrm{m}} = H + D_{\mathrm{min}}$ in the water and $H_{\mathrm{m}} = -(h_{\mathrm{B}} + D_{\mathrm{min}})$ on the land, the Wet/Dry criterion for node points is given as

$$\begin{aligned} &\text{wet, if } D = H_{\mathrm{m}} + \zeta \ > \ D_{\mathrm{min}} \\ &\text{dry, if } D = H_{\mathrm{m}} + \zeta \ \leq \ D_{\mathrm{min}} \end{aligned} \tag{3-15}$$

And for triangular cells, it is given as:

$$\begin{aligned} &\text{wet, if } D = \min\left(H_{\mathrm{m,i}}, H_{\mathrm{m,\hat{j}}}, H_{\mathrm{m,\hat{k}}}\right) + \max\left(\zeta_{\hat{\imath}}, \zeta_{\hat{\jmath}}, \zeta_{\hat{k}}\right) > D_{\mathrm{min}} \\ &\text{dry, if } D = \min\left(H_{\mathrm{m,i}}, H_{\mathrm{m,\hat{j}}}, H_{\mathrm{m,\hat{k}}}\right) + \max\left(\zeta_{\hat{\imath}}, \zeta_{\hat{\jmath}}, \zeta_{\hat{k}}\right) \leq D_{\mathrm{min}} \end{aligned} \tag{3-16}$$

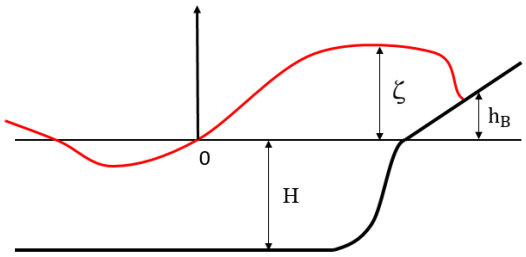

Figure 3.1 Reference depth (H), surface level (ζ) and bathymetry height (h_{B})

where, D_{min} is the thickness of the viscous layer specified at the bottom, h_{B} is the bathymetric height, and $\hat{\imath}, \hat{\jmath}, \hat{k}$ are the integer numbers to identify the three nodes of a triangle cell. When a triangle cell is treated as dry, the velocity at the centroid of this triangle is given as zero and no flux is on the three boundaries of this triangle.

3.1.5 Hotstart

In FVCOM, there are four model startup types. They are Hotstart, Coldstart, Forecast and Crash-restart. Coldstart is the way that model starts from a zero velocity field and forcings are ramped from zero to their full values over IRAMP. In Hotstart mode, the model starts using a restart file which contains the computed output extracted from other simulations at a selected time. This is usually used for the restart case with a NetCDF output. In Forecast mode, similar to the Hotstart type, but the time for the

restart is set up for forecast operation, and in practical use, the forecast operation usually runs with outputs of a series of restart files over given time intervals. Once the Forecast mode is selected and a restart time is specified, the model would try to find the restart data containing in the restart files at the time. In Crash-restart mode, the model searches for the latest restart file saved before the run crashes, and restarts running the model automatically at the time.

In this study, the Hotstart mode is firstly used and validated in the application of tsunami simulation, and then, it is applied in the multi-hazard vulnerability assessment. In tsunami simulation application, the Hotstart file contains the initial water surface elevation data calculated using the Okada[100] model. In the multi-hazard simulation, the Hotstart file contains the initial surface elevation values that consist of the tsunami initial condition and the water surface elevation values extracted from storm surge simulation output. Python scripts are developed to generate the Hotstart file for FVCOM simulation in this study.

3.2 Typhoon model

3.2.1 Introduction

The accuracy of wind and atmospheric pressure data is important to storm surge hindcasting. Numerous typhoon models have been developed to reproduce realistic atmospheric pressure and wind fields during typhoon events, such as Takahashi formula[101], Fujita formula[102], Jelesnianski formula[103], Myers formula[104], Mitsuta–Fujii formula[105] (M–F), and Holland formula[106]. In these models, the maximum wind radius ($r_{\max}$) that controls the maximum wind speed is a key parameter in determining the wind field, specifically the peak wind speed which could be estimated using several empirical formulae[107-109]. In contrast, the long-term reanalysis wind data obtained from data assimilation models has been widely used for storm surge hindcasting owing to its global availability and convenience. The data provided by the National Centers for Environmental Prediction (NCEP)[110, 111], European Center for Medium-Range Weather Forecasts (ECMWF)[112, 113], and Japanese Reanalysis (JRA)[114, 115] are the most commonly used reanalysis datasets.

However, previous studies[116, 117] have shown that the wind speeds obtained near the typhoon center from the reanalysis data cannot accurately reproduce the observed wind fields. Thus, modifications of the reanalysis data is needed. Chao et al.[118] proposed a framework to blend data from NCEP's operational Global Forecast System (GFS) with that from a higher-resolution hurricane prediction model and successfully demonstrated an appropriately blended wind field for the typhoon-generated wind-wave prediction. However, the proposed method seems complex and impractical. Shao et al.[119] presented two critical values as applicable ranges for ECMWF reanalysis wind data and Holland formula application for typhoon events that occurred in the South China Sea and East China Sea. With these two critical values, a weighting coefficient was given to combine two sets of wind data; however, the weighting coefficient was not clearly explained. Pan et al.[120] proposed a similar superposition method and applied it to Typhoon Fanapi and Typhoon Meranti in 2010 by analyzing the cross-calibrated multi-platform (CCMP) reanalysis wind data. However, their method was not validated in storm surge hindcasting.

Thus, a practical method for creating accurate wind and atmospheric pressure fields is proposed by blending a reanalysis dataset and a parametric typhoon formula. The widely used ERA-Interim wind and

atmospheric reanalysis dataset (ERA-I), and M–F model were employed. Two hybrid models for creating the fields were proposed, and their performances were validated using the observed meteorological data provided by JMA. Using the created atmospheric boundary data, hindcasting of two historical storm surges in Tokyo Bay was performed using FVCOM, which has been applied to storm surge computations in several studies[121-127].

The locations of the meteorological observation stations in Tokyo Bay and its surrounding areas are shown in Figure 3.2(a). The stations recorded the tide levels, including the storm surge anomaly, and wind speed in a one-hour time interval. The detailed information, including the station names, longitudes, and latitudes, is shown in Table 3.1.

Table 3.1 Meteorological observation stations

Observation stations	Longitude (°)	Latitude (°)	Time period
Tokyo	139.775315	35.619923	1983/05/19-2017/12/31
Honmoku	139.699144	35.435539	1978/08/23-2017/12/31
Dainikaiho	139.744066	35.312913	2004/02/20-2016/12/31
Izuoshima	139.392261	34.809532	1978/08/23-2017/12/31
Osaka	135.42587	34.6551	1977/01/01-2016/12/31
Daiozaki	136.892271	34.275416	1976/11/13-2017/12/31
Hegurajima	136.923521	37.842592	1977/01/01-2016/12/31
Shionomisaki	135.728214	33.418954	1977/01/01-2017/12/31

Table 3.2 Selected typhoon cases and associated meteorological observation stations

Typhoon number	Period	Observation stations
8506	1985/06/24 06:00- 1985/07/07 18:00	Tokyo, Honmoku, Hegurajima, Shionomisaki
9805	1998/09/12 00:00- 1998/09/18 06:00	Izuoshima, Daiozaki
0115	2001/09/03 00:00- 2001/09/12 18:00	Honmoku
0709	2007/08/27 18:00- 2007/09/08 00:00	Tokyo
0918	2009/09/29 06:00- 2009/10/11 00:00	Tokyo, Osaka
1115	2011/09/09 12:00- 2011/09/24 13:00	Tokyo, Honmoku, Daiozaki, Dainikaiho
1217	2012/09/20 00:00- 2012/10/03 00:00	Tokyo, Honmoku, Dainikaiho, Izuoshima, Daiozaki
1721	2017/10/15 06:00- 2017/10/23 18:00	Tokyo

Table 3.3 Storm surge observation stations

Station name	Longitude (°)	Latitude (°)	Storm surge case
Tokyo Harumi	139.766667	35.666667	Typhoon 8506, Typhoon 1115
Tokyo Light House	139.828056	35.566111	Typhoon 8506, Typhoon 1115
Chiba	140.045556	35.568056	Typhoon 8506, Typhoon 1115
Yokohama	139.633333	35.466667	Typhoon 8506
Yokosuka	139.651389	35.288056	Typhoon 8506, Typhoon 1115
Kawasaki	139.75	35.516667	Typhoon 8506

Table 3.4 Data source of observation stations

Station name	Source
Tokyo Harumi	JMA*
Tokyo Light House	Bureau of Port and Harbor TMG*, [92]
Chiba	Bureau of Port and Harbor TMG*
Yokohama	JMA*
Yokosuka	JCG*, [128]
Kawasaki	JMA*

*JMA: Japan Meteorological Agency; TMG: Tokyo Metropolitan Government; JCG: Japan Coast Guard

Among the historical typhoons and storm surges that occurred in Tokyo Bay between 1951 and 2017, 15 typhoon cases with large storm surge anomalies (greater than 0.8 m) were screened out and eight typhoons (see Figure 3.2(b)) were selected as summarized in Table 3.2. Typhoon 8506 (or T8506) denotes the sixth typhoon generated in 1985.

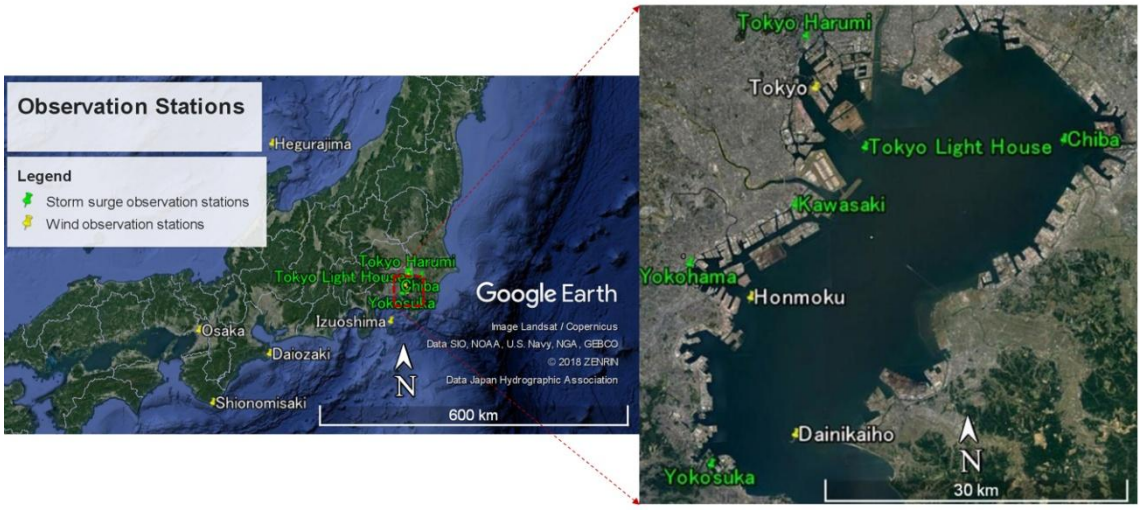

(a)

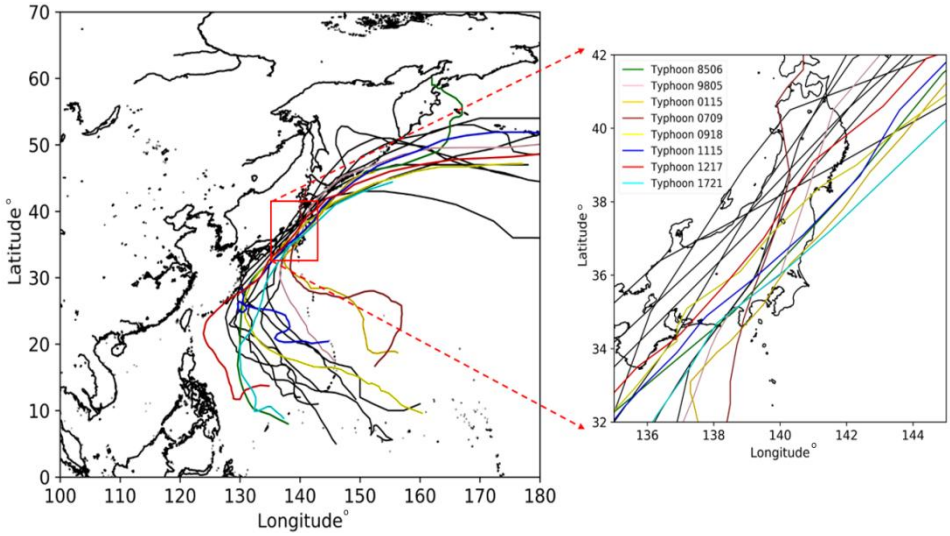

(b)

Figure 3.2 (a) Map of Tokyo Bay and its western region of Japan with meteorological and tide observation stations (source: Google Earth, Data SIO, NOAA, U.S. Navy, NGA, GEBCO), (b) historical typhoon tracks causing significant storm surge anomalies in Tokyo Bay from 1951 to 2017

3.2.2 Wind data analysis

Several reanalysis datasets are for wind and pressure fields, including the ERA-I, NCEP-DOE reanalysis II, and parametric typhoon models. A preliminary investigation was performed on the data consistency by a comparison with observed data from eight typhoon cases. ERA-I and M–F model were used because both of them were more consistent with the measured data for the eight typhoon cases in Tokyo Bay during the preliminary study. Moreover, this method is applicable to any combination of reanalysis datasets and typhoon formulas.

ERA-Interim (ERA-I) is a global atmospheric reanalysis production provided by the European Center for Medium-Range Weather Forecasts (ECMWF), which started in 1979 and has since been continuously updated. In this study, ERA-I data of 6-hour interval wind speeds at a 10-m height from the mean sea level and the sea surface level atmospheric pressure were used. One-hour interval time series datasets for ERA-I were also created by interpolation. To obtain the most accurate ERA-I at the target stations, a 0.125° grid in the longitude and latitude was used.

Figure 3.3 shows a comparison of the ERA-I and the measured wind data provided by Japan Oceanographic Data Center[129] (JODC) at four stations during Typhoon 8506 and Typhoon 1115.

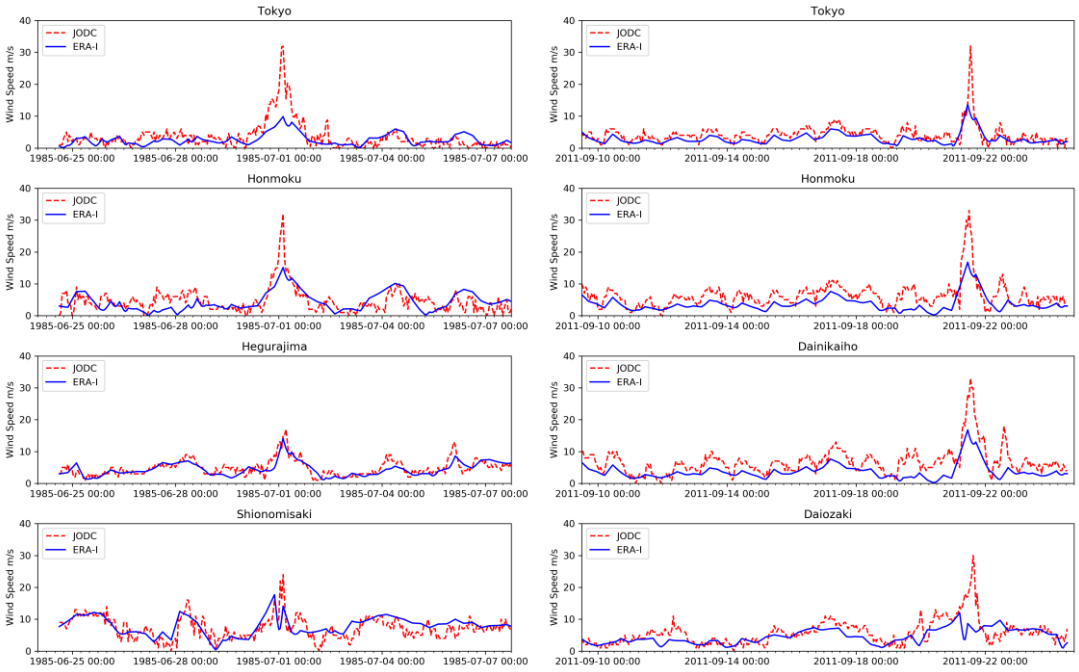

(a) (b)

Figure 3.3 Time-series comparison of ERA-I and JODC measured wind data during Typhoon 8506 (a) and Typhoon 1115 (b)

With the typhoon center far from the stations, the wind speeds were fairly consistent with the observed data with the corresponding approaching and departing distances between the typhoon center and Station Tokyo, Station Honmoku, and Station Shionomisaki ranging from $3.94r_{\max}$ to $1.84r_{\max}$ (1985/7/1/0:00-1985/7/1/10:00), $3.09r_{\max}$ to $2.23r_{\max}$ (1985/6/30/18:00-1985/7/1/10:00), and $2.15r_{\max}$ to $2.44r_{\max}$ (1985/6/29/12:00-1985/7/1/12:00), respectively. With the aforementioned distances, large discrepancies between the observed data and ERA-I were noted.

After the ERA-I analysis for the eight typhoon events and the JODC observation data at eight stations, the applicable ranges for ERA-I are summarized in Table 3.5. The critical value, D_1, is defined as the applicable distance limit from the typhoon center. It was proposed to identify the applicable range of ERA-I at a target location during the typhoon approach. ERA-I is applicable at a location when the distance from the typhoon center to the location is greater than D_1. A similar explanation can be applied to D_2, which is defined for the typhoon departure condition. The distances D_1 and D_2 consist of the applicable boundaries for ERA-I.

The first step in determining D_1 and D_2 values is the plotting of the time-series ERA-I data and JODC observed data at each station during the selected typhoon events. Instances with large discrepancies are then noted. The distance from the typhoon center to the station at the noted instance is finally calculated as the D_1 value for this typhoon. The distance of D_2 is similarly determined under the departing condition. As shown in Table 3.5, different stations experienced the whole processes of the eight selected typhoon events. Statistics at the eight stations under different typhoon events resulted in different D_1 values. It can be seen that D_1 and D_2 values are approximately $2r_{\max}$. Hence, to simplify

the following analysis, D_1 and D_2 are set as $2r_{\max}$.

Table 3.5 Critical values of D_1-D_4 at eight stations under eight selected Typhoons

Typhoon	Station	$D_1/r_{\max}$	$D_2/r_{\max}$	$D_3/r_{\max}$	$D_4/r_{\max}$
8506	Tokyo	3.940	1.840	1.550	0.880
8506	Honmoku	3.090	2.230	0.810	0.970
8506	Hegurajima	3.610	1.560	1.730	1.410
8506	Shionomisaki	2.150	2.440	1.090	1.153
9805	Izuoshima	1.580	1.760	0.890	1.000
9805	Daiozaki	1.470	1.810	1.060	0.800
0115	Honmoku	2.080	2.050	1.200	0.928
0709	Tokyo	2.036	2.079	1.070	1.110
0918	Tokyo	2.300	2.460	0.850	1.360
0918	Osaka	1.950	2.860	1.480	1.530
1115	Tokyo	3.000	2.160	0.980	0.608
1115	Honmoku	2.790	2.400	1.068	1.150
1115	Daiozaki	1.930	2.600	0.89	0.730
1115	Dainikaiho	2.770	1.830	1.050	0.600
1217	Tokyo	2.530	1.997	0.970	0.870
1217	Honmoku	1.530	1.800	0.910	0.950
1217	Dainikaiho	2.430	2.110	0.910	1.000
1217	Izuoshima	2.152	2.076	0.750	0.760
1217	Daiozaki	1.770	1.790	1.680	1.100
1721	Tokyo	2.140	2.720	0.590	0.540

3.2.3 Parametric typhoon model

The Myers formula based on the exponential distribution of the atmospheric pressure field is given by:

$$P(r) = P_{\mathrm{c}} + (P_0 - P_{\mathrm{c}})e^{-\frac{r_{\max}}{r}} \tag{3-17}$$

where $P(r)$ is the pressure at a radial distance *r* from the typhoon center, P_{c} (hPa) is the typhoon central pressure, P_0 ($= 1013.25$ hPa) is the ambient or environmental pressure, *r* is the distance from the computational mesh node to the typhoon center, and $r_{\max}$ (km) is the maximum wind speed radius.

After reviewing similar studies[109, 130], M–F model was selected to compute the wind field as presented in equation (3-18) and the estimated pressure by equation (3-17) was applied to the M–F wind model.

$$U_{\mathrm{w}}(r) = U_{\mathrm{w1}}(r) + U_{\mathrm{w2}}(r),$$
$$U_{\mathrm{w1}}(r) = C_1\left(-\frac{fr}{2} + \sqrt{\left(\frac{fr}{2}\right)^2 + \frac{r}{\rho_{\mathrm{a}}}\frac{\partial P}{\partial r}}\right), \tag{3-18}$$

$$U_{w2}(r) = C_2 \frac{U_{w1}(r)}{U_{w1}(r_{max})} V_T$$

U_w is the total wind vector, U_{w1} is the wind vector induced by the rotating component, U_{w2} is the moving component, $P(r)$ is the pressure field calculated by Myers formula, C_1 and C_2 are dimensionless coefficients ranging from 0.6 to 0.75, f is the Coriolis parameter, r is the distance from the typhoon center, ρ_a is the atmospheric density, and V_T is the typhoon forward speed obtained from the best track data provided by the JMA including the typhoon center location and central pressure. The time-varying radius of the maximum wind speed, r_{max}, was determined as a function of central pressure, P_c, following the empirical formula:

$$r_{max} = 0.769P_c - 650.55, \text{when } 880 \text{ hPa} < P_c \leq 950 \text{ hPa}$$
$$r_{max} = 1.633P_c - 1471.35, \text{when } P_c > 950\ hPa \quad (3\text{-}19)$$

Applying this model to the eight typhoon cases, the estimated wind speeds were compared with the observed data for Typhoon 8506 and Typhoon 1115 cases as shown in Figure 3.6. Generally, for large wind speeds, the estimated values were consistent with that of the measured data. Following the steps introduced in Section 3.2.2, the applicable boundary distances of D_3 and D_4 were determined for the M–F model from the typhoon center to the target location when the typhoon is respectively approaching and departing, as shown in Table 3.5 (D_3 and D_4 are approximately equal to r_{max}). Thus, M–F is applicable in the area between the typhoon center ($r = 0$) and the boundary ($r = r_{max}$).

3.2.4 Hybrid methods for wind and atmospheric pressure data

By introducing the radius of R_b and the transition bandwidth of W_b, a generalized hybrid method is proposed where the M–F model is applied in the $0 \leq r \leq R_b$ region and switching to ERA-I in the $r \geq R_b + W_b$ region (outer region of the transition band) while interpolating the two models in the transition band of $R_b < r < R_b + W_b$. In Section 3.2.4.2, this generalized idea (hybrid model II) is introduced with a method to determine the R_b and W_b parameter values. Before that, as a special case, hybrid model I is introduced in Section 3.2.4.1 by applying the M–F model in the region between the typhoon center ($r = 0$) and the applicable boundary, $r = r_{max}$, and switching to ERA-I in the region where $r \geq 2r_{max}$. ERA-I and M–F model were smoothly interpolated in the transition band of $r_{max} < r < 2r_{max}$.

3.2.4.1 Hybrid model I

The direct method of determining the wind field is given by:

$$F_B = F_{M-F} \quad (0 < r \leq r_{max})$$
$$F_B = \frac{2r_{max} - r}{r_{max}} F_{M-F} + \frac{r - r_{max}}{r_{max}} F_{ERA} \quad (r_{max} < r \leq 2r_{max}) \quad (3\text{-}20)$$
$$F_B = F_{ERA} \quad (r > 2r_{max})$$

where F_B is the resultant wind velocity component in *x* or *y* direction, or the atmospheric pressure, F_{M-F} and F_{ERA} are the wind velocity or atmospheric pressure from M–F model and ERA-I, respectively, r is the distance between the target location and typhoon center, and r_{max} is given by equation (3-19). Compared to the method of Shao et al.[119], the proposed hybrid formula can be easily used and the

weighting coefficient is explicitly explained.

In the formula, when the distance from the typhoon center to the target location is less than r_{max}, the blended wind speed value is more consistent with M–F model than ERA-I if the distance between the typhoon center and the target location is close to r_{max}, while if the distance is close to 0, ERA-I contributes more to the final blended wind speed than M–F model. The similar explanation can be applied to the second range ($r_{max} < r \leq 2r_{max}$) of the formula. When the distance from the typhoon center to the target location is greater than $2r_{max}$, the blended wind speed equals ERA-I.

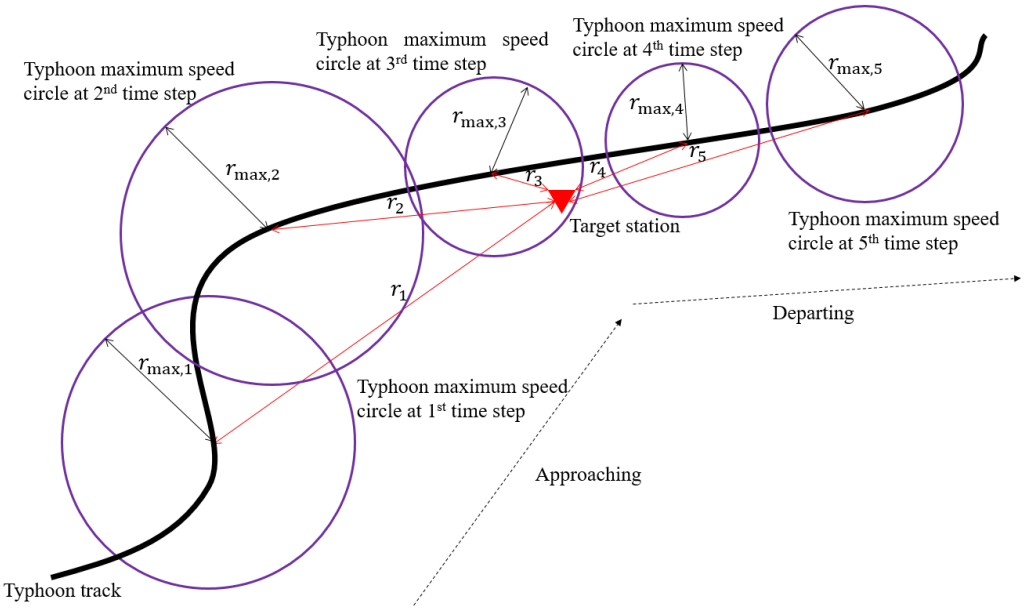

Figure 3.4 Hybrid model I ($r_{max,1}$ represents the maximum wind radius of typhoon at the 1st time step, r_1 represents the distance from the target station to typhoon center at the 1st time step, r_1 is greater than $2r_{max,1}$, therefore, the wind speed at the target station when typhoon center moves to the 1st step location is F_{ERA}; for the 2nd time step typhoon circle, as r_2 is between $r_{max,2}$ and $2r_{max,2}$, therefore, the blended wind speed is calculated using the second formula in equation (3-20); for the 3rd time step typhoon circle, as r_3 is less than $r_{max,3}$, the blended wind speed is calculated using the third formula in equation (3-20); similar explanation can be made for departing condition)

Comparing the wind velocity distributions between the ERA-I and hybrid model I (see Figure 3.5), ERA-I and M–F models dominated outside and inside the typhoon region, respectively, and the transition between these two models was continuous.

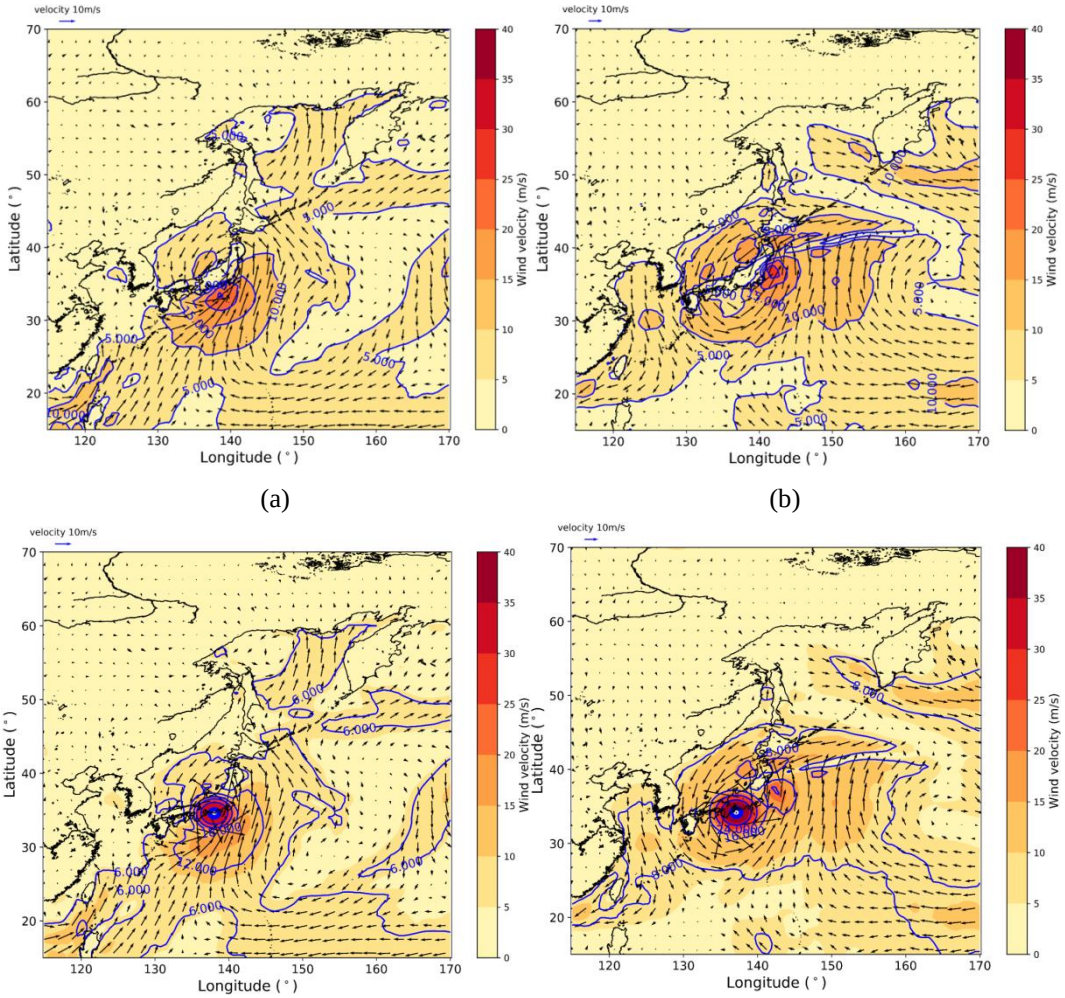

Figure 3.5 Wind velocity distribution using ERA-I and hybrid wind data selecting large values in transition zone at 18:00 on June 30th, 1985, during Typhoon 8506 and at 06:00 on September 21st, 2011, during Typhoon 1115 (a: ERA-I for Typhoon 8506; b: ERA-I for Typhoon 1115; c: hybrid wind data for Typhoon 8506; d: hybrid wind data for Typhoon 1115)

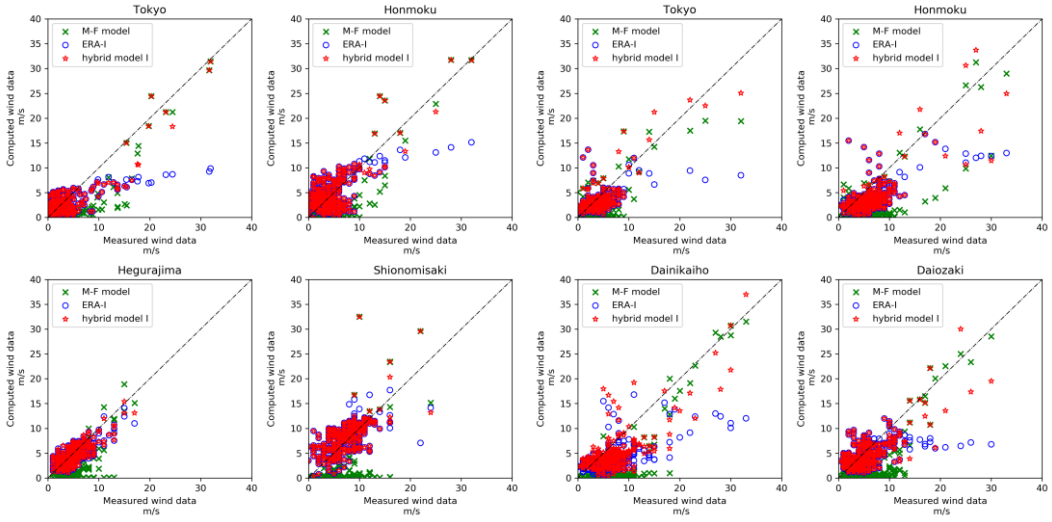

(a) (b)

Figure 3.6 Scatter plots of computed wind data (ERA-I, M–F model, hybrid model I) and JODC measured data during Typhoon 8506 (a) and Typhoon 1115 (b) (the legend of subplot Shionomisaki is the same as those in other subplots in (a))

Comparisons between the computed (ERA-I, M–F, and hybrid model I) and observed (JODC) wind speeds are shown in Figure 3.6. Their coefficients of determination are presented in Table 3.6 and Table 3.7. It can be seen that wind speeds computed by hybrid model I were more consistent with those of the observed (JODC) values during Typhoon 8506 and Typhoon 1115 than those computed by the M–F model or ERA-I.

Table 3.6 Comparison of R^2 value (coefficient of determination) among ERA-I, M–F, hybrid model I and hybrid model II for Typhoon 8506

Station	M–F	ERA-I	Hybrid model I	Hybrid model II
Tokyo	0.584	0.498	0.704	0.682
Honmoku	0.464	0.334	0.469	0.479
Hegurajima	0.345	0.591	0.605	0.592
Shionomisaki	0.145	0.386	0.405	0.416

Table 3.7 Comparison of R^2 value (coefficient of determination) among ERA-I, M–F, hybrid model I and hybrid model II for Typhoon 1115

Station	M–F	ERA-I	Hybrid model I	Hybrid model II
Tokyo	0.405	0.270	0.547	0.609
Honmoku	0.464	0.457	0.529	0.512
Dainikaiho	0.492	0.370	0.506	0.539
Daiozaki	0.514	0.263	0.520	0.559

3.2.4.2 Hybrid model II

The second hybrid model is based on the analysis of the difference between ERA-I and M–F model. As shown in Section 3.2.4.1, the accuracy of M–F is higher than that of ERA-I around the typhoon center while the accuracy of ERA-I is higher than that of M–F away from the typhoon center. Thus, an optimum switching method between the M–F model in the central part and ERA-I in the outer typhoon region was obtained by interpolating the two data in the transition band at each time step for the typhoon track. At each time step, both the distance $r = R_b$ from the typhoon center to the inner side of the transition band and the bandwidth W_b were investigated from $r = 0$ until $r \le L_{max}$ (L_{max} is the maximum searching length) to minimize the mean value of the differences between the ERA-I and M–F model across the computational grids within the transition band. For simplicity, a variable of the searching increment, Δr, was introduced where $R_b = (m-1)\Delta r$ (m is an integer number and $1 \le m \le n$) and the maximum integer number of n was determined to satisfy $(n-1)\Delta r = L_{max} - W_b$. The formula for hybrid model II is given by:

$$
\begin{aligned}
F_B &= F_{M-F} \quad (0 < r \le R_b) \\
F_B &= \frac{R_b + W_b - r}{W_b} F_{M-F} + \frac{r - R_b}{W_b} F_{ERA} \quad (R_b < r \le R_b + W_b) \\
F_B &= F_{ERA} \quad (r > R_b + W_b)
\end{aligned}
\tag{3-21}
$$

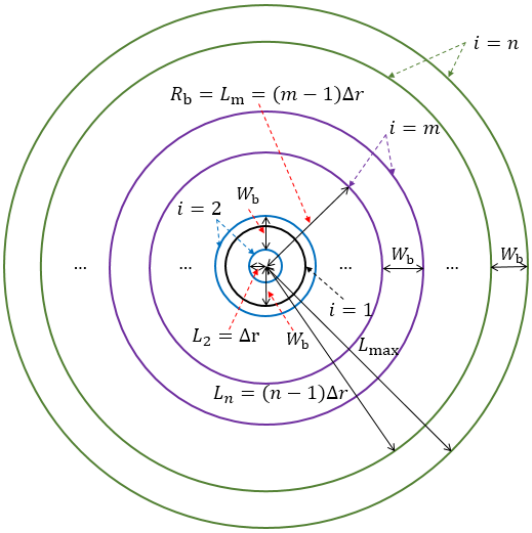

Figure 3.7 Searching band areas in hybrid model II (the first parameter is the increment of searching distance Δr, the second parameter is the maximum searching radius L_{max}, and all searching bands have same bandwidth W_b, which is the third parameter, the fourth parameter is the distance from the typhoon center to the inner side of the transitional annulus band area L_i ($i = 1,2,\ldots,n$). R_b equals L_m if the (m)th annulus is the band area within which the difference of ERA-I and M–F model is minimum. Searching starts from the first circle (black color) i=1 with radius W_b, then the blue color annulus i=2 with internal radius $L_2 = \Delta r$, etc. The investigation will be stopped when $L_n + W_b = 1000$ km. It is obvious that in the proposed searching method, part of the neighbouring band area is overlapped since the searching band area expands with Δr gradually.)

The increment value of Δr was set as 5 km and the maximum searching length of $L_{\max}$ was set as 1000 km, considering the balance between the accuracy and computational cost. Figure 3.8 shows the time series of the optimum R_{b} to $r_{\max}$ ratio for ten cases of W_{b} to obtain the optimum bandwidth. The ratios were always 0 when the distances from the typhoon center to the computational nodes were greater than 1000 km, e.g., in the period until 18:00 on June 28th in Figure 3.8(a). For all ten cases, the ratios were generally less than 2, which is consistent with the applicable radius, r, range for the M–F model ($0 \leq r \cong r_{\max}$) as suggested by hybrid model I.

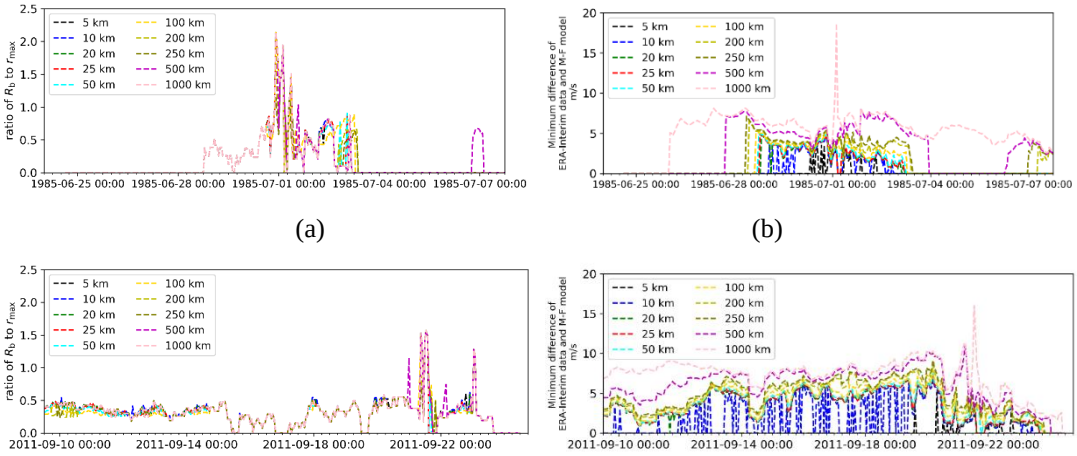

Figure 3.8 Time series ratio of R_{b} to $r_{\max}$ and the minimum difference of ERA-I and M–F model computed using hybrid model II for different bandwidths ((a): ratio of R_{b} to $r_{\max}$ for Typhoon 8506; (b) minimum difference of ERA-I and M–F model for Typhoon 8506; (c) ratio of R_{b} to $r_{\max}$ for Typhoon 1115; (d) minimum difference of ERA-I and M–F model for Typhoon 1115)

Comparisons between the computed winds (ERA-I, M–F model, and hybrid model II) and the JODC measured data during Typhoon 8506 and Typhoon 1115 are shown in Figure 3.9. Their coefficients of determination are summarized in Table 3.6 and Table 3.7, including the results of hybrid model I. According to Table 3.6 and Table 3.7, in some cases, such as Station Tokyo for Typhoon 8506 and Station Honmoku for Typhoon 1115, hybrid model I performed better than hybrid model II. In other cases, such as Station Honmoku for Typhoon 8506 and Station Tokyo for Typhoon 1115, hybrid model II was more accurate than hybrid model I. Thus, results show that the accuracies of these two methods varied with cases and stations.

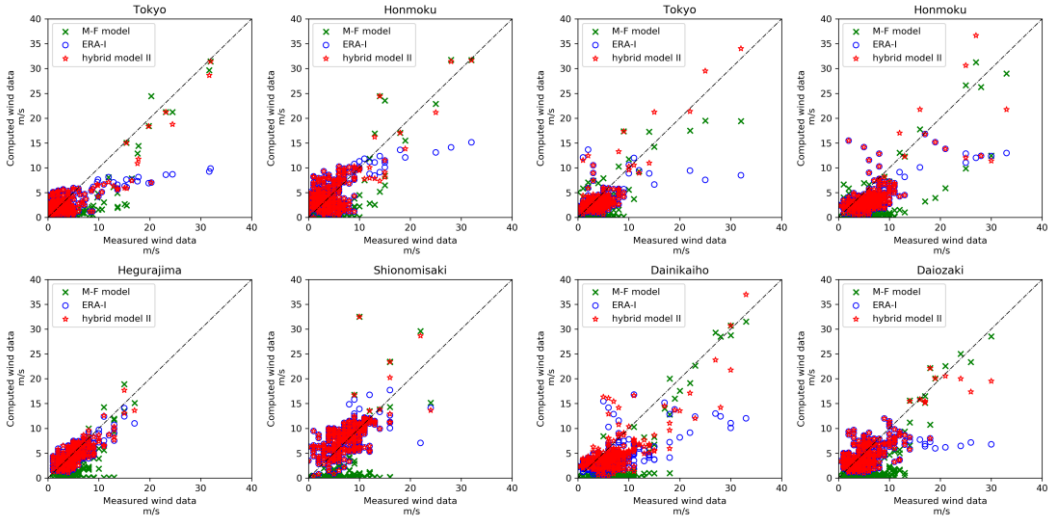

(a) (b)

Figure 3.9 Scatter plots of computed wind data (ERA-I, M–F model and hybrid model II) and JODC measured data during Typhoon 8506 (a) and Typhoon 1115 (b) (the legend of subplot Shionomisaki is the same as those in other subplots in (a))

To further evaluate the performance of hybrid models I and II, eight selected typhoon cases were analyzed, and their corresponding root mean square errors (RMSE) were calculated by:

$$\mathrm{RMSE} = \sqrt{\frac{1}{N}\sum_{i=1}^{N_\mathrm{T}}(F_{\mathrm{hb-I,i}} - F_{\mathrm{JODC,i}})^2} \tag{3-22}$$

where $F_{\mathrm{hb-I,i}}$ is the wind velocity value or atmospheric pressure at the (i)th time step during a certain typhoon computed by hybrid model I, $F_{\mathrm{JODC,i}}$ is the corresponding measured wind speed or atmospheric pressure, and N_T is the total number of typhoon time steps.

Table 3.8 and Table 3.9 present comparisons of the RMSE values among ERA-I and hybrid models I and II with different bandwidths. Compared with the original ERA-I RMSE values, both hybrid models were found to improve accuracy. However, the results from other cases showed that hybrid model II performed better with varying optimal bandwidths, compared with hybrid model I. Hybrid model I was considered a special case of hybrid model II where the bandwidth and band distance from the typhoon center were determined based on ERA-I and M–F. Although the computational cost for hybrid model II was slightly higher, its performance was better and thus, would be a better choice for enhancing the accuracy of storm surge computation.

Table 3.8 Comparison of RMSE values between hybrid model I and hybrid model II with different bandwidths (5 km to 50 km; Cyan color highlights the smaller value in the row)

Typhoon	Station	RMSE (m/s)				
		5 km	10 km	20 km	25 km	50 km
8506	Tokyo	3.096	3.088	3.083	3.080	2.917
8506	Honmoku	3.040	3.002	2.948	2.941	2.945
8506	Hegurajima	1.673	1.673	1.673	1.673	1.673
8506	Shionomisaki	3.099	3.099	3.081	3.037	2.972
9805	Izuoshima	2.451	2.451	2.451	2.451	2.353
9805	Daiozaki	2.648	2.648	2.648	2.648	2.609
0115	Honmoku	2.837	2.774	2.381	2.382	2.406
0709	Tokyo	1.711	1.711	1.711	1.725	1.702
0918	Tokyo	1.990	2.000	1.997	2.000	1.940
0918	Osaka	2.076	2.076	2.076	2.076	1.988
1115	Tokyo	2.645	2.645	2.580	2.498	2.402
1115	Honmoku	3.754	3.763	3.768	3.769	3.778
1115	Daiozaki	3.438	3.438	3.438	3.438	3.323
1115	Dainikaiho	3.827	3.827	3.827	3.827	3.801
1217	Tokyo	1.728	1.728	1.717	1.716	1.718
1217	Honmoku	3.247	3.247	3.247	3.247	3.247
1217	Dainikaiho	3.414	3.414	3.414	3.414	3.414
1217	Izuoshima	3.038	3.038	3.038	3.038	3.038
1217	Daiozaki	3.525	3.525	3.525	3.525	3.525
1721	Tokyo	2.174	2.153	2.150	2.151	2.154

Table 3.9 Comparison of RMSE values between hybrid model I and hybrid model II with different bandwidths (100 km to 1000 km; Cyan color highlights the smaller value in the row)

Typhoon	Station	RMSE (m/s)						
		100 km	200 km	250 km	500 km	1000 km	Hybrid-I	ERA-I
8506	Tokyo	2.871	2.694	2.548	2.511	2.807	2.397	3.392
8506	Honmoku	2.981	2.954	2.944	2.963	2.967	2.964	3.181
8506	Hegurajima	1.673	1.663	1.654	1.673	1.779	1.640	1.653
8506	Shionomisaki	2.972	2.948	2.942	2.919	2.960	2.943	2.981
9805	Izuoshima	2.192	2.252	2.326	2.500	2.688	2.503	3.109
9805	Daiozaki	2.595	2.593	2.575	2.566	2.947	2.484	2.675
0115	Honmoku	2.418	2.322	2.239	2.593	2.731	3.055	2.731
0709	Tokyo	1.784	1.791	1.799	1.869	2.094	2.051	1.986
0918	Tokyo	1.708	1.667	1.667	1.770	1.977	1.682	1.977
0918	Osaka	1.895	1.876	1.863	2.014	2.175	1.845	2.175
1115	Tokyo	2.321	2.282	2.279	2.249	2.294	2.308	2.789
1115	Honmoku	3.710	3.688	3.684	3.696	3.685	3.619	3.879
1115	Daiozaki	3.091	3.227	3.233	3.158	3.551	3.338	3.511
1115	Dainikaiho	3.669	3.665	3.666	3.667	3.718	3.758	4.602
1217	Tokyo	1.719	1.711	1.691	1.718	1.783	1.745	1.761
1217	Honmoku	3.213	3.218	3.200	3.218	3.352	3.206	3.258
1217	Dainikaiho	3.417	3.427	3.404	3.405	3.494	3.359	4.355
1217	Izuoshima	3.036	3.051	3.061	3.057	3.149	3.092	3.237
1217	Daiozaki	3.378	3.370	3.370	3.366	3.514	3.063	3.420
1721	Tokyo	1.875	1.852	1.850	1.939	2.031	2.203	1.877

The hybrid model II concept was then applied to the atmospheric pressure fields, which is also vital in enhancing the storm surge computation accuracy. Comparisons of the time series of atmospheric pressures at Station Tokyo and Station Yokohama for Typhoon 8506 and Typhoon 1115 between ERA-I, Myers formula, hybrid model II, and observed data are shown in Figure 3.10. The blended atmospheric pressures obtained by hybrid model II were more consistent with that of the measured value. Hence, the superiority of hybrid model II was confirmed to be superior.

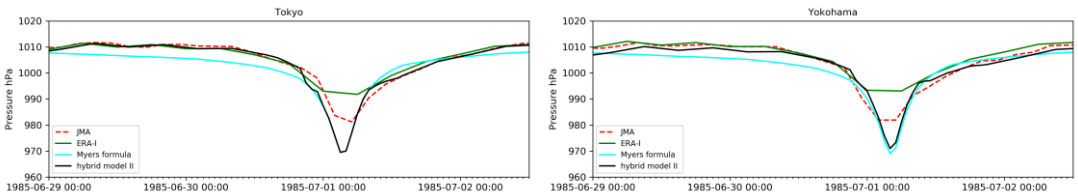

(a)

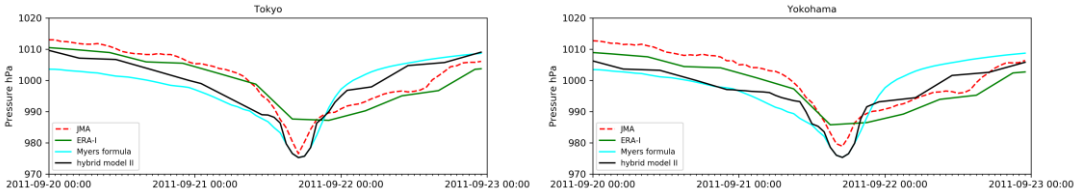

(b)

Figure 3.10 Comparison of computed atmospheric pressure (ERA-I, Myers formula and hybrid model II) and JMA measured pressure data at Station Tokyo and Station Yokohama for Typhoon 8506 (a) and Typhoon 1115 (b) (ERA-I over-predict the atmospheric pressure at 05:00 on July 1st, 1985 for Typhoon 8506 and the atmospheric pressure at 18:00 on September 21st, 2011 for Typhoon 1115)

3.2.5 Sub-conclusion

Although parametric typhoon models, including the M–F model, and reanalysis datasets, including ERA-I, are widely used for storm surge simulation, only a few studies seek their optimum combination to enhance the accuracy of storm surge computation. In this study, two hybrid models were proposed for wind fields, where M–F was applied between the typhoon center ($r = 0$) and a certain radius ($r = R_b$) and switched to ERA-I when the radius is greater than $R_b + W_b$ through the linearly interpolated transition band with the width of W_b. In case of hybrid model I, both R_b and W_b were fixed to be the time-varying radius of r_{max}, which was determined by the M–F formula at a distance from the typhoon center where the maximum wind speed occurred. On the other hand, in hybrid model II, the optimum combination of R_b and W_b were determined to minimize the mean difference between M–F and ERA-I within the transition band. Thus, hybrid model II was considered to be the generalization of hybrid model I. The wind fields of the eight historical typhoon cases approaching Tokyo Bay were compared among ERA-I, M–F, hybrid model I, and hybrid model II. The accuracy of the typhoon wind fields calculated by ERA-I, M–F, hybrid model I, and hybrid model II were verified by a comparison with the observed wind field provided by JODC. Results showed that while both hybrid models performed better than ERA-I and M–F, the accuracy of hybrid model II was higher than that of hybrid model I. Modification for the atmospheric pressure fields was also performed using hybrid model II.

3.3 Tsunami model

3.3.1 Introduction

The tsunami modeling approach can be divided into two different ways. One of them is called forward modeling[131]. Forward modeling of tsunami starts from given initial condition, then computes the tsunami wave propagation in the ocean, and calculates tsunami arrival times and water heights on coasts. Once the initial condition is provided, the propagation and coastal behavior can be numerically computed on actual bathymetry. From given initial condition, the propagation of tsunami waves is computed and the tsunami arrival times and run up heights along the coasts can also be calculated.

The second method is inverse modeling. In this approach, the tsunami sources are quantified based on the observations which includes the instrumental sea level data and run up heights. The earthquake

fault parameters are obtained by inversion of tsunami wave data.

The first method is commonly used when the geological parameters or the initial condition can be estimated. It usually consists of three steps, the generation of initial condition, the propagation of tsunami wave, and the behavior of the tsunami wave at the coastal region.

3.3.2 Fault model

The common form of earthquake moment magnitude is given as a dimensionless number M_w[132]. The earthquake moment magnitude M_w and seismic moment M_0 has such a relation as below[133]:

$$M_w = \frac{2}{3}\log M_0 - 10.73 \tag{3-23}$$

Unit of M_0 is: dyne/cm, 1 dyne-cm = 10^{-7} N-m

The length L_F (km) and the width W_F (km) of earthquake fault are determined by equation (3-24) and equation (3-25), respectively, for a given earthquake moment magnitude M_0 (Nm).

$$\log_{10} M_0 = 2.5 \log_{10} L_F + 7.96 \tag{3-24}$$

$$\log_{10} W_F = 0.667 \log_{10} L_F + 1.24 \tag{3-25}$$

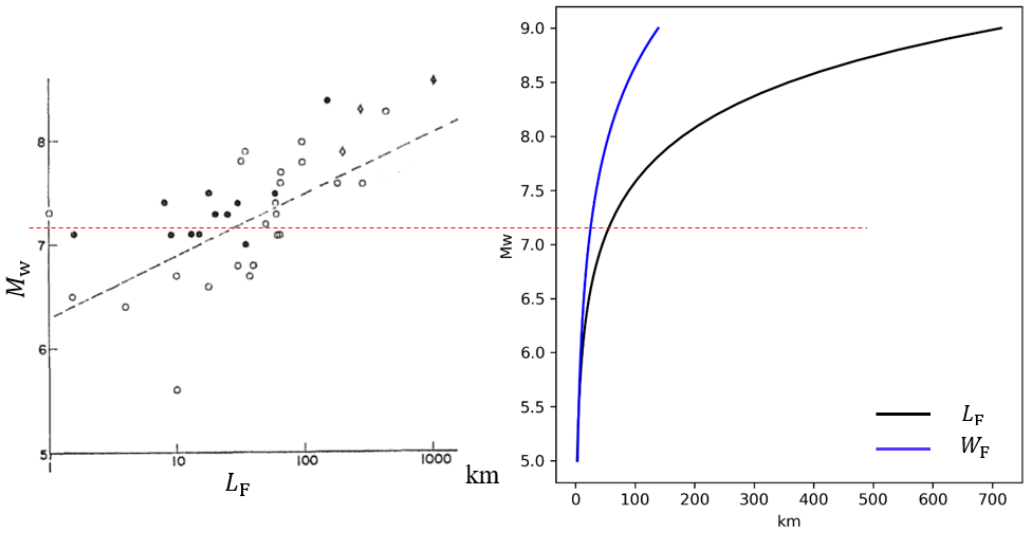

Figure 3.11 Comparison between literature's data[134] (left panel) and selected formulas (right panel) regarding the fault rupture length and width (The figure in left shows the relation between earthquake magnitude M_w and length of earthquake fault L_F. Black dots: data in the vicinity of Japan; white circle: data all over the world. The figure in right shows the calculated results using equation 3-24 and equation 3-25)

And the average net slip is calculated using following equation:

$$U_s = \frac{M_0}{\mu L_F W_F} \tag{3-26}$$

Then, the tsunami initial water surface condition can be calculated using Okada model. There are nine basic parameters in Okada model. They are latitude (Y_0), longitude (X_0), top depth (d_c), strike (θ),

dip (δ) and rake angle (λ), fault length (L_F), width (W_F), and net slip (U_s).

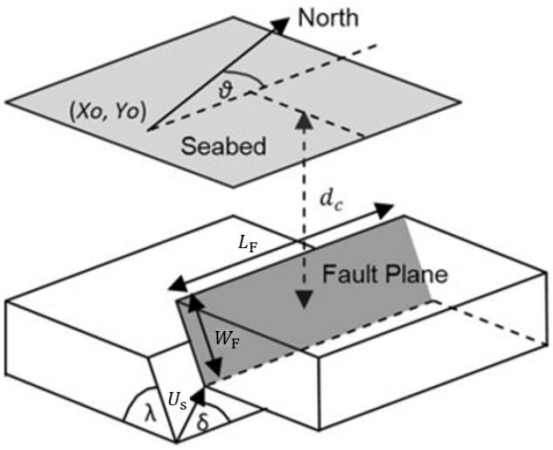

Figure 3.12 Seismic parameters used in the Okada (1985) formulation to generate the tsunami initial condition

Okada model is derived from a Green's function solution to the elastic half space problem. To develop the initial water surface elevation condition, the following steps are necessary:

1) Calculation of sub-fault displacement: this process is performed using Okada model. As input values, following fault parameters are necessary: sub-fault geometry (longitude, latitude, depth, strike, dip, length, width) and dislocation components (rake and slip). Beauducel (2009) developed Matlab script to compute solution of Okada (1985) for the surface deformation due to tensile faults in an elastic half-space, and Sasaki (2011) developed Matlab scripts to input the sub-fault parameters and produce sub-fault displacement figures.

2) Coordinate conversion for sub-fault displacement: after calculating the sub-fault displacement in the original spherical coordinate, the sub-fault displacement is transformed to UTM coordinate using Ruby and Bash scripts that were coded by Sasaki (2011).

3) Combination of sub-fault outputs: all sub-fault outputs are combined to develop one complete initial surface displacement using Ruby and bash scripts that were coded by Sasaki (2011).

3.4 Drainage pipe model

3.4.1 Introduction

A drainage pipe network is a complex system usually composed of various hydraulic structures such as pipes, manholes, inlets, outfalls and so on. The flow in a drainage pipe may vary quickly from open channel flow state to surcharged flow condition and the surcharged flow may also become overflow from the manhole, and flood the street surface. The real flow in drainage pipes may always keep the unsteady condition because of the spatial and temporal variations of rainfall events.

Description of unsteady flow has always been a challenge topic in hydraulics study community, and a large number of works have been published since the first basic work done by De Saint-Venant (1871)

appeared. With the advent of digital computer, a number of numerical methods have been proposed and compared for solving these flow equations. The unsteady flow equations containing the continuity equation and the exact momentum equation are:

$$\frac{\partial Q}{\partial x}+\frac{\partial A}{\partial t}=q_L \tag{3-27}$$

$$\frac{1}{gA}\frac{\partial Q}{\partial t}+\frac{1}{gA}\frac{\partial}{\partial x}\left(\frac{\beta}{A}Q^2\right)+\cos\theta\frac{\partial}{\partial x}(Ky_s)+(K-K')y_s\cos\alpha\frac{1}{A}\frac{\partial A}{\partial x}=$$

$$S_0-S_f+\frac{1}{\gamma A}\frac{\partial T_s}{\partial x}+\frac{q_L U_x}{gA} \tag{3-28}$$

where, Q is the flow, g is the gravity acceleration, t is time, x is the distance along the pipe, A is the flow cross section, y_s is the water surface elevation, α is the angle of the pipe with respect to horizontal, S_0 is the slope of the drainage, S_f is the friction slope, β is a momentum flux correction coefficient, K is a piezometric correction coefficient that accounts for the non-hydrostatic pressure distribution, K' is a correction coefficient for ambient piezometric pressure, T_s is the force due to internal stresses acting normal to the area A, γ is the specific weight of the liquid, q_L is the lateral flow rate per unit length of x, while U_x is the x component of the lateral flow velocity.

Equation (3-27) is built based on the principle of mass conservation, while equation (3-28) states the law of conservation of the linear momentum in the x direction. The coefficients in equation (3-28) have the following physical meaning:

β reflects that the pipe flow velocity distribution is not uniform over the cross section A. It is defined as:

$$\beta=\frac{\int u^2 \mathrm{d}A}{V^2 A} \tag{3-29}$$

where u represents the point velocity and V is the mean velocity over the section A. For drainage pipes, the value of β varies from 1.01 to 1.12.

K is defined as:

$$K=\frac{\int \bar{P}\mathrm{d}A}{\gamma_a A y_s \cos\alpha} \tag{3-30}$$

where γ_a is the flow cross section average specific weight of the fluid and P is the local piezometric pressure. For a constant density fluid and if the pressure distribution is hydrostatic, K=1.

K' reflects the effect of the ambient pressure when there is a spatial change in flow cross section and become equal to unity for constant density and hydrostatic pressure distribution.

The physical meaning of the terms in equation (3-28) is briefly described by:

1) The term $\frac{\partial Q}{\partial t}$ represents local acceleration, i.e., the time rate of change of momentum flux and is zero for steady flow

2) The term $\frac{\partial}{\partial x}\left(\frac{\beta}{A}Q^2\right)$ is the convective acceleration, i.e., the rate of spatial change of momentum flux

3) The pressure term $\cos\alpha\frac{\partial}{\partial x}(Ky_s)+(K-K')y_s\cos\alpha\frac{1}{A}\frac{\partial A}{\partial x}$ composes of the rate of spatial change of the piezometric pressure acting on the cross section and the component of the force due to the mean and

fluctuating ambient piezometric pressure acting on the boundary surface. The value of these terms is zero for uniform flow but can be very large for rapidly varied flow

4) The channel slope $S_0 = \sin\alpha$ represents the component of the gravitational force

5) The friction slope S_f accounts for the resistance due to external shear stresses in the x direction. The well-known equations Manning, Chezy or Weisbach are the most used equations to express this term. For flows with sufficiently large values of the Reynolds number in prismatic channels with rigid boundary, Manning's coefficient is nearly constant and hence the Manning equation is preferred for the estimation of the friction slope

6) The internal stress term, $\frac{1}{\gamma A}\frac{\partial T_\mathrm{S}}{\partial x}$ represents the rate of spatial change of the internal deformation stresses of the mean motion acting on the cross section. This term is related to the ratio between the viscous and Reynold stresses. Generally the internal stresses can be large, but their variation with *x* is usually small

7) The last term is the lateral flow term, $\frac{q_\mathrm{L}U_\mathrm{X}}{gA}$ represents the momentum flux of the lateral flow

In general, the following assumptions are made on equation (3-28):

1) Hydrostatic pressure distribution over A ($K = K' = 1$)

2) Uniform velocity distribution over the cross section A ($\beta = 1$)

3) Small spatial gradient of the force due to internal stress ($\frac{\partial T_\mathrm{S}}{\partial x}$ is negligible)

4) No lateral flow ($q_\mathrm{L} = 0$)

Then, equation (3-28) becomes the complete dynamic wave equation. The purpose of this part is to illustrate the basic theory and the assumptions in the development of an unsteady flow routing model of dynamic wave type and it is based on the complete one-dimensional equations of unsteady flow. The model is able to simulate mixed flow conditions such as rapidly varying transient flows, backwater effects, and reverse flows in storm drainage pipe networks with mild bed slopes. The model is solved by a weighted four-point implicit finite difference scheme, and at each time step, a set of nonlinear discretized algebraic finite difference equations are figured out for the unknowns including the flow value and water surface elevation at specified computational nodes along the storm drainage pipe. Newton-Raphson iteration method is applied to solve the nonlinear algebraic equations, and it is combined with a specially constructed Gaussian elimination matrix technique which is able to provide efficient computational properties. The cross-section of the studied storm drainage pipe may be of circular or arbitrary shape. The drainage pipe network may also consist of a single pipe or a dendritic system of pipes including multiple outlets, bypasses, and cross connections.

Storm drainage pipes are originally designed to work as open channels, but sometimes, under-design or exceptional rainfall may cause the surcharge of the drainage pipe. The transition between open channel flow and pressurized flow is not smooth, which could involve instabilities induced by the air entertainment. Substantially, there are two available techniques for simulation of a surcharge flow in a drainage pipe. The first method divides the open channel flow from the surcharged flow and expresses them using different sets of mathematical equations. The other is Preissmann slot technique which was introduced by Cunge and Wegner[135] and is referred as the Preissmann slot. It uses an imaginary narrow open slot on the top of

the drainage pipe to transform the surcharged flow into an equivalent open channel flow. The greatest advantage of using the slot concept is that it allows a single form of the Saint-Venant equations to be applied in a mixed flow model, which would largely simplify the numerical part.

A mixed flow model describes three distinct flow situations: when the conduit is flowing partially full (open channel or gravity flow conditions) and when the conduit is flowing completely full (surcharged or pressurized flow conditions) or a combination of both. When a partially full conduit starts to flow fully full, the conduit surcharges or pressurizes, and the free surface flow concept is maintained by the narrow slot, and the water surface level rises in the slot to the level of the piezometric pressure head. In this thesis work, the fluid surface elevation will be referred as the elevation of the piezometric surface. When the drainage pipe is flowing partially full, the slot has no influence upon the flow if the fluid level does not rise to the crown of the pipe.

In practical applications, the slot does not add to the total section conveyance, and never exceeds that of a pipe flowing completely full[136]. To avoid any possible errors in the continuity of overall volume, the true cross-sectional area and wetted perimeter of the closed conduit section plus the slot is accounted for.

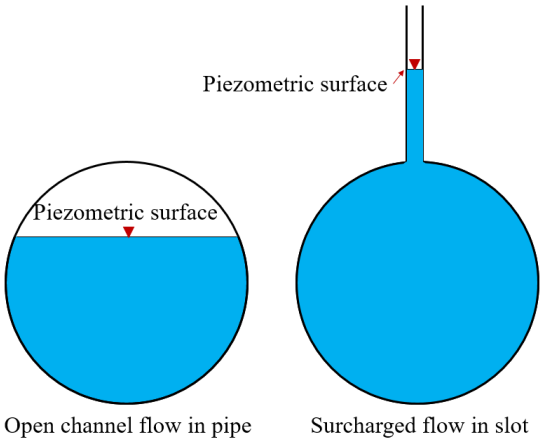

Figure 3.13 Preissmann slot free surface flow concept

The narrow slot is expected to produce a proper wave celerity for pressurized flow[137]. The width of the slot should be narrow enough so that it will not introduce appreciable error in the volume of water. The width is determined so that the surge celerity in the slotted drainage pipe is equal to the pressure wave speed in a non-slotted pipe. The surge celerity, C_s, m/s, of the slotted conduit is given by:

$$C_s = \sqrt{\frac{gA}{b_{slot}}} \tag{3-31}$$

where A is the area of the flow cross-section, b_{slot} is the slot width.

3.4.2 Governing equations

The mixed flow model is based on the one-dimensional Saint-Venant equations of unsteady flow:

$$\frac{\partial Q}{\partial x}+\frac{\partial A}{\partial t}=0 \tag{3-32}$$

$$\frac{\partial Q}{\partial t}+\frac{\partial (Q^2/A)}{\partial x}+gA(\frac{\partial (y_{\mathrm{s}})}{\partial x}+(S_{\mathrm{f}}-S_0))=0 \tag{3-33}$$

$$S_{\mathrm{f}}=\frac{{n_{\mathrm{m}}}^2|Q|Q}{A^2R^{\frac{4}{3}}} \tag{3-34}$$

where, Q is the flow (m^3/s), A is the flow cross section area (m^2), x is the distance along the pipe (m), t is the time (s), g is the gravity acceleration ($\mathrm{m/s}^2$), y_{s} is the water surface elevation (m) in the pipe, S_{f} is the friction slope (m/m), S_0 is the drainage pipe bed slope, R is the hydraulic radius (m), $R=A/P_{\mathrm{w}}$, where P_{w} is the wetted perimeter (m) of the flow cross section, n_{m} is the Manning roughness coefficient.

3.4.3 Numerical methods

The Saint-Venant equations are nonlinear partial differential equations and their analytical solution cannot be obtained except in special cases. Thus, numerical methods are used to find approximation solutions, such as the water level and discharge hydrographs at a specific number of nodes in the time-space domain. Various numerical methods commonly used to solve the Saint-Venant equations include the method of characteristics, the finite element method, and the finite difference method. Among these methods, the finite element method is rarely used when flow is approximated as one-dimensional, for example in the case of Saint-Venant equations. The other two methods have been commonly applied to solve the numerical solution of one-dimensional unsteady flow since 1960s.

The finite difference methods can be further classified as explicit and implicit schemes, and each of them has its distinct numerical characteristics. A major advantage of the implicit finite difference scheme over the method of characteristic and the explicit finite difference technique is its inherent stability without the requirement to satisfy the Courant condition, because the requirement to satisfy Courant condition often makes the method of characteristics and explicit finite difference scheme method inefficient in terms of computation time. Moreover, certain implicit schemes such as the four-point weighted implicit finite difference scheme (Preissmann, 1961) allow the use of various time and spatial steps, which makes it convenient for applications in the routing of flood hydrographs in river channel systems.

On account of these advantages, the implicit finite difference technique is commonly used to solve the governing partial differential equations. In the implicit formulation, all derivative terms and other parameters are approximated by using the unknowns at the forward time line (j+1) as seen in the x-t grid, and the implicit finite difference method advances to solve the solutions from one time line to the next simultaneously for all computational nodes along the time line.

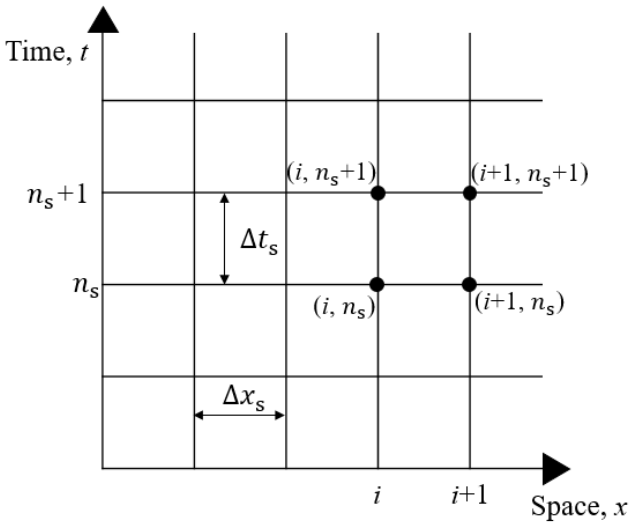

Figure 3.14 Time line and space line in the four-point weighted implicit finite difference scheme

In the four-point weighted implicit finite difference scheme, the four grid points from the (j)th and (j+1)th time lines are used to approximate the terms in the differential equation. A weighing factor, θ_s, is used in the approximation of all terms of the equation except for the time derivatives, in order to adjust the influence of the points (i) and (i+1). The sensitivity analysis of the finite difference parameter θ_s can be found in Section 4.2.

The approximations of the derivatives and constant terms in the four point weighted difference scheme are given as follows:

Space derivatives:

$$\frac{\partial Q}{\partial x} = \theta_s \frac{Q_{i+1}^{j+1} - Q_i^{j+1}}{\Delta x_s} + (1-\theta_s)\frac{Q_{i+1}^{j} - Q_i^{j}}{\Delta x_s} \tag{3-35}$$

$$\frac{\partial \left({}^{Q^2}/_{A} \right)}{\partial x} =$$

$$\theta_s \frac{({}^{Q^2}/_{A})_{i+1}^{j+1} - ({}^{Q^2}/_{A})_{i}^{j+1}}{\Delta x_s} + (1-\theta_s)\frac{({}^{Q^2}/_{A})_{i+1}^{j} - ({}^{Q^2}/_{A})_{i}^{j}}{\Delta x_s} \tag{3-36}$$

$$\frac{\partial y_s}{\partial x} = \theta_s \frac{y_{s\,i+1}^{j+1} - y_i^{j+1}}{\Delta x_s} + (1-\theta_s)\frac{y_{s\,i+1}^{j} - y_i^{j}}{\Delta x_s} \tag{3-37}$$

Time derivatives:

$$\frac{\partial A}{\partial t} = 0.5\frac{A_{i+1}^{j+1} - A_{i+1}^{j}}{\Delta t_s} + 0.5\frac{A_i^{j+1} - A_i^{j+1}}{\Delta t_s} \tag{3-38}$$

$$\frac{\partial Q}{\partial t} = 0.5\frac{Q_{i+1}^{j+1} - Q_{i+1}^{j}}{\Delta t_s} + 0.5\frac{Q_i^{j+1} - Q_i^{j+1}}{\Delta t_s} \tag{3-39}$$

Constant terms:

$$S_f = \theta_s S_{f\,i+1/2}^{j+1} + (1-\theta_s) S_{f\,i+1/2}^{j} \tag{3-40}$$

$$(S_f)_{i+\frac{1}{2}} = \frac{\overline{n_i}^2 |\overline{Q}_i| \overline{Q}_i}{\overline{A_i}^2 \overline{R}_i^{\frac{4}{3}}} \tag{3-41}$$

$$\overline{Q}_i = \frac{Q_i + Q_{i+1}}{2} \tag{3-42}$$

$$A = \theta \frac{A_{i+1}^{j+1} + A_i^{j+1}}{2} + (1-\theta) \frac{A_{i+1}^{j} + A_i^{j}}{2} = \theta \overline{A}_i^{j+1} + (1-\theta) \overline{A}_i^{j} \tag{3-43}$$

$$\overline{A}_i = \frac{A_i + A_{i+1}}{2} \tag{3-44}$$

$$\overline{R}_i = \frac{\overline{A}_i}{\overline{B}_i} \tag{3-45}$$

3.4.4 Initial and boundary conditions

The initial conditions are the values of $y_{s_i}^{j}$ and Q_i^{j}, for all nodes (i = 1, 2, ..., N_p) along the x axis at time (t = 0) or (j = 1). In this model, these values may be obtained by either specifying them as input to the model or by letting the model compute them assuming that it is steady state, and spatially varied flow at t = 0. When they are specified as input, the model uses them to obtain solutions at the former time step, and then uses the solutions to obtain other solutions. This process would be repeated for a couple times until any small errors of the initial values have been damped out in the successive solutions. If the initial values do not contain large errors, this process may converge quickly. However, the model may not be convergent if the errors are too large.

The adopted method is to let the model compute the initial conditions using the following steady gradually varied flow equation, i.e.,

$$(Q^2/A)_{i+1} - (Q^2/A)_i + g\bar{A}_i\left(y_{s_{i+1}} - y_{s_i} + \bar{S}_{fi}\Delta x_{s_i}\right) = 0 \tag{3-46}$$

The computation proceeds in the upstream direction from a specified value for $y_{s_{i+1}}$, at the most downstream point of the system. Thus, equation (3-46) is recursively solved for y_{s_i}. Since equation (3-46) is nonlinear, it is solved by the Newton-Raphson iterative method for a single equation. The model determines all the flow values by a simple summation process of inflow values at t = 0 for all specified inflow computational nodes. The water surface elevation value y_s and flow value Q can be calculated in this way for either a single pipe or a complex dendritic network of drainage pipe systems.

Boundary conditions are specified values of either y_s or Q, or a known relation between them, at all the most upstream and downstream computational nodes in a drainage pipe network. In this model, the upstream boundary conditions are known inflow discharge hydrographs as a function of time. The downstream boundary condition can be a known water surface elevation as a function of time such as for submerged outlets in lakes or estuaries. Also, the downstream boundary can be a known relation between Q and h_{out} such as normal flow, critical flow, etc., which is input in the form of a table of Q and h_{out} values.

In a drainage pipe system, complex internal hydraulics due to the presence of manholes, flood gates, overflow weirs, pumping stations, and drop inlet structures are simulated via appropriate equations introduced within the nonlinear flow equations as internal boundary conditions. These internal boundaries

are usually the locations along the drainage pipe network where the Saint-Venant equations are not applicable, and critical flow occurs. The internal boundary consists of two equations that are used to replace the two Saint-Venant equations. The equations relate Q and y_s at the entrance to a short Δx_s reach within which the two internal boundary equations describe the hydraulics. For instance, manholes are located where the drainage pipe changes size, slope, or direction, or where there is a junction connecting two or three conduits. The two internal boundary equations are:

$$Q_i^{j+1} + m_s Q_{i'}^{j+1} - Q_{i'+1}^{j+1} + Q_{in} - Q_w - {}^{\Delta s}/_{\Delta t_s} = 0 \tag{3-47}$$

$$y_{s_i}^{j+1} - y_{s_{i'+1}}^{j+1} - y_{f_i} = 0 \tag{3-48}$$

$$y_{s_{i'}}^{j+1} - y_{s_{i'+1}}^{j+1} - y_{f_{i'}} = 0 \tag{3-49}$$

where Q_i is the inflow (m^3/s) to the manhole from the upstream pipe, $Q_{i'}$ is the inflow from the branch pipe (m_s = 0 if there is no branches, otherwise m_s = 1), $Q_{i'+1}$ is the outflow from the manhole through the exiting downstream pipe (when there is no branch pipe, $i' = i$), y_{s_i}, $y_{s_{i'}}$, and $y_{s_{i'+1}}$, are the water surface elevations (m) at the upstream, branch, and downstream conduits, respectively, Q_{in} is the surface inflow to the manhole which is a specified function of time, Q_w is the flow entering or leaving the manhole via a weir-type control structure, $\Delta s/\Delta t_s$ is the change of storage associated with the manhole during a Δt_s time step, y_{f_i} and $y_{f_{i'}}$ are the head losses incurred by the incoming and exiting flow.

3.4.5 Solving technique

The discretized governing finite difference approximation equations can be solved once the initial conditions and all boundary conditions are specified. The Newton-Raphson method provides a means for correcting the trial values until the residuals are reduced to a suitable tolerance level. The solving process is usually accomplished in one or two iterations by use of linear extrapolation for the first trial values. A system of linear equations relates the corrections of the residuals and a Jacobian coefficient matrix which is composed of partial derivatives of each equation with respect to the unknown variables in the formulas. The coefficient matrix of the linear system had a banded structure which allows the system to be solved by a compact penta-diagonal Gaussian elimination algorithm, and it is efficient in terms of computation time.

The Newton-Raphson method is the most common iterative technique used for the solution of a system of non-linear equations. It provides an efficient means for converging to a root once given a sufficiently good initial guess. Denoting the system of equations in vector form:

$$F_i\left(x_1, x_2, x_3, \dots, x_{2N_p}\right) = 0, \tag{3-50}$$

$$i = 1,2,3, \dots, 2N_p$$

If $\vec{x}$ denotes the entire vector of unknown variables, x_i, and $\vec{F}$ denotes the entire vector of functions, F_i, N_p is the number of computational nodes in a pipe system. Each of the functions F_i, can be expanded in the neighborhood of $\vec{x}$ as a Taylor series expansion.

$$F_i(\vec{x} + \delta\vec{x}) = F_i(\vec{x}) + \sum_{k=1}^{2N} \frac{\partial F_i}{\partial x_k} \partial x_j + O(\partial \vec{x}^2), \tag{3-51}$$

$$i = 1,2,3,\ldots,2N$$

The matrix of first partial derivatives in above equation is called Jacobian matrix:

$$\vec{J} = \frac{\partial F_i}{\partial x_{\mathrm{k}}} \tag{3-52}$$

Then, equation (3-51) becomes

$$\vec{F}(\vec{x} + \delta\vec{x}) = \vec{F}(\vec{x}) + \vec{J} \cdot \partial\vec{x} + O(\partial\vec{x}^2) \tag{3-53}$$

Neglecting the higher order terms and setting the left hand-side part equal to zero, one can obtain a set of linear equations that are solved for the corrections $\partial\vec{x}$

$$\vec{J} \cdot \partial\vec{x} = -\vec{F} \tag{3-54}$$

This matrix equation is solved by a matrix solver such as Gaussian elimination or LU decomposition for the unknown, $\partial\vec{x}$, and the improved estimate of the solution is obtained by,

$$\vec{x}_{\mathrm{new}} = \vec{x}_{\mathrm{old}} + \partial\vec{x} \tag{3-55}$$

The iteration process is continued until a predetermined convergence level is achieved. The drainage pipe network model is coded in Fortran 90 programming language in order to match with the host model FVCOM. The code structure and model running flow chart are shown in Figure 3.15 and Figure 3.16, respectively.

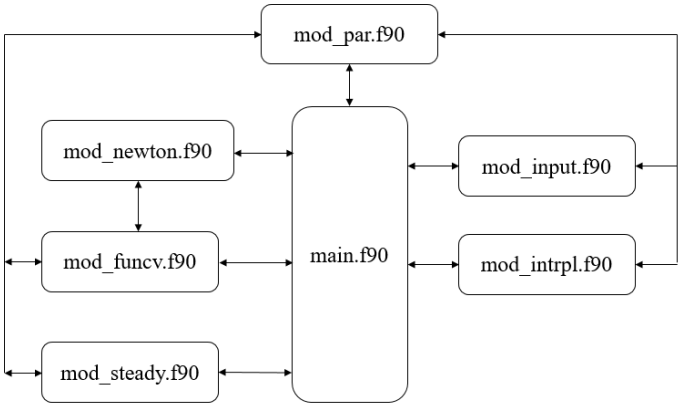

Figure 3.15 Code structure of the Drainage pipe model

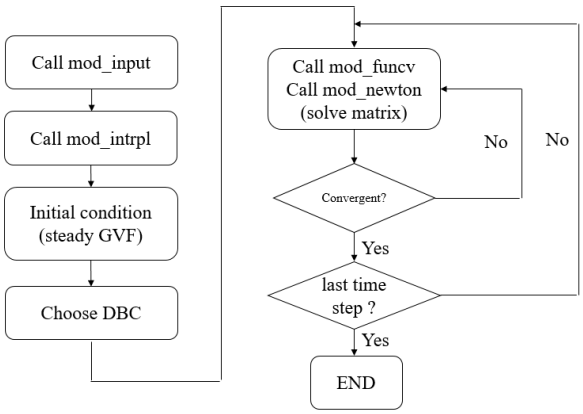

Figure 3.16 Flow chart of the Drainage pipe model

3.5 Integrated FVCOM and drainage pipe model

3.5.1 Flow exchange between ground surface and drainage pipe

Since the effect of drainage pipe system during local inundation needs to be investigated and the original FVCOM code does not have such a module, the integrated FVCOM and drainage pipe model is developed by embedding the drainage pipe model in the FVCOM source code. The integrated model would have the capability of simulating the flow exchange between the ground surface and drainage pipe system. Figure 3.17 shows the possible flow state in the land-pipe system.

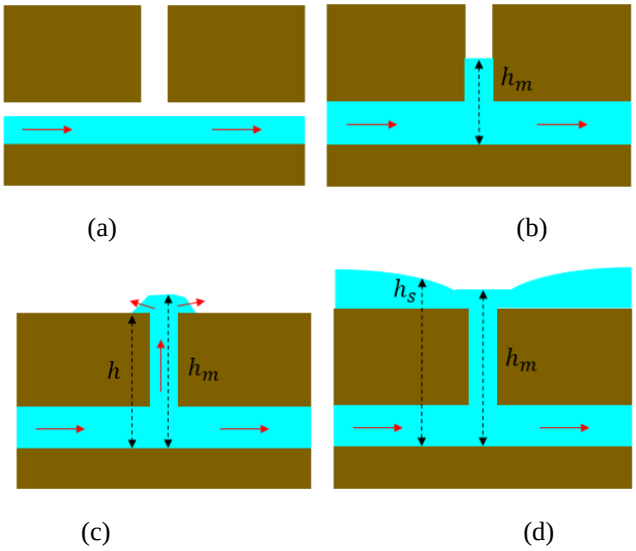

Figure 3.17 Flow state in the land-pipe system

In Figure 3.17(a) and (b), there is no dike overflow inundation on the ground surface and no pipe overflow. Thus, no exchange between ground surface and pipe system happens.

In Figure 3.17(c), dike overflow inundation does not happen, but pipe overflow occurs. There is currently no specific theory or widely accepted methods used to accurately describe the overflow from manhole to surface. Therefore, in this study, the overflow discharge is calculated during the iteration process of solving the manhole water levels and is given as:

$$V_{\mathrm{gw}} = (h_{\mathrm{m}} - h) \times A/\Delta t_{\mathrm{p}} \tag{3-56}$$

In Figure 3.17(d), dike overflow inundation and pipe overflow both happen. Whether the flow in the manhole goes into the pipe or out of the manhole to the ground surface depends on the water head in the manhole, h_{m}, and the surface inundation elevation above the pipe bottom, h_s. In this condition, the overflow discharge is calculated as:

$$V_{\mathrm{gw}} = (h_{\mathrm{m}} - h_{\mathrm{s}}) \times A/\Delta t_{\mathrm{p}} \tag{3-57}$$

where V_{gw} is the discharge from the drainage pipe to the ground surface through manholes if it is positive, or from the ground surface back to the drainage pipe if it is a negative value; A is the horizontal cross section area of the manhole; Δt_{p} is the drainage pipe model running time step.

If inundation on the ground surface happens but the water level in the manhole does not exceed its

height, either weir equation or an orifice equation can be used to compute the discharge flowing into the manhole.

3.5.2 Modification of source code

The information exchange between FVCOM program and drainage pipe model is based on the original groundwater function. At every drainage pipe model running step, the "groundwater" flux (m^3/s) is updated by the drainage pipe program depending on the flow condition in the drainage pipes. The manholes are treated as groundwater nodes in the model.

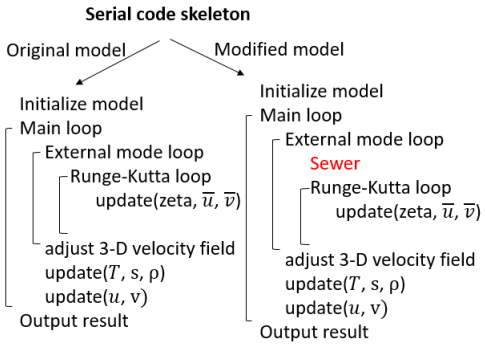

Figure 3.18 Code structure of the original FVCOM model (left panel) and modified one (right panel) (Sewer: the drainage pipe model)

3.5.3 Determination of running time step

The Courant-Friedrichs-Lewy (CFL)[138] condition is a condition for the stability of unstable numerical methods. It plays an important role in the computational fluid dynamics (CFD). The CFL condition expresses that the distance that any fluid information travels during the time step length within the mesh must be lower than the distance between mesh elements. In other words, the fluid information from a given node or mesh cell must propagate only to its immediate neighbors. The general form of CFL condition is as following:

$$\Delta t_{\mathrm{E}} \leq \frac{\Delta L}{\sqrt{g D_{\max}}} \tag{3-58}$$

where, Δt_{E} is the time step of the external mode of FVCOM, ΔL is the shortest edge length of the unstructured mesh, g is the gravity acceleration, $D_{\max}$ is the maximum bathymetry depth.

The mode split number between external mode and internal mode in FVCOM is 10 in default, which means the internal mode program is called by the main program one time when external mode runs 10 steps. The drainage pipe network model is controlled by the variables declared in FVCOM, and they are presented in Table 3.10.

Table 3.10 Variables used for controlling the drainage pipe model in FVCOM

Name	Meaning
N_{ext}	External running step number in one internal step
N_{int}	Internal mode running step
Δt_{E}	External time step
Δt_{out}	FVCOM output time interval
T_{F}	FVCOM model time
N_{gw}	External mode running steps
N_{F}	Total internal mode steps

```
Initialize model
Main loop:
do N_int=1, N_F (Internal mode loop)
    do N_ext=1, 10 (external mode loop)
        N_gw=(N_int-1)×10+N_ext
        if mod(N_gw, Δt_out/Δt_E)==0 then
            call sewer
        end if
    end do
end do
Output result
```

Figure 3.19 Integrated FVCOM and drainage pipe model (the Fortran 90 internal function mod(a, b) gives the remainder when a is divided by b) (Sewer: the drainage pipe model)

To ensure that the drainage pipe model can provide manhole fluxes to FVCOM at a proper time interval, the output time interval of FVCOM could be primarily specified as the time step of the drainage pipe model. For each external mode step, the controlling number N_{gw} is calculated and if this number is a multiple of $\Delta t_{\text{out}}/\Delta t_{\text{E}}$, the drainage pipe model program is called once. For instance, model time is 14400 s (T_{F}=14400 s), external time step is 0.1 s (Δt_{E}=0.1 s), and the output time interval is 300 s (Δt_{out}=300 s). Then, every 3000 external mode steps, the drainage pipe model runs one time, and in this example, the external mode runs 144000 steps, internal mode runs 14400 steps, and drainage pipe model runs 48 steps. The way of running the integrated FVCOM and drainage pipe model can be specified by the user according to the explanation on the coupling strategy.

Implicit schemes are unconditionally stable and have no restrictions on the size of time step due to numerical stability. However, accuracy considerations require some limitations on the size of time step. Cunge[139] suggested that the implicit scheme is most numerically accurate when the ratio $\Delta x_{\text{s}}/\Delta t_{\text{s}}$ is approximately equal to the wave celerity of undisturbed flow as in equation (3-31). However, a circular conduit presents a unique problem comparing to rectangular shape pipes. When the circular pipe is flowing nearly full, the value of the celerity becomes very large. Therefore, a celerity of 5.0 m/s was selected as the basis for sizing the finite difference grid. The celerity of 5.0 m/s satisfies the criterion described in equation (3-31) for almost all open channel flow with respect to the pipe sizes in the study area. Hence, for practical use, the time step of drainage pipe model depends on the minimum length pipe in a pipe system.

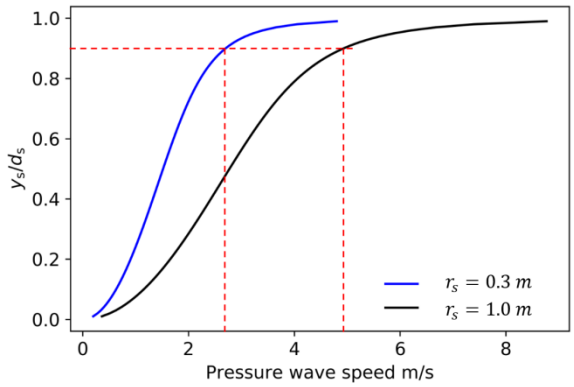

Figure 3.20 Celerity in circular pipe (y_s: water depth in the pipe; d_s: diameter of the pipe; r_s: radius of the pipe)

Based on the above analysis, in the current application of the integrated FVCOM and drainage pipe model, determination of the time step of the drainage pipe network model is balanced between the output time interval of integrated model and the proper time step of the drainage pipe model itself. The output time interval is usually much larger than the time step of drainage pipe model. However, it seems that decreasing the time step of drainage pipe model would not reduce the computational efficiency largely. Thus, the time step of drainage pipe model could be the same as that of the integrate model.

An example code of the embedded drainage pipe module is attached in the Appendix.

3.6 Vulnerability measurement

Flood map generated using inundation computation is a common and straightforward way to measure coastal vulnerability. However, it is computationally expensive when the major purpose of the investigation is just to identify the vulnerable coastline instead of the spatial distribution of vulnerable inland areas. In this section, a simple approach using overflow volume to measure coastal vulnerability is introduced.

The vulnerability analysis process is composed of two parts, one is the numerical simulation, and the other is the vulnerability calculation. First, numerical simulation of the hazard scenario is performed. Then, vulnerability is estimated using the overflow volume calculated from simulation output. For example, V_{dike}(A) and V_{dike}(B) are the estimated total dike overflow volume from all overflow coastline nodes under scenario A and scenario B, respectively. If V_{dike}(A) is larger than V_{dike}(B), the target coastline area under scenario A is more vulnerable than under scenario B. To distinguish which part of coastal areas is more vulnerable under a certain scenario, after extracting the overflow depth of all overflow nodes, it would be easy to identify at which node, the nodal overflow volume is the largest, and the coastline node with the largest nodal overflow volume is the most vulnerable place.

To conduct the vulnerability assessment, the process is shown step by step as follows:

1) Prepare and perform the numerical simulations for multi-hazard scenarios, and in this work, the hazards include storm surge, river flood, and tsunami.

2) Extract the water elevations from the simulation output and calculate the overflow volume along the

target coastline.

3) Produce the multi-hazard vulnerability map.

Figure 3.21 shows the parameters involved in dike overflow process, including the overflow depth h_c, and the overflow velocity v_c. Flow section 1-1 is located in the coastal areas, section 2-2 is the overflow on the sea dike or river bank. The vertically averaged horizontal velocity in section 1-1 is almost 0, namely, $v_1 = 0$, H_1 is the water surface elevation at section 1-1, which could be obtained from the numerical simulation output. Between section 1-1 and section 2-2, Bernoulli energy equation could be applied:

$$P_1 + \frac{1}{2}\rho {v_1}^2 + \rho g H_1 = P_2 + \frac{1}{2}\rho {v_c}^2 + \rho g(H_2 + h_c) \tag{3-59}$$

where, P_1 and P_2 are the atmospheric pressure, hPa; ρ is the water density, $\mathrm{kg/m^3}$; g is the gravitational acceleration, $\mathrm{m/s^2}$; v_1 is the vertically averaged horizontal velocity in section 1-1, and it is 0, m/s; H_1 is the water surface elevation at section 1-1, m; v_c is the overflow velocity in section 2-2, m/s; H_2 is the height of sea dike or river bank, m; h_c is the overflow depth above the sea dike or river bank, m.

Rearranging equation (3-59), it becomes:

$$v_c = \sqrt{2g(H_1 - H_2 - h_c)} \tag{3-60}$$

In equation (3-60), there are two unknowns, v_c and h_c. Then, in the overflow section 2-2, critical flow condition is applied.

In open channel hydraulics, the Froude number is an important non-dimensional parameter. The Froude number provides a means of classifying flow conditions and is based not on the paths that strands of water molecules follow, but on the relation between flow velocity and flow depth. The Froude number is defined as the ratio of gravitational forces to inertial forces:

$$F_r = \overline{v} \Big/ \sqrt{g\overline{h}} \tag{3-61}$$

Average flow velocity provides a measure of gravitational forces, while the combination of gravity and depth provides a measure of inertial forces. Inertia measures an object's resistance to a change in motion. Heavy objects or substances have more inertia than light objects or substances. It is much harder to set a heavy object in motion than a light one, and once in motion, a heavy object is much more difficult to redirect, slow down or speed up compared to a light one. The combination of gravity and depth provides a measure of the weight of the water, its inertia. Thus, deep water has much more inertia than shallow water. Assuming a constant discharge along a channel, the Froude number implies that the discharge can be transmitted along the channel as deep slow flow or as shallow fast flow. With deep slow flow, inertial forces dominate flow conditions while with shallow fast flow, gravitational forces dominate flow conditions. When F_r is equal to 1, the flow condition could be called critical flow. Combining equation (3-60) and equation (3-61), the overflow depth and the overflow velocity in section 2-2 can be solved:

$$h_c = 2/3 \times (H_1 - H_2) \tag{3-62}$$

$$v_{\mathrm{c}} = \sqrt{g(\frac{2}{3} \times (H_1 - H_2))} \tag{3-63}$$

Then, the overflow volume at this node is estimated by:

$$V_{\mathrm{nodal}} = \sum_{i=1}^{N_{\mathrm{out}}} (h_{\mathrm{c}}^{i} \times v_{\mathrm{c}}^{i}) \times \Delta t_{\mathrm{out}} \tag{3-64}$$

where, V_{nodal} is the nodal overflow volume at a coastline node, m^2; i is the time step number; N_{out} is the total time steps; Δt_{out} is the output time interval, s; other parameters have been introduced.

To measure the vulnerability, overflow volume is calculated by:

$$V_{\mathrm{dike}} = \sum_{j=1}^{m_{\mathrm{c}}} V_{\mathrm{nodal_j}} \tag{3-65}$$

Or

$$V_{\mathrm{dike}} = \sum_{j=1}^{m_{\mathrm{c}}} (\sum_{i=1}^{N_{\mathrm{out}}} \left(h_{\mathrm{c_j}}^{i} \times \mathrm{v}_{\mathrm{c_j}}^{i}\right) \times \Delta t_{\mathrm{out}}) \tag{3-66}$$

where, V_{dike} is total overflow volume of the coastline, m^2; j is the node number; m_{c} is the total number of the coastline nodes; other parameters have been introduced.

If $H_2 > H_1$, there is no overflow at the node, and V_{nodal} at this node equals 0.

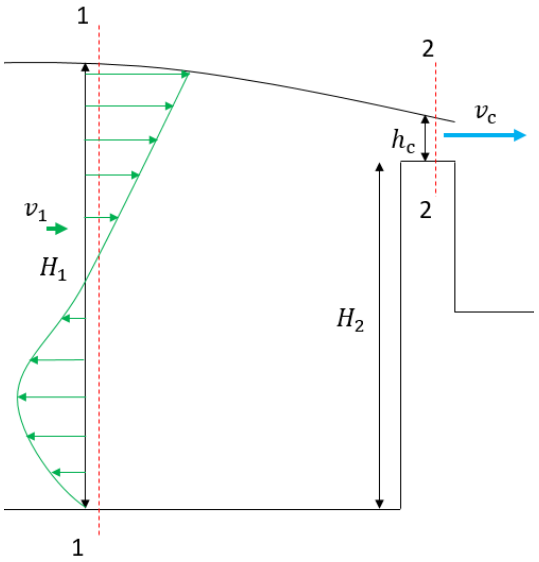

Figure 3.21 Parameters in dike overflow process

4. Methods Verification

In this chapter, the proposed hybrid method used in storm surge model, the tsunami model, drainage pipe network model and the proposed multi-hazard vulnerability assessment method have been validated separately.

4.1 Storm surge model

4.1.1 Introduction

On June 24th, 1985, Typhoon 8506 was formed as an extratropical cyclone above the northwestern Pacific Ocean as shown in Figure 4.1. It then moved north at 25 km/h with increasing intensity. It intensified into a tropical storm on June 26th, and upgraded to a typhoon at 6 am on June 27th. The maximum wind speed was more than 30 m/s and the lowest central pressure was 960 hPa. The typhoon landed at Suruga Bay and passed through Tokyo area at 5 am on 1st of July, 1985, with the maximum storm tide height of 3.5 m (above the datum line). After landfall, the typhoon gradually weakened and eventually disappeared. The storm surge induced by the co-effect of the typhoon's landfall and the high tide, resulted in serious damage along the coastal regions of Chiba fishery ports.

Typhoon 1115 started as a tropical depression in the Pacific Ocean east of the Philippines on September 10th, 2011. It made landfall on the west coastline of Shizuoka prefecture and crossed Tokyo area. It eventually dissipated in the north Hokkaido. Because Typhoon 1115 had the features of low pressure, large scale and strong wind, and coincided with high tide level, it caused great damage to the coastal areas of Chiba prefecture, especially to the fishery industry.

Owing to the substantial effect on Tokyo Bay, especially the coastal areas in Chiba prefecture, storm surges caused by Typhoon 8506 and Typhoon 1115 are selected as the validation study cases for the storm surge model.

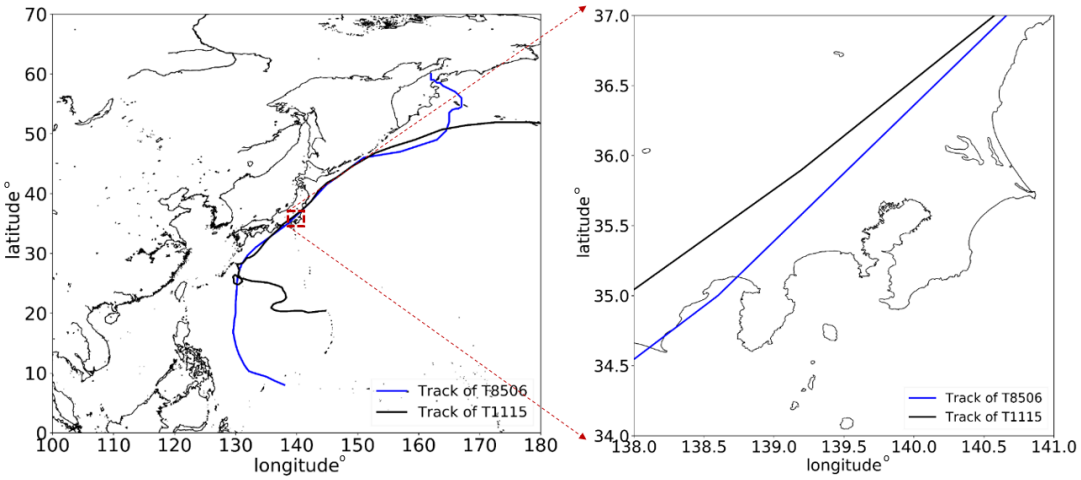

Figure 4.1 Track of Typhoon 8506 and Typhoon 1115

Since 1951, 1753 typhoon cases happened in the Northwest Pacific Ocean area have been recorded in the Japan Meteorological Agency (JMA). Among these records, 298 typhoon which passed through the

area that is near Tokyo Bay area, between N 32° and 40° in latitude and E 134° and 142° in longitude, have been screened out to compare with Typhoon 8506 and Typhoon 1115.

The selected typhoons were analyzed in terms of the lowest atmospheric central pressure and maximum forward translation speed. The lowest atmospheric central pressure of Typhoon 8506 and Typhoon 1115 is 960 hPa and 940 hPa, respectively, while the maximum forward translation speed of Typhoon 8506 and Typhoon 1115 is about 22 m/s and 21 m/s, respectively. In the 298 historical typhoon cases, the lowest atmospheric central pressure is 870 hPa, and the lowest central atmospheric pressure of most typhoons is between 930 hPa and 980 hPa. Regarding the forward translation speed, the maximum value is about 51 m/s, which occurred only one time. The forward translation speed of most typhoons is between 11 m/s and 26 m/s.

4.1.2 Model setup

To validate the performance of the proposed hybrid models for wind and atmospheric pressure fields that has been introduced in Section 3.2.4, a hindcasting of storm surges in Tokyo Bay was performed using the finite volume community ocean model (FVCOM) forced by the wind and pressure data of ERA-I, M–F model with Myers formula, and two hybrid models. To further consider the effect of possible water volume exchange between the ocean from a far place and the inner side of the bay, and also to reduce the boundary influence, a wide area was selected as the computational domain (20° N-60° N, 120° E-160° E) as shown in Figure 4.2(a) and (b). A total of 34,255 computational nodes and 61,905 triangular elements were used.

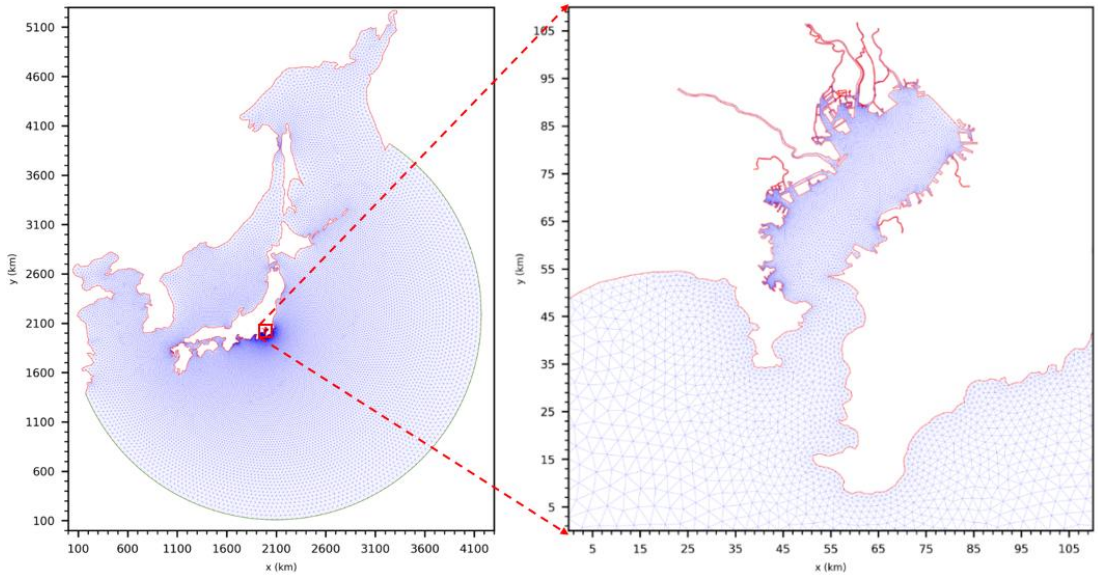

(a) (b)

Figure 4.2 Triangular mesh for the study domain.

Table 3.3 in Section 3.2 presents the information on the storm surge observation stations and Figure 3.2(a) shows the station locations in Tokyo Bay. To compare the performance of the hybrid wind data, the

same set of parameters and boundary conditions were adopted except for the wind and atmospheric pressure data. The computation started with the still water condition with a mean sea level and zero velocities across the domain. For the wind data, ERA-I, M–F model, hybrid model I, and hybrid model II were used. For the atmospheric pressure data, Myers formula, ERA-I, and hybrid model II were applied.

4.1.3 Results and discussion

Figure 4.3 shows comparisons of the storm surge anomalies between the hindcasting results and observed data at six stations in Tokyo Bay for Typhoon 8506. Before the storm surge peaked at 5:00 on July 1st, 1985, the observed sea level anomalies at six stations were generally higher than the mean sea level (=0). ERA-I reproduced the observed tendency better than the M–F model with Myers formula. This indicates the significant influence of the atmospheric pressure fields on the reproducibility of sea level anomalies before the typhoon approach. However, ERA-I data substantially under-predicted the storm surge peak at all six stations, which implies the insufficient spatial resolution of ERA-I data to reproduce the surge peak. Comparing all the model results, hybrid model II (for both wind and atmospheric pressure fields) performed better in reproducing the storm surge anomalies during the typhoon approach, the surge peak, and the following oscillations induced by bay-scale resonance.

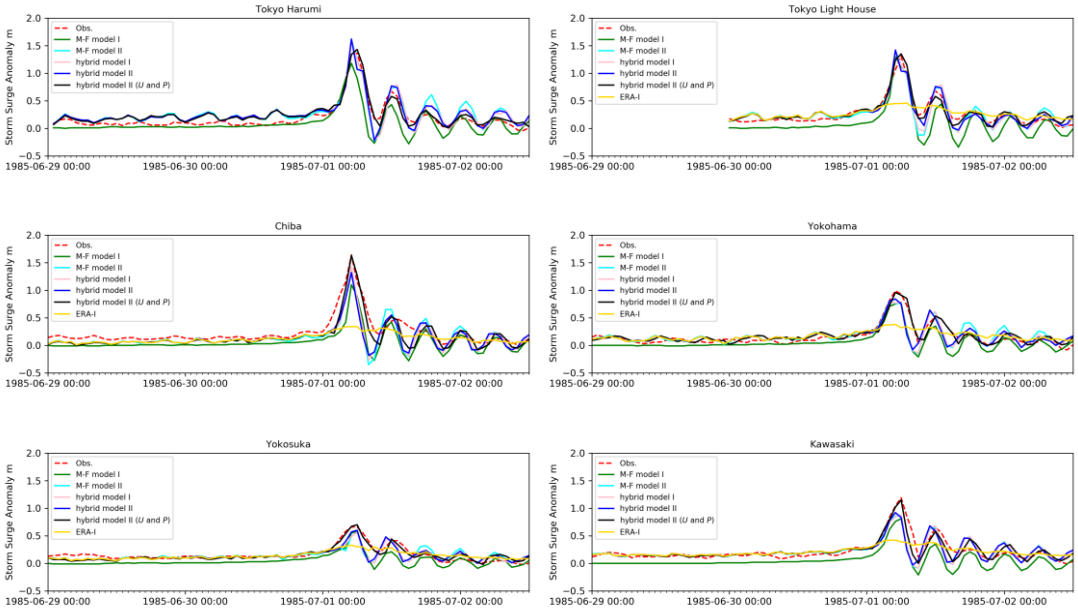

Figure 4.3 Time series comparison of storm surge simulation results based on different wind and pressure data for Typhoon 8506 (Obs.: the measured storm surge anomaly; M–F model I: storm surge model using wind data computed by M–F model and pressure data computed by Myers formula; M–F model II: storm surge model using wind and atmospheric pressure data computed by M–F model and ERA-I, respectively; Hybrid model I: storm surge model using wind and atmospheric pressure data computed by hybrid model I and ERA-I, respectively; Hybrid model II: storm surge model using wind and atmospheric pressure data computed by hybrid model II and ERA-I, respectively; Hybrid model II (*U* and *P*): storm surge model using wind and atmospheric pressure data computed by hybrid model II; ERA-I: same name as the

ERA-Interim reanalysis data, but here it represents the storm surge model that uses wind and surface atmospheric pressure data of ERA-I).

Figure 4.4 shows comparisons of the storm surge anomalies between the computed values using six models and the observed values for Typhoon 1115 at four stations in Tokyo Bay. M–F model cannot reproduce the storm surge anomalies before the peak, and the peak anomalies in Station Tokyo Harumi, Station Chiba and Station Yokosuka are significantly lower than the observations. Similarly, ERA-I cannot reproduce the peak anomalies at four stations. Among the six storm surge models, only hybrid model II (for both wind and atmospheric pressure fields) exhibited better results in reproducing the storm surge anomalies.

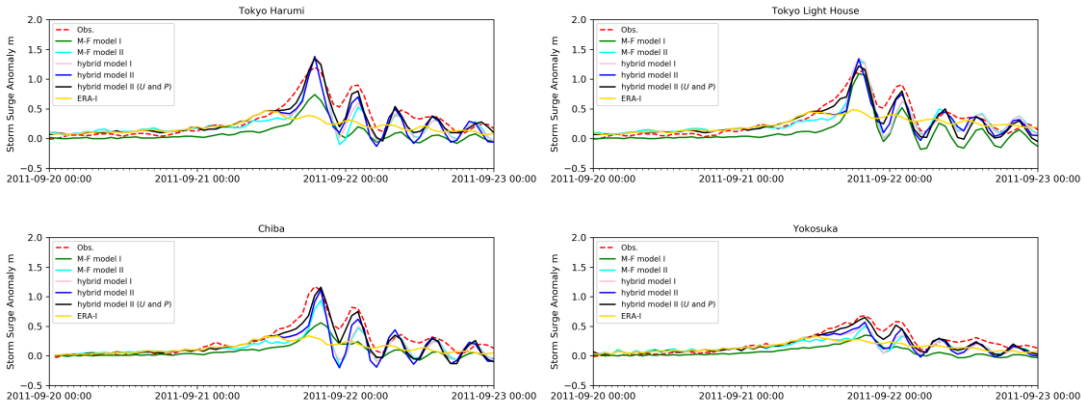

Figure 4.4 Time series comparison of storm surge between the measured and computed results of different wind field data and atmospheric pressure data for Typhoon 1115 (Obs.: the measured storm surge anomaly; other legends are introduced in Figure 4.3)

To further evaluate the accuracy among the six models, the RMSE (defined by equation (3-22)) between the computed and observed values are presented in Table 4.1 for Typhoon 8506 and Table 4.2 for Typhoon 1115. The periods of comparisons are from 6:00 on June 29th to 9:00 on July 2nd, 1985, for Typhoon 8506, and 3:00 on September 20th to 23:00 on September 23rd, 2011, for Typhoon 1115. According to Table 4.1 and Table 4.2, it can be concluded that the wind and atmospheric pressure fields obtained by hybrid model II should be used for hindcasting of storm surges.

Table 4.1 Statistics of storm surge simulation results from different model for Typhoon 8506

Station	RMSE (m)					
	M–F model I	M–F model II	Hybrid model I	Hybrid model II	Hybrid model II (U and P)	ERA-I
Tokyo Harumi	0.172	0.155	0.140	0.133	0.098	0.214
Tokyo Light House	0.223	0.126	0.113	0.099	0.084	0.176
Chiba	0.243	0.213	0.191	0.192	0.121	0.242
Yokohama	0.153	0.137	0.122	0.122	0.064	0.147
Yokosuka	0.136	0.106	0.092	0.091	0.053	0.093
Kawasaki	0.200	0.137	0.134	0.138	0.083	0.156

Table 4.2 Statistics of storm surge simulation results from different model for Typhoon 1115

Station	RMSE (m)					
	M–F model I	M–F model II	Hybrid model I	Hybrid model II	Hybrid model II (U and P)	ERA-I
Tokyo Harumi	0.290	0.213	0.189	0.209	0.113	0.266
Tokyo Light House	0.256	0.159	0.158	0.144	0.121	0.221
Chiba	0.242	0.227	0.204	0.226	0.117	0.258
Yokosuka	0.195	0.137	0.120	0.117	0.071	0.150

4.1.4 Sub-conclusion

Using the unstructured-grid finite volume community ocean model (FVCOM), hindcasting of storm surges in Tokyo Bay was performed by forcing six combinations of modeled wind and atmospheric pressure fields. The results showed that the modification of both atmospheric pressure and wind data significantly improved the accuracy of the storm surge anomalies. Both proposed hybrid models performed better than the computations using only ERA-I or M–F model. Hybrid model II can be easily tuned for each storm surge cases using only ERA-I and M–F data with high accuracy.

4.2 Drainage pipe model

4.2.1 Parameter sensitivity analysis

The aim of the sensitivity analysis is to evaluate how each parameter affects the unsteady open channel flow in an enclosed drainage pipe so as to determine proper parameter values especially for model parameters. The studied parameters include the finite difference parameters (Δx_s, Δt_s, θ_s, and ε) and the hydraulic parameters (S_0, n_m, d_s, and b_{slot}).

The difference between finite difference parameters and hydraulic control parameters is that the former parameters are related to the numerical method of solving the governing equations, while the latter are more with respect to the physical attributes of specific pipes.

4.2.1.1 Finite difference parameters

A summary of the hydraulic conditions for finite difference parameter analysis is described in Table 4.3.

Table 4.3 Hydraulic conditions of study pipe

Parameter name	Value
Pipe length (L_s)	100 m
Pipe diameter (d_s)	1.5 m
Bottom slope (S_0)	0.001
Roughness (n_m)	0.013
Base flow	0.4 m^3/s
Peak flow	2.6 m^3/s
Outfall condition	Critical flow

The flow discharge input data in upstream is plotted in Figure 4.5.

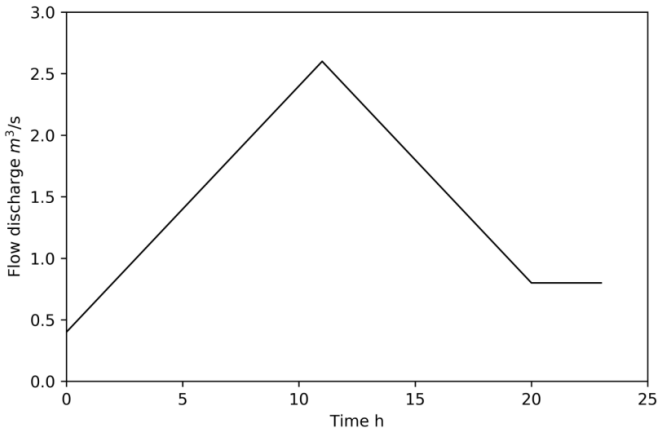

Figure 4.5 Input flow discharge in upstream

As illustrated in Section 3.5.3 regarding the determination of time step of drainage pipe model, the distance and time increment values increased and the ratio of spatial and temporal is equal to 5. The finite difference grid space increment Δx_s varies between 5 m and 50 m, and the temporal step Δt_s varies between 1 s and 10 s accordingly (see Table 4.4). The values of other finite difference parameters are fixed.

Table 4.4 Variation in finite difference grid space Δx_s

Run	Δx_s (m)	Δt_s (s)
1	5	1
2	10	2
3	20	4
4	50	10
ε	0.00001	
θ_s	0.55	

The resultant upstream water depth hydrographs are shown in Figure 4.6. With the grid space increasing from 5 m to 50 m, the solutions are nearly identical.

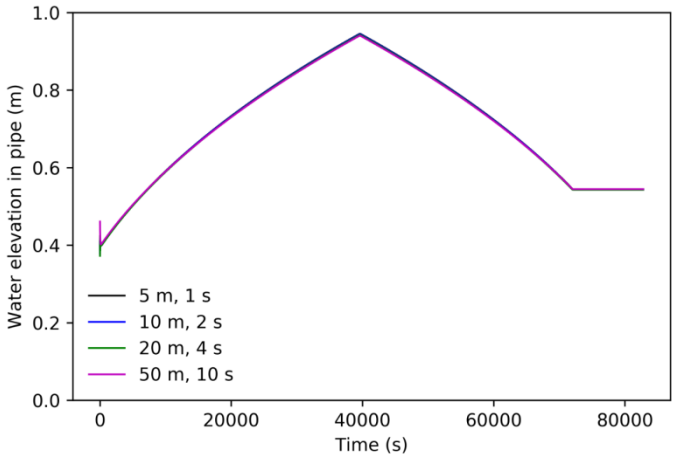

Figure 4.6 Upstream water elevation computed with different Δx_s

The second test is to check the effect of variation of the finite difference weighting parameter θ_s, the grid space and temporal step for the test is 50 m and 10 s, respectively. When θ_s equals 1.0, a fully implicit scheme is formed, and $\theta_s = 0$ results in an explicit scheme. The box scheme[140, 141] ($\theta_s = 0.5$) is accurate and stable for slowly varying flows, but it produces numerical oscillations under certain transient conditions, and these oscillations do not arise for θ_s ranging between 0.55 and 1.0. The influence of weighting factor θ_s on stability and convergence was examined by Fread[142], who concluded that the accuracy of the computation decreases as θ_s departs from 0.5 and approaches 1.0. Fread[143] also recommended a value of $\theta_s = 0.55$ as this minimizes loss of accuracy and avoids numerical oscillations for transient conditions. Schaffranek et al.[144] recommended a practical lower limit of θ_s as 0.6 to avoid numerical oscillation. Hence, usually the value of θ_s is taken over 0.55 to 0.6, and here the value of θ_s varying from 0.55 to 1.0 is investigated for the developed model.

Table 4.5 Variation in the finite difference weighting factor θ_s

Run	θ_s
1	0.55
2	0.6
3	0.7
4	0.8
5	0.9
6	1.0
$\Delta x_s/\Delta t_s$	50 m/10 s
ε	0.00001

The resulting water depth hydrographs at the upstream are shown in Figure 4.7. The change of the finite difference weighting factor does not affect much on the computed water depth.

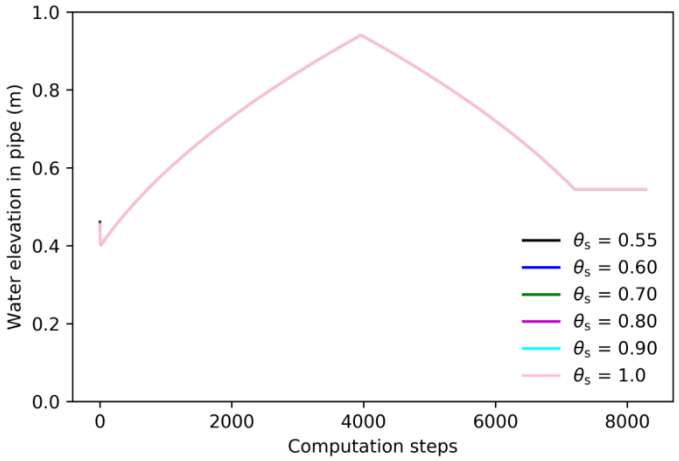

Figure 4.7 Upstream water elevation computed with different θ_s

The third test is on the variation in the finite difference convergence parameter. The grid space and temporal step for the test is 50 m and 10 s, respectively.

Table 4.6 Variation in the finite difference convergence parameter ε

Run	ε
1	0.00001
2	0.0001
3	0.001
4	0.01
5	0.1
$\Delta x_s/\Delta t_s$	50 m/10 s
θ_s	0.55

The resulting water depth hydrographs at the upstream are shown in Figure 4.8. The change of the finite difference convergence parameter does not affect much on the computed water depth.

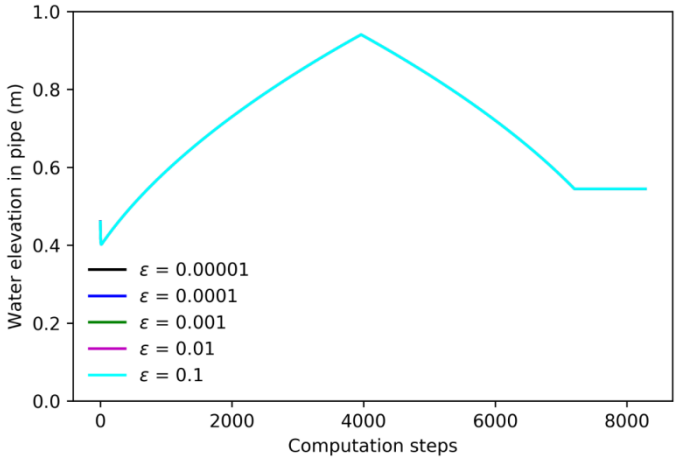

Figure 4.8 Upstream water elevation computed with different ε

4.2.1.2 Hydraulic parameters

A summary of the studied pipe property for hydraulic parameter analysis is described in Table 4.7. The input flow value is the same as that introduced in Section 4.2.1.1. The first test is on the variation in the pipe bottom slope. The grid space and temporal step for the test is 50.0 m and 10.0 s, respectively.

Table 4.7 Hydraulic conditions and model parameters

Parameter name	Value
Pipe length (L_s)	100 m
$\Delta x_s/\Delta t_s$	50 m/10 s
Convergence criteria (ε)	0.00001
Weighting factor (θ_s)	0.55
Base flow	0.4 m^3/s
Peak flow	2.6 m^3/s
Outfall condition	Critical flow

Table 4.8 Variation in the pipe bottom slope S_0

Run	S_0
1	0.00001
2	0.0001
3	0.0005
4	0.001
5	0.0015
n_m	0.012
d_s	1.5

The resulting upstream water depth hydrographs are shown in Figure 4.9. Variation in the pipe bottom slope has a significant influence on the water depth at the upstream. For very flat slopes, maximum upstream water depths are observed.

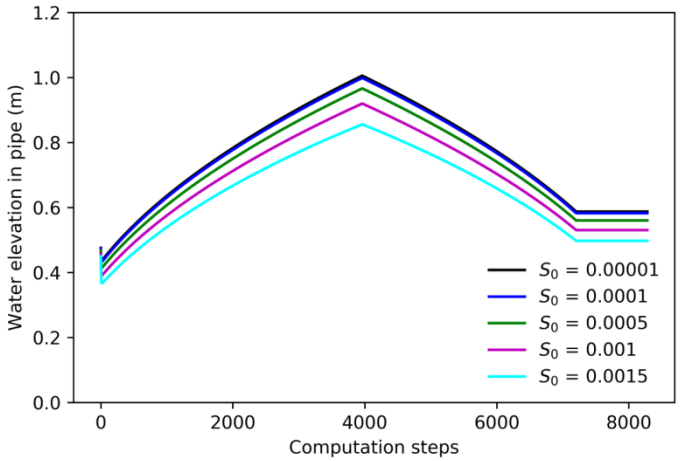

Figure 4.9 Upstream water elevation computed with different S_0

The second test is on the variation in manning roughness coefficient. The grid space and temporal step for the test is 50 m and 10 s, respectively.

Table 4.9 Variation in the manning roughness coefficient n_{m}

Run	n_{m}
1	0.010
2	0.012
3	0.017
4	0.025
S_0	0.0001
d_{s}	1.5

The effect of the variation of the manning roughness coefficient on the upstream water depth is shown in Figure 4.10. A higher value of manning roughness coefficient results in an increase in upstream water depth.

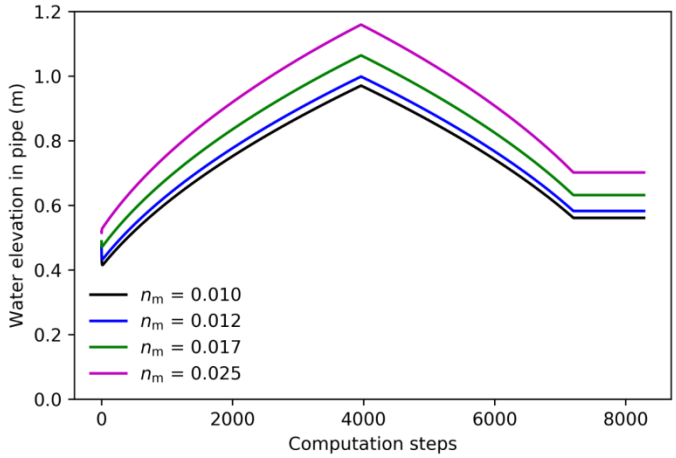

Figure 4.10 Upstream water elevation computed with different n_m

The third test is on the variation in the pipe diameter d_s. The grid space and temporal step for the test is 50 m and 10 s, respectively.

Table 4.10 Variation in the pipe diameter d_s

Run	d_s (m)
1	1.2
2	1.5
3	1.8
4	2.1
S_0	0.0001
n_m	0.012

The effect of pipe diameter on the upstream depth hydrograph is shown in Figure 4.11. As the pipe diameter decreases, the water depth increases.

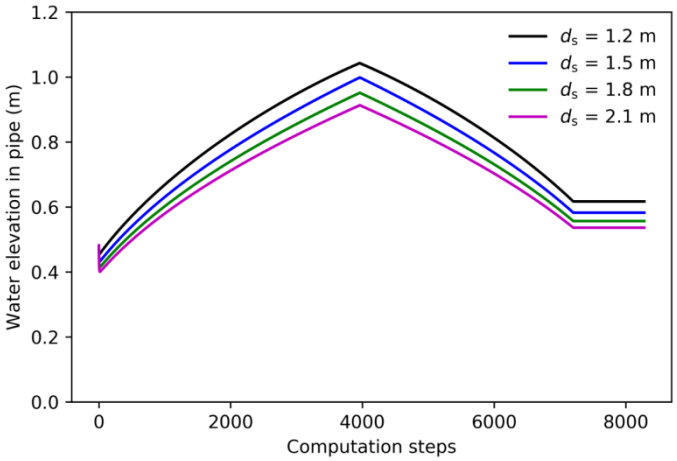

Figure 4.11 Upstream water elevation computed with different d_s

The fourth test is on the variation in slot width b_{slot}. A series of numerical simulations has been performed in order to determine the influence of the width of the Preissmann slot on the flow profile. The slot width is based on the pressure wave speed, C_s, of the fluid when the pipe is under pressurized flow state. The pressure wave speed can be computed and it varies with the pipe material and the volume of entrained air[145]. The slot width is computed using equation (3-31). A plot of the slot width and pressure wave speed for pipe diameter of 1.0 m is shown in Figure 4.12. The grid space and temporal step for the test is 50 m and 10 s, respectively, and the pipe diameter is 1.2 m.

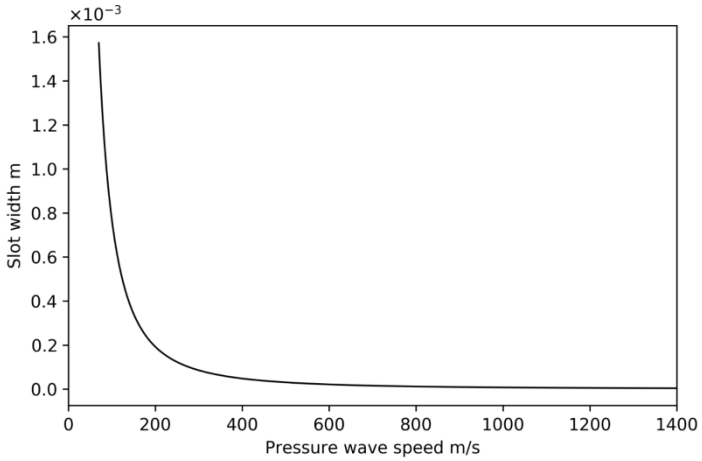

Figure 4.12 Slot width and pressure wave speed for pipe diameter of 1.0 m

Table 4.11 Variation in slot width b_{slot}

Run	b_{slot} (m)
1	0.00005
2	0.0001
3	0.001
4	0.003

The upstream input discharge is plotted in Figure 4.13. The effect of slot width on the upstream water depth is plotted in Figure 4.14. It demonstrates that the computed flow hydrographs are found to be almost insensitive to the variations in the slot width.

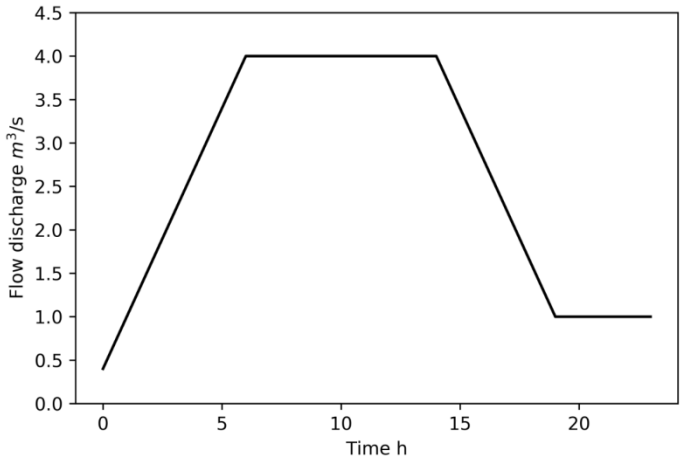

Figure 4.13 Input flow discharge in the upstream node for investigation of slot width

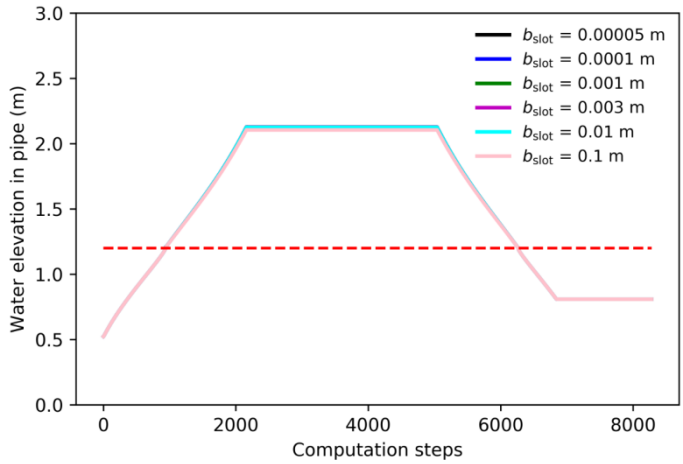

Figure 4.14 Upstream water elevation computed with different b_{slot}

4.2.2 Model comparison

Due to the lack of experimental data for validation of the developed unsteady flow drainage pipe model, a commonly used Storm Water Management Model (SWMM) is used to demonstrate the model capability. The Storm Water Management Model (SWMM) is a dynamic wave rainfall-runoff-routing model originally developed by the USEPA (United States Environmental Protection Agency). It can be used for a single event or long-term simulation projects of surface runoff and water quality from urban regions. The runoff component of SWMM uses nonlinear reservoir concept methods and Horton or Green-Ampt loss functions for describing the hydrologic process in the sub-catchment areas that receive precipitation and generate runoff and pollutant loads. The routing part of SWMM transports the runoff via pipes, channels, storage treatment infrastructures, pumps, and regulators. SWMM can track the quantity and quality of runoff within sub-catchments, the flow state, and quality of water in each pipe and channel during a simulation.

The model comparison is divided into two parts, the first one is for single pipe scenarios, including the circular cross-section pipe and trapezoidal shape pipe, the second part is for a drainage pipe network,

including surcharged flow condition and open channel flow state.

4.2.2.1 Single pipe scenarios

The first test is for circular cross-section pipe. The property value of the pipe is shown in Figure 4.15. A summary of finite difference parameter values for the comparison is described in Table 4.12. Input flow at the upstream node is shown in Figure 4.16.

Table 4.12 Finite difference parameters

Parameter name	Value
Δt_s	10 s
Δx_s	50 m
Convergence criteria (ε)	0.00001
Weighting factor (θ_s)	0.55
Outfall condition	Critical flow

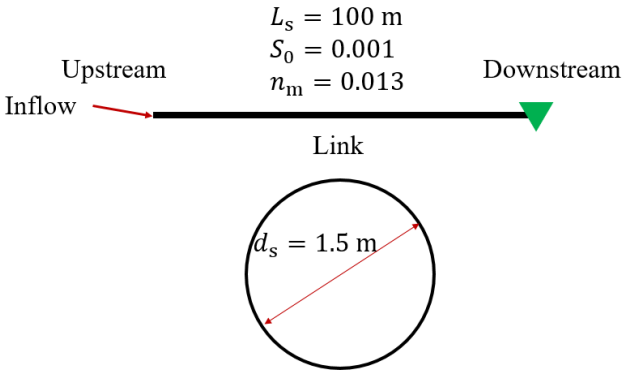

Figure 4.15 Studied pipe with circular cross section

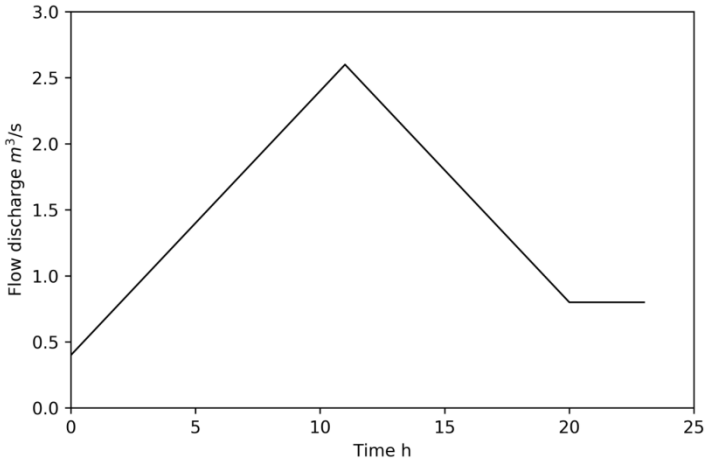

Figure 4.16 Upstream input flow

The computed water depth at upstream node and outfall, and the link discharge hydrographs of two

models are plotted in Figure 4.17, and the RMSE values are presented in Table 4.13. The flow in the pipe, the water depth of the pipe outfall, and the peak value of water depth in the upstream node computed using the developed model is consistent with that of SWMM, although the developed model slightly over-predicts the increasing part and decreasing stage.

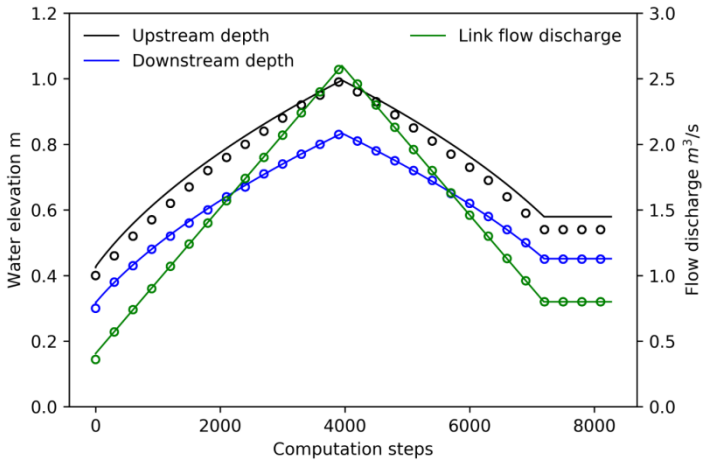

Figure 4.17 Comparison of the computed water depth and link flow discharge between developed model and SWMM (Solid lines: developed model; Circles: SWMM)

Table 4.13 RMSE

Variable name	RMSE
Upstream depth	0.085 m
Downstream depth	0.003 m
Link flow	0.003 m^3/s

The second test is for the trapezoidal cross-section pipe. The property value of the pipe is shown in Figure 4.18. A summary of finite difference parameter values for comparison is described in Table 4.14. Input flow at the upstream node is the same as that in test 1.

Table 4.14 Finite difference parameters

Parameter name	Value
Δt_s	10 s
Δx_s	50 m
Convergence criteria (ε)	0.00001
Weighting factor (θ_s)	0.55
Outfall condition	Critical flow

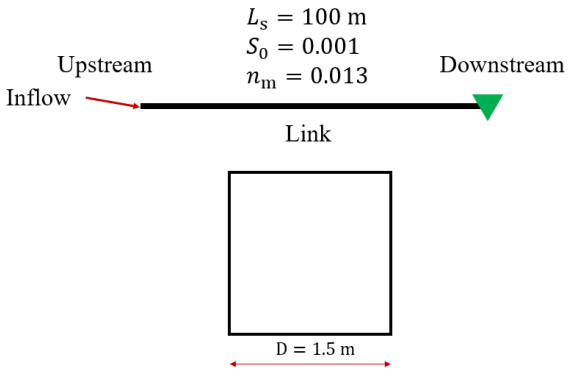

Figure 4.18 Studied pipe with rectangular cross section

The computed water depth at upstream node and outfall, and the link discharge hydrographs of two models are plotted in Figure 4.19, and the RMSE values are presented in Table 4.15. The result shows that the developed model is consistent with the output of SWMM under the same computational conditions.

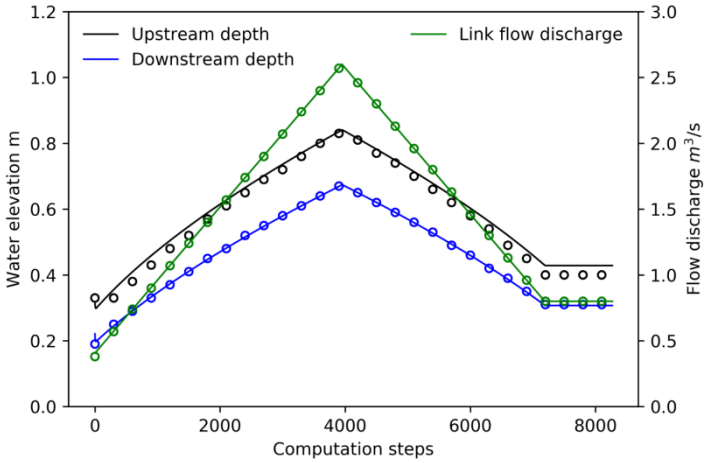

Figure 4.19 Comparison of the computed water depth and link flow discharge between developed model and SWMM (Solid lines: developed model; Circles: SWMM)

Table 4.15 RMSE

Variable name	RMSE
Upstream depth	0.0219 m
Downstream depth	0.0029 m
Link flow	0.0037 m^3/s

4.2.2.2 Drainage pipe networks

In order to demonstrate the capability of the developed drainage pipe model for the application of a drainage network, a simple drainage system consisting of two upstream pipes and one downstream pipe is used for the numerical experiment. The properties of the studied drainage pipe network are shown in Figure 4.20. A summary of finite difference parameter values for comparison of the first test (open

channel flow state) is described in Table 4.16. Input flow at the upstream node is shown in Figure 4.21.

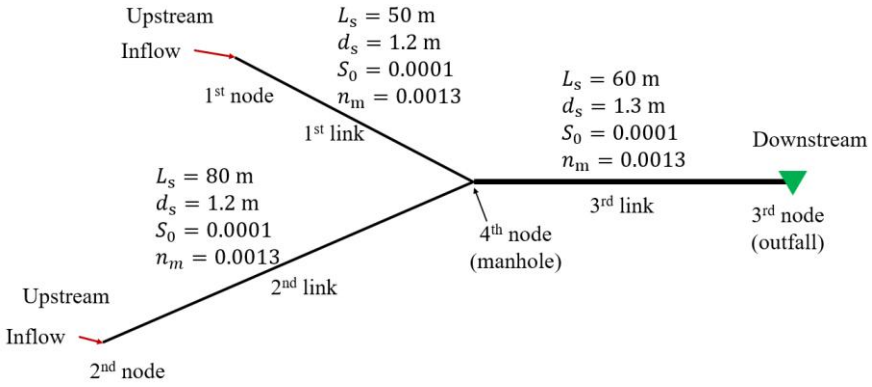

Figure 4.20 Drainage pipe network

Table 4.16 Finite difference parameters

Parameter name	Value
Δt_s	10 s
Δx_s	50 m, 60 m, 80 m
Convergence criteria (ε)	0.00001
Weighting factor (θ_s)	0.55
Outfall condition	Critical flow

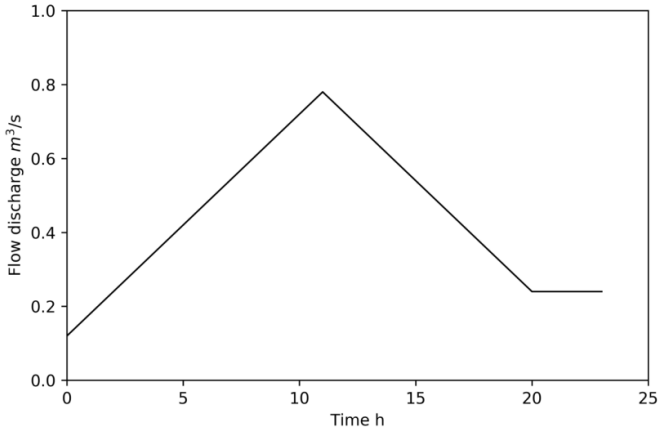

Figure 4.21 Input flow discharge in the two upstream inlets

The computed water depth and link flow discharge hydrographs are shown in Figure 4.22. For the computed water depth at upstream nodes (1st, 2nd, and manhole), the developed model slightly over-predicts than SWMM. For the outfall water depth and link flow discharge, the developed model is consistent with SWMM well.

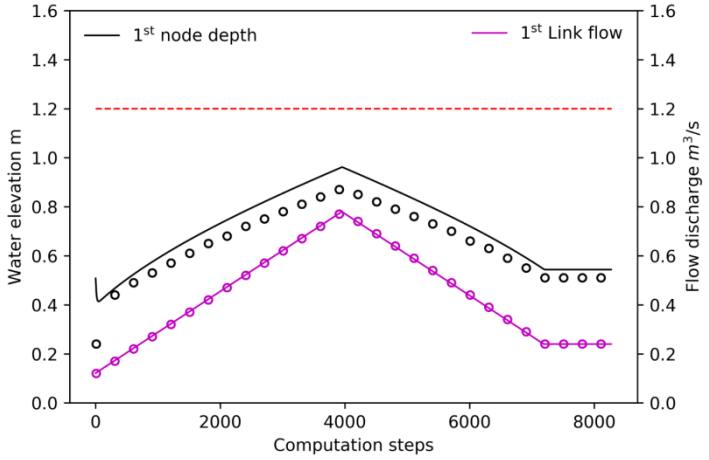
1st node depth
1st Link flow
Water elevation m
Flow discharge m^3/s
Computation steps
0.0
0.2
0.4
0.6
0.8
1.0
1.2
1.4
1.6
0
2000
4000
6000
8000

(a)

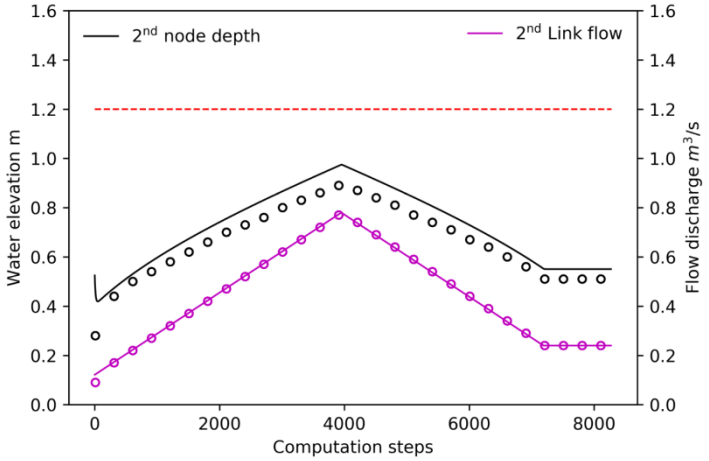
2nd node depth
2nd Link flow
Water elevation m
Flow discharge m^3/s
Computation steps
0.0
0.2
0.4
0.6
0.8
1.0
1.2
1.4
1.6
0
2000
4000
6000
8000

(b)

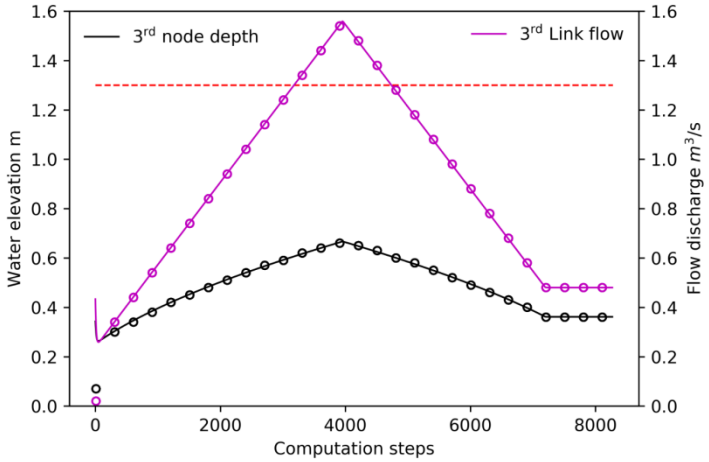
3rd node depth
3rd Link flow
Water elevation m
Flow discharge m^3/s
Computation steps
0.0
0.2
0.4
0.6
0.8
1.0
1.2
1.4
1.6
0
2000
4000
6000
8000

(c)

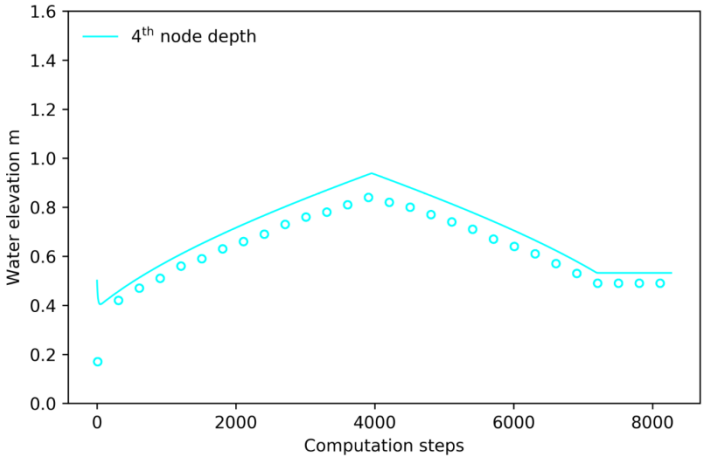

(d)

Figure 4.22 Computed water depth and link flow discharge hydrographs of developed model (Solid lines) and SWMM (Circles) ((a), (b), (c): water depth and link flow discharge for the 1st, 2nd and 3rd pipe, respectively; (d): water depth at manhole; Red dashed line: crown of the pipe)

The second test is for surcharged flow state in drainage pipe network. The properties of the drainage pipe network are the same as those in test 1. A summary of finite difference parameter values for comparison (surcharged flow state) is described in Table 4.17. Input flow at the upstream nodes is shown in Figure 4.23.

Table 4.17 Finite difference parameters

Parameter name	Value
Δt_s	10 s
Δx_s	50 m, 60 m, 80 m
Convergence criteria (ε)	0.00001
Weighting factor (θ_s)	0.55
Outfall condition	Critical flow

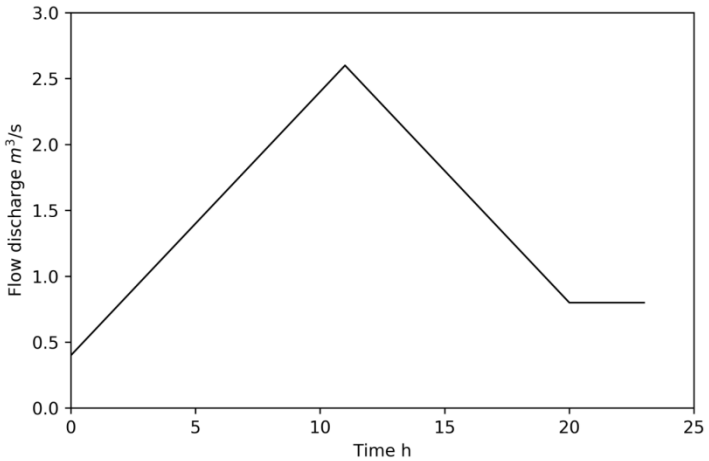

Figure 4.23 Input flow discharge in the two upstream inlets

The computed water depth and link flow discharge hydrographs are shown in Figure 4.24. For the computed water depth at upstream nodes (1st, 2nd, and manhole), the developed model slightly over-predicts than SWMM. The water depth at upstream nodes and link flow first increase from 0 to 2,000 computation steps, and then pipe flow at upstream of the 1st and 2nd links becomes pressurized state, after 6,000 computation steps, the flow in the upstream starts returning back to open channel flow state. In SWMM, it captures the increasing (0-2,000 steps) and decreasing (6,000-7,200 steps) stage of water depth and link flow, and for the surcharged flow period, the water depth keeps the value that is identical to the pipe diameter, and the link flow keeps unchanged. In the developed model, the water depth during surcharged flow state represents the piezometric water head pressure, and for the increasing and decreasing stage, it is consistent with the change in SWMM.

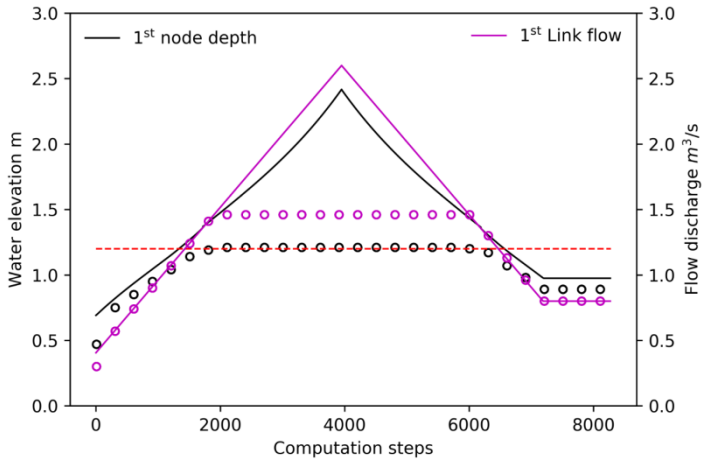

(a)

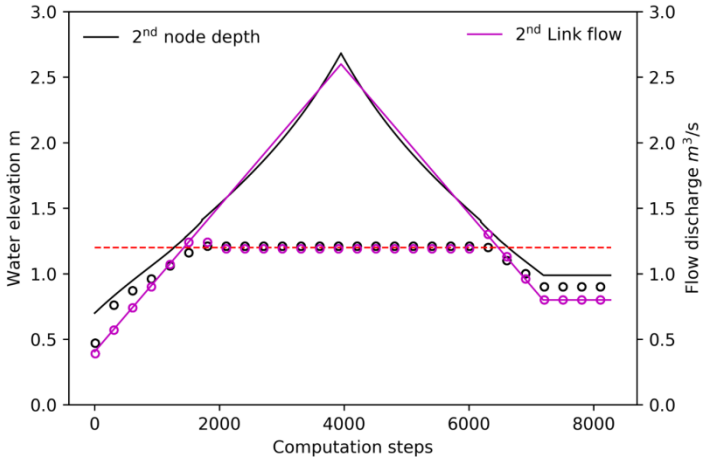

(b)

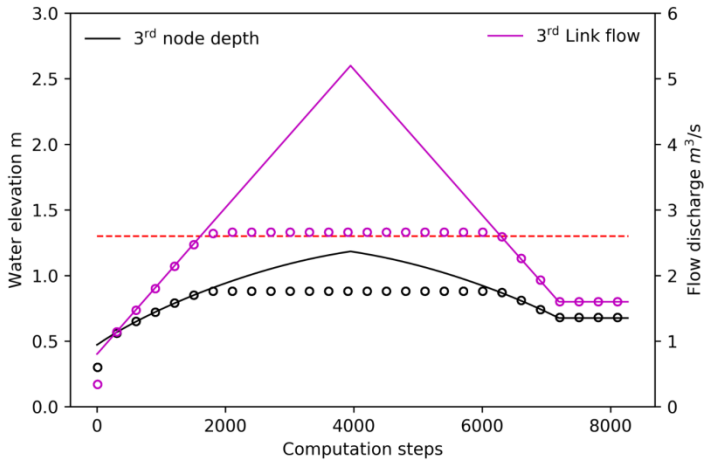

(c)

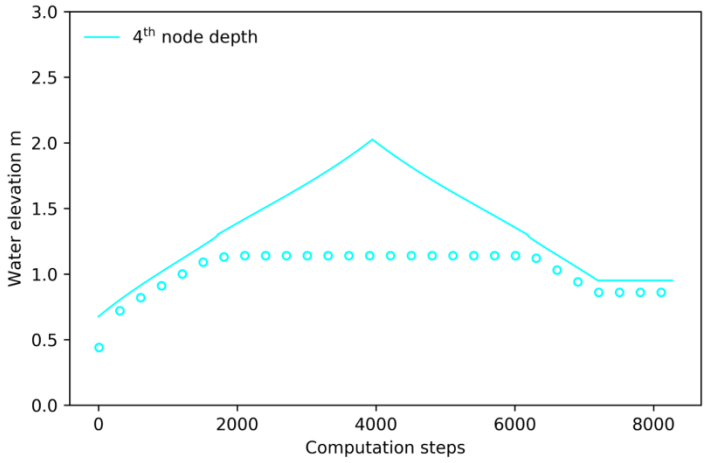

(d)

Figure 4.24 Computed water depth and link flow discharge hydrographs of developed model (Solid lines) and SWMM (Circles) ((a), (b), (c): water depth and link flow discharge for the 1st, 2nd and 3rd pipe, respectively; (d): water depth at manhole; Red dashed line: crown of the pipe)

4.2.3 Sub-conclusion

An unsteady flow drainage pipe model capable of simulating flows that varies from free surface open channel flow to pressurized flow and back to free surface condition has been developed. The model is based on the complete one dimensional Saint-Venant equations and solved by a four-point weighted implicit finite difference scheme. A narrow fictitious slot along the crown of the pipe-the Preissmann slot technique is adopted to create the proper pressure wave when the pipe is under surcharged flow state.

The unsteady flow drainage pipe model was validated through comparison with the EPA model SWMM under various conditions including single pipe scenarios with different cross-section types and drainage network scenarios with surcharged flow state and open channel flow state. The sensitivity analysis on the finite difference parameters and hydraulic control parameters has been carried out for better selection of the values, especially the time step and slot width. Numerical experiments based on a series of scenarios demonstrated the capabilities of the model in reproducing the drainage pipe flow under

multiple types of flow conditions.

4.3 Integrated FVCOM and drainage pipe model

4.3.1 Introduction

On March 11th, 2011, a devastating tsunami accompanied with *M* 9.0 earthquake attacked the Tohoku coast of Japan, and completely destroyed many coastal communities[146]. The mega-tsunami generated by the earthquake also propagated to Tokyo Bay, and damaged part of the coast in the bay. Much effort has been made by the government to protect the area against natural disasters including earthquakes, storm surges, and tsunamis. As disaster prevention against storm surge is considered as the first priority in Tokyo Bay, protection structures are designed against storm surges and the height of the structure is lower in the southern part of the bay and higher in the northern. Tsunami is considered less dangerous than storm surges in Tokyo Bay before 2011 Tohoku earthquake tsunami because the worst tsunami case used by local governments was the 1923 Taisho Kanto earthquake tsunami, which did not cause huge damage in the head of the bay. Sasaki et al.[7] studied the behavior of 2011 Tohoku earthquake tsunami in Tokyo Bay using field survey and numerical simulations, in their study, FVCOM was adopted and part of the source code was modified in order to include the tsunami initial water surface condition. The 2011 Tohoku earthquake tsunami height at Kisarazu Fishery Port is about 2.2 m, which is lower than the height of the parapet of the seawalls; however, overflow from the road side ditch when the water level rose. In Kisarazu Port, the road between the port and the store was inundated. Thus, as the existing studies[37-39] reported, the coastal area still has risks of being flooded by the overflow from the drainage pipe system during tsunami events.

In this part, the Hotstart mode in FVCOM is firstly adopted to setup the initial water surface condition, and the computed water levels in the stations of Tokyo Bay are compared to the observed data. The overflow inundation in Kisarazu Port during the 2011 Tohoku earthquake tsunami is used as the validation case to demonstrate the reliability of the model. Two numerical experiments are prepared for the validation. One contains the drainage pipe module in the simulation, and in the other, the drainage module is excluded.

4.3.2 Model setup

High resolution grid is necessary to simulate storm surge and tsunami wave propagation owing to the large spatial gradients in the geometric and topographic features around Tokyo Bay. The geometry and bathymetry of the study area are similar as that used in the storm surge model in Section 4.1. Bathymetry data and coastline data of different data sources are illustrated in Section 3.1.1.2. An unstructured mesh system was constructed using the Surface Water Modeling System 11.1 (Aquaveo) covering a large area, and in order to provide dynamically reliable information regarding water levels in Tokyo Bay especially around the coastal areas, the outer boundary of the model has been chosen far from the area of interest. The general mesh size varied from 50 km at the open boundary to 50 m in the inner side of Tokyo Bay. The total number of the computational nodes and triangular elements in 2011 Tohoku earthquake tsunami simulation mesh is 197,407 and 388,010, respectively. The major difference between the mesh used in the

storm surge simulation and the one used in the tsunami simulation is that in the mesh for tsunami simulation, the mesh resolution at the Tohoku coast area (the tsunami fault area) is 1 km, but in the mesh for storm surge simulation, there is no such a feature.

The fault model parameters[147] are inputted in the rectangular fault model-Okada model (1985), it is adopted in this study as the tsunami source model, which is used to generate an initial sea surface displacement. Therefore, the temporal variation of the fault model displacement during the seismic motion is not considered. The initial water surface condition is included in the Hotstart file. The BKI radiation boundary condition was used in the simulation to prevent the wave reflection from the boundary.

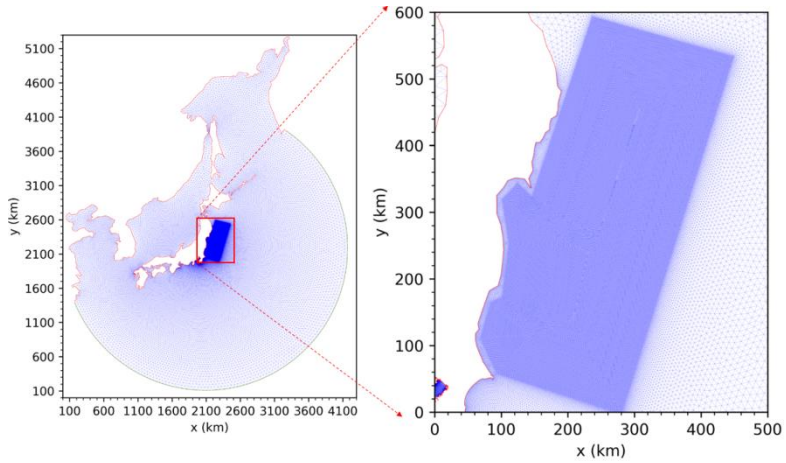

(a)

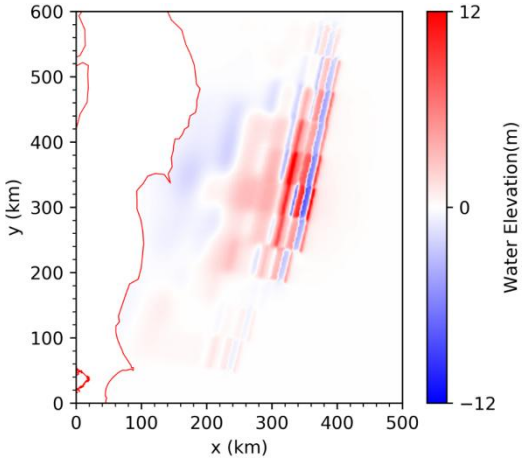

(b)

Figure 4.25 (a) Unstructured mesh for 2011 Tohoku tsunami simulation and (b) Tsunami initial surface displacement using parameters of Fujii et al. 2011

The mesh in Kisarazu Port is resolved and the mesh size for the inundation area is 5 m. Figure 4.26 shows the study area, resolved mesh and DEM data in land for inundation simulation. The configuration of the inundation mesh in Kisarazu Port is presented in Table 4.18 including the number of nodes and

elements. The model time and external time step of simulation is 6 hours and 0.1 s, respectively. The simulation is performed in HPC supercomputer of Research Institute for Information Technology, Kyushu University. The wall clock time for the simulation is about 40 minutes.

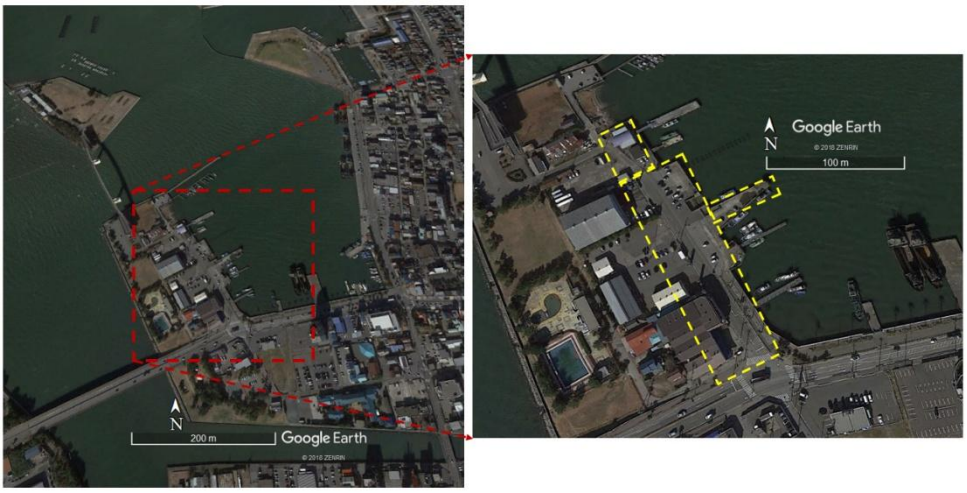

(a)

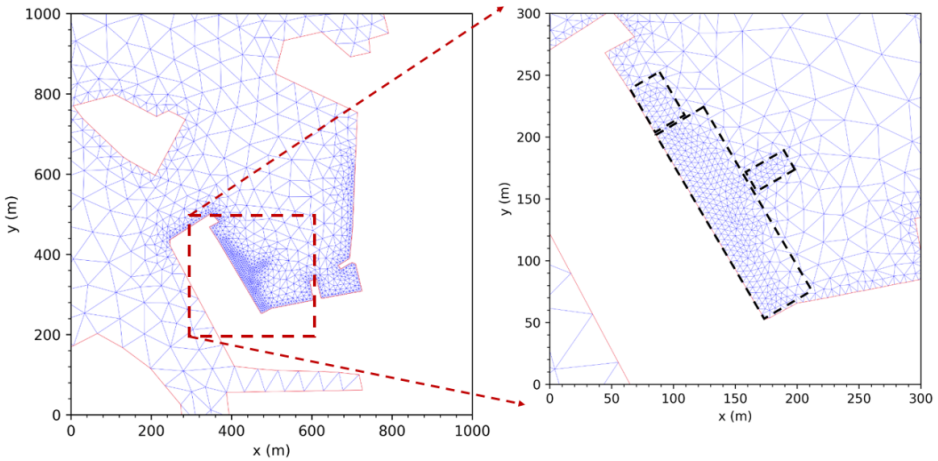

(b)

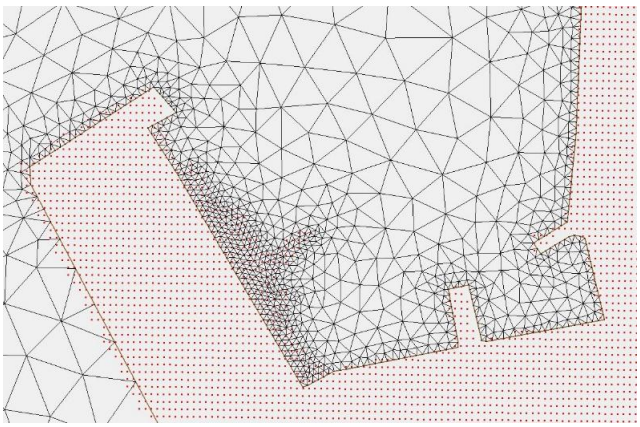

(c)

Figure 4.26 Resolved mesh in Kisarazu Port (red dash rectangle area in (a) and (b) is the study area; yellow dash rectangles in (a) and black rectangles in (b) are the inundation propagation area; (c): DEM data points (red scattered)) ((a), source: Google Earth, Data SIO, NOAA, U.S. Navy, NGA, GEBCO)

Table 4.18 Information of the inundation mesh

Mesh name	Nodes	Elements
Inundation mesh in Kisarazu	299	487

The drainage pipe which overflew during the 2011 Tohoku earthquake tsunami in the study area is shown in Figure 4.27. It is a road side ditch and about 56 m long and 0.3 m width. The outlet of the ditch is submerged underwater. In the current work, the ditch is conceptualized as a rectangular shape cross section drainage channel with 56 m long and 0.3 m width, and connected by 11 manholes. Each manhole has an area of 0.5 m^2. The schematic diagram of the drainage channel is shown in Figure 4.28.

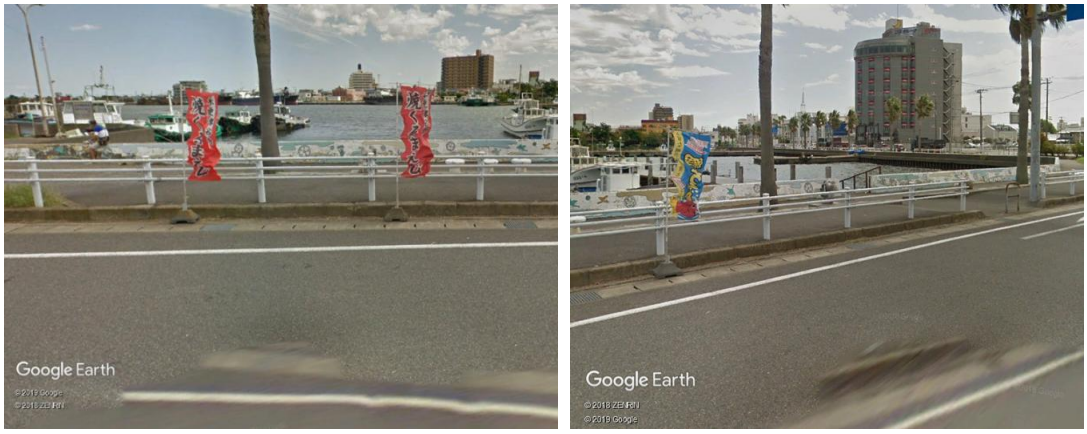

(a)

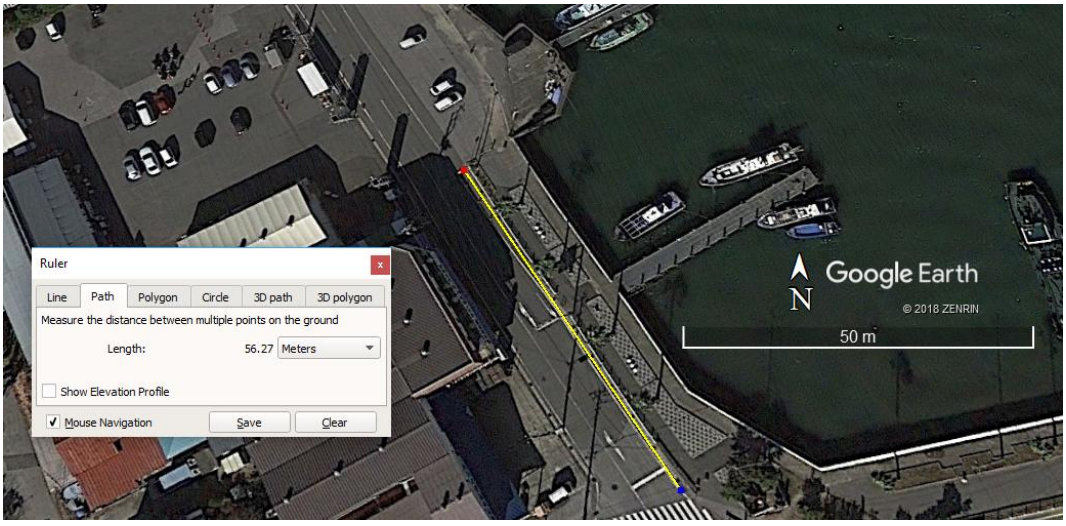

(b)

Figure 4.27 Road ditch in the study area ((a): real shoot image; (b): length of the ditch) (source: Google Earth, Data SIO, NOAA, U.S. Navy, NGA, GEBCO)

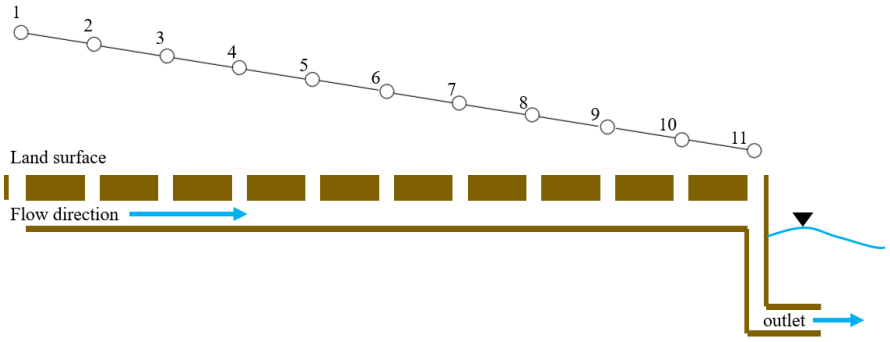

Figure 4.28 Conceptualized drainage channel

4.3.3 Results and discussion

Figure 4.29 shows the comparison of time series anomaly between observations and computed results at Chiba Light House station, Yokohama station, Yokosuka station and Kurihama station. The RMSE values at the four stations are presented in Table 4.19. The simulation results are consistent with the observations.

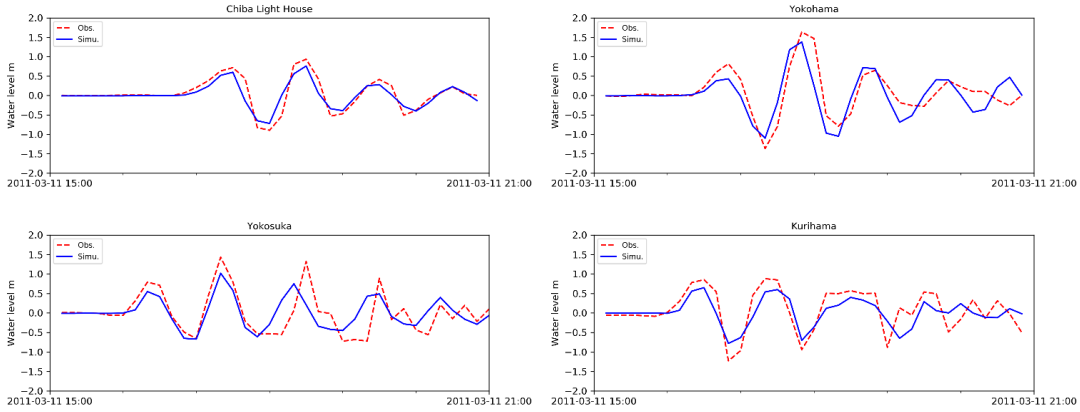

Figure 4.29 Comparison of time-series tsunami profiles between observations (Obs.) and computed results at Chiba Light House station, Yokohama station, Yokosuka station, and Kurihama station

Table 4.19 RMSE values of tsunami anomaly between observation and simulation

Stations	RMSE (m)
Chiba Light House	0.182
Yokohama	0.369
Yokosuka	0.403
Kurihama	0.343

The simulation results of the tsunami induced pipe overflow in Kisarazu area are shown in Figure 4.30. According to the previous study made by Sasaki et al. 2012, in Kisarazu Port, they interviewed employees of a fishery store, Kousei Suisan. They reported that the road between the port and the store was inundated and that the water reached the entrance of the store. However, by judging from the local

decaying vegetation on the seaside sidewalk of the road, the sidewalk was only partially inundated; thus, the inundation was not attributed to overflowing the parapet of the seawalls but rather flooding through the side ditch when the water level rose. It can be concluded that the integrated model could reproduce the pipe-induced overflow well.

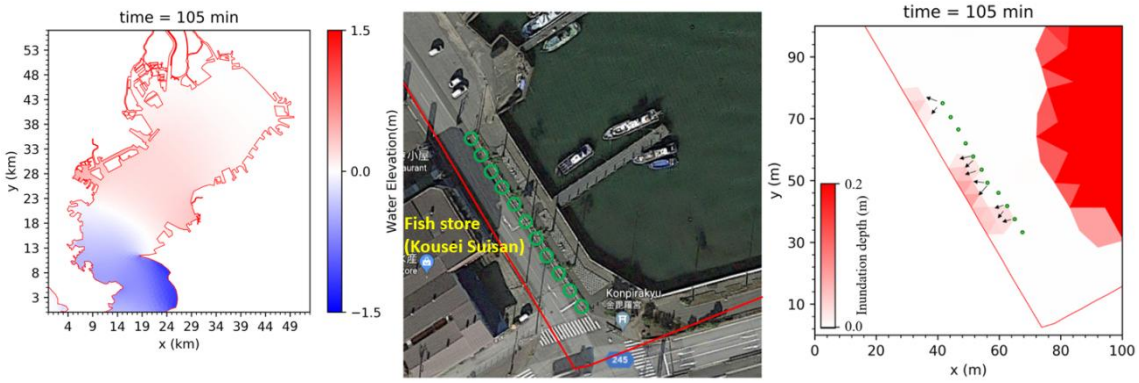

Figure 4.30 Pipe-induced overflow in Kisarazu Port simulated using integrated model (left panel: tsunami anomaly in Tokyo Bay; middle panel: inundated area, the front of Kousei Suisan, a fishery store in the port, green circles are the manholes; right panel: simulated overflow from road side ditch) (source: Google Earth, Data SIO, NOAA, U.S. Navy, NGA, GEBCO)

4.3.4 Sub-conclusion

Tsunami simulation using Hotstart mode in FVCOM was firstly validated. The 2011 Tohoku earthquake tsunami case was selected as the study case due to available data. Result shows that the Hotstart mode in FVCOM can be used for the setup of initial water surface elevation condition.

The drainage pipe module which was embedded in the FVCOM source code was validated using a tsunami induced pipe-overflow inundation case in Kisarazu Port during the 2011 Tohoku earthquake tsunami. Results show that the integrated model performs better than the original one under the circumstance that overflow inundation occurs from the drainage pipe in coastal areas.

4.4 Vulnerability assessment method

4.4.1 Introduction

In this section, the vulnerability measurement method using overflow volume is validated by comparing with inundation computation through a series of numerical experiments. It is assumed that in the areas where overflow volume is large, serious inundation would also happen, as a consequence, this region would be vulnerable. Therefore, the consistency of overflow volume estimated using the approach and inundation volume computed using inundation simulation is discussed to demonstrate the applicability of the method. The applicable conditions and limitations of this approach are also discussed and clarified.

4.4.2 Experiment setup

4.4.2.1 Mesh configuration and experiment condition

The computational domain is divided into two parts: the propagation area and inundation area. Figure 4.31(a) shows the mesh system which consists of two meshes, one is Mesh A (the propagation area), the mesh size ranges from 50 m at the left hand ocean side to 5 m at the right hand coastline. The length and width of Mesh A are both 1000 m, and the bathymetry is 15 m through the whole domain. The other is Mesh B (land inundation area), it is a narrow and long rectangular domain with 1000 in width (y direction) and 200 m in length (x direction), and the typical mesh resolution of this area is 5 m. Figure 4.31(b) shows the bathymetry setting of the computational domain. The mesh information is listed in Table 4.20.

The coastline (nodes at x = 1000 m in Mesh A and Mesh B) is composed of 201 nodes. The 1st coastline node is located at x = 1000 m, y = 1000 m, and the 201st coastline node is located at x = 1000 m, y = 0 m.

A uniform inflow ($100\ m^3/s$ per node) is given at the left-side boundary. When experiment starts, the water firstly enters and propagates in the propagation area, and with the increasing of water level, at a certain moment, the water starts to overflow the coastal dike (red dash line). After that, the inundation depth in the inundation area grows gradually, and finally, the inundation depth would exceed the dike height. In this process, the estimated dike overflow volume is compared with the inundation volume in the inundation area.

Table 4.20 Mesh configuration

Mesh name	Node number	Nele number
Mesh A	6471	12580
Mesh B	9601	18720

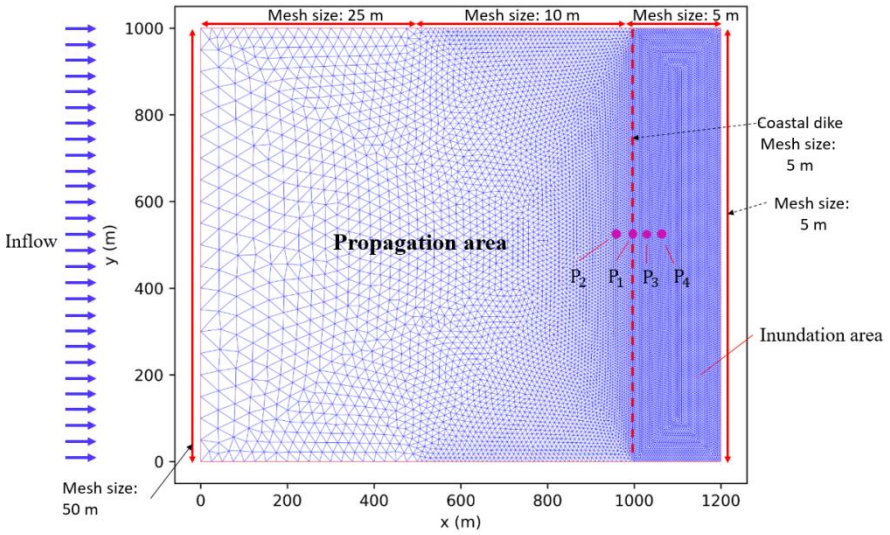

(a)

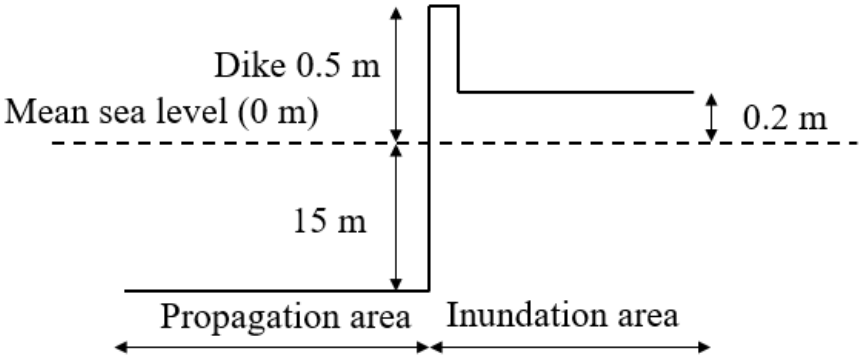

(b)

Figure 4.31 (a): Uniform inflow ($100\ m^3/s$ per node) is given at the left-side boundary; P_1, P_2, P_3 and P_4 are assumed as 4 observation floats, they can only move vertically with the water level change at its location, P_1 is on the dike, the distance of P_2 to dike, P_3 to dike, and P_3 to P_4 is 10 m, 5 m, and 10 m, respectively; (b): Bathymetry configuration for dike height 0.5 m

4.4.2.2 Inundation volume

For the overflow volume in scenarios in Mesh A (propagation area), it is estimated using the method introduced in Section 3.6, and for the inundation volume in Mesh B, it is computed based on an interpolation method (Barycentric interpolation). The area of the triangle is:

$$A_c = A_1 + A_2 + A_3 \tag{4-1}$$

The percent of the red color is:

$$\alpha_1 = \frac{A_1}{A_c} \tag{4-2}$$

The percent of the green color is:

$$\alpha_2 = \frac{A_2}{A_c} \tag{4-3}$$

The percent of the blue color is:

$$\alpha_3 = \frac{A_3}{A_c} \tag{4-4}$$

Then, the value (e.g., inundation height) at center of this triangle is:

$$\frac{A_1 \times Z_1 + A_2 \times Z_2 + A_3 \times Z_3}{A_c} \tag{4-5}$$

For gravity center in triangles,

$$\alpha_1 = \alpha_2 = \alpha_3 = 1/3 \tag{4-6}$$

Thus, the water elevation value at gravity center is:

$$Z = 1/3 \times (Z_1 + Z_2 + Z_3) \tag{4-7}$$

By knowing the coordinates of three vertexes, the length of three sides could be computed. Then, the area of this triangle is:

$$A_c = \sqrt{S_c \times (S_c - a_s) \times (S_c - b_s) \times (S_c - c_s)}, \tag{4-8}$$

$$S_c = \frac{a_s + b_s + c_s}{2} \tag{4-9}$$

Therefore, the inundation water volume at this triangle mesh cell is calculated by:

$$V_{\text{inundation}} = A_c \times Z \tag{4-10}$$

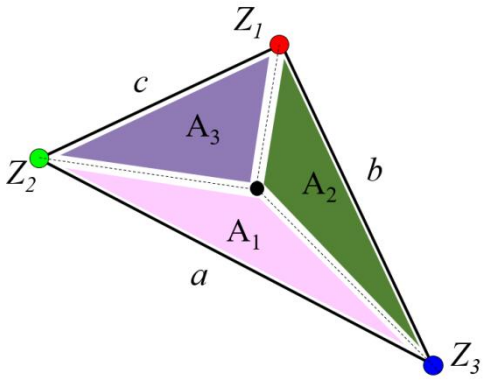

Figure 4.32 Parameters for computation of the inundation water volume in one triangle mesh cell

4.4.3 Results and discussion

As dike height determines the time when overflow happens (as inflow is constant), a series of dike height values are set. The dike height value varies from 0.5 m to 1.5 m with an interval of 0.5 m. The comparison of the estimated dike overflow volume and inundation volume, and the time series of water level change of the four observation floats is shown in Figure 4.33.

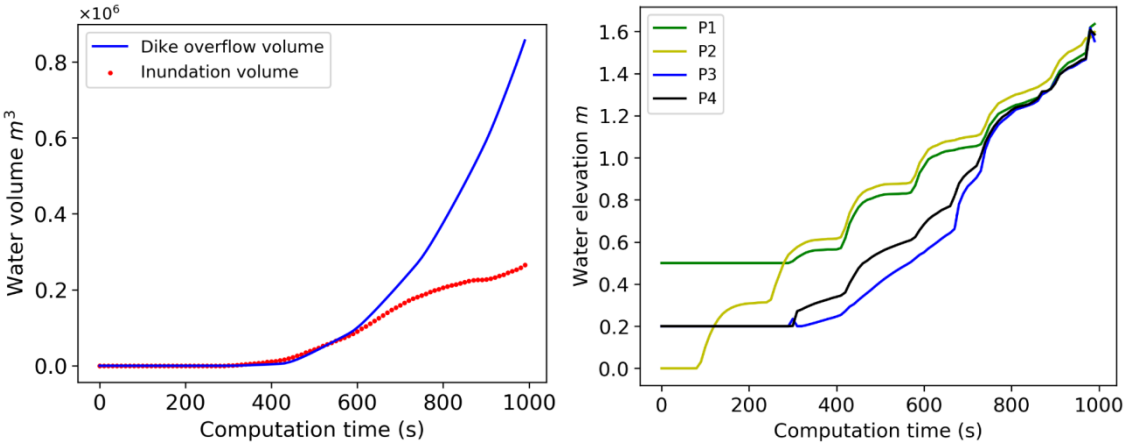

(a)

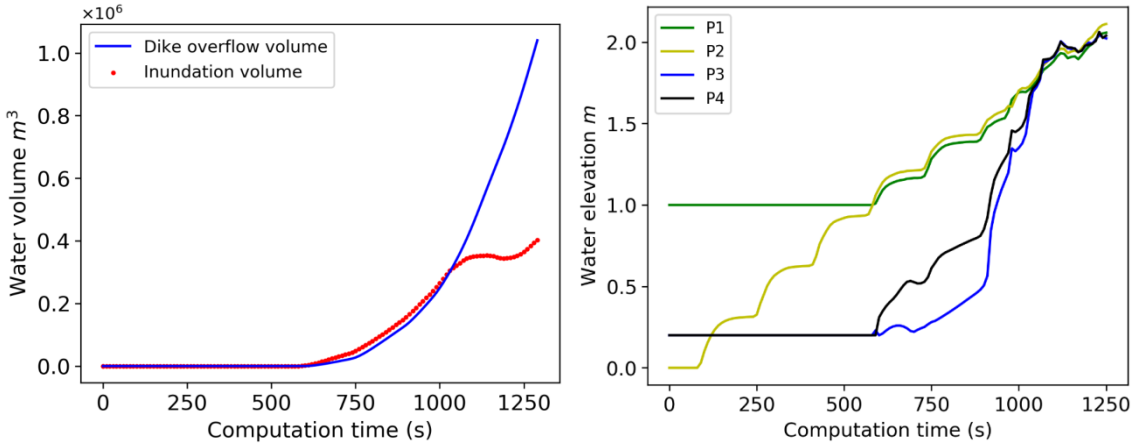

(b)

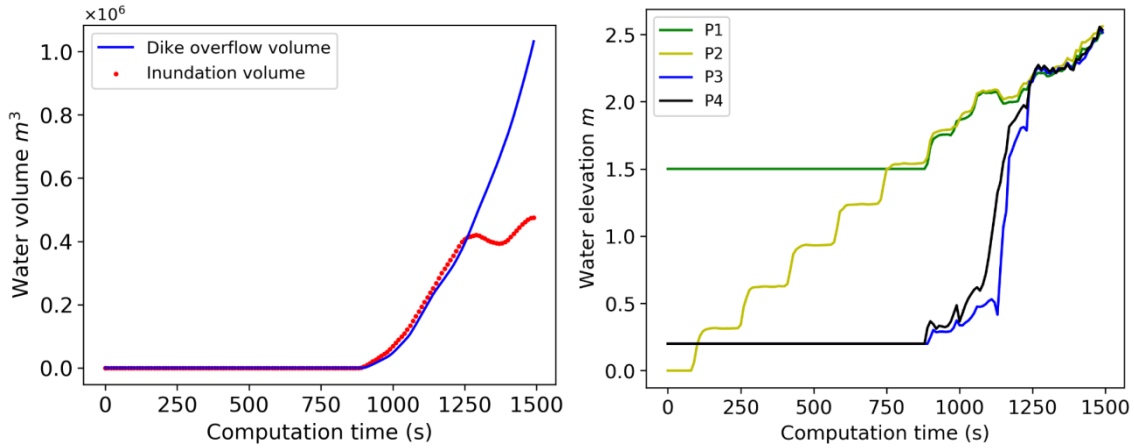

(c)

Figure 4.33 Comparison between estimated dike overflow volume and inundation volume (left panel) and time-series water level change of 4 observation floats (right panel) ((a): dike height is 0.5 m; (b): dike height is 1.0 m; (c): dike height is 1.5 m)

The discussion on the comparison is presented hereafter. With the change of dike heights, the consistency between estimated dike overflow volume and inundation volume also varies. For instance, in the case that dike height is 1.5 m (see left panel figure of Figure 4.33(c)), from around 900 s to 1250 s, estimated dike overflow volume is consistent with the inundation volume, after that, large discrepancy between them can be observed. In Figure 4.33(a) and (b), the consistent period is from 280 s to 600 s and from 600 s to 1100 s, respectively. This phenomenon could be explained from the time-series water level change of the four observational points (P_1, P_2, P_3 and P_4). In the left panel figure of Figure 4.33(c), from 0 s to around 900 s, the elevation of three observation points (P_1, P_3 and P_4) does not change and always equals the elevation of its topography, e.g., green color line (P_1) is 1.5 m, which is the dike height; blue color line (P_3) is 0.2 m, which is the elevation of the inundation area; black color line (P_4) can be explained similarly as P_3. This is because during this period, the water only propagates in the propagation area, it does not reach the dike crown. However, the situation of P_2 is different, it starts from 0 m, and

just after a short time period (about 80 s), the elevation of P_2 (yellow color line) begins to grow, which is due to the reason that the inflow needs short time to reach P_2 from the left boundary. When time is 900 s, P_2 reaches the dike crown height, and P_3 and P_4 start to rise. At time = 1250 s, P_3 and P_4 reach the same elevation as other two points, and the overflow becomes completely submerged type. From this moment, the overflow volume is not consistent with the inundation volume.

This phenomenon has also been observed by other study. Shimozono et al. (2016)[55] studied the relationship between overflow discharge and energy head upstream of the levee. They found that in submerged overflow condition, the model would underestimate the actual overflow discharge, while in free overflow condition, the computed overflow discharge would have a favorable agreement with the empirical overflow discharge equation.

In the present study, it is assumed that the inundation depth would not exceed the summation of dike elevation and overflow depth, which means free overflow type is dominant. The dike overflow estimation method can be used for those conditions with minor dike overflow.

4.4.4 Sub-conclusion

In order to demonstrate the applicability of the method for measuring coastal vulnerability compared to inundation computation approach, a series of idealized boundary inflow cases are prepared. The inundation volume of each scenario using inundation simulation method is computed and compared with the overflow volume estimated by the adopted method. Results shows that the overflow volume estimated by the adopted approach is consistent with inundation simulation method when free overflow type is dominant.

5. Multi-hazard Vulnerability Assessment

In this chapter, the integrated model is applied to multi-hazard scenarios including storm surge, river flood, and tsunamis. First, each component of multiple hazards is analyzed, and the scenarios for vulnerability assessment are described. Then, the vulnerability of Tokyo Bay is assessed and discussed under different types of hazards. The effect of drainage pipe system on the vulnerability of local areas is also investigated.

5.1 Multi-hazard scenarios

In this section, the multi-hazard scenarios are described including storm surge, tsunami and river flood. Firstly, the cases and data of each hazard component are introduced. Then, numerical investigation for each type of hazard is performed, from which the multi-hazard scenarios are prepared.

5.1.1 Computational mesh and tidal stations

SMS 11.1 software is used to generate the unstructured mesh for multi-hazard simulation. The unstructured mesh is shown in Figure 5.1, and the number of nodes and elements is 141,003 and 274,482, respectively.

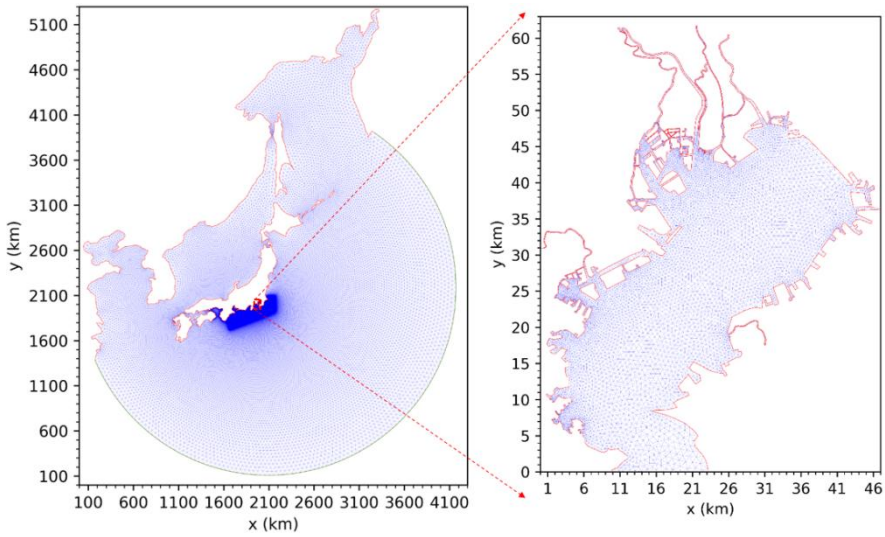

Figure 5.1 Mesh system for multi-hazard simulation (mesh size ranges from 50 km at the open boundary to 1 km in the ToKai-ToNankai area, and around 50 m in the most inner side of Tokyo Bay)

Table 5.1 presents the information of the major tidal stations in Tokyo Bay including the station names and locations, and the anomalies induced by storm surge or tsunami at these stations are compared and analyzed.

Table 5.1 Tidal stations in Tokyo Bay

Station name	Longitude (°)	Latitude (°)
Kurihama	139.716667	35.233333
Yokosuka	139.651389	35.288056
Yokohama	139.633333	35.466667
Kawasaki	139.75	35.516667
Shibaura	139.753611	35.636944
Tokyo Harumi	139.766667	35.666667
Chiba	140.045556	35.568056

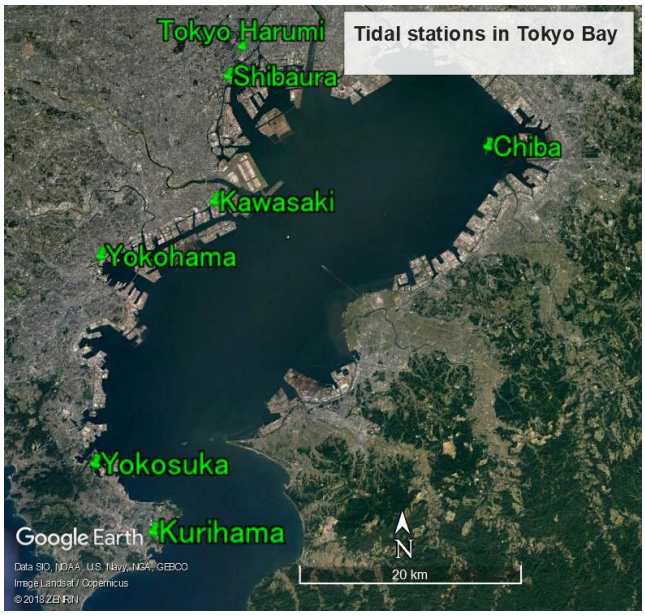

Figure 5.2 Tidal stations in Tokyo Bay (source: Google Earth, Data SIO, NOAA, U.S. Navy, NGA, GEBCO)

5.1.2 Single hazard

5.1.2.1 Storm surge

The typhoon cases prepared by Chiba Prefecture Storm Surge Committee (2018)[94] are adopted. They are composed of 4 typical typhoon courses, each one has several assumed parallel tracks but with the same intensity, as shown in Figure 5.3(a).

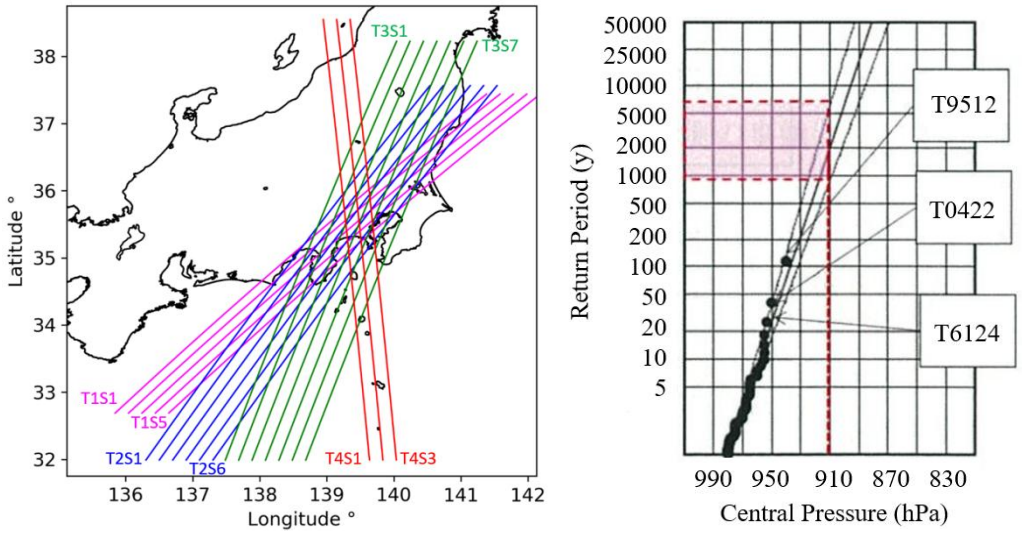

(a) (b)

Figure 5.3 (a) Assumed typhoon tracks (Magenta color lines: T7920 course; Blue color lines: Taisho 6th year Typhoon course; Green color lines: Isebay Typhoon course; Red color lines: 1949 Typhoon Kitty course) and (b) Return period of typhoon intensity passing through Tokyo Bay (JMA, 1951-2013)

Table 5.2 Typhoon scenario number

Course name	Scenario number
T7920	T1S1,T1S2,T1S3,T1S4,T1S5
Taisho 6th year Typhoon	T2S1,T2S2,T2S3,T2S4,T2S5,T2S6
Isebay Typhoon	T3S1,T3S2,T3S3,T3S4,T3S5,T3S6,T3S7
1949 Typhoon Kitty	T4S1,T4S2,T4S3

The intensity of assumed typhoon cases is fixed. The central pressure is 910 hPa, the radius of maximum wind speed is 75 km, and the forward translational wind speed is 30 m/s. Figure 5.3(b) shows the return period of typhoon intensity for historical typhoons passing through Tokyo Bay. Totally more than 1750 typhoons are included. The selected typhoon intensity is around 1,000~5,000 year(s) return period.

All assumed typhoon tracks have eleven time steps, and the time interval is one hour. They are firstly interpolated into half an hour data, and in order to avoid unstable issues in the initial period of simulation, nine time steps' ramp for central pressure and wind speed is applied (see Figure 5.4), which means the typhoon intensity keeps strengthening without changing locations in the first nine time steps.

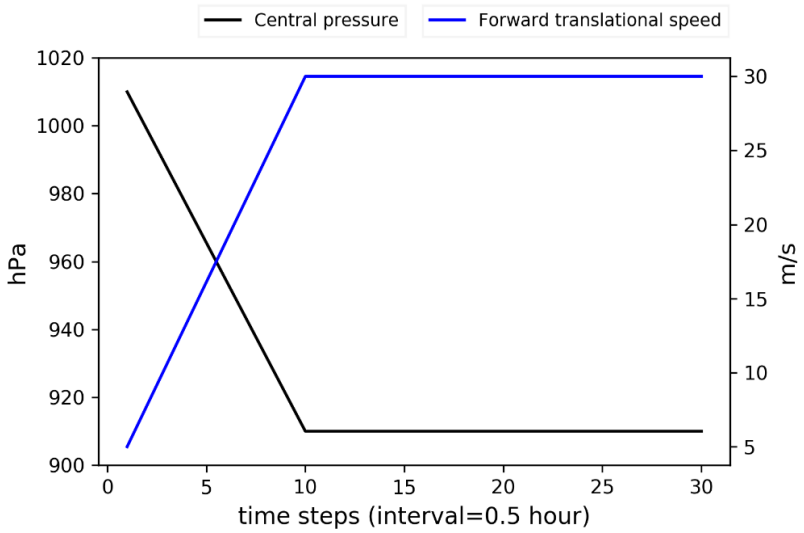

Figure 5.4 Setup of central pressure and forward translational speed for assumed typhoon cases

Table 5.3 Maximum storm surge anomaly (m) at stations in Tokyo Bay for the assumed typhoon courses

Course name	Kurihama	Yokosuka	Yokohama	Kawasaki	Shibaura	Tokyo Harumi	Chiba
T1	1.02	0.90	1.07	1.24	1.34	1.38	1.98
T2	1.05	0.87	1.07	1.20	1.37	1.43	2.04
T3	1.03	0.96	1.25	1.24	1.43	1.54	1.89
T4	0.96	1.01	1.29	1.35	1.58	1.71	1.86

Table 5.4 Scenario number of maximum water elevation at stations in Tokyo Bay for the assumed typhoon courses

Course name	Kurihama	Yokosuka	Yokohama	Kawasaki	Shibaura	Tokyo Harumi	Chiba
T1	T1S5	T1S3	T1S3	T1S3	T1S4	T1S2	T1S3
T2	T2S6	T2S6	T2S3	T2S4	T2S3	T2S3	T2S4
T3	T3S5	T3S7	T3S4	T3S4	T3S3	T3S3	T3S4
T4	T4S2	T4S1	T4S1	T4S2	T4S1	T4S1	T4S2

Table 5.3 presents the maximum storm surge anomalies at seven stations in Tokyo Bay for the assumed typhoon scenarios, and Table 5.4 presents the scenarios in which the maximum storm surge anomaly was observed. For instance, in Chiba station, the maximum storm surge anomaly among the T7920 course scenarios was observed in the 3rd track (scenario T1S3). The maximum storm surge anomaly in the inner side of Tokyo Bay is larger than that in the southern part of the bay, and the maximum storm surge anomaly happened in Chiba station was 2.04 m. In the multi-hazard assessment section, scenario T1S2, T2S3, T3S3, T4S1 and T4S2 are selected as the multi-hazard components because

these five cases generate largest anomaly in the northern part of the bay and also significant overflow volume for only storm surge compared to other typhoon cases.

5.1.2.2 Tsunami

In history, a few earthquake tsunamis attacked Tokyo Bay including the 1703 Genroku Kanto earthquake tsunami (M_w 8.1), the 1854 Ansei ToKai earthquake tsunami (M_w 8.4), the 1923 Taisho Kanto earthquake tsunami (M_w 7.9), and the 1960 Chilean earthquake tsunami. The return period of the Kanto type earthquakes is believed to be approximately 200 years. The largest tsunami ever happened in Tokyo Bay would be the 1703 Genroku Kanto earthquake tsunami, which generated higher water level in the southern part of the bay and the resultant water level was similar at the bay head when compared to the 2011 Tohoku tsunami.

Currently, tsunami induced by the ToKai-ToNankai-Nankai type earthquakes and a potential inland earthquake that may happen near Tokyo metropolitan area is the major concern in Tokyo Bay. Particularly, there is a high possibility that a ToKai-ToNankai-Nankai type earthquake would happen in the near future due to its small return period (about 120 years). The heights of coastal disaster countermeasures are generally larger in the northern part of Tokyo Bay, while the expected tsunami is more likely larger in the southern part of the bay.

The earthquake fault area is calculated in Okada (1985) model using a combination of the fixed rupture length and width of 50 km × 25 km rectangular sub-faults. Thus, Zone 1 (the potential maximum fault area of ToKai-ToNankai type earthquake, red color mesh) and Zone 2 (the potential maximum fault area of Tokyo inland type earthquake, blue color mesh) was divided by a number of 50 km × 25 km cells (see Figure 5.5).

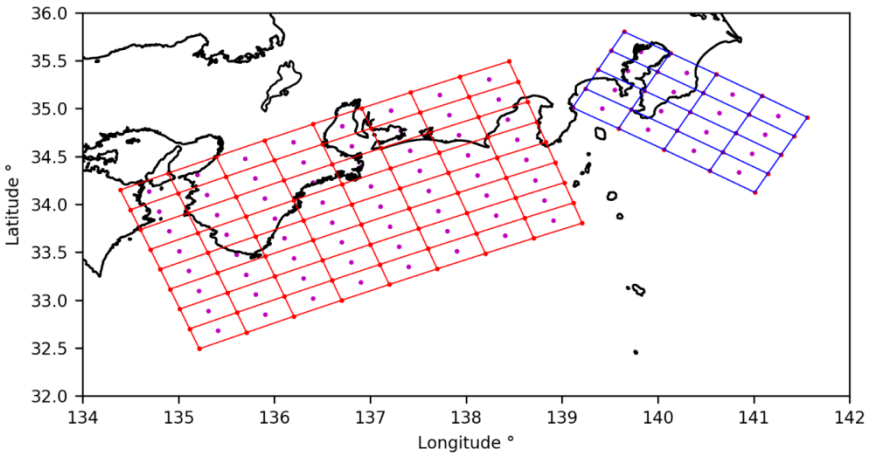

Figure 5.5 Potential maximum fault areas for ToKai-ToNankai type earthquake (red color), and Tokyo inland type earthquake (blue color)

The calculated L_F and W_F from equation (3-24) and equation (3-25) were rounded off to be multiples of 50 km and 25 km, respectively. Figure 5.6 shows an example of how fault areas are built for a M_w 8.0 earthquake. The total number N of possible rectangular tsunami faults for a given earthquake

M_w in Zone 1 is estimated by:

$$N = (N_{L_F} + 1 - N_L) \times (N_{W_F} + 1 - N_W) \quad (5\text{-}1)$$

$$N_{L_F} = 8, N_{W_F} = 8 \quad (5\text{-}2)$$

$$N_L \approx \frac{L}{50}, N_W \approx \frac{W}{25} \quad (5\text{-}3)$$

For a M_w 8.0 earthquake, according to equation (3-24) and equation (3-25), the fault rupture length and width are:

$$L_F = 179.47 \text{ km}, \ W_F = 55.29 \text{ km}$$

Then,

$$N_L \approx 4, \ N_W \approx 2,$$

and

$$N = (8 + 1 - 4) \times (8 + 1 - 2) = 35$$

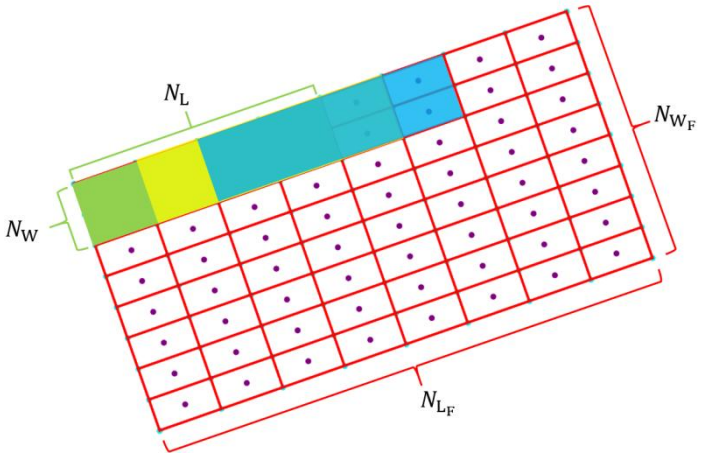

Figure 5.6 Fault areas for a M_w 8.0 earthquake in Zone 1 (N_{L_F} and N_{W_F} are the total numbers of the meshes covering the length and width of the potential maximum fault area, N_L and N_W are the total numbers of sub-faults covering the length L_F and width W_F for a specific earthquake fault. Green color rectangle covering four mesh cells in length and two mesh cells in width represents one possible sub-fault for a M_w 8.0 earthquake, and by shifting the green color rectangle along the direction in length every time one mesh cell space, in this example, from green color rectangle to yellow color rectangle, and then from yellow color rectangle to blue color rectangle, etc., all the possible sub-faults can be obtained)

According to the historical earthquake tsunami events happened in Tokyo Bay, the magnitude of tsunamigenic earthquakes mostly ranged from 7.9 to 8.4. Therefore, magnitude ranging from 7.2 to 8.4 with an interval of 0.2 is selected for Zone 1, and magnitude ranging from 7.2 to 8.0 with an interval of 0.2 is selected for Zone 2. The number of possible tsunami fault scenarios for each of the earthquake magnitudes determined by equation (5-1) is summarized in Table 5.5. For smaller earthquakes, there are many possible combinations of sub-faults, while large earthquakes have a fewer possible tsunami fault scenarios. This probability approach would cover most of the possible tsunami fault scenarios, and in the present research, a total number of 334 tsunami scenarios were considered.

A set of Python scripts have been developed to handle the preparation process of tsunami scenarios, including the determination of the potential maximum fault area (Zone 1 and Zone 2), mesh generation of Zone 1 and Zone 2, output of sub-fault combinations for each considered magnitude earthquake (epicenter locations, combination numbers, etc.), and also the development of the initial water surface condition for each scenario using Okada (1985) model.

Table 5.5 Number of possible tsunami fault scenarios (*N*) for the selected range of earthquake M_w

Zone 1 (ToKai-ToNankai type)		Zone 2 (Kanto type and Tokyo inland type earthquake)	
M_w	Number of scenarios (*N*)	M_w	Number of scenarios (*N*)
7.2	64	7.2	16
7.4	56	7.4	12
7.6	49	7.6	9
7.8	42	7.8	6
8.0	35	8.0	3
8.2	24	-	-
8.4	18	-	-

The calculation of tsunami initial water surface condition requires the input of the longitude and latitude of the epicenter location, depth of fault centroid, dip angle, strike angle, rake angle, fault length, fault width, and fault slip. The actual earthquake slips may not be uniform throughout the fault area, but in order to simplify the preparation procedure in the present work, a uniform slip throughout the entire rupture area is assumed. Thus, the main parameter to be modified is the magnitude of the earthquake. For tsunamigenic earthquakes happened in Zone 1, the fault parameters of Keicho earthquake[88] are presented in Table 5.6, and for Zone 2, the fault parameters of Tokyo inland earthquake are used according to the materials provided by Tokyo Metropolitan Government Disaster Mitigation Report (2012). Manning roughness coefficient n = 0.025 is used in the model to describe the ocean bottom.

Table 5.6 Fault parameters of tsunamigenic earthquakes in Zone 1 and Zone 2
(longitude, latitude, fault length, fault width, and slip extent are determined according to the earthquake moment magnitude and the scenarios)

Earthquake type	Longitude (°)	Latitude (°)	Depth (km)	Strike (°)	Dip (°)	Rake (°)	Fault length (km)	Fault width (km)	Slip (m)
Zone 1	-	-	1	250	60	270	-	-	-
Zone 2	-	-	1	296	23	138	-	-	-

Table 5.7 presents the maximum tsunami anomaly (m) at seven stations in Tokyo Bay for the selected earthquake magnitude M_w range in Zone 1. With the increasing of earthquake magnitude M_w,

the induced tsunami anomaly in seven stations also increased. For a specific earthquake magnitude, the tsunami anomaly at the stations that are located in the southern part of Tokyo Bay are slightly larger than that at the stations in the inner side of the bay.

Table 5.7 Maximum tsunami anomaly (m) at stations in Tokyo Bay for the selected earthquake magnitude M_w range in Zone 1

M_w	Kurihama	Yokosuka	Yokohama	Kawasaki	Shibaura	Tokyo Harumi	Chiba
7.2	0.17	0.13	0.07	0.03	0.05	0.07	0.03
7.4	0.24	0.15	0.13	0.04	0.08	0.11	0.04
7.6	0.39	0.32	0.38	0.14	0.31	0.38	0.16
7.8	0.60	0.41	0.48	0.19	0.41	0.49	0.23
8.0	0.63	0.46	0.57	0.26	0.51	0.61	0.31
8.2	1.11	0.70	0.95	0.47	0.82	0.96	0.60
8.4	1.42	0.98	1.25	0.59	1.00	1.17	0.79

Table 5.8 Scenario number of maximum tsunami anomaly at stations in Tokyo Bay for the selected earthquake magnitude M_w range in Zone 1

M_w	Kurihama	Yokosuka	Yokohama	Kawasaki	Shibaura	Tokyo Harumi	Chiba
7.2	56	31	32	32	20	32	32
7.4	34	27	18	19	18	18	18
7.6	27	19	28	12	12	12	12
7.8	24	24	24	11	10	10	10
8.0	20	20	8	9	8	8	9
8.2	8	8	7	7	7	8	8
8.4	6	6	4	5	6	6	6

Table 5.9 Maximum tsunami anomaly (m) at stations in Tokyo Bay for the selected earthquake magnitude M_w range in Zone 2

M_w	Kurihama	Yokosuka	Yokohama	Kawasaki	Shibaura	Tokyo Harumi	Chiba
7.2	0.25	0.44	0.29	0.27	0.36	0.32	0.23
7.4	0.24	0.39	0.37	0.29	0.40	0.35	0.18
7.6	0.71	0.84	0.48	0.65	0.60	0.77	0.51
7.8	0.81	1.09	0.62	0.77	0.69	0.90	0.61
8.0	0.99	1.32	0.87	0.94	0.77	0.94	0.67

Table 5.10 Scenario number of maximum tsunami anomaly at stations in Tokyo Bay for the selected earthquake magnitude M_w range in Zone 2

M_w	Kurihama	Yokosuka	Yokohama	Kawasaki	Shibaura	Tokyo Harumi	Chiba
7.2	9	5	5	5	1	1	1
7.4	7	4	4	4	1	1	1
7.6	7	1	1	1	1	1	1
7.8	3	1	3	1	1	1	1
8.0	2	1	1	1	1	1	1

For tsunami happened in Zone 1 with earthquake magnitude ranging from 7.2 to 8.4, the scenario number corresponding to the maximum tsunami anomaly is 32, 18, 12, 10, 8, 8, and 6, respectively, which means, for example, among the scenarios with earthquake magnitude M_w 7.2, the maximum tsunami anomaly happened in the 32nd scenario among all 64 cases (see Table 5.5). The initial water surface elevation condition is shown in Figure 5.7.

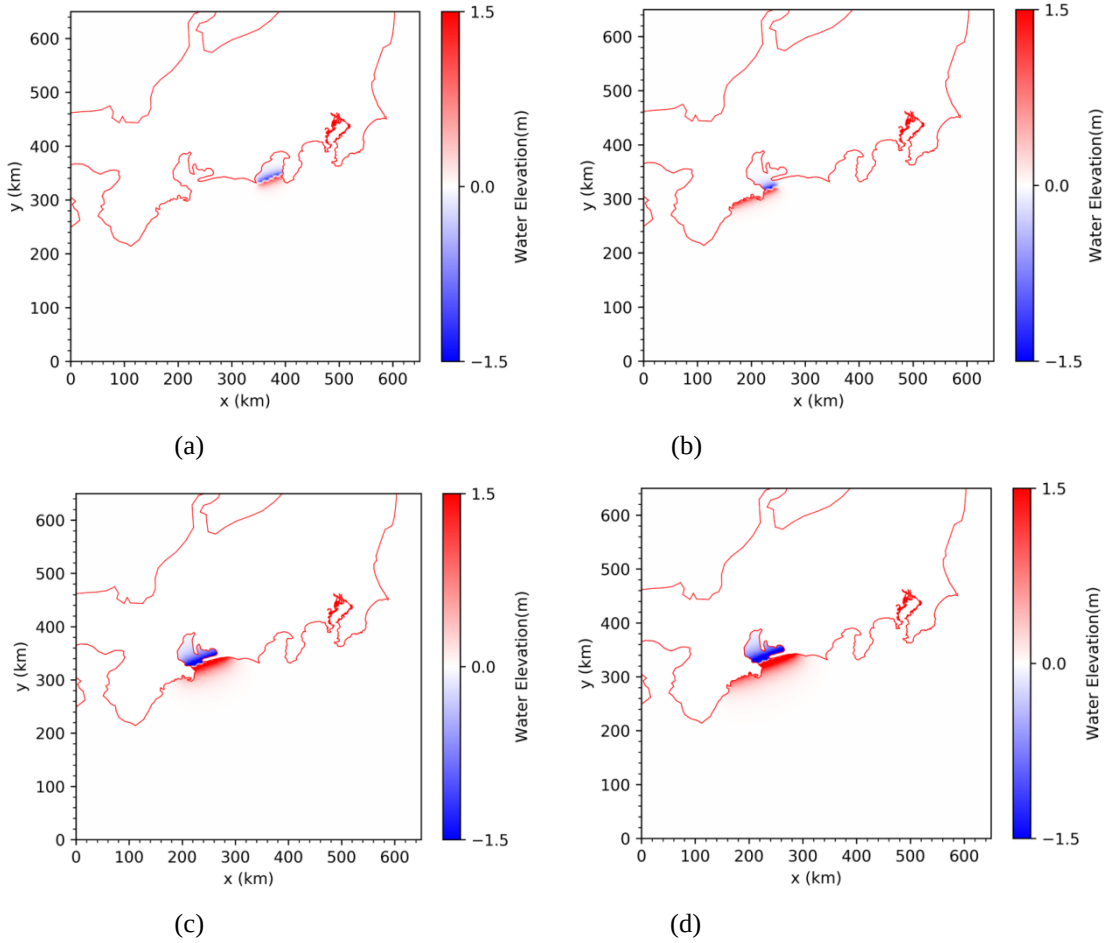

(a) (b)

(c) (d)

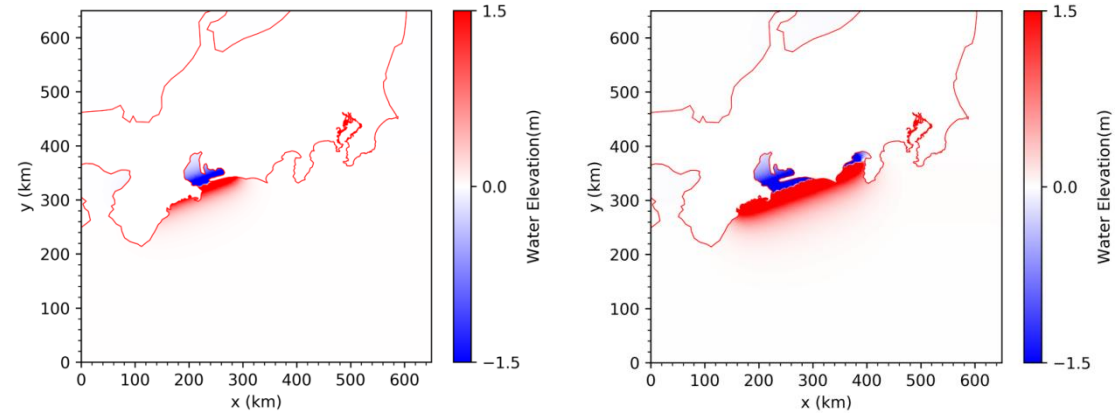

(e)

(f)

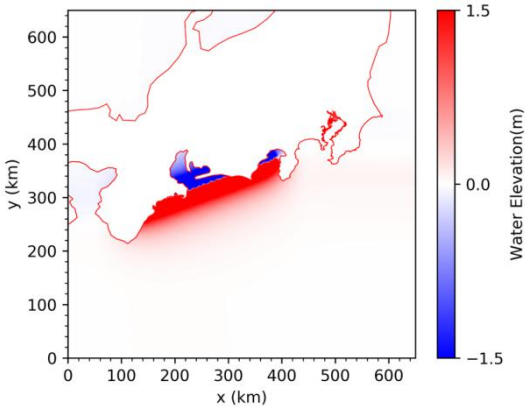

(g)

Figure 5.7 Initial water surface elevation condition for Zone 1 cases that resulted in maximum tsunami anomaly in seven stations ((a): 32nd scenario of M_w 7.2; (b) 18th scenario of M_w 7.4; (c) 12th scenario of M_w 7.6; (d) 10th scenario of M_w 7.8; (e) 8th scenario of M_w 8.0; (f) 8th scenario of M_w 8.2; (g) 6th scenario of M_w 8.4)

For tsunami happened in Zone 2 with earthquake magnitude ranging from 7.2 to 8.0, the scenario number corresponding to the maximum tsunami anomaly is 1, 1, 1, 1, and 1, respectively. The initial water surface elevation condition is shown in Figure 5.8.

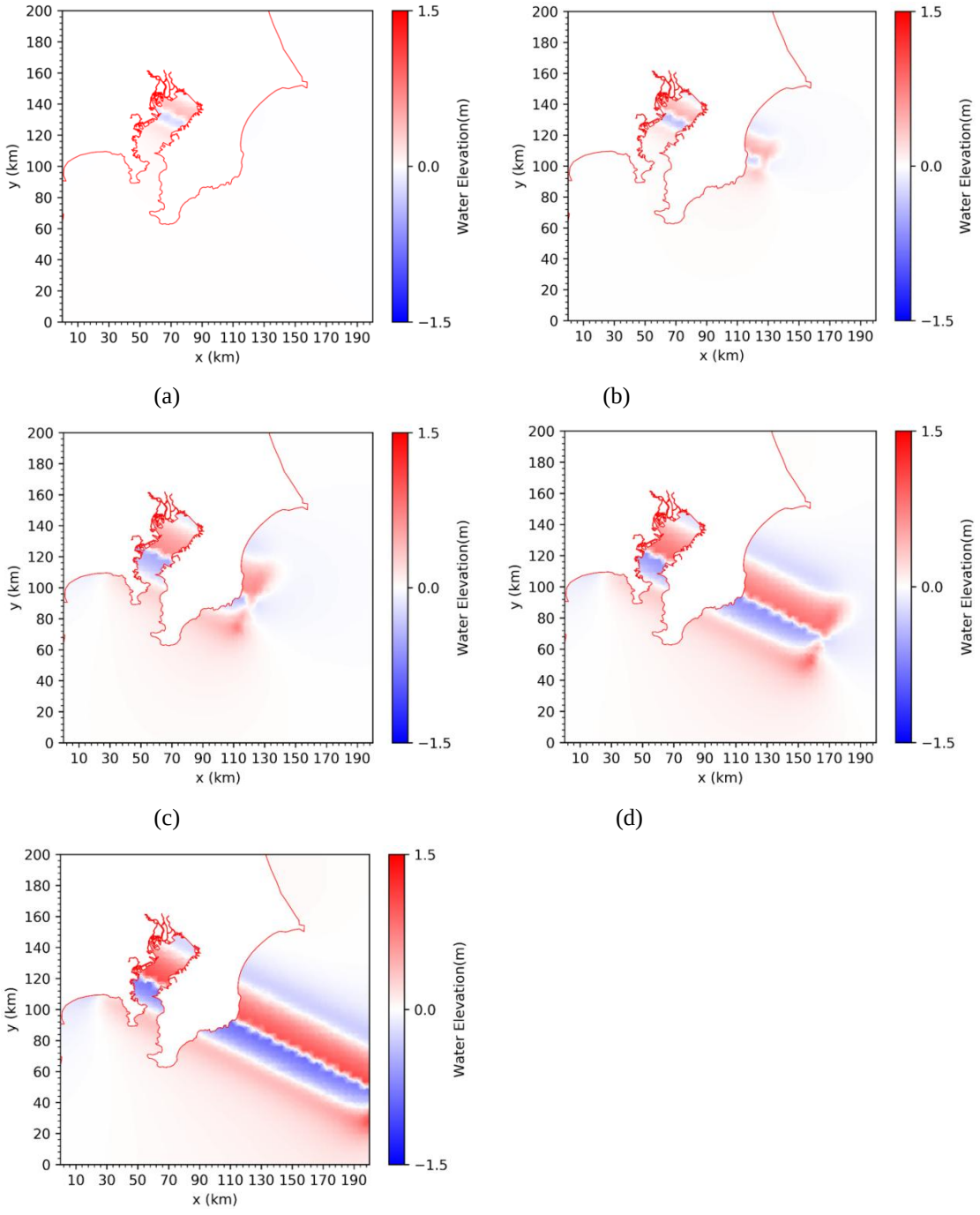

Figure 5.8 Initial water surface elevation condition for Zone 2 cases that resulted in maximum tsunami height in seven stations ((a): 1st scenario of M_w 7.2; (b) 1st scenario of M_w 7.4; (c) 1st scenario of M_w 7.6; (d) 1st scenario of M_w 7.8; (e) 1st scenario of M_w 8.0)

The 6th scenario of M_w 8.4 earthquake tsunami in Zone 1 and the 1st scenario of M_w 8.0 earthquake tsunami in Zone 2 are further selected as the hazard components in the multi-hazard scenarios because they caused the largest anomaly in the bay. Under the tsunami scenarios, no overflow has been

found in the northern part of Tokyo Bay.

5.1.2.3 River flood

In the inner side of Tokyo Bay, two major rivers are connecting to the bay, they are Edogawa River and Arakawa River. Due to the availability of river discharge data, only the daily discharge data of Edogawa River is obtained, and the data covers the year of 1955 to 2015. Figure 5.9(a) shows the annual maximum discharge of Edogawa River, and Figure 5.9(b) shows its return period. The average flow discharge of Edogawa River and Arakawa River is 82.34 m^3/s and 87.54 m^3/s, respectively. Thus, the flow discharge of Arakawa River and Nakagawa River is estimated using the following equation:

$$Q_{\mathrm{Ara}} = Q_{\mathrm{Edo}} \times 87.54/82.34 \tag{5-4}$$

where, Q_{Ara} is the flow discharge of Arakawa River, Q_{Edo} is the flow discharge of Edogawa River, m^3/s.

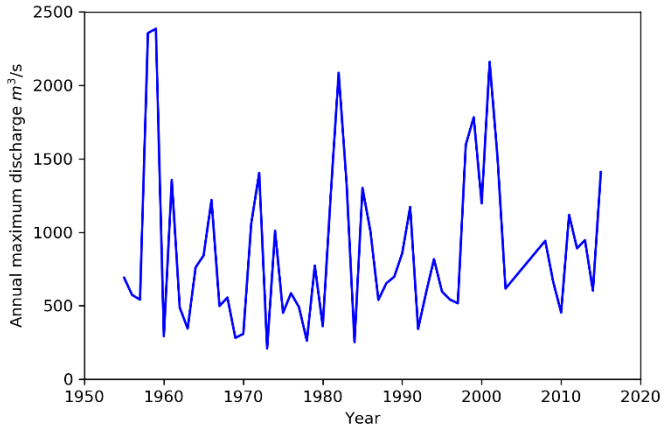

(a)

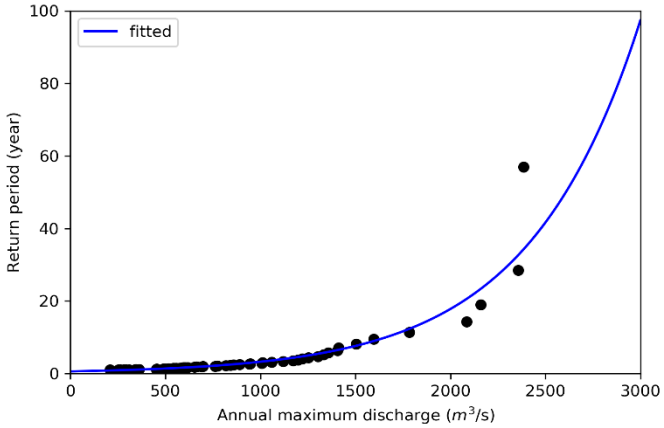

(b)

Figure 5.9 Annual maximum discharge (a) and return period of annual maximum discharge (b) for Edogawa River

The discharge, salinity and temperature values are shown in Table 5.11, which are constant values for three rivers. For Edogawa River, the flow discharge is given as 2,600 m^3/s, which is about 50-year return period discharge according to the Figure 5.9(b).

Table 5.11 Simulation condition of rivers

River names	Discharge m^3/s	Salinity PSU	Temperature ℃
Arakawa River	2800	0	25
Nakagawa River	1000	0	25
Edogawa River	2600	0	25

Because the bathymetry data does not contain reliable river channel depth, the river bathymetry is estimated using DEM data and Google earth software. Firstly, the DEM data that covers the target rivers is downloaded and properly arranged. Then, in Google earth, the center lines of the target rivers are plotted using the Path function. The center lines are exported as *.kmz files and converted into *.xyz files. In the processed *.xyz files, the longitude and latitude of the paths are obtained. The elevation of the points on the center lines is assumed to be equal to that of the river bank, which can be known from the DEM data. Thus, the bathymetry of the river at this point can be obtained using the formula below:

$$H_r = -1 \times (Z_{bank} - D_r) \quad (5\text{-}5)$$

where, -1 is because in FVCOM, the bathymetry is negative; H_r is the bathymetry of the river, m; Z_{bank} is the elevation of the river bank, m; D_r is the water depth of the river, which is assumed to be 5 m.

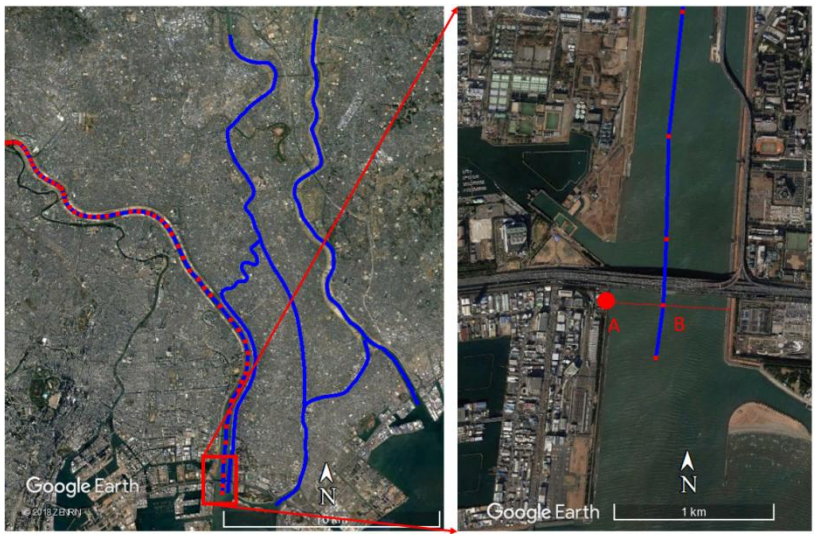

Figure 5.10 Estimation of river bathymetry (Blue color solid lines are plotted along the center of rivers, red rectangle scattered dots are the path points. In the right panel figure, point A represents a river bank point that is closest to the center path point B. Elevation of point B is equal to that of A, and then, the bathymetry of point B can be obtained using equation (5-5)) (source: Google Earth, Data SIO, NOAA, U.S. Navy, NGA, GEBCO)

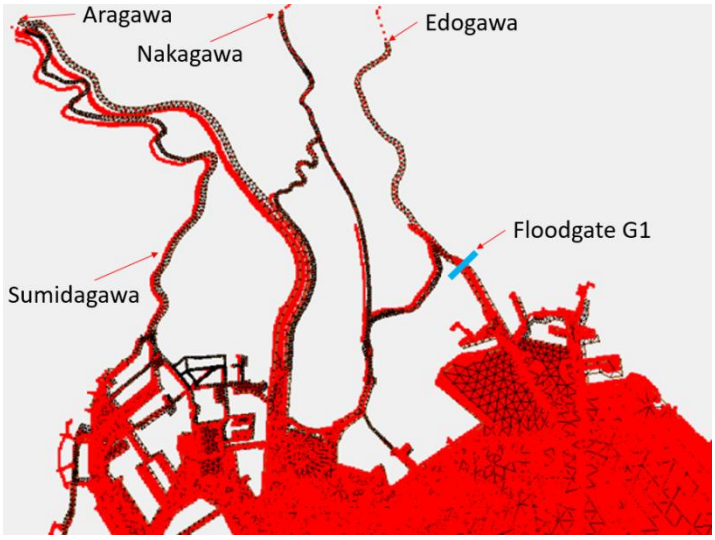

Figure 5.11 Interpolation of final bathymetry data in SMS 11.1

Using SMS 11.1, the final bathymetry was interpolated into the unstructured mesh (see Figure 5.11). For the simulation setup, the surface boundary condition is the atmospheric pressure and wind speed field, three river forces are given as part of the boundary condition, the locations of the river sources specified in the model are shown in Figure 5.11, and the floodgate G1 in the Edogawa River is thought to be open.

In order to feed the river data into FVCOM, river flow discharge, river salinity, and river temperature data are prepared in a proper way including the file format and the time interval of data. As for the typhoon condition, assumed typhoon course scenarios as introduced in Section 5.1.1 are applied. Totally, there are 21 scenarios. Similar pre-process for the typhoon inputs are handled including the time interpolation. In the first 9 time steps, the wind and pressure ramp in a linear way. The simulation output time interval is 30 minutes.

Table 5.12 shows the maximum storm surge anomaly at stations in Tokyo Bay for four typhoon course scenarios combining the river conditions. Compared to the scenarios excluding rivers in Section 5.1.2.1, the maximum storm surge anomalies at the seven stations are similar except Tokyo Harumi station. It may be due to the reason that Tokyo Harumi station is close to the mouth of Sumidagawa River, which is a branch of Edogawa River. Similar in Section 5.1.1, the maximum water elevation happened in Chiba station in typhoon scenario T2S4.

Table 5.12 Maximum storm surge anomaly (m) at stations in Tokyo Bay for the assumed typhoon courses

Course name	Kurihama	Yokosuka	Yokohama	Kawasaki	Shibaura	Tokyo Harumi	Chiba
T1	1.03	0.92	1.06	1.22	1.34	1.44	1.96
T2	1.06	0.88	1.05	1.18	1.38	1.51	2.01
T3	1.03	0.98	1.24	1.23	1.44	1.61	1.89
T4	0.97	1.00	1.29	1.34	1.60	1.78	1.86

Table 5.13 Scenario number of maximum water elevation at stations in Tokyo Bay for the assumed typhoon courses

Course name	Kurihama	Yokosuka	Yokohama	Kawasaki	Shibaura	Tokyo Harumi	Chiba
T1	T1S5	T1S5	T1S3	T1S3	T1S3	T1S3	T1S3
T2	T2S6	T2S6	T2S3	T2S3	T2S3	T2S3	T2S4
T3	T3S5	T3S7	T3S4	T3S4	T3S3	T3S3	T3S4
T4	T4S2	T4S2	T4S1	T4S2	T4S1	T4S1	T4S2

5.1.3 Sub-conclusion

Single hazard scenarios including storm surge and tsunami are prepared and analyzed. The studied typhoon courses are developed based on the historical records of JMA and government report. From each course, one or two typhoon cases are selected as the multi-hazard components because they caused largest anomaly and overflow volume in the northern part of Tokyo Bay.

Tsunami scenarios are prepared based on a probability approach, which would cover most of the possible scenarios in the ToKai-ToNankai area and the Tokyo Bay area. The tsunami anomaly in the southern part of the bay is generally higher than that in the northern part. The maximum tsunami anomaly is 1 m in the inner side of Tokyo Bay, and no overflow has been found. The 6th scenario of M_{w} 8.4 earthquake tsunami in Zone 1 and the 1st scenario of M_{w} 8.0 earthquake tsunami in Zone 2 are further selected as the hazard components in the multi-hazard scenarios.

River flood is also investigated. Compared to storm surge, the combined storm surge and river flood does not result in significantly larger anomaly in the selected tidal stations. It may be due to the reason that the tidal stations are located in the bay, which has a wide space. However, the upstream of the river may suffer more overflow and flood.

5.2 Vulnerability of Tokyo Bay

5.2.1 Introduction

To investigate the joint effect of river flood, storm surge and tsunami on the coastal areas, a series of multi-hazard scenarios are prepared. Considering the initial typhoon location and tsunami source area, the multi-hazard scenarios are divided into two main groups, Group A (see Table 5.14) and Ground B (see Table 5.15). Group A contains the combinations of tsunami scenarios in Zone 1 and typhoon scenarios (A1 to A35). Group B contains the combinations of tsunami scenarios in Zone 2 and typhoon scenarios (B1 to B5). As tsunami scenarios in Zone 2 are located in Tokyo Bay, typhoon starts from locations that are near Tokyo Bay in Group B. Hotstart mode is adopted in FVCOM.

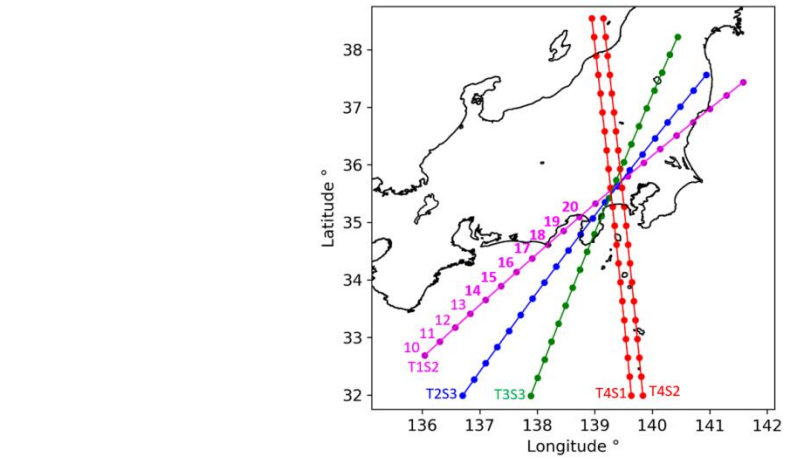

(a)

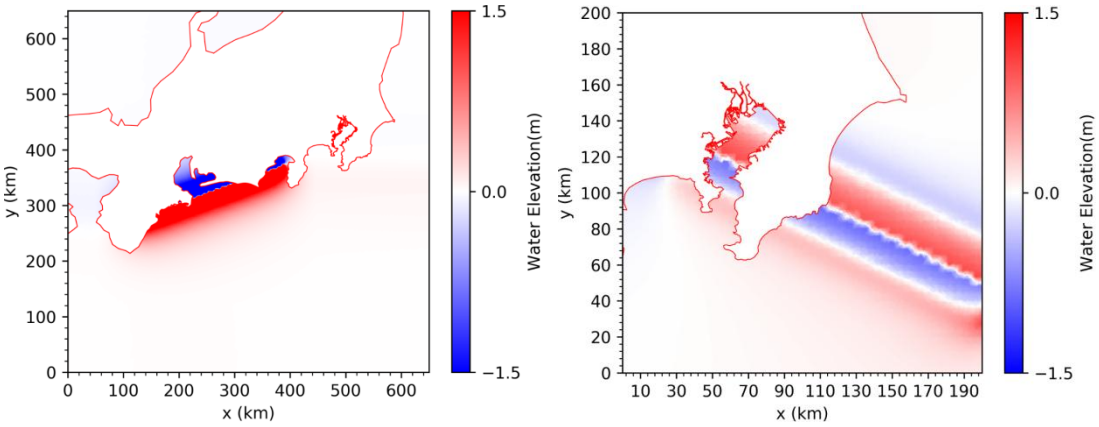

(b)

Figure 5.12 Initial conditions for multi-hazard scenarios, (a): Typhoon cases included in multi-hazard scenarios, and numbers from 10 to 20 represent the typhoon initial locations, (b) left panel: 6th scenario of M_w 8.4 tsunami in Zone 1, (b) right panel: 1st scenario of M_w 8.0 tsunami in Zone 2

Table 5.14 Multi-hazard scenarios for Zone 1

Scenario name	Tsunami case	Typhoon case	Typhoon initial location
A1	6th scenario of M_w 8.4 in Zone 1	T1S2	14
A2		T2S3	
A3		T3S3	
A4		T4S1	
A5		T4S2	
A6	6th scenario of M_w 8.4 in Zone 1	T1S2	15
A7		T2S3	
A8		T3S3	
A9		T4S1	
A10		T4S2	
A11	6th scenario of M_w 8.4 in Zone 1	T1S2	16
A12		T2S3	
A13		T3S3	
A14		T4S1	
A15		T4S2	
A16	6th scenario of M_w 8.4 in Zone 1	T1S2	17
A17		T2S3	
A18		T3S3	
A19		T4S1	
A20		T4S2	
A21	6th scenario of M_w 8.4 in Zone 1	T1S2	18
A22		T2S3	
A23		T3S3	
A24		T4S1	
A25		T4S2	
A26	6th scenario of M_w 8.4 in Zone 1	T1S2	19
A27		T2S3	
A28		T3S3	
A29		T4S1	
A30		T4S2	
A31	6th scenario of M_w 8.4 in Zone 1	T1S2	20
A32		T2S3	
A33		T3S3	
A34		T4S1	
A35		T4S2	

Table 5.15 Multi-hazard scenarios for Zone 2

Scenario name	Tsunami case	Typhoon case	Typhoon initial location
B1	1st scenario of M_w 8.0 in Zone 2	T1S2	20
B2		T2S3	
B3		T3S3	
B4		T4S1	
B5		T4S2	

The tsunami condition of A1 to A35 is same (see Figure 5.12), while the initial location of typhoon changes. Initial water surface condition of the multi-hazard scenarios is made up of two components, one is the tsunami initial water condition, the other is extracted from the output of storm surge simulation. The final initial water surface condition is obtained by summation of the two water level distributions throughout the computational domain. For scenarios A1 to A20, typhoon starts at a close location to the tsunami source area, while for scenarios A21 to A35, typhoon starts around Tokyo Bay. For scenarios in Group B, typhoon starts near Tokyo Bay.

Figure 5.13 shows the initial water surface condition of scenario A5, A10, A15, A20, A25, A30, A35, and B1. The tsunami condition of A1 to A35 is same, while with changing the initial Hotstart time, the initial location of typhoon changes. As tsunami in Zone 2 is in Tokyo Bay, the number of initial condition of scenarios in Group B is less than that of Group A. Initial typhoon location of scenario A5, A10, A15, A20 is near the tsunami fault area, while in scenario A30 and A35, the initial typhoon location is around Tokyo Bay area. For scenarios A1 to A20, typhoon starts at a close location to the tsunami source area, while for scenarios A21 to A35, typhoon starts around Tokyo Bay.

To match with the initial location of typhoon track, the input files of Typhoon model have been pre-processed accordingly. The unstructured mesh used in multi-hazard simulation is the same in Section 5.1.1.

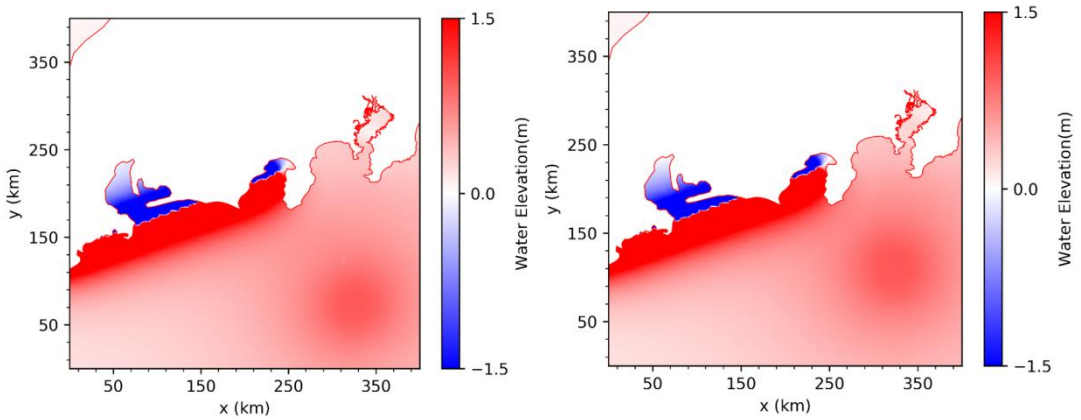

(a) (b)

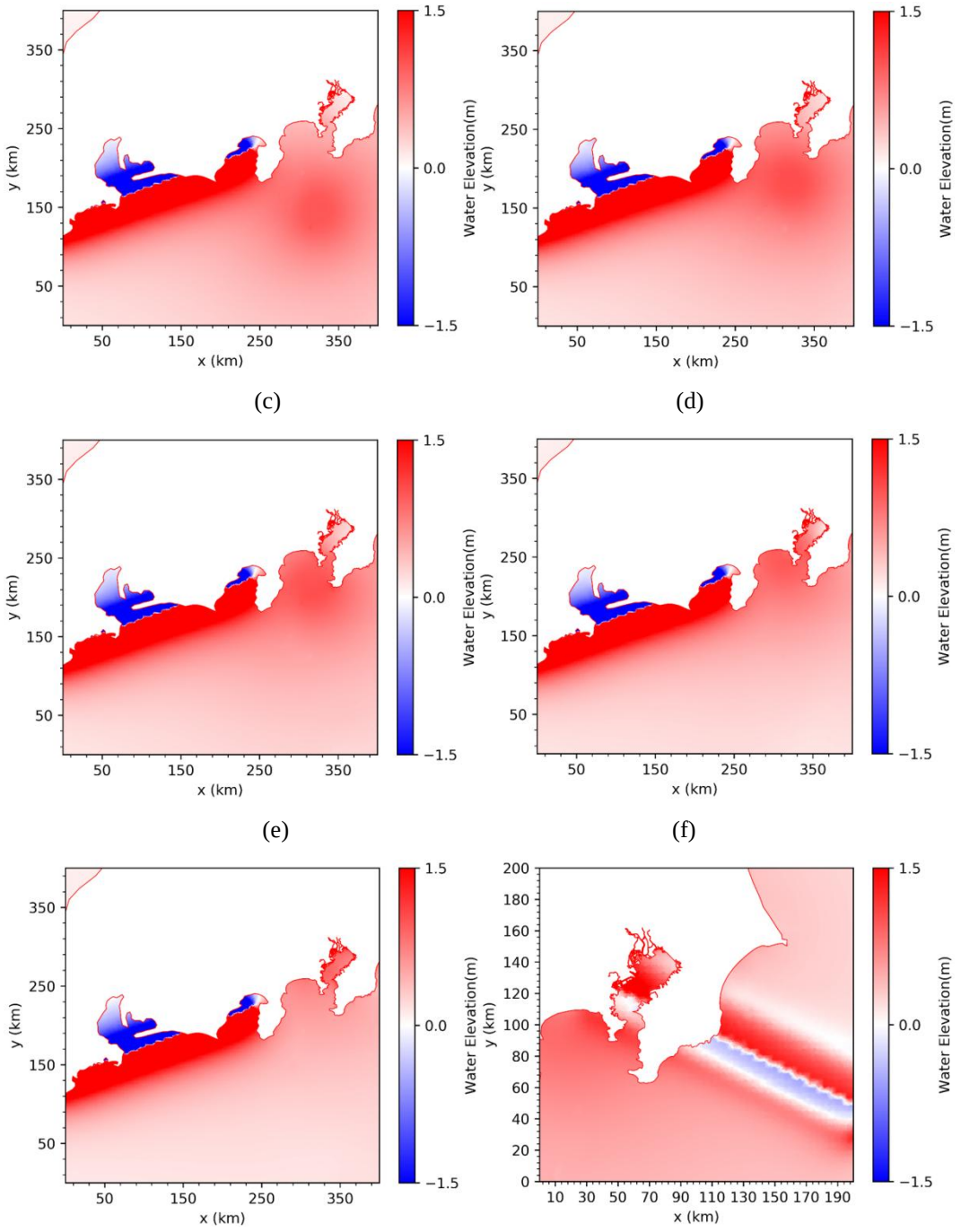

Figure 5.13 Initial water surface condition of Scenario A5, A10, A15, A20, A25, A30, A35, and B1

5.2.2 Dike height data

DEM is downloaded from the Geospatial Information Authority of Japan. This dataset provides 5-meter resolution land elevation data.

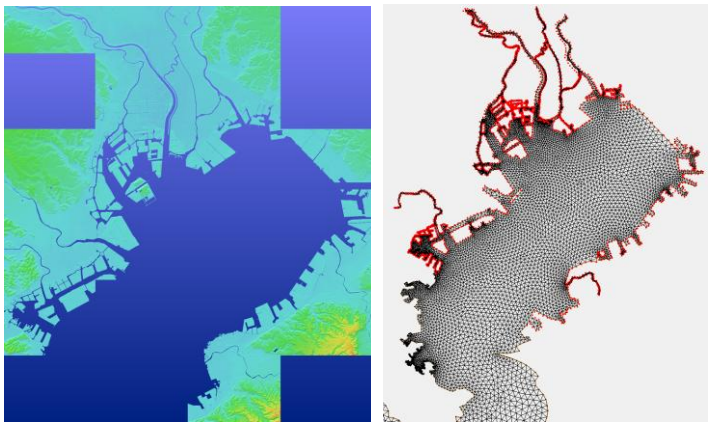

(a) (b)

Figure 5.14 (a) DEM and (b) Estimation of dike height in SMS 11.1

Since the dike height data was not available, it was estimated from DEM. First, the digital elevation data points (x, y, z) along the coastal dike and river banks were manually extracted from the DEM data. Then, these data points (red color) were imported in SMS software (see Figure 5.14(b)), and interpolated into the coastline nodes. The final dike elevation map along the northern part of the bay is shown in Figure 5.15. To verify the estimated dike elevation, examples of the original DEM altitudes are selected as shown in Figure 5.16 for verification.

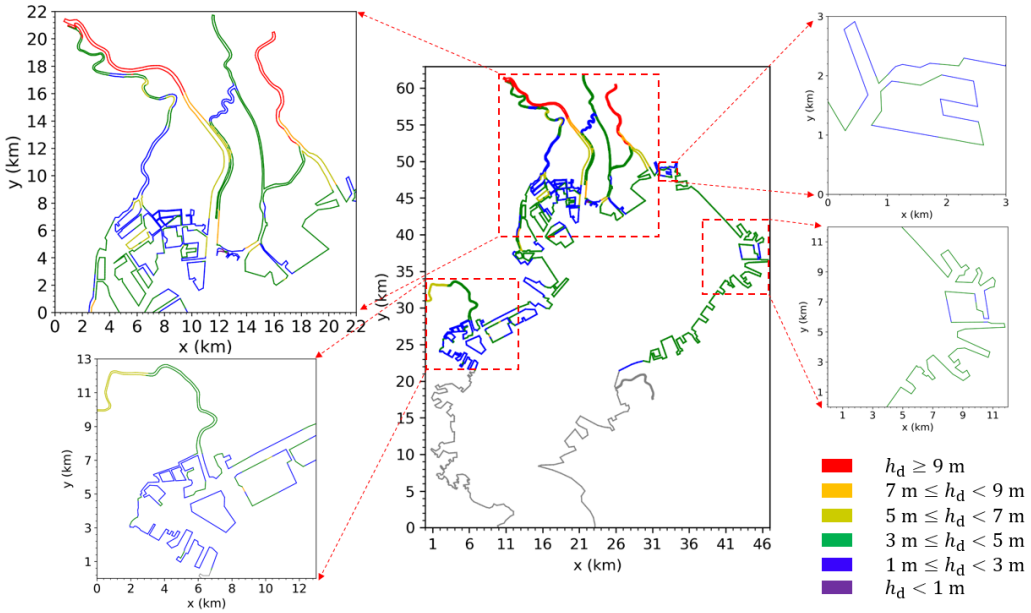

Figure 5.15 Estimated dike height map of the northern part of Tokyo Bay (h_d is the dike height above the mean sea level)

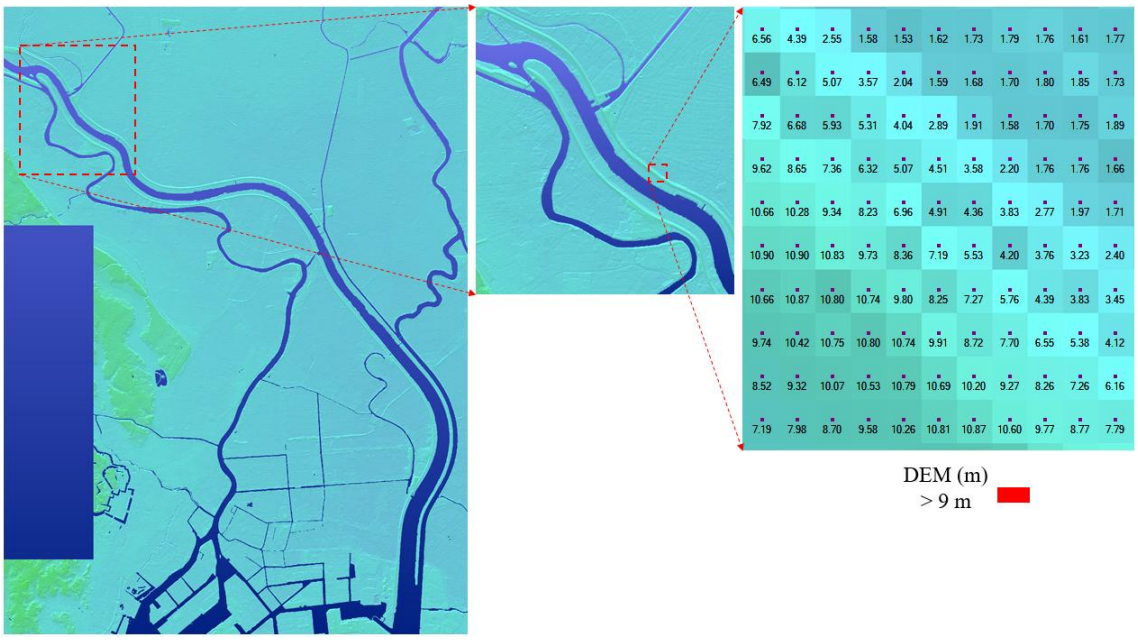
6.56 4.39 2.55 1.58 1.53 1.62 1.73 1.79 1.76 1.61 1.77
6.49 6.12 5.07 3.57 2.04 1.59 1.68 1.70 1.80 1.85 1.73
7.92 6.68 5.93 5.31 4.04 2.89 1.91 1.58 1.70 1.75 1.89
9.62 8.65 7.36 6.32 5.07 4.51 3.58 2.20 1.76 1.76 1.66
10.66 10.28 9.34 8.23 6.96 4.91 4.36 3.83 2.77 1.97 1.71
10.90 10.90 10.83 9.73 8.36 7.19 5.53 4.20 3.76 3.23 2.40
10.66 10.87 10.80 10.74 9.80 8.25 7.27 5.76 4.39 3.83 3.45
9.74 10.42 10.75 10.80 10.74 9.91 8.72 7.70 6.55 5.38 4.12
8.52 9.32 10.07 10.53 10.79 10.69 10.20 9.27 8.26 7.26 6.16
7.19 7.98 8.70 9.58 10.26 10.81 10.87 10.60 9.77 8.77 7.79
DEM (m)
> 9 m

(a)

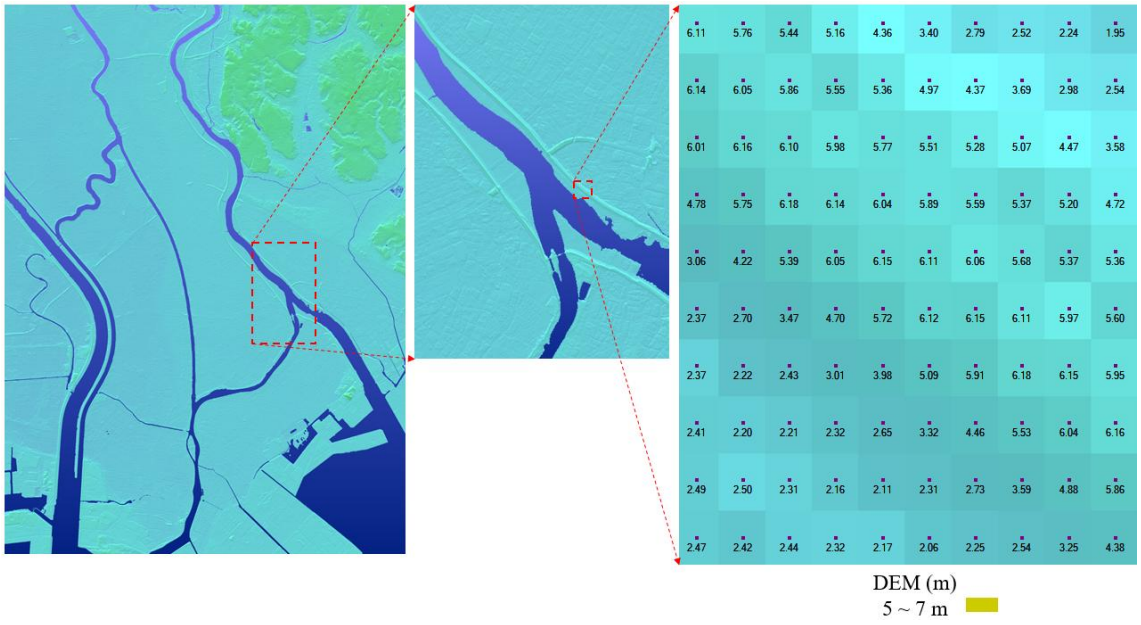
6.11 5.76 5.44 5.16 4.36 3.40 2.79 2.52 2.24 1.95
6.14 6.05 5.86 5.55 5.36 4.97 4.37 3.69 2.98 2.54
6.01 6.16 6.10 5.98 5.77 5.51 5.28 5.07 4.47 3.58
4.78 5.75 6.18 6.14 6.04 5.89 5.59 5.37 5.20 4.72
3.06 4.22 5.39 6.05 6.15 6.11 6.06 5.68 5.37 5.36
2.37 2.70 3.47 4.70 5.72 6.12 6.15 6.11 5.97 5.60
2.37 2.22 2.43 3.01 3.98 5.09 5.91 6.18 6.15 5.95
2.41 2.20 2.21 2.32 2.65 3.32 4.46 5.53 6.04 6.16
2.49 2.50 2.31 2.16 2.11 2.31 2.73 3.59 4.88 5.86
2.47 2.42 2.44 2.32 2.17 2.06 2.25 2.54 3.25 4.38
DEM (m)
5 ~ 7 m

(b)

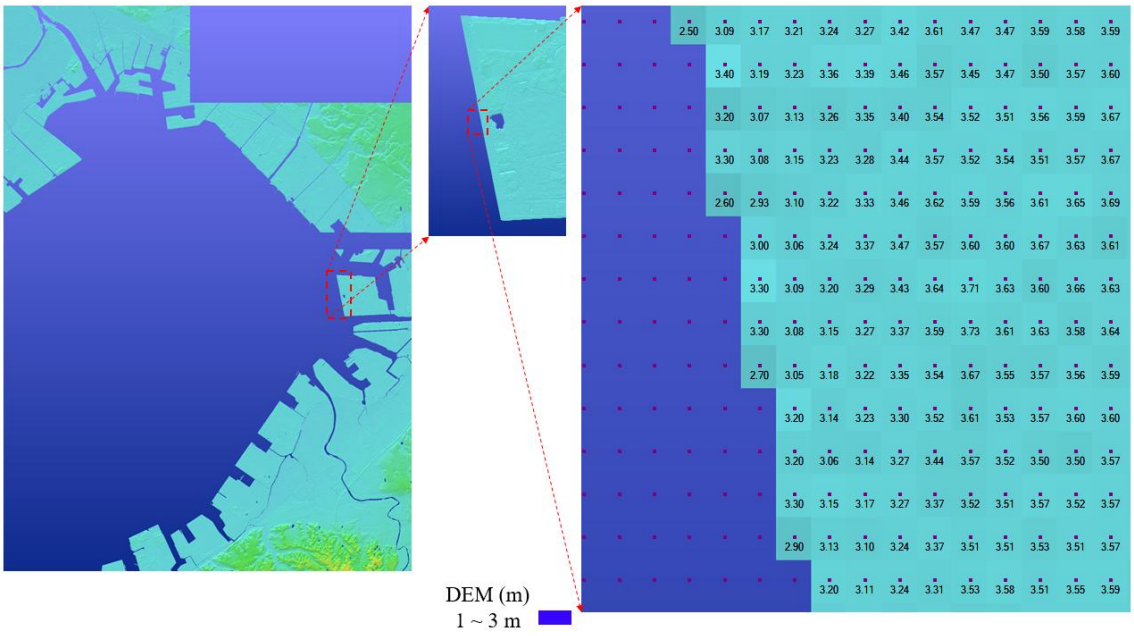

(c)

Figure 5.16 DEM data in Arakawa River (a), Edogawa River (b), and Chiba coast (c)

5.2.3 Results and discussion

5.2.3.1 Anomaly in tidal stations

Table 5.16 presents the maximum anomalies at stations in Tokyo Bay for Group A scenarios. Compared to the scenarios shown in Section 5.1.2, the maximum anomalies at the seven stations increased by about 0.5 m to 1.5 m, which means when tsunami, river food, and storm surge happen at the same time, the water level in Tokyo Bay would be elevated more compared to a single hazard or two of them.

The difference among Scenario A1 to A5, Scenario A6 to A10, Scenario A11 to A15, Scenario A16 to A20, Scenario A21 to A25, and Scenario A26 to A35 is the initial location of typhoon. In Table 5.17, all maximum anomalies (red color highlighted) were observed in scenario A1-A25, it means when typhoon starts near the tsunami source area, the maximum anomalies tend to occur. Another interesting phenomenon is that almost all maximum anomalies at the seven stations happened when typhoon scenario was T4S2 or T4S1, except in Chiba station (A17, T2S4). For example, for Kurihama station, the peak anomaly occurred in Scenario A10 (T4S2), for Yokosuka station, the peak anomaly occurred in Scenario A5 (T4S2), for Yokohama station, the peak anomaly happened in Scenario A25 (T4S2), for Kawasaki station, the peak anomaly happened in Scenario A25 (T4S2), for Shibaura station, the peak anomaly happened in Scenario A14 (T4S1), for Tokyo Harumi station, the peak anomaly happened in Scenario A14 (T4S1). It may be due to the locations of the stations. The Stations of Kurihama, Yokosuka, Yokohama and Kawasaki are located in the west side of Tokyo Bay and the distance to the track of T4S2 or T4S1 is within the maximum wind radius, while Station Chiba is located in another side of the bay. In addition, Tokyo Harumi station is located near the mouth of Sumidagawa River, the anomaly is the highest among the seven stations.

Table 5.16 Maximum water elevation (m) at stations in Tokyo Bay for Group A scenarios
(red color highlights the maximum water elevation value of the column)

Scenario number	Kurihama	Yokosuka	Yokohama	Kawasaki	Shibaura	Tokyo Harumi	Chiba
A1-A5	2.34	1.87	2.23	1.58	2.33	2.74	2.18
A6-A10	2.50	1.72	2.26	1.73	2.55	2.79	2.41
A11-A15	2.35	1.58	2.13	1.76	2.59	2.82	2.56
A16-A20	2.31	1.59	2.07	1.87	2.39	2.51	2.65
A21-A25	2.11	1.57	2.32	2.00	2.24	2.38	2.46
A26-A30	1.93	1.72	2.21	1.88	2.23	2.31	2.17
A31-A35	1.87	1.66	2.15	1.80	1.88	2.01	2.17

Table 5.17 Scenario number of maximum water elevation at stations in Tokyo Bay for Group A scenarios

Scenario number	Kurihama	Yokosuka	Yokohama	Kawasaki	Shibaura	Tokyo Harumi	Chiba
A1-A5	A5	A5	A4	A4	A4	A4	A2
A6-A10	A10	A10	A9	A9	A9	A9	A10
A11-A15	A13	A12	A12	A13	A14	A14	A13
A16-A20	A17	A17	A17	A19	A18	A18	A17
A21-A25	A22	A25	A25	A25	A22	A21	A22
A26-A30	A27	A30	A28	A26	A27	A27	A26
A31-A35	A33	A31	A32	A32	A32	A32	A32

Table 5.18 presents the maximum anomalies in Group B scenarios, the maximum value occurred in Tokyo Harumi station when the scenario is B4. It means in typhoon scenario T4S1, the water level reaches the largest.

Table 5.18 Maximum water elevation (m) at stations in Tokyo Bay for Group B scenarios

Scenario number	Kurihama	Yokosuka	Yokohama	Kawasaki	Shibaura	Tokyo Harumi	Chiba
B1-B5	1.37	2.00	1.91	1.92	1.84	2.07	1.75

Table 5.19 Scenario number of maximum water elevation at stations in Tokyo Bay for Group B scenarios

Scenario number	Kurihama	Yokosuka	Yokohama	Kawasaki	Shibaura	Tokyo Harumi	Chiba
B1-B5	B2	B3	B3	B4	B5	B4	B3

5.2.3.2 Vulnerability map

Four types of hazard scenarios are prepared for the vulnerability investigation (see Table 5.20). The levels of the vulnerability have been determined as seven classes: “I” (grey), “II” (purple), “III” (blue),

“IV” (green), “V” (olive), “VI” (orange), “VII” (red). Level “VII” (red) represents that the part of coastline under the hazard scenario is the most vulnerable, and Level “I” (grey) represents that it is the least vulnerable. This approach has been widely used for the visualization of vulnerability in many studies[148-153]. The range of vulnerability level is specified according to the calculated results of overflow volume, for example, the maximum value 65,000 is chosen because among all cases in the four types of hazards, this value is the largest. To better show the difference and similarity among the four types of hazards, same classification value is used. The classification of the vulnerability levels is presented in Table 5.21.

Figure 5.17 shows the vulnerability map for the worst case of four hazard types. For Type 1 hazard (only storm surge), no Level “VII” (red) areas have been found, and the most vulnerable grade is Level “III” (blue), they are located in the middle part of Sumidagawa River, and reclamation land (see Figure 5.17(a)). Except the rivers and Koto ward, Funabashi coast and Chiba coast also have overflows. After combining river flood, the overflow areas in the upstream rivers expand (see Figure 5.17(b)), especially in the Sumidagawa River and Nakagawa River. After adding tsunami, the vulnerable areas further increase significantly, and in Type 3 hazard (storm surge, ToKai-ToNankai earthquake tsunami, and river flood), the overflow extent including the overflow coastal areas and overflow volume grow largely compared to other types of hazards (see Figure 5.17(c)).

From Figure 5.17(a) and Figure 5.17(b), river flood could increase the overflow areas in the major rivers of Tokyo Bay. By comparison of Figure 5.17(b) and Figure 5.17(c) or Figure 5.17(b) and Figure 5.17(d), east coasts of Kanagawa Prefecture (Kawasaki ward, and Yokohama Port) and Chiba coasts would suffer more overflow after combing ToKai-ToNankai earthquake tsunami or Tokyo inland earthquake tsunami.

Table 5.20 Hazard types for vulnerability assessment

Type No.	Hazard component
1	Only storm surge (21 cases)
2	Storm surge and river flood (21 cases)
3	Storm surge, tsunami (ToKai-ToNankai) and river flood (35 cases)
4	Storm surge, tsunami (Tokyo inland type) and river flood (5 cases)

Table 5.21 Classification of Vulnerability levels

Vulnerability Level	Overflow volume m^3
VII	(65000, +∞)
VI	(52000, 65000]
V	(39000, 52000]
IV	(26000, 39000]
III	(13000, 26000]
II	(0, 13000]
I	0

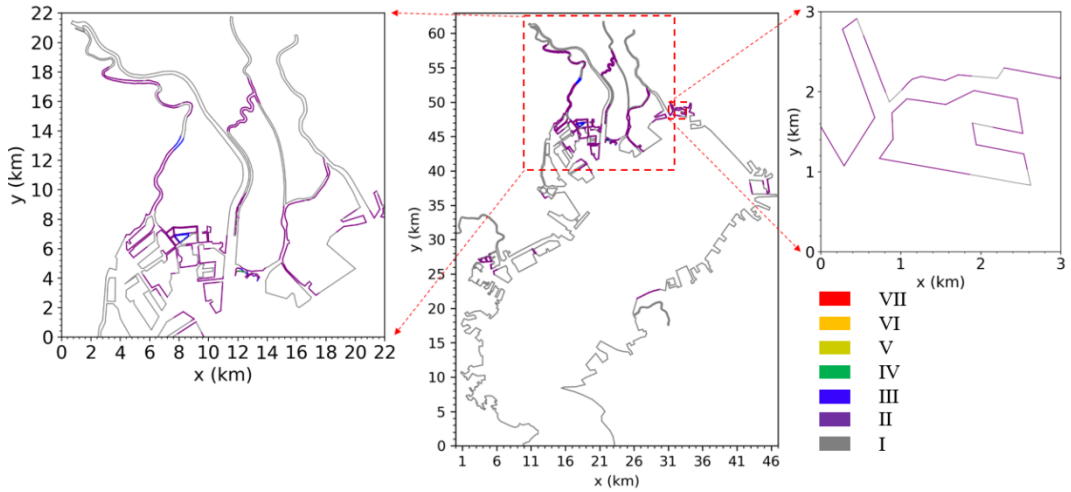
y (km)
x (km)
VII
VI
V
IV
III
II
I

(a)

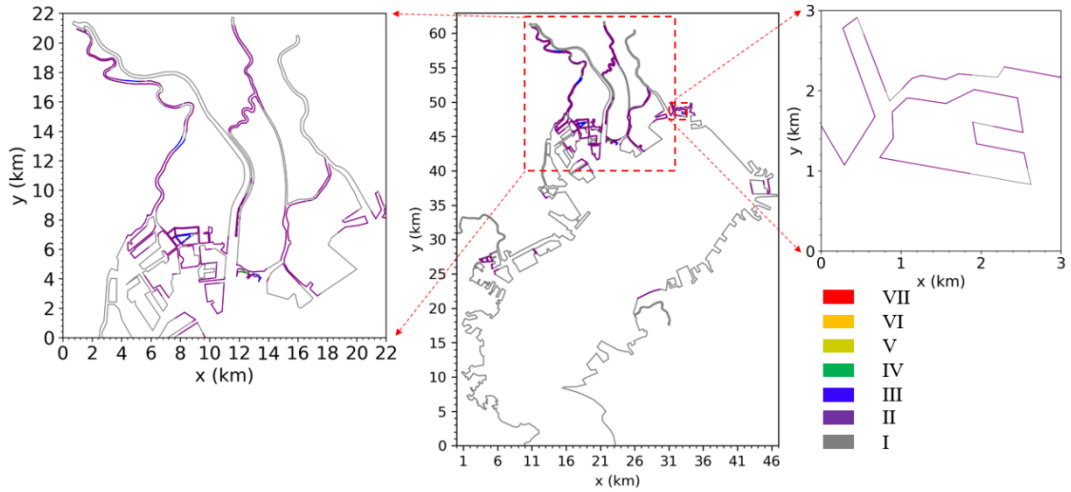
y (km)
x (km)
VII
VI
V
IV
III
II
I

(b)

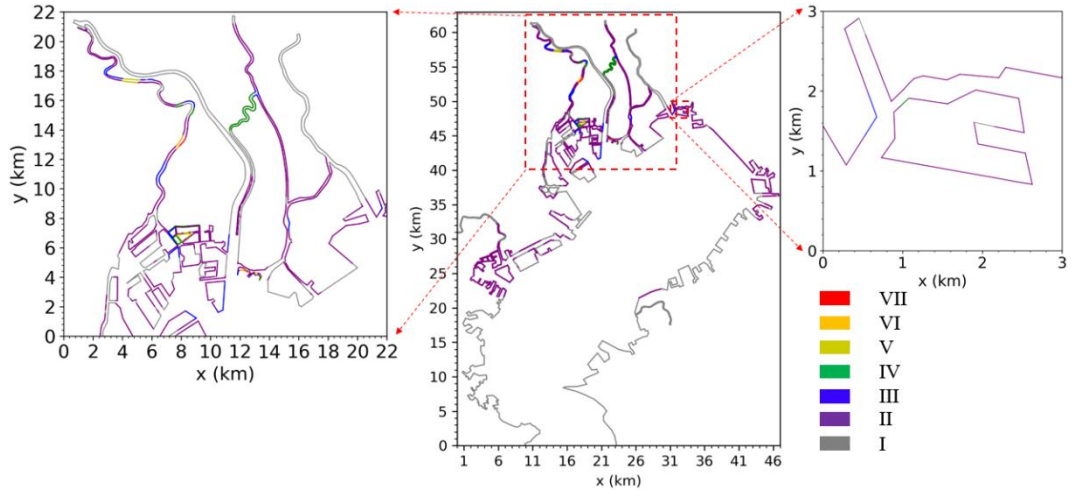
y (km)
x (km)
VII
VI
V
IV
III
II
I

(c)

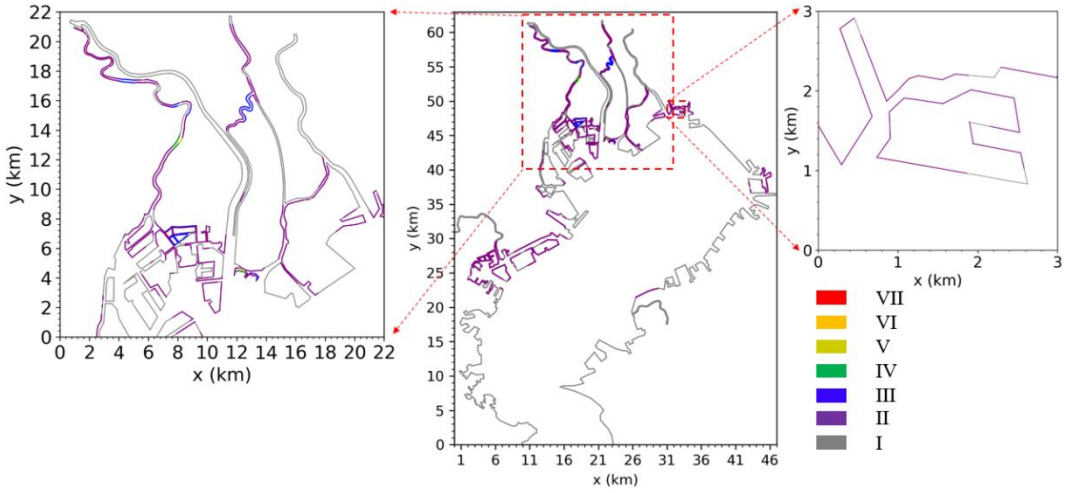

(d)

Figure 5.17 Vulnerability map of overflow volume for (a) worst storm surge cases, (b) worst storm surge and river flood cases, (c) worst storm surge, ToKai-ToNankai earthquake tsunami and river flood cases, and (d) worst storm surge, Tokyo inland earthquake tsunami and river flood cases

5.2.3.3 Comparison with government report

Figure 5.18 shows the storm surge inundation map made by Chiba Prefecture Government[94] and Tokyo Metropolitan Government[92]. It is assumed that in the place where overflow volume is large, the inundation depth is also high. By comparing Figure 5.17(a) and Figure 5.18, the inundation extent is consistent with that in the map of overflow volume including the Koto ward areas, Funabashi areas and most part of river basin though there are still some differences in the Arakawa River and Chiba coasts, which may be caused by the accuracy of dike height data used in the computation.

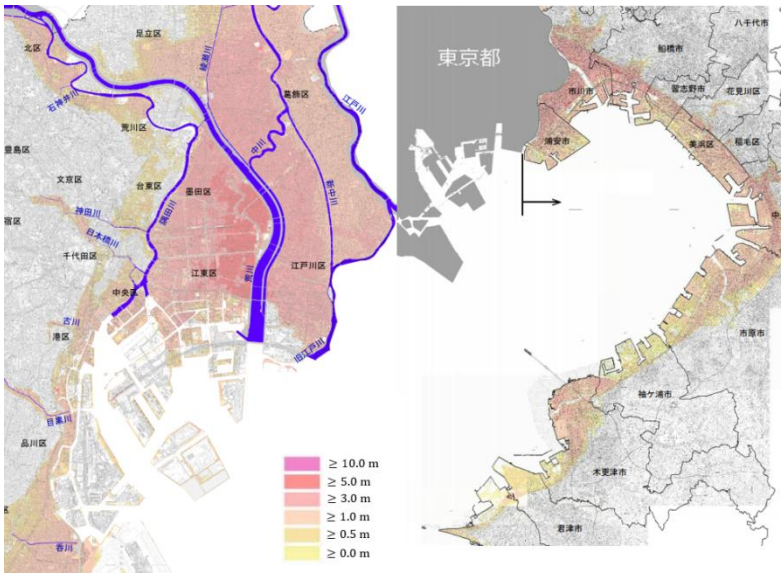

Figure 5.18 Storm surge inundation map made by Tokyo Metropolitan Government (left) and Chiba

Prefecture Government (right)

5.2.4 Sub-conclusion

The multi-hazard vulnerability of Tokyo Bay has been investigated and different types of hazards are analyzed using numerical simulation method.

The vulnerable areas of Tokyo Bay under multiple coastal hazards (storm surge, tsunami and river flood) are firstly identified. Under the worst condition of Type 3 hazard (storm surge, ToKai-ToNankai earthquake tsunami, and river flood), the northern part of Tokyo Bay suffers the most serious overflow compared to other cases.

River flood added in storm surge cases could increase the vulnerable areas, which are mostly located in the upstream of Sumidagawa River and Nakagawa River. Tsunami added in storm surge and river flood cases could also increase the overflow extent in the bay, and the vulnerable areas include the east coast of Kanagawa Prefecture and Chiba coasts. The relative location of tsunami and storm surge and the time when they happen together have a significant influence on the final overflow condition in the bay.

5.3 Effect of drainage pipe system

5.3.1 Introduction

In last section, the vulnerability of coastal areas in Tokyo Bay to multiple hazards has been identified using scenario-based simulation, Scenario A6-A10 caused more serious overflow compared to other scenarios in Group A. It could be concluded that the type of the hazard, the location of the area and the dike height could largely affect the vulnerability of the region. However, except these factors, drainage pipe system may also have an influence on the flood risk as introduced in the literature review. Thus, in this section, the integrated FVCOM and drainage pipe model is applied to a local region for detailed inundation simulation combining the drainage pipe system. Two cases are prepared for the comparison and discussion. One includes the drainage pipe system, and the other excludes it. By comparing the inundation volume and inundation period of these two cases in the study area, the role of drainage pipe system in determination of local vulnerability could be clarified.

As the inundation volume is one of the important indicators, the study area is better to be easy for the statistic of it. In other words, if the study area is in an urban area and with solid boundaries, inundation may accumulate at the boundary, which would never happen in actual case. Therefore, an island may be a good choice. On islands, the inundation (no matter it is directly flooded by the high water level or due to the overflow from the manholes) could flow freely only depending on the topography, it could accumulate somewhere, or flow back into the sea. Funabashi Sanbanze Seashore Park which is located in the northern head of Tokyo Bay is one of the vulnerable areas. In this section, it is selected as the study area (see Figure 5.19).

In addition to storm surge, tsunami and river flood, a 5-year return period rainfall intensity is assumed to be a component of the multi-hazard inundation scenarios. The upstream flow input of the storm water drainage pipe system is computed using the rainfall intensity formula of 5-year return period.


Google Earth
Image Landsat / Copernicus
Data SIO, NOAA, U.S. Navy, NGA, GEBCO
30 km
N
Google Earth
400 m
N

(a)

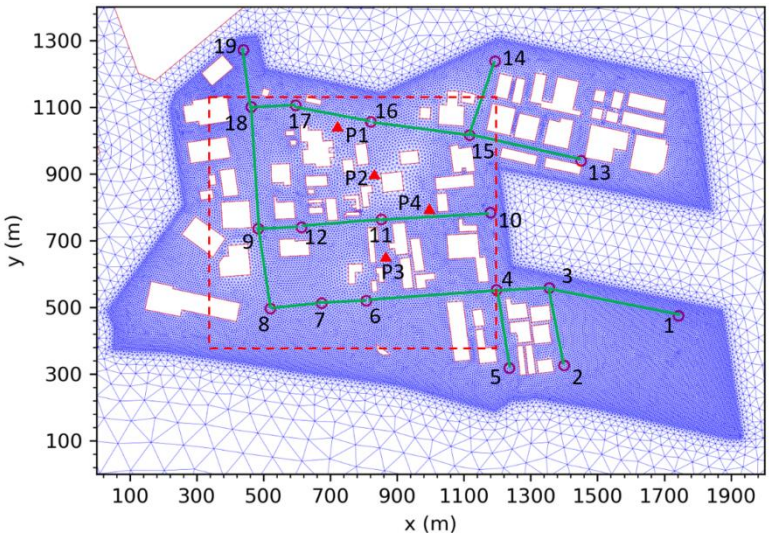
1300
1100
900
700
500
300
100
y (m)
100
300
500
700
900
1100
1300
1500
1700
1900
x (m)
19
14
18
17
16
P1
15
13
P2
P4
10
9
12
11
P3
4
3
8
7
6
1
5
2

(b)

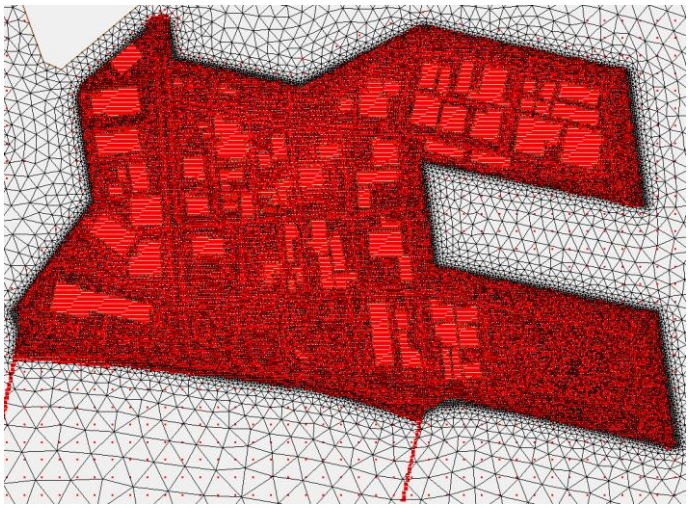

(c)

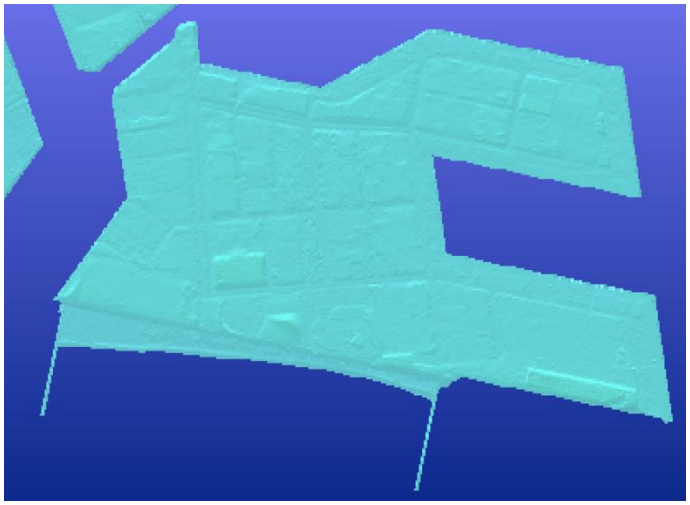

(d)

Figure 5.19 Location of the study area and mesh ((a): Tokyo Bay and Funabashi Sanbanze Seashore Park; (b): mesh in the study area, red circles are the manholes of drainage pipe system in the study area, number 1 to 19 represents the manhole ID, P1, P2, P3, and P4 are 4 observation points, red dash box area is used for analysis of inundation period; (c): Digital elevation data in the study area; (d): DEM in this area) ((a), source: Google Earth, Data SIO, NOAA, U.S. Navy, NGA, GEBCO)

5.3.2 Model configuration

The base mesh which includes the tsunami source area and propagation area is the same as the one which has been introduced in Section 5.1.1. The local mesh in Funabashi Sanbanze Seashore Park is resolved for inundation simulation (see Figure 5.19(c)), and the typical mesh size in the inundation area is 5 m. The multi-hazard scenario is composed of M_w 8.4 earthquake tsunami in ToKai-ToNankai area, 1949 Typhoon Kitty course (see Section 5.1.2.1) and 50-year return period river discharge. The boundary condition is the wind and atmospheric pressure field of the corresponding typhoon model output. The model time is 29,400 s and the external time step is 0.05 s. The simulation took about 3 hours in Kyushu ITO supercomputer.

Since the drainage pipe system data is not publicly available in this area, it is assumed by referring to other areas, e.g., Chiba city. It should be noted that the major purpose of this part of work is not to really evaluate the performance of the local drainage pipe system in an inundation event, e.g., whether it functions well or not, but to clarify the role of a drainage system, e.g., whether the existence of the system really matters to the inundation and how important it is. The former is more like a consulting work while the latter is not. Thus, with proper assumption of the local drainage pipe system, the major goal could be achieved. The principle of assuming pipe system is that the pipe is constructed under the roadways, and as it is drainage system, gravitational flow in the pipe is dominant. With reference to the design in other neighboring areas. The property of the assumed drainage pipe system in the study area is presented in Table 5.22.

Table 5.22 Information of the drainage pipe system in the study area

Pipe ID	Manhole ID	Length (m)	diameter (m)	Slope (m/m)	Upstream bottom elevation (m)	Downstream bottom elevation (m)
1	1,3	320.00	0.45	0.0032	1.006	0.816
2	2,3	200.00	0.45	0.0034	1.214	0.81
3	3,4	102.62	0.50	0.00423	0.80	0.792
4	5,4	202.30	0.50	0.0049	1.284	1.06
5	4,6	324.02	0.45	0.00343	1.044	0.893
6	6,7	93.90	0.45	0.00173	0.821	0.814
7	7,8	104.01	0.45	0.00155	0.812	0.725
8	8,9	204.13	0.45	0.00181	0.723	0.663
9	10,11	243.07	0.45	0.0042	1.261	1.08
10	11,12	153.29	0.40	0.00462	0.92	0.874
11	12,9	84.81	0.45	0.00094	0.872	0.830
12	9,18	389.88	0.45	0.00294	0.648	0.642
13	13,15	260.66	0.45	0.00224	1.166	1.043
14	14,15	215.44	0.45	0.00088	1.101	1.05
15	15,16	244.97	0.45	0.00042	0.999	0.88
16	16,17	210.22	0.50	0.00131	0.81	0.755
17	17,18	99.23	0.45	0.00251	0.745	0.64
18	18,19	165.24	0.80	0.0125	0.62	-0.78

A small flow (0.1 m^3/s) is assumed to be in the upstream of the drainage pipe system (manhole with ID number 1, 3, 6, 12, 15). This flow value is estimated based on a rough computation of the rainfall intensity in the area.

The rainfall flow is estimated as:

$$Q_r = \frac{1}{360} \times C_L \times I \times A_r \tag{5-6}$$

where, Q_r is the rain flow, m^3/s; C_L is the land surface runoff coefficient; I is the rainfall intensity, mm/h; A_r is the area of the study zone. The formula of rainfall intensity I is developed based on the long term rainfall observations in different areas. A 5 year return period rainfall is common. Thus, equation (5-7) is used to calculate the rainfall intensity.

$$I = \frac{1406}{t^{3/4} + 9.3} \tag{5-7}$$

where, t is the flow time of collected rain water in the pipe, and computed as:

$$t = t_1 + t_2 \tag{5-8}$$

where, t_1 is the time for the rainwater collection in the catchment area, usually 5-15 mins, t_2 is the time for the rainwater flowing in the pipe, and it could be calculated by:

$$t_2 = \frac{L_{\max}}{\overline{v}} \tag{5-9}$$

where, $L_{\max}$ is the longest drainage pipe, m; $\overline{v}$ is the average flow velocity in the pipe, m/s, usually 1.0 m/s, after calculation, the rainfall flow is about 0.1 m^3/s.

5.3.3 Results and discussion

Figure 5.20 shows the comparison of inundation volume for cases including and excluding drainage pipe system. In Figure 5.20(a), inundation happens from around 185 mins of model time, and inundation volume reaches the peak at 210 mins of model time. Then, the inundation volume decreases gradually in both cases (including and excluding drainage pipe system). However, from about 210 mins, inundation volume in the case including drainage pipe system decreases more quickly than that excluding the drainage pipe system, and after about 350 mins, the inundation volume of both cases becomes nearly stable.

Figure 5.20(b) shows the time-series change of inundation depth at 4 observation points. Similar phenomenon could be observed that inundation depth in the case including drainage pipe system decreases more quickly.

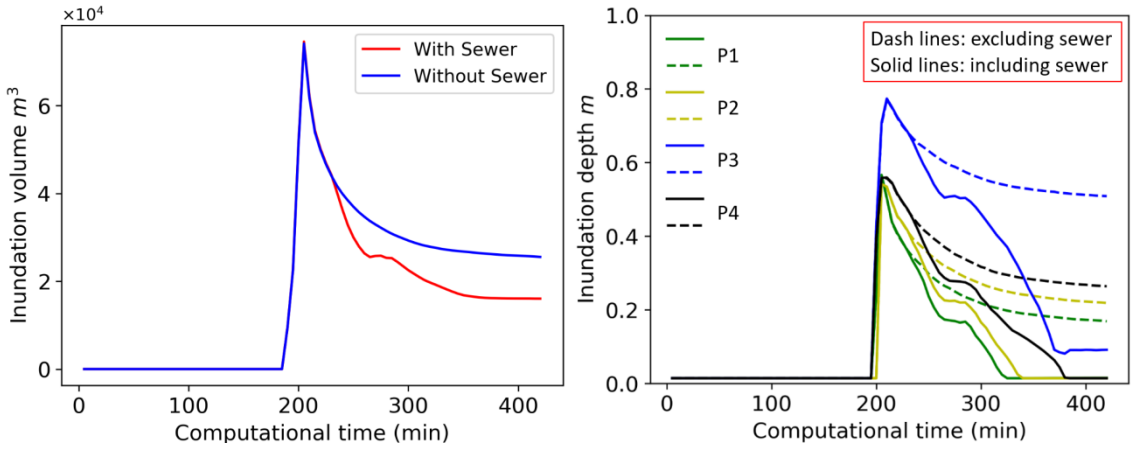

(a) (b)

Figure 5.20 Time-series change of inundation volume (a) and inundation depth at 4 observation points (b) for cases including and excluding drainage pipe system

Figure 5.21 shows the snapshot figures from the inundation simulation. It is clear that at 335 mins of model time, the inundation extent in case that includes drainage pipe system is much less. However, in the case that excludes drainage pipe system, the inundation volume does not keep unchanged after the peak time. Instead, it also decreases. To identify the reason, the velocity field in the northern part area (black dash box area in Figure 5.21) was made as shown in Figure 5.22. It could be found that part of the inundation flows back to the ocean through the road. Figure 5.23 shows the local topography in that area. The coastal land area is inclined to the ocean, and that is why in both cases (including and excluding drainage pipe system), the inundation volume reduces since the peak time.

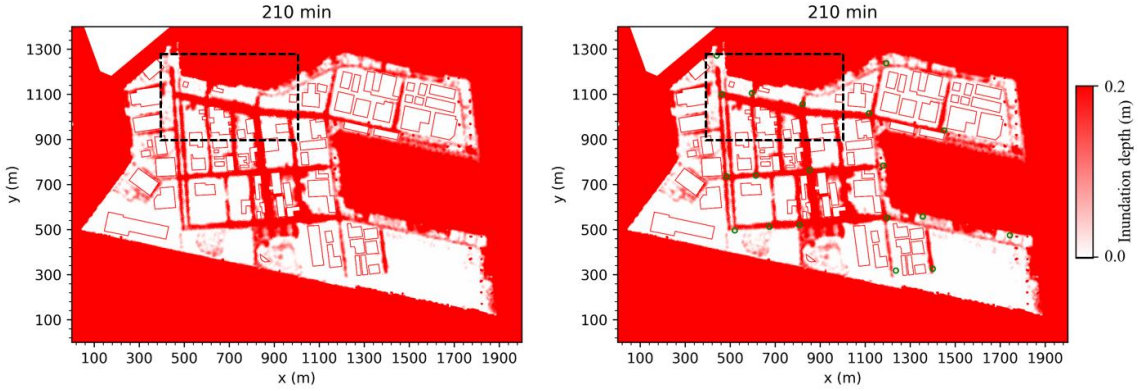

(a)

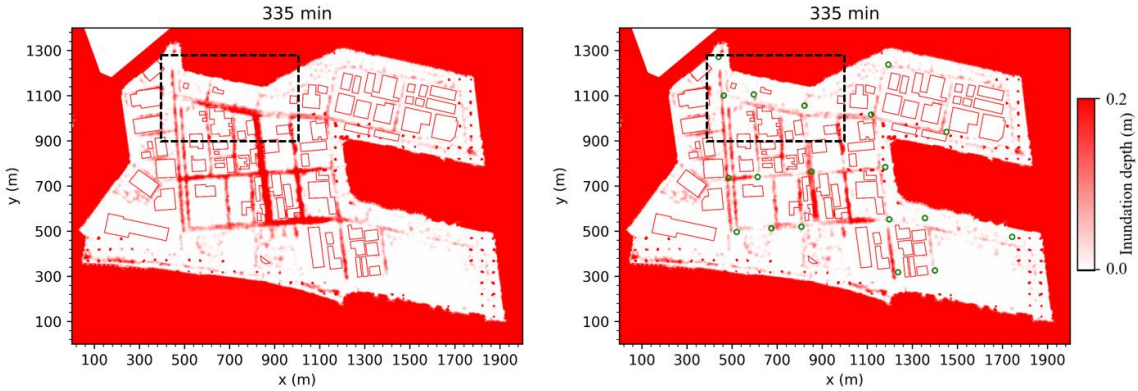

(b)

Figure 5.21 Inundation distribution at peak time (a) and steady period (b) (left panel: excluding drainage pipe system; right panel: including drainage pipe system; black dash box is zoomed in Figure 5.22)

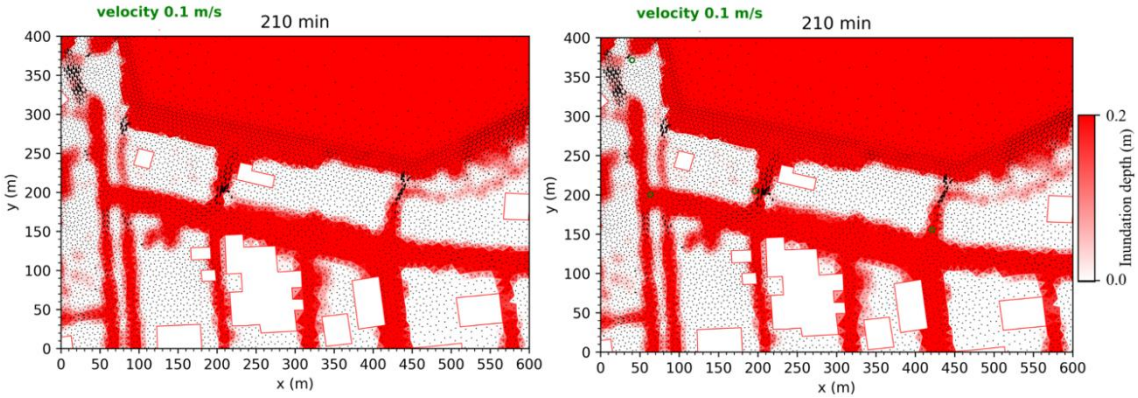

(a)

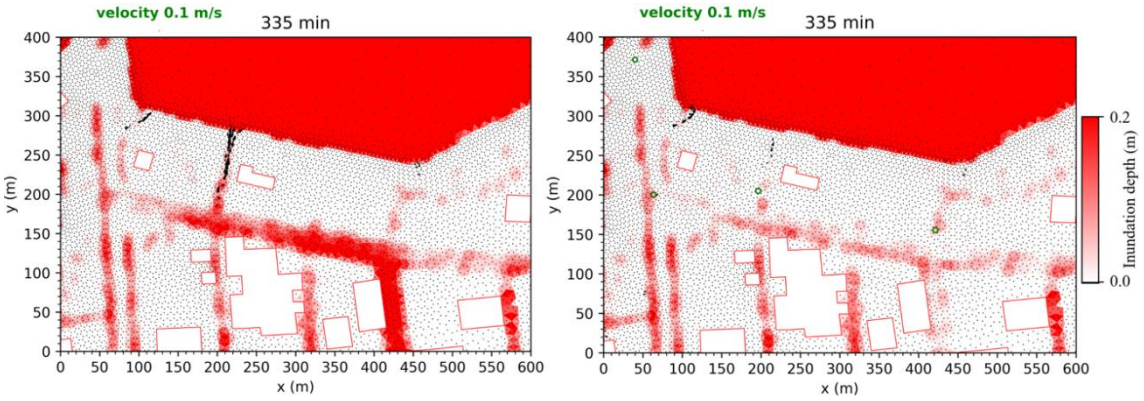

(b)

Figure 5.22 Inundation flows back to the ocean due to the topography

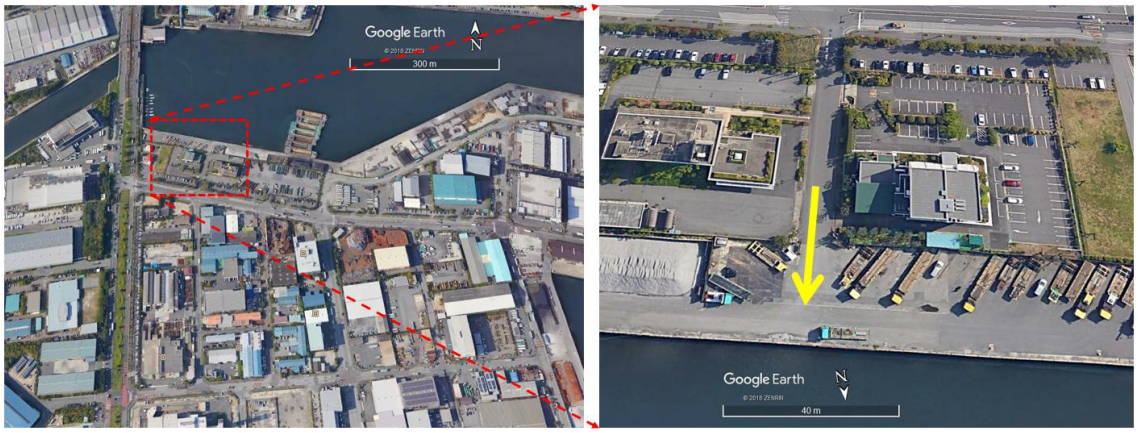

Figure 5.23 Local topography (yellow arrow shows the inundation flow direction) (source: Google Earth, Data SIO, NOAA, U.S. Navy, NGA, GEBCO)

5.3.4 Sub-conclusion

In this section, inundation simulation has been carried out in Funabashi Sanbanze Seashore Park area using the integrated FVCOM and drainage pipe model. By comparison of inundation volume and inundation period between two cases (one includes drainage pipe system and the other excludes), it has been demonstrated that the existence of drainage pipe system could help reduce the inundation extent including the inundation volume and inundation period. It is believed that with proper designing and planning, the drainage pipe system could reduce the vulnerability of coastal areas and somehow enhance the resilience of the region against coastal flood. However, as the drainage pipe system data is not publicly available in this area, an assumed drainage system with reference to neighboring areas was applied. From this part of work, lessons could also be learnt, e.g., for city planners or municipal engineers, when designing the drainage system in flood-prone areas, the performance of the system for draining post-disaster ground surface inundation may also need to be considered.

6. Discussion

This chapter first discusses the characteristics of the multi-hazard surge by tsunami and storm surge. Then, the author discusses the multi-hazard vulnerability in Tokyo Bay and the possible measures to be taken for reducing its impact. Finally, limitations of this study are presented.

6.1 Characteristics of multi-hazard surge by tsunami and storm surge

To understand the difference between single hazard (tsunami or storm surge) and multi-hazard case, a comparison between a multi-hazard case and a case linearly superposing each single hazard case extracted from the multi-hazard case was conducted.

The anomaly difference along the coast between the concurrent multi-hazard case and the superposing case is shown in Figure 6.1. The value is obtained by subtracting the anomaly of concurrent multi-hazard case from that of superposing case. It could be found that the difference varies spatially significantly and it is larger in ports and river channels than in other coastal areas. In most coastal areas, the anomaly of superposing case is greater than that of concurrent case, but in some places, concurrent case results in larger anomalies than superposing case. However, the difference of these two methods (concurrent computation and superposing way) is not large, e.g., more than 1 m, for most areas. Therefore, the superposing method is still an acceptable way for measuring multi-hazard vulnerability in coastal areas.

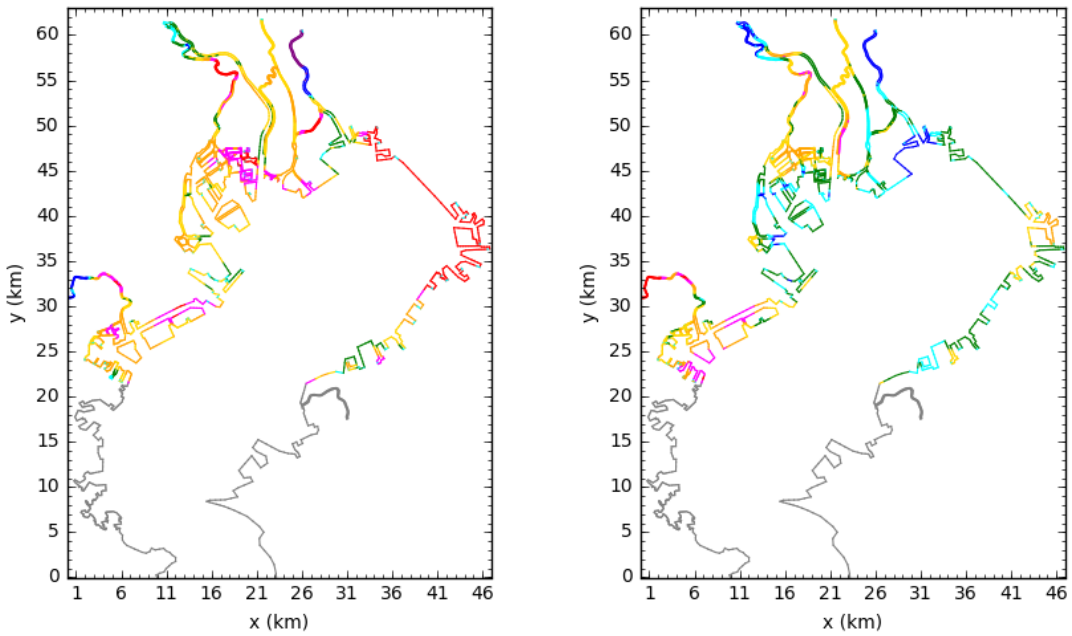

(a) (b)

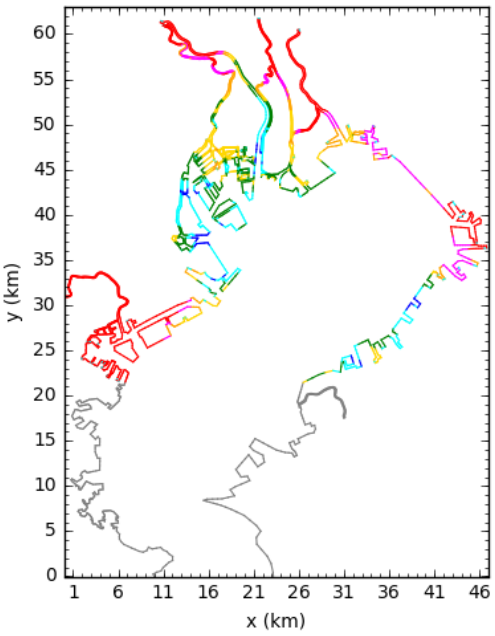
y (km)
x (km)
0 5 10 15 20 25 30 35 40 45 50 55 60
1 6 11 16 21 26 31 36 41 46

(c)

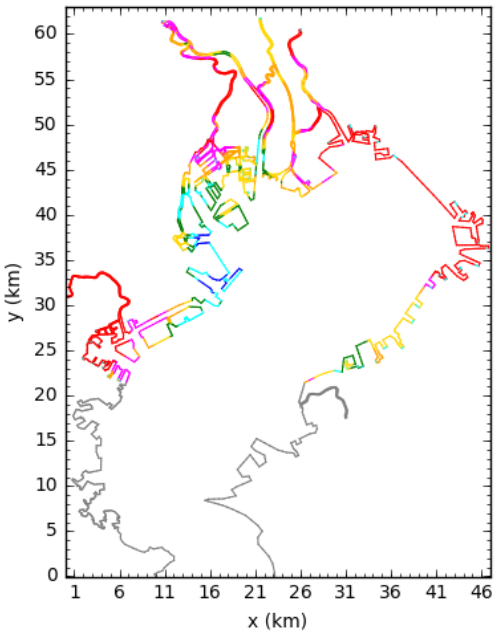
y (km)
x (km)
0 5 10 15 20 25 30 35 40 45 50 55 60
1 6 11 16 21 26 31 36 41 46

(d)

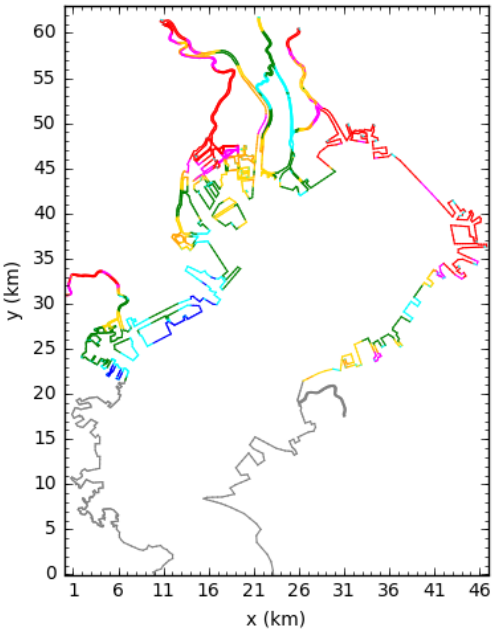
y (km)
x (km)
0 5 10 15 20 25 30 35 40 45 50 55 60
1 6 11 16 21 26 31 36 41 46

(e)

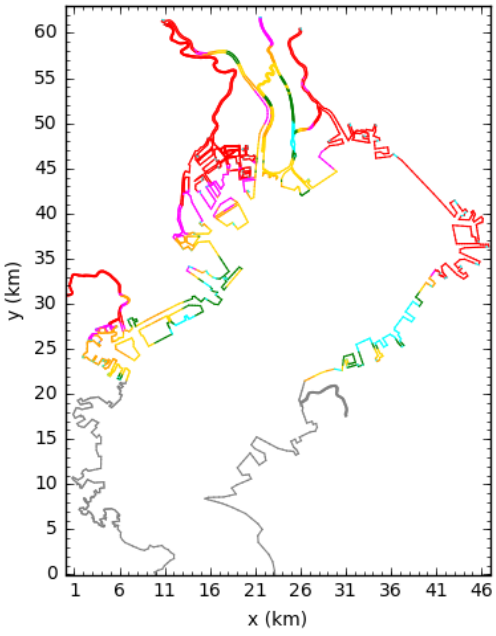
y (km)
x (km)
0 5 10 15 20 25 30 35 40 45 50 55 60
1 6 11 16 21 26 31 36 41 46

(f)

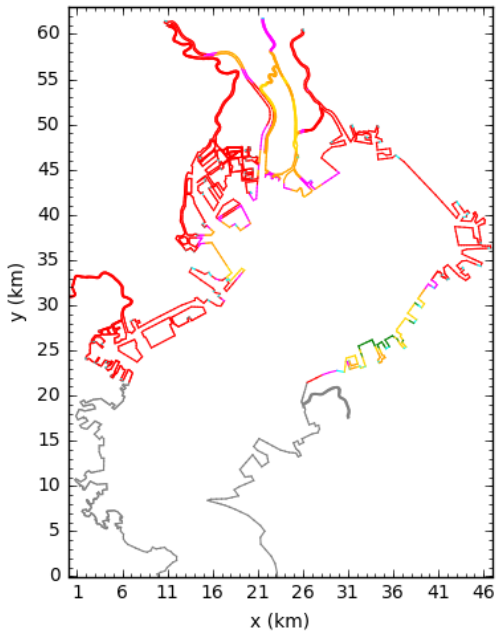

(g)

Figure 6.1 Anomaly difference of the concurrent multi-hazard case and the superposing case, (a) to (g): tsunamigenic earthquake happens when typhoon moves at Location 14 to Location 20 (red: 0.5 m~; magenta: 0.4 m~0.5 m; orange: 0.3 m~0.4 m; gold: 0.2 m~0.3 m; green: 0.1 m~0.2 m; cyan: 0.0 m~0.1 m; blue: -0.3 m~ 0.0 m; purple: -0.6 m~-0.3 m)

Tsunamis entering semi-enclosed bays and estuaries are influenced by three major processes, which are amplification and shoaling due to the coastline and bathymetry, damping due to the bottom friction, and reflection at the head of the bay. Although the interaction between storm surge and tsunami is a mutual process, the multi-hazard surge could be regarded as tsunami changed by storm surge since the period of storm surge is larger than tsunami. In the multi-hazard case, storm surge changes the water depth, thereby altering the shorelines and the balance between the bottom dissipation and coastline convergence, while in the superposing case, the surge level is obtained by the linear summation of tsunami and storm surge, in which tsunami is generated under original bathymetry (still water).

In concurrent cases, storm surge elevates the whole water level in the bay including that of coastal areas, which may weaken the tsunami wave shoaling compared to only tsunami case (starting from still water). Thus, the anomalies caused by concurrent case are smaller than superposing case in most areas. In addition, the areas where the anomaly of superposing case is larger than that of concurrent case vary with the time when tsunami happens during the typhoon movement. It also shows that the reason of larger anomaly in superposing case could be attributed to the change of bathymetry. Because in Figure 6.1, tsunami conditions of the seven sub-figures are same, only the time when tsunami and storm surge happen together changes, which causes different water level distributions for tsunami propagation, and further affects the tsunami wave shoaling. As for some areas (blue and purple color in Figure 6.1) where concurrent cases cause larger anomalies than superposing case, it is similarly affected by the time when

tsunami happens during the typhoon movement, and the majority of these local areas are located in the narrow channel areas such as the upstream of rivers. Therefore, except the effect of bathymetry change for tsunami propagation, the local coastline geometry may also contribute to this phenomenon due to reasons like reflection.

A comparison of the multi-hazard case (moderate storm surge and moderate tsunami) and the single hazard case (worst storm surge) is conducted. The return period of the storm surge and tsunami is around 5 years and 200 years, respectively, while the return period of the worst storm surge is more than 1000 years. From Figure 6.2, it could be found that in the worst storm surge case, anomalies are larger than those of moderate multi-hazard case, and for worst storm surge (see Figure 6.2(d)), anomaly is much larger in the north of the bay, while for multi-hazard case (see Figure 6.2(c)), the difference of anomaly in the north and south is not significant. Using similar concurrent computation method illustrated in the thesis, more numerical experiments could be carried out for performing detailed comparison between multi-hazard case and single hazard case, e.g., identifying the typhoon storm surge which would cause equivalent coastal damage as the multi-hazard case consisting of moderate storm surge and tsunami cases.

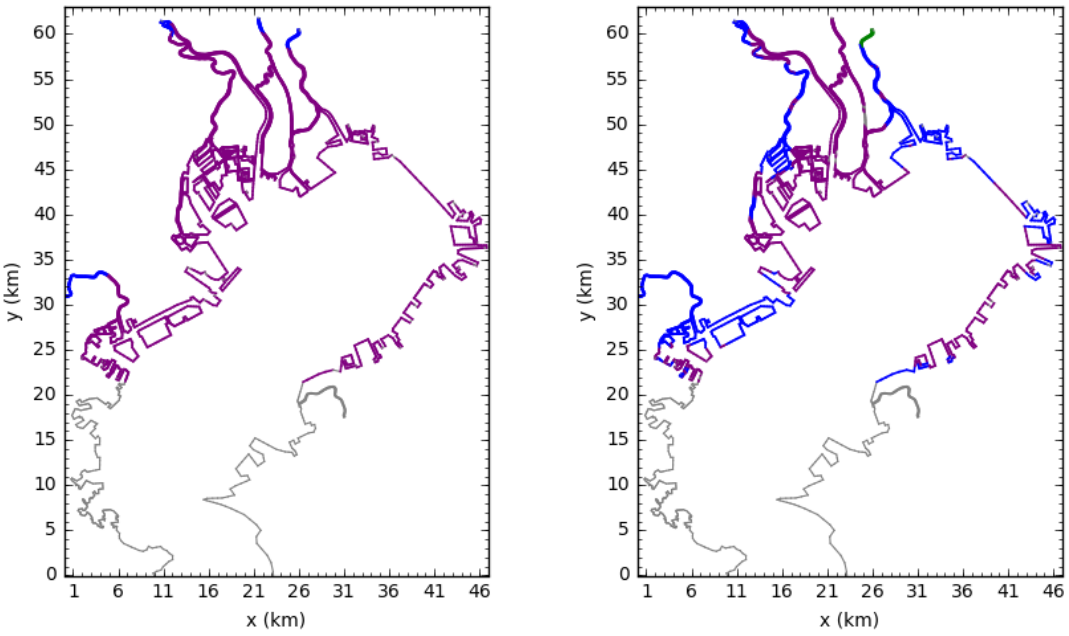

(a) (b)

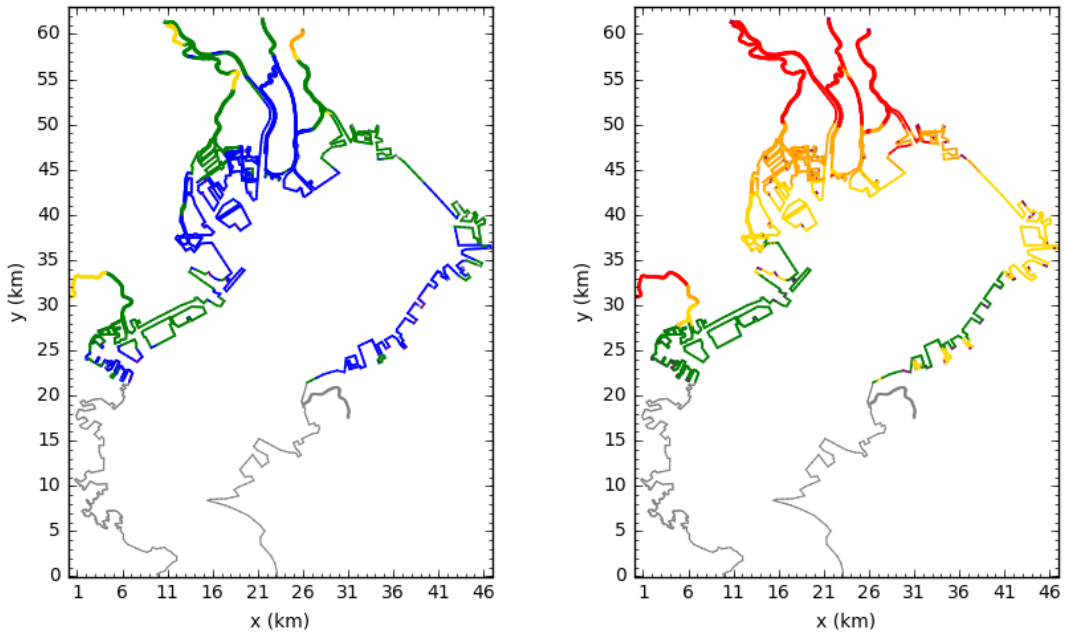

(c) (d)

Figure 6.2 Anomalies of moderate multi-hazard case and worst storm surge case (a: moderate typhoon storm surge; b: moderate earthquake tsunami; c: concurrent moderate storm surge and moderate tsunami; d: worst storm surge) (red: 3.0 m~; orange: 2.5 m~3.0 m; gold: 2.0 m~2.5 m; green: 1.5 m~2.0 m; blue: 1.0 m~1.5 m; purple: 0.5 m~1.0 m; grey: ~0.5 m)

According to the analysis in Section 5.1.2.3, combined storm surge and river flood would not result in much increase of anomaly in stations of Tokyo Bay. From the perspective of overflow volume, Figure 6.3 shows the comparison of overflow volume between single hazard (only storm surge) and multiple hazards (storm surge and river flood). By adding the river flow discharge in the upstream of Arakawa River, Nakagawa River and Edogawa River, the overflow volume increases for all cases. It could be inferred that large river discharge would only affect the riverside areas.

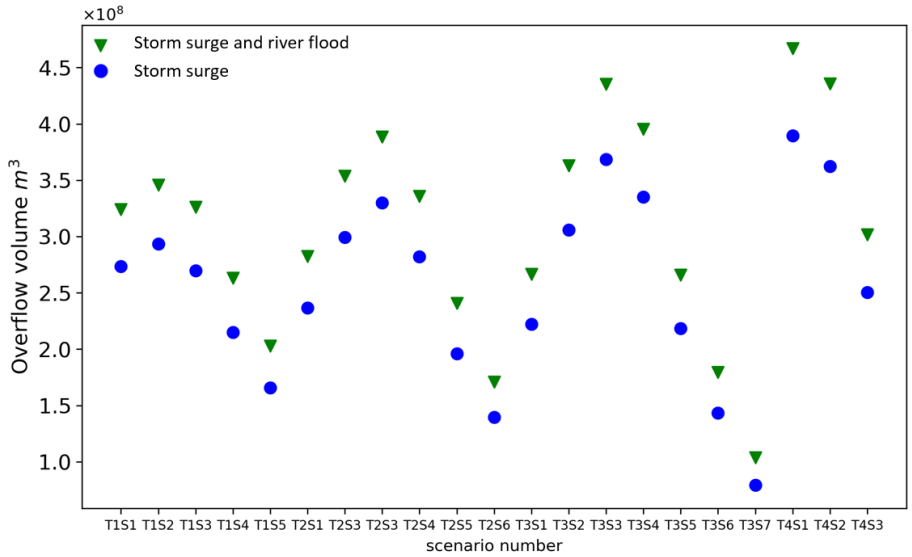

Figure 6.3 Comparison of overflow volume between single hazard (storm surge) and multiple hazards (storm surge and river flood).

Figure 6.4 shows the comparison of overflow volume for the multi-hazard cases with tsunami and without it. For both group scenarios (Group A and Group B), after adding tsunami, the overflow volume increases significantly. With the change of typhoon initial location from Location 14 to 20, the overflow volume first reaches peak at Location 15 (Scenario A9), and then gradually decreases. Combining the analysis on the anomaly difference in Figure 6.1, it may be because under the moving speed of typhoon, when it starts at Location 15, the peak storm surge happens at almost same time as the tsunami at the head of the bay. The maximum overflow volume for Group A scenarios happens in Scenario A9, in which the typhoon course is T4S1. Similarly, for Group B scenarios, the maximum overflow volume happens in Scenario B4, in which the typhoon course is also T4S1. The typhoon track T4S1 is the worst track for only storm surge, and after combing tsunami and river flood, this track still results in the maximum overflow.

Therefore, both the typhoon track and the time when tsunami happens during the typhoon movement could have a significant influence on the final overflow volume in Tokyo Bay.

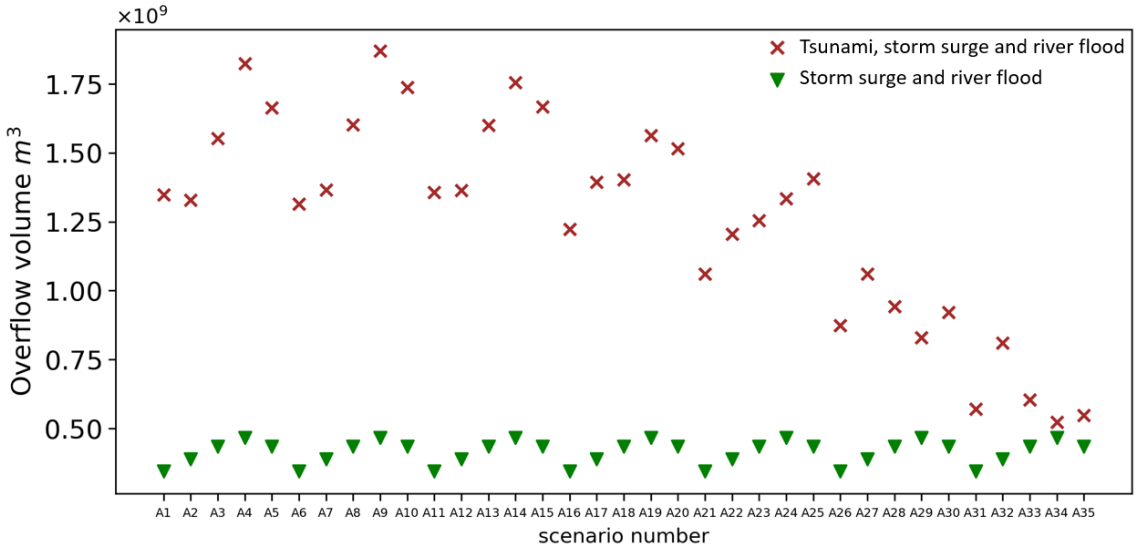

(a)

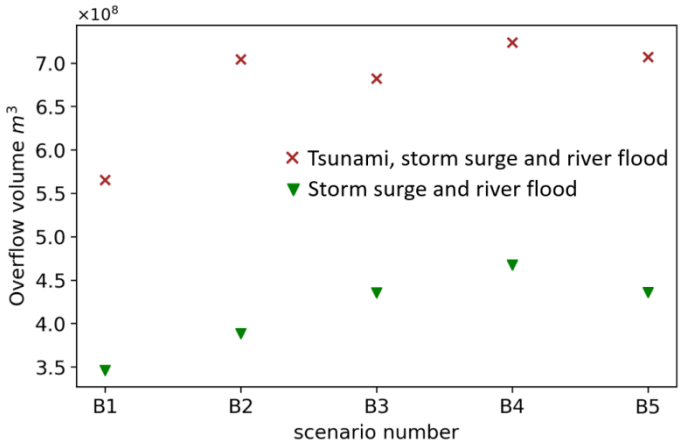

(b)

Figure 6.4 Comparison of overflow volume, (a) Group A scenarios for ToKai-ToNankai earthquake tsunami, (b) Group B scenarios for Tokyo Inland earthquake tsunami

6.2 Multi-hazard vulnerability in Tokyo Bay

Numerical assessment of multi-hazard vulnerability using FVCOM is firstly tried, which is one of the most important contributions in this study. It has been demonstrated that combined storm surge, tsunami and river flood would increase the flood hazard in the northern part of Tokyo Bay. Tokyo Metropolitan Government has elaborated detailed plans including the designing of infrastructure, e.g., sea dikes and floodgates, and the evacuation route for disaster prevention of storm surge and river flood. However, the effect of multiple hazards, especially the storm surge and tsunami, is ignored.

The return period of Kanto type earthquakes is believed to be approximately 200 years. Particularly, there is a high possibility that a ToKai-ToNankai-Nankai type earthquake would happen in the near future due to its small return period (about 120 years). Compared to the large return period of earthquake tsunami,

almost every year, in Japan, typhoon storm surge happens from July to October, and river flood is also more likely to happen in typhoon weather as it brings large amount of rainfall. Although in history, occurrence of combined tsunami and storm surge is rare, it does not mean that they would never happen in the future. In the recent typhoon (No. 19) on October 12, 2019, when it was just passing through Tokyo area at that night, an earthquake with magnitude 5.7 happened in Chiba-ken Nanto-oki. At the same time, the typhoon brought heavy rainfall, and hundreds of thousands of residents living in the Edogawa-ward were told to evacuate due to the possible river flood. Luckily, the earthquake did not generate tsunami though the epicenter location was not far from the south of Tokyo Bay mouth, but it would be reasonable to imagine that if the earthquake was big and a tsunami happened, the hazard extent in the Tokyo Bay area would be more serious. However, it should be noted that the occurrence probability of multi-hazard events quite depends on the time resolution, which means the return period of multi-hazard events is determined by the resolution of time that is used to describe the concurrent occurrence of them.

In addition, according to the 2019 IPCC Special Report on the Ocean and Cryosphere in a Changing Climate[156], frequency of Extreme Sea Level (ESL, water level heights that consist of contributions from mean sea level, storm surges and tides) events is projected to increase, and even a small increase in mean sea level can significantly augment the frequency and intensity of flooding, which is because sea level rise elevates the platform for storm surges, tides, and waves. Future rise in Global Mean Sea Level (GMSL) caused by thermal expansion, melting of glaciers and ice sheets and land water storage changes, is strongly dependent on Representative Concentration Pathway (RCP) emission scenario including RCP2.6, RCP4.5, RCP6.0, and RCP8.5. Due to projected GMSL rise, ESLs that are historically rare, e.g., today's hundred-year event, will become common by 2100. Many low-lying cities and small islands at most latitudes will experience such events annually by 2050. After an increase of sea level from 1–2 mm/year in most regions over the past century, rates of 3–4 mm/year are now being experienced that will further increase to 4–9 mm/year under RCP2.6 and 10–20 mm/year at the end of the century under RCP8.5. Nevertheless, up to 2050, uncertainty in climate change-driven future sea level is relatively small, which provides a robust basis for short-term (within 30 years) adaptation planning. GMSL will rise between 0.24 m (0.17–0.32 m, likely range) under RCP2.6 and 0.32 m (0.23–0.40 m, likely range) under RCP8.5. The combined effect of mean and extreme sea levels results in events which are rare in the historical context (return period of 100 years or larger) occurring yearly at some locations by the middle of this century under all emission scenarios. This includes areas such as the parts of the intertropical low-lying coasts that are currently exposed to storm surges only infrequently. For some locations, this change will occur as soon as mid-century for RCP8.5 and by 2100 for all emission scenarios. The affected locations are particularly located in low-latitude regions, away from the tropical cyclone tracks. In these locations, historical sea level variability due to tides and storm surges is small compared to projected mean SLR. Therefore, even limited changes in mean sea level will have a noticeable effect on ESLs, and for some locations, even RCP2.6 will lead to the annual occurrence of historically rare events by mid-century. Hence, additional adaptation is needed considering the increasing frequency of storm surge due to climate change and the resultant multi-hazard risks in future.

Drainage pipe model was integrated in FVCOM, and it was applied to the Funabashi Sanbanze Seashore Park considering the multi-hazard scenario. It has been demonstrated that the drainage system

could reduce the inundation period by draining the flood after the inundation peak period. However, some inundation would still accumulate and stay in land because of the topography. The integration of FVCOM and the drainage pipe model was another important contribution in this work. It expands the function of the original model by bridging the coastal ocean circulation, ground surface inundation and the underground drainage flow. By using triangular unstructured grid, detailed local inundation could be analyzed considering drainage systems. In the disaster mitigation planning and prediction, drainage systems should be considered. In some places like Tokyo, it has already been included, for example, the Metropolitan Area Outer Underground Discharge Channel, it is used as a reservoir to store extra water caused by heavy rainfall, but it may not be common and applicable to other areas considering its high price and difficulty of construction. Therefore, from a more practical point of view, ordinary drainage system may play such a role in draining expected flood quickly just by for example re-planning and slight improvement in order to accelerate the speed of post-disaster recovery.

Based on the research, although the moderate multi-hazard event may cause smaller damage than largest single storm surge, the damage risk of multi-hazard event and single hazard one for local coastal areas may vary due to the different spatial patterns as shown in Section 6.1. To prevent the inundation and reduce the loss caused by multiple hazards, upgrading the dike heights in some local areas such as the upstream river banks as shown in Section 6.1 where superposing method underestimates the multi-hazard anomalies may need to be considered. In view of expected increase in the frequency of multi-hazard events, policymakers should carefully consider the possible vulnerability owing to them. The function of floodgates should also be re-evaluated considering the impact of multiple hazards. Early-warning and hazard prediction system are useful tools for disaster mitigation, which has already been widely applied to typhoon storm surge, earthquake tsunami and river flood. However, the current system in the study region may not be able to directly provide the possible flood information when storm surge and tsunami happen. Moreover, for more detailed flood warning, incorporation of drainage system is needed, otherwise, it may cause large inaccuracy. Thus, the capability of multi-hazard computation combining drainage systems is necessary to provide more accurate hazard information.

6.3 Limitations of the study

Real dike height data was not available, and it was estimated by extracting from DEM. Although the estimated data was verified by comparing to the altitudes of DEM, the estimation process may be still lack of accuracy. Furthermore, different types of coastal dikes and river banks may influence the overflow process, which were not included in the present study.

The flow discharge data of the three major rivers was set as constant in the numerical simulation because the major purpose was to identify the worst multi-hazard case, and it was assumed that storm surge and tsunami happen during the peak period of river flood. However, variations of river flow discharge may affect the change of storm surge anomaly when typhoon passes.

In the verification of the efficient method for vulnerability measurement, it could only be concluded that this approach was consistent with inundation simulation method at the initial phase of overflow when the inundation at the backside of dike did not exceed the dike. As for the discrepancy after the inundation

depth became higher than the dike, this method is not applicable.

In the validation of the integrated model using the tsunami-induced pipe overflow case at Kisarazu Port, due to the lack of observation, e.g., photos taken by people to show how the overflow happened, the comparison was made by referring previous studies. If photos of overflow at that site were available, the validation would be more persuasive.

It has been proved that the drainage system could contribute to the decrease of inundation period, but it is under normal conditions. However, whether the drainage system could still work well under accident conditions, e.g., garbage accumulation, needs more investigations.

6.4 Sub-conclusion

The difference of single hazard and multiple hazards is discussed. Possible measures are discussed for better disaster prevention such as the upgrading of dike systems, enhancement of drainage systems, and incorporating the capability of predicting multi-hazard inundation in the early-warning and hazard prediction system.

7. Conclusions and Recommendations

7.1 Conclusions

To improve the accuracy of storm surge hindcasting, a practical method combining a reanalysis dataset and a parametric typhoon formula was proposed. Using the created atmospheric boundary data, hindcasting of two historical storm surges in Tokyo Bay was performed using FVCOM. Results show that the hybrid method can improve the accuracy of wind and atmospheric pressure field significantly and could be used in the areas where accurate reanalysis meteorological data is lacking.

A drainage pipe model was implemented in FVCOM source code. By using a tsunami-induced pipe overflow event in Kisarazu Port during the 2011 Tohoku earthquake tsunami, it is shown that the integrated model performs well for reproducing the inundation overflow from the drainage pipe in coastal areas.

An efficient method was proposed using an estimated overflow volume without computing inundation, which was validated by comparing with inundation simulation. It shows that when free dike overflow is dominant, this method is consistent with inundation simulation approach, while if the overflow becomes submerged type, this approach seems not applicable.

Using Tokyo Bay as a study area, the efficient method was then applied to the multi-hazard vulnerability assessment. A series of assumed typhoon courses (T7920 course, Taisho 6th year Typhoon course, Isebay Typhoon course, and 1949 Typhoon Kitty course), river discharge scenario (50-year return period), and tsunami scenarios (ToKai-ToNankai type and Kanto type) were prepared based on government reports. Results show that compared to single hazard like only tsunami, in multi-hazard case, e.g., concurrent tsunami and storm surge, the tsunami shoaling process is changed because the anomaly difference of superposing case and concurrent case varies. In most coastal areas, the anomaly of superposing case is greater than that of concurrent case, but in some places, concurrent case results in larger anomalies than superposing case, which demonstrates the interaction between storm surge and tsunami. The anomaly difference of superposing case and concurrent case is basically larger in ports and river channels than in other coastal areas. Worst storm surge would cause larger anomalies than moderate multiple hazards, in which the return period of these two types of hazards is basically identical. Superposing method is an acceptable way for analyzing multi-hazard risks compared to concurrent computation.

The role of drainage system in local coastal flood was investigated using the integrated model, which showed that the drainage pipe system could help drain the inundation so that the total inundation volume and water logging period can be reduced significantly.

For better disaster prevention, upgrading the dike heights in areas where superposing method underestimates the multi-hazard anomalies may need to be considered. The function of floodgates should also be re-evaluated considering the effect of multiple hazards. The current early-warning and hazard prediction system in the study region may not be able to directly provide the multi-hazard flood information, and for more detailed flood warning, drainage system needs to be incorporated. Thus, the capability of multi-hazard computation combining drainage systems is necessary to provide more

accurate hazard information.

7.2 Recommendations

When considering the multi-hazard influence on the coastal areas, the tide effect is usually included, while in the current study, it is excluded. Thus, it may be necessary to incorporate the tide in the numerical simulation for investigation of the tide effect on the total water level change with other hazards.

The upstream inflow in the drainage pipe system is estimated based on an average runoff depth calculation because the study area is a small region, the spatial variation of rainfall on the runoff volume in different upstream pipe inlets is believed to be negligible. However, it may be necessary to consider the routing process of rain water on the land surface when the study area covers a large domain or it is somewhere the rainfall varies significantly in space, e.g., the mountain area.

For the interaction of storm surge and tsunami, since tsunami period is also one of the important factors in determining the amplification effect in ports. More numerical investigations are needed to identify the relations between the tsunami period and anomaly difference between multi-hazard case and superposing case.

References

[1] Miyazaki, M. Study of Storm Surge. Seizando Publishing, ISBN4-425-51181-6, 134pp (in Japanese) (2003).

[2] Hoshino, S., Esteban, M., Mikami, T. & Takagi, H. Estimation of increase in storm surge damage due to climate change and sea level rise in the Greater Tokyo area. *Nat Hazards.*, **80**(1), 539-565 (2016).

[3] Kawai, H., Hashimoto, N. & Matsuura, K. Improvement of stochastic typhoon model for the purpose of simulating typhoons and storm surges under global warming. Proc. 30th Int. Conf. Coast. Eng. (ICCE2006), **2**, 1838-1850 (2006).

[4] Tokyo Metropolitan Government, Kanagawa Prefectural Government and Chiba Prefectural Government, 2004. "Tokyo Bay Basic Plan on Coastal Management (in Japanese)".

[5] Hatori, T. Behaviors of the 1703 Genroku Kanto, the 1854 Ansei Tokai and other tsunamis along the coast of the Tokyo Bay to Uraga Strait. *Rekishijisin*, **21**, 37-45 (in Japanese) (2006).

[6] Yasuda, T. & Hiraishi, T. Experimental study of tsunami inundation in coastal urban area. *Proc. 14th Int. Offshore and Polar Eng. Conf.*, 740-746 (2004).

[7] Sasaki, J. *et al.* Behavior of the 2011 Tohoku earthquake tsunami and resultant damage in Tokyo Bay. *Coast. Eng. J.*, **54**(1), 1250012 (2012).

[8] Wiyono, R. U. A., Sasaki, J. & Suzuki, T. Numerical assessment of the 2011 Tohoku earthquake tsunami in ports of Tokyo Bay with the effectiveness of floodgates. *J. Coastal Res.*, **65**(SI), 844-849 (2013).

[9] Japan Meteorological Agency (https://www.jma.go.jp/jma/indexe.html).

[10] Zheng, L. Y., Weisberg, R. H., Huang, Y. et al. Implications from the comparisons between two- and three- dimensional model simulations of the Hurricane Ike storm surge. *Journal of Geophysical Research: Oceans*, **118**, 3350-3369 (2013).

[11] Takabatake, T. et al. Field survey of 2018 Typhoon Jebi in Japan: lessons for disaster risk management. *Geosciences*, **8**(11), 19pp (2018).

[12] Trenberth, K. E. Warmer Oceans, Stronger Hurricanes. *Scientific American*, vol. 297, 44-51 (2007).

[13] Bender, M. A. et al. Modeled impact of anthropogenic warming on the frequency of intense Atlantic hurricanes. *Science*, vol. 327, 454-458 (2010).

[14] Disaster Management in Japan. Cabinet Office, Government of Japan (2015).

[15] Shimazaki, K. et al. Geological evidence of recurrent great Kanto earthquakes at the Miura Peninsula, Japan. *Journal of Geophysical Research*, **116**, 16pp (2011).

[16] Shishikura, M. History of the paleo-earthquakes along the Sagami Trough, central Japan: review of coastal paleoseismological studies in the Kanto region. *Episodes*, **37**(4), 246-257 (2014).

[17] Hino, M. & Hino, K. Response characteristics of Tokyo Bay to incident long waves. *Coast. Eng. Jpn.* **8**, 57-69.

[18] Takayama, T., Nagai, N. & Hiraishi, T. The numerical calculation of tsunami in Tokyo Bay. Technical Note of the Port and Harbor Research Institute, Ministry of Transport, Japan, 100pp (1983). (in Japanese).

[19] Yasuda, T. & Hiraishi, T. Experimental study of tsunami inundation in coastal urban area. *Proc, 14th Int. Offshore and Polar Engrg. Conf.*, 740-746 (2004).

[20] Yasuda, T. & Hiraishi, T. Experimental risk assessment of tsunami inundation in coastal urban area. *Rep. Port Airport Res. Inst*. **42**(3), 46pp (2003). (in Japanese).

[21] Chen, C., Liu, H. & Beardsley, R. C. An unstructured, finite-volume, three-dimensional primitive equation ocean model application to coastal ocean and estuaries. *J. Atmospheric and Oceanic Technology*, **20**(1), 159-186 (2003).

[22] Hervouet, J. M. Telemac modeling system: an overview. *Hydrological Processes*, **14**(13), 2209-2210 (2000).

[23] Blumberg, A. F., Mellor, G. L. A description of a three-dimensional coastal ocean circulation model. *Three Dimensional Coastal Ocean Models*, 1-16 (1987).

[24] Blumberg, A. F. A primer for ECOM-si, technical report. HydroQual, Mahwah, N. J., 66pp (1994).

[25] Haidvogel, D. B., Beckmann, A. Numerical Ocean Circulation Modelling. Imperial College Press, London, 318pp (1999).

[26] Chen, C., et al. A finite volume numerical approach for coastal ocean circulation studies: Comparison with finite difference models. *Journal of Geophysical Research*, **112**, 34pp (2006).

[27] Delft3D-Flow, Simulation of Multi-Dimensional Hydrodynamic Flows and Transport Phenomena, Including Sediments, User Manual (2014).

[28] Westerink, J. J. et al. ADCIRC: an advanced three-dimensional circulation model for shelves, coasts, and estuaries (2006).

[29] Warren, I. R. & Bach, H. K. MIKE 21: a modelling system for estuaries, coastal waters and seas. *Environmental Software*, **7**(4), 229-240 (1992).

[30] Rossman, L. A. Storm Water Management Model User's Manual version 5.0 (2010).

[31] Wallingford Software, Nfoworks CS, version 7.5, Documentation, Wallingford, Oxfordshire, England (2006).

[32] DHI (Danish Hydraulic Institute): MIKE Urban User Manual, Denmark, 240pp (2012).

[33] Brian, R. et al. Hydrological Simulation Program-Fortran User's Manual for version 11 (1997).

[34] Alley, W. M. & Smith, P. E. Distributed routing rainfall runoff model version II. U. S. Geological Survey Open File Report, 82-344, 201p (1982).

[35] Mizuhashi, K. et al. Development of tsunami inundation model with effects of underground pipelines. *Coastal Engineering Journal of Japan*, **69**(2), 396-400 (2012).

[36] ITO, K. et al. Simulation of inundation caused by tsunami via underground channels. *Coastal Engineering*, 13pp (2012).

[37] Takabatake, T. et al. Simulation of inundation disasters by tsunami via underground drainage channel network. *Proc. 24th International Ocean and Polar Engineering Conference, ISOPE Busan. International Society of Offshore and Polar Engineers*, 17-28 (2014).

[38] Takabatake, T. et al. Integrated simulation for tsunami overflow from water channel network and inland inundation. *Coastal Engineering Journal of Japan*, **71**(2), 521-526 (2015).

[39] Takabatake, T. & Shibayama, T. Study on the risks of tsunami inundation via underground pipelines. *Asian and Pacific Coast*, 268-279 (2018).

[40] Natural Disasters and Vulnerability Analysis. Office of the United Nations Disaster Relief Co-ordinator (1979).

[41] Birkmann, J. et al. Framing vulnerability, risk and societal responses: the MOVE framework. *Nat Hazards.*, **67**, 193-211 (2013).

[42] David, K. & Colin, Macgregor. Using social indicators to measure community vulnerability to natural hazards. *Australian Journal of Emergency Management*, **15**(3), 52-57 (2000).

[43] Dominey-Howes, D. & Papathoma, M. Validating a tsunami vulnerability assessment model (the PTVA model) using field data from the 2004 Indian ocean tsunami. *Nat Hazards.*, **40**(1), 113-136 (2007).

[44] Dias, WPS et al. Tsunami vulnerability functions from field surveys and Monte Carlo simulation. *Civ Eng Environ Syst*, 26, 181-194 (2009).

[45] Koshimura, S. et al. Tsunami Fragility: a new measure to assess tsunami damage. *J. Disaster Res.*, **4**, 479-488 (2009).

[46] Leone, F. et al. A spatial analysis of the December 26th, 2004 tsunami-induced damages: lessons learned for a better risk assessment integrating buildings vulnerability. *Appl Geogr.*, **31**, 363-375 (2011).

[47] Suppasri, A. et al. Field survey and damage characteristic of the 2011 Tohoku tsunami in Miyagi prefecture. *Coast Eng J*., **54**, 1250005 (2012a).

[48] Suppasri, A. et al. Developing tsunami fragility curves from the surveyed data of the 2011 Great East Japan tsunami in Sendai and Ishinomaki Plains. *Coast Eng J*., **54**, 1250008 (2012b).

[49] Suppasri, A. et al. Building damage characteristics based on surveyed data and fragility curves of the 2011 Great East Japan tsunami. *Nat Hazards.*, **66**, 319–341 (2013).

[50] Valencia, N. et al. New tsunami damage functions developed in the framework of SCHEMA project: application to European-Mediterranean coasts. *Nat Hazards Earth Syst Sci*., **11**, 2835–2846 (2011).

[51] Papathoma, M. & Dominey-Howes, D. Tsunami vulnerability assessment and its implications for coastal hazard analysis and disaster management planning, Gulf of Corinth, Greece. *Nat Hazards Earth Sys Sci*., **3**, 733–747 (2003).

[52] Papathoma, M. et al. Assessing tsunami vulnerability, an example from Herakleio, Crete. *Nat Hazards Earth Syst Sci.*, **3**, 377–389 (2003).

[53] Benchekroun, S. et al. Tsunami impact and vulnerability in the harbor area of Tangier, Morocco. *Geomatics, Natural Hazards and Risk*, **6**(8), 718-740 (2015).

[54] Omira, R. et al. Tsunami vulnerability assessment of Casablanca Morocco using numerical modelling and GIS tools. *Nat Hazards.*, **54**, 75–95 (2101).

[55] Shimozono, T., Sato, S. Coastal vulnerability analysis during tsunami-induced levee overflow and breaching by a high-resolution flood model. *Coastal Engineering*, **107**, 116-126 (2016).

[56] Valchev, N. et al. Assessment of vulnerability to storm induced flood hazard along diverse coastline settings. *3rd European Conference on Flood Risk Management*, 7, 11pp (2016).

[57] Rana, M. S. et al. Vulnerability assessment of cyclonic hazards in coastal region of Bangladesh. *Urban and Regional Planning*, **3**(2), 34-43 (2018).

[58] Sajjad, M. et al. Assessing hazard vulnerability, habitat conservation, and restoration for the

enhancement of mainland China's coastal resilience. *Earth's Future*, **6**, 326-338 (2018).

[59] Park, S. J. and Lee, D. K. A stochastic approach to coastal multi-hazard risk analysis in South Korea. Geophysical Research Abstracts, **21**, (2019).

[60] Rao, A. D. et al. Vulnerability from storm surges and cyclone wind fields on the coast of Andhra Pradesh, India. *Nat Hazards.*, **41**, 515-529 (2007).

[61] Lapidez, J. P. et al. Identification of storm surge vulnerable areas in the Philippines through the simulation of Typhoon Haiyan-induced storm surge levels over historical storm tracks. *Nat Hazards Earth Syst Sci.*, **3**, 919-939 (2015).

[62] Lee, G. et al. Multi-criteria surge vulnerability assessment with long-term reanalysis. *Journal of Coastal Research*, **75**, 1172-1176 (2016).

[63] Yuan, S. et al. Integrated weighting technique for coastal vulnerability to storm surges. *Journal of Coastal Research*, **80**, 6-12 (2017).

[64] Kunte, P. D. Multi-hazards coastal vulnerability assessment of Goa, India, using geospatial techniques. *Ocean Coast. Manage.*, **95**, 264-281 (2014).

[65] Rahman, M. M. et al. Multi-hazard vulnerability assessment of an urban area: A case study on ward 34 of Dhaka south city corporation. *J. Asiat. Soc. Bangladesh, Sci.* **43**(2), 181-195 (2017).

[66] Vivek, G. et al. Multi-hazard vulnerability assessment along the coast of Visakhapatnam, north-east coast of India. *Living Planet Symposium, Proceedings of the conference in Prague*, **740**, 10pp (2016).

[67] Islam, M. A. et al. Coastal multi-hazard vulnerability assessment along the Ganges deltaic coast of Bangladesh-A geospatial approach. *Ocean & Coastal Management*, **127**, 1-15 (2006).

[68] Depietri, Y. et al. Multi-hazard risks in New York city. *Nat. Hazards Earth Syst. Sci*., **18**, 3363-3381 (2018).

[69] Clarke, J., Obrien, E. A multi-hazard risk assessment methodology, stress test framework and decision support tool for transport infrastructure networks. *6th Transport Research Arena*, 18-21 (2016).

[70] Mulyani, R. et al. A multi-hazard risk assessment of buildings in Padang city. *The 5th International Conference of Euo Asia Civil Engineering Forum*, **125**, 1094-1100 (2015).

[71] Appelquist, L. R., Balstrom, T. Application of the coastal hazard wheel methodology for coastal multi-hazard assessment and management in the state of Djibouti. *Climate Risk Management*, **3**, 79-95 (2014).

[72] Appelquist, L. R., Balstrom, T. Application of a new methodology for coastal multi-hazard-assessment & management on the state of Karnataka, India. *Journal of Environmental Management*, **152**, 1-10 (2015).

[73] Sahoo, B., Bhaskaran, P. K. Multi-hazard risk assessment of coastal vulnerability from tropical cyclones-A GIS based approach for the Odisha coast. *Journal of Environmental Management*, **206**, 1166-1178 (2018).

[74] Mahendra, R. S. et al. Coastal multi-hazard vulnerability mapping: A case study along the coast of Nellore district, east coast of India. *Italian Journal of Remote Sensing*, **42**(3), 67-76 (2010).

[75] Eshrati, L. et al. Multi hazard vulnerability analysis: The casualty model and its implementation. *International Journal of Health System and Disaster Management*, **3**(3), 177-183 (2015).

[76] Kumar, T. S. et al. Coastal vulnerability assessment for Orissa state, east coast of India. *Journal of*

Coastal Research, **26**(3), 523-534 (2010).

[77] Wiley, K. A. S. and Gianotti, A. G. S. Risk perception in a multi-hazard environment. *World Development*, **97**, 138-152 (2017).

[78] Furlan, E. et al. Spatially explicit risk approach for multi-hazard assessment and management in marine environment: The case study of the Adriatic Sea. *Science of the Total Environment*, **618**, 1008-1023 (2018).

[79] Mukhtar, R. Review of national multi-hazard early warning system plan of Pakistan in context with Sendai framework for disaster risk reduction. *7th International Conference on Building Resilience*, **212**, 206-213 (2018).

[80] Haigh, R. et al. A capacity analysis framework for multi-hazard early warning in coastal communities. *7th International Conference on Building Resilience*, **212**, 1139-1146 (2018).

[81] Gallina, V. et al. A review of multi-risk methodologies for natural hazards: consequences and challenges for a climate change impact assessment. *Journal of Environmental Management*, **168**, 123-132 (2016).

[82] Johnson, K. et al. Multi-hazard risk assessment of two Hong Kong districts. *Centro Euro-Mediterraneo sui Cambiamenti Climatici*, 43pp (2015).

[83] Borg, R. P. et al. The Android case study; Venice and its territory: vulnerability and resilience in multi-hazard scenarios. *4th International Conference on Building Resilience*, **18**, 825-836 (2014).

[84] Ahammed, K. K., Pandey, A. C. Geoinformatics based assessment of coastal multi-hazard vulnerability along the east coast of India. *Spatial Information Research*, **27**(3), 295-307 (2019).

[85] Maryam, M. B. et al. A spatial vulnerability analysis of multi-hazard threat in Zayandeh-Roud basin in Isfahan, Isfahan province, Iran. *Journal of Environmental Chemistry and Toxicology*, **2**(1), 12-19 (2018).

[86] Younus, M. A. F., Sharna, S. S. Combination of community-based vulnerability and adaptation to storm surges in coastal regions of Bangladesh. *Journal of Environmental Assessment Policy and Management*, **16**(4), 36pp (2014).

[87] Matsuda, I. Verifying vulnerability to natural disasters in Tokyo. *Journal of Geography*, **122**(6), 1070-1087 (2013) (in Japanese).

[88] Takabatake, T., Shibayama, T. Predicting the risk of storm surge and tsunami in Tokyo Port. *Journal of Japan Society of Civil Engineering*, **68**(2), 894-899 (2012) (in Japanese).

[89] Tatekoji, A. et al. Influence of historical bathymetry changes due to urbanization on the vulnerability of storm surge in Tokyo Bay. *Coastal Engineering*, 12pp (2012).

[90] Hirano, K. et al. Prediction of typhoon storm surge flood in Tokyo Bay using unstructured model ADCIRC under global warming scenario. *Proceedings of the ASME 2014 4th Joint US-European Fluids Engineering Division Summer Meeting and 12th International Conference on Nanochannels, Microchannels, and Minichannels*, 11pp (2014).

[91] Ishikawa, T., Akoh, R. Assessment of flood risk management in lowland Tokyo areas in the seventeenth century by numerical flow simulations. *Environmental Fluid Mechanics*, 13pp (2018).

[92] Bureau of Port and Harbor, Tokyo Metropolitan Government. (http://www.kouwan.metro.tokyo.jp/)

[93] Bureau of Construction.

(http://www.kensetsu.metro.tokyo.jp/)

[94] Chiba Prefecture Government Report (https://www.pref.chiba.lg.jp/kakan/shinsui/takashio.html) (2018).

[95] Cowles, G. Parallelization of the FVCOM coastal ocean model. *Int. J. High Performance Computing*, **22**(2), 177-193 (2008).

[96] Chen, C. et al. A finite volume numerical approach for coastal ocean circulation studies: comparison with finite difference models. *Journal of Geophysical Research*, **112**, 34pp (2007).

[97] Huang, H. et al. FVCOM validation experiments: comparisons with ROMS for three idealized barotropic test problems. *Journal of Geophysical Research*, **113**, 14pp (2008).

[98] Large, W. G. & Pond, S. Open ocean momentum flux measurements in moderate to strong winds. *Journal of Physical Oceanography*, **11**(3), 324-336 (1981).

[99] Blumberg, A. F. & Khanta, L. H. Open boundary conditions for circulation models. *J. Hydraul. Eng*, **111**(2), 237-255 (1985).

[100] Okada, Y. Surface deformation due to shear and tensile faults in a half-space. *Bulletin of the Seismological Society of America*, **75**(4), 1135-1154 (1985).

[101] Takahashi, K. Distribution of pressure and wind in a typhoon. *J. Meteorological Soc. Japan*, **17**(2), 417-421 (1939).

[102] Fujita, T. Pressure distribution within typhoon. *Geophysical Magazine*, **23**(4), 437-451 (1952).

[103] Jelesnianski, C. P. A numerical calculation of storm surges induced by a tropical storm impinging on a continental shelf. *Monthly Weather Review*, **93**(6), 343-358 (1965).

[104] Myers, V. A. Maximum hurricane winds. *Bulletin of the American Meteorological Soc.*, **38**(4), 227-228 (1957).

[105] Mitsuta, Y. & Fujii, T. Analysis and synthesis of typhoon wind pattern over Japan. *Bulletin of the Disaster Prevention Res. Inst., Kyoto Univ.*, **37**(4), 169-185 (1987).

[106] Holland, G. J. An analytic model of the wind and pressure profiles in Hurricanes. *Monthly Weather Review*, **108**(8), 1212-1218 (1980).

[107] Graham, H. E. & Nunn, D. E. Meteorological Conditions Pertinent to Standard Project Hurricane. Atlantic and Gulf Coasts of United States, Weather Bureau, U.S. Department of Commerce, Washington, D.C (1959).

[108] Knaff, J. A. *et al.* Statistical tropical cyclone wind radii prediction using climatology and persistence. *Weather Forecast*, **22**(4), 781-791 (2007).

[109] Kato, F. Study of storm surge risk assessment. *National Institute for Land and Infrastructure Management Reports* (2005).

[110] Kistler, R. *et al.* The NCEP–NCAR 50-year reanalysis: monthly means CD-ROM and documentation. *Bulletin of the American Meteorological Soc.*, **82**, 247–267 (2001).

[111] Saha, S. *et al.* The NCEP climate forecast system reanalysis. *Bulletin of the American Meteorological Soc.*, **91**, 1015–1057 (2010).

[112] Uppala, S. M. *et al.* The ERA-40 re-analysis. *Quarterly J. Royal Meteorological Soc.*, **131**(612), 2961–3012 (2005).

[113] Kiss, P. & Jánosi, I. M. Comprehensive empirical analysis of ERA-40 surface wind speed distribution

over Europe. *Energy Conversion and Management*, **49**(8), 2142–2151 (2008).

[114] Onogi, K. *et al.* The JRA-25 Reanalysis. *J. Meteorological Soc. Japan*, **85**, 369-432 (2007).

[115] Kobayashi, C. & Iwasaki, T. Brewer-Dobson circulation diagnosed from JRA-55. *J. Geophys. Res.: Atmospheres*, **121**(4), 1493-1510 (2016).

[116] Cavaleri, L. & Sclavo, M. The calibration of wind and wave model data in the Mediterranean Sea. *Coast. Eng.*, **53**(7), 613-627 (2006).

[117] Signell, R. P. *et al.* Assessment of wind quality for oceanographic modeling in semi-enclosed basins. *J. Marine Systems*, **53**(1-4), 217-233 (2005).

[118] Chao, Y. Y., Alves, J. H. G. M. & Tolman, H. L. An operational system for predicting hurricane-generated wind waves in the North Atlantic Ocean. *Weather and Forecasting*, **20**, 652-671 (2005).

[119] Shao, Z. X., Liang, B. C., Li, H. J., Wu, G. X. & Wu, Z. H. Blended wind fields for wave modeling of tropical cyclones in the South China Sea and East China Sea. *Applied Ocean Res.*, **71**, 20-33 (2018).

[120] Pan, Y., Chen, Y. P., Li, J. X. & Ding, X. L. Improvement of wind field hindcasts for tropical cyclones. *Water Sci. and Eng.*, **9**(1), 58–66 (2016).

[121] Chen, C. *et al.* Extratropical storm inundation testbed: Intermodel comparisons in Scituate, Massachusetts. *J. Geophys. Res.: Oceans*, **118**(10), 1-20 (2013).

[122] Sun, Y. F. *et al.* Impact of current-wave interaction on storm surge simulation: A case study for Hurricane Bob. *J. Geophys. Res.: Oceans*, **118**(5), 2685-2701 (2013).

[123] Yoon, J. J., Shim, J. S., Park, K. S. & Lee, J. C. Numerical experiments of storm winds, surges, and waves on the southern coast of Korea during Typhoon Sanba: the role of revising wind force. *Nat Hazards Earth Syst Sci.*, **14**(12), 3279-3295 (2014).

[124] Rego, J. & Li, C. Storm surge propagation in Galveston Bay during Hurricane Ike. *J. Marine Systems*, **82**(4), 265-279 (2010).

[125] Aoki, A. & Isobe, A. Application of finite volume coastal ocean model to hindcasting the wind-induced sea level variation in Fukuoka Bay. *J. Oceanography*, **63**(2), 333-339 (2007).

[126] Ma, Z., Han, G. & Young, B. Modelling the response of Placentia Bay to hurricanes Igor and Leslie. *Ocean Modelling*, **112**, 112-124 (2017).

[127] Ding, Y. & Ding, L. A numerical simulation of extratropical storm surge and hydrodynamic response in the Bohai Sea. *Discrete Dynamics in Nat. and Soc.*, **2014**, 8pp (2014).

[128] Japan Coast Guard. (http://www1.kaiho.mlit.go.jp/)

[129] JODC (2013).
(Available: http://www.godac.jamstec.go.jp/bismal/j/JODC_J-DOSS)

[130] Tajima, Y. et al. Study on locally varying inundation characteristics induced by super Typhoon Haiyan. Part 1: Dynamic behavior of storm surge and waves around San Pedro Bay. *Coast. Eng. J.*, **58**(1), 29 pp (2016).

[131] Jaffe, B. et al. Uncertainty in tsunami sediment transport modeling. *Journal of Disaster Research*, **11**(4), 647-660 (2016).

[132] Kanamori, H. Quantification of earthquakes. *Nature*, **271**, 411-414 (1978).

[133] Hanks, T. C. & Kanamori, H. A moment magnitude scale. *Journal of Geophysical Research*, **84**, 2348-2350 (1979).

[134] Iida, K. Earthquake energy and earthquake faults. *J. Earth Sci*., **7**, 98-107 (1959).

[135] Cunge, J. A. & Wegner, M. Numerical integration of barre de Saint-Venant flow equations by means of an implicit scheme of finite differences. *La Houille Blanche*, **1**, 33-39 (1964).

[136] Cunge, J. A. & Mazaudou, B. Mathematical modeling of complex surcharged systems: difficulties in computation and simulation of physical situations. *Proc. Int. Conf. on Urban Storm Drainage, 3rd. P. Balmer, P. A. Malmquist and A. Sjoberg, (eds)*. *Chambers Univ. of Technology, Goteborg, Sweden*, 363-373 (1984).

[137] Fread, D. L. An implicit dynamic wave model for mixed flows in storm drainage networks. *Proc. Intern. Symp. Urban Hydrol., Hydraul., and Sediment Control, Univ. of Kentucky, Lexington, Kentucky*, 215-222 (1984).

[138] Courant, R. et al. Uber die partiellen differenzengleichungen der mathematischen physic. *Mathematische Annalen | Mathematische*, **43**, 32-74 (1927).

[139] Cunge, J. A. Rapidly varying flows in power and pumping canals, unsteady flow in open channels. Ed by K. Mahmood and V. Yevjevich, Vol II, *Water Resource Publications, Ft. Collins, Colorado*, 539-562 (1975).

[140] Amein, M., Chu, H. Implicit numerical modeling of unsteady flows. *Journal of Hydraulics Division*, **101**(6), 717-731 (1975).

[141] Amein, M., Fang, C. S. Implicit flood routing in natural channels. *Journal of Hydraulics Division*, **96**(12), 2481-2500 (1970).

[142] Fread, D. L. Numerical properties of implicit four point finite difference equations of unsteady flow. *NOAA Technical memorandum NWS HYDRO*, **18**, NOAA.

[143] Fread, D. L. National weather service operational dynamic wave model. *National Weather Service*, NOAA.

[144] Schaffarnek, R. W., Baltzer, R. A., Goldberg, D. E. A model for simulation of flows in singular and interconnected channels. *Techniques of Water-Resources Investigation Report, Chapter C3, U.S. Geological Survey, Denver*.

[145] Wylie, E. B. & Streeter, V. L. Fluid transients. *Feb Press, Ann Arbor, Michigan*. 384 (1982).

[146] Koshimura, S., Hayashi, S., Gokon, H. The impact of the 2011 Tohoku earthquake tsunami disaster and implications to the reconstruction. *Solids and Foundations*, **54**(4), 560-572 (2014).

[147] Fujii, Y. et al. Tsunami source of the 2011 off the pacific coast of Tohoku earthquake. *Earth, Planets and Space*, **63**, 815-820 (2011).

[148] MANI MURALI, R. et al. Coastal vulnerability assessment of Puducherry coast, India, using the analytical hierarchical process. *Nat Hazards Earth Syst Sci.*, **13**(12), pp. 3291-3311 (2013).

[149] RANA, M.S. et al. Vulnerability Assessment of Cyclonic Hazards in Coastal Region of Bangladesh. *Urban and Regional Planning*, **3**(2), 34pp (2018).

[150] RUŽIĆ, I. et al. Assessment of the Coastal Vulnerability Index in an Area of Complex Geological Conditions on the Krk Island, Northeast Adriatic Sea. *Geosciences*, **9**(5), 17pp (2019).

[151] SAJJAD, M. et al. Assessing hazard vulnerability, habitat conservation, and restoration for the

enhancement of mainland China's coastal resilience. *Earth's Future*, **6**(3), pp. 326-338 (2018).

[152] TRAGAKI, A. et al. Coastal hazard vulnerability assessment based on geomorphic, oceanographic and demographic parameters: The case of the Peloponnese (Southern Greece). *Land*, **7**(2), 16pp (2018).

[153] VALCHEV, N. et al. Assessment of vulnerability to storm induced flood hazard along diverse coastline settings, *E3S Web of Conferences 2016*, *EDP Sciences*, 11pp (2016).

[154] CHANG, C. et al. Hazard Assessment of Typhoon-Driven Storm Waves in the Nearshore Waters of Taiwan. *Water*, **10**(7), 20pp (2018).

[155] YOON, J. and SHIM, J. Estimation of storm surge inundation and hazard mapping for the southern coast of Korea. *Journal of Coastal Research*, **65**(sp1), pp. 856-862 (2013).

[156] IPCC Special Report on the Ocean and Cryosphere in a Changing Climate, 2019. (https://www.ipcc.ch/srocc/)

Publications

Hybrid methods combining atmospheric reanalysis data and a parametric typhoon model to hindcast storm surges in Tokyo Bay. *Scientific Reports*, 9, 12222, 2019.

Appendix

Note: The Fortran code below is the drainage pipe model that is integrated in FVCOM.

```
module mod_par_drainage
real(8), allocatable, save :: xq(:),xqold(:)
real(8), allocatable, save :: AA(:,:),A(:,:),R(:,:),RR(:,:),bb(:,:),b(:,:)
real(8), allocatable, save :: ffnew(:,:),fi(:,:),ffi(:,:),SSf(:),Sf(:)
real(8), allocatable, save :: AAs(:,:),RRs(:,:),bbs(:,:),ffis(:,:),ssfs(:)
real(8), allocatable, save :: f(:)
real(8) :: qx1
real(8), allocatable, save :: qin(:),qin1(:),qin_new(:,:)
real(8) dt, sigma
real(8) :: exdt, outdt, tot
integer :: nt_s, num, m2, num_p
real(8), parameter :: g=9.81
integer :: num_fv
real(8),allocatable,save :: LL(:), di(:), soo(:), mann(:), drop(:) !di(:): the bottom width
real(8) :: x1, x2, da
integer :: num_slot ! record the time of surcharge
logical :: flag_cir
real(8) :: h_out ! in fvcom.F and mod_gw_load; mod_funcv
real(8), allocatable, save :: gwdis1(:)
end module mod_par_drainage
```

```
module mod_gw_load
use all_vars, only: iint, iext, gwdis_g1
use mod_par_drainage, only: outdt, exdt
use mod_main
implicit none

contains
subroutine gw_load
integer :: i, gw_num, gw_num1
integer, allocatable, save :: manhole(:)
integer :: n_dis_line1, stat_dis1
character(len=80) :: buffer1
real(8) :: flux0(1)

!==================then, below to cal. control number===========
gw_num=((iint-1)*10+iext)
gw_num1=int(gw_num*1.0/(outdt*1.0/exdt))
!==================then, depending on the control number, call drainage==
if (Mod(gw_num*1.0, outdt/exdt)==0) then
   write(80,*) '==below starts content of big loop at step = ',gw_num1, '====='
   write(80, *) 'In mod_gw_load, gw_num1 is :', gw_num1
   call drainage1(gw_num1, flux0)
!==========readin manhole node num====
   n_dis_line1=0
   open(103,file='0pipe_node_num.txt')
   do while(.true.)
      read(103, fmt='(a79)', iostat=stat_dis1) buffer1
      if (stat_dis1==0) then
         n_dis_line1 = n_dis_line1 + 1
      else if (stat_dis1>0) then
         write(*,*) 'There is something wrong with reading, check your data!'
      else
         exit
      end if
   end do
   close(103)

   allocate(manhole(n_dis_line1))
   open(103,file='0pipe_node_num.txt')
   do i=1,size(manhole)
```

```
      read(103,*) manhole(i)
    end do
    close(103)

    do i = 1, size(manhole)
      gwdis_g1(manhole(i)) = flux0(1)/size(manhole)
    end do
    write(80,*) 'In gw_load, flux0 is :', flux0
    write(80,*) '======== one drainage loop content end ====='

    deallocate(manhole)

  end if

  end subroutine gw_load
  end module mod_gw_load
```

```
module mod_main
use mod_par_drainage
use mod_intrpl
use mod_funcv
use mod_newton

implicit none

contains
subroutine drainage1(gw_num1, flux2)

integer :: i,j,k,z,gw_num1
real(8) :: fq,tol=1e-5
character(len=80) :: filename, form, buffer
integer :: n_dis_line, stat_dis
real(8) :: flux2(1), h_out1(49), mhele(2)

flux2=0.0
flag_cir=.false.

num_p=1
num_fv=4

dt=outdt
n_dis_line=0
open(3010,file='0input_dis.txt')
do while(.true.)
   read(3010, fmt='(a79)', iostat=stat_dis) buffer
   if (stat_dis==0) then
      n_dis_line = n_dis_line + 1
   else if (stat_dis>0) then
      write(*,*) 'There is something wrong with reading, check your data!'
   else
      exit
   end if
end do
close(3010)

allocate(qin(n_dis_line))
open(3010,file='0input_dis.txt')
```

```
do i=1,size(qin)
   read(3010,*) qin(i)
end do
close(3010)

m2=size(qin)
nt_s=int(3600./dt)
num=m2+(m2-1)*(nt_s-1)

allocate(f(num_fv), xq(num_fv), xqold(num_fv))
allocate(AA(num_p,2),A(num_p,2),R(num_p,2),RR(num_p,2),bb(num_p,2),b(num_p,2),ffnew(num_p,2)
,fi(num_p,2),ffi(num_p,2),ssf(num_p),sf(num_p))
allocate(LL(num_p),di(num_p),soo(num_p),mann(num_p),drop(num_p))
allocate(qin_new(nt_s,m2-1),qin1(num))

!==========data interpolation=========
call intrpl(qin,nt_s,m2,qin1)
!==================end================
open(3021,file='0input_LL.txt')
do i=1,size(LL)
   read(3021,*) LL(i)
end do
close(3021)

open(3022,file='0input_di.txt')
do i=1,size(di)
   read(3022,*) di(i)
end do
close(3022)

open(3023,file='0input_soo.txt')
do i=1,size(soo)
   read(3023,*) soo(i)
end do
close(3023)

mann=0.013
drop=0.

da=0.3*50.0
```

```
!=======parameter setting=======
x1=0.001
x2=di(num_p)
!============================
open(3020,file='0kisarazu2.txt')
do i=1,49
   read(3020,*) h_out1(i)
end do
close(3020)

write(80, *) 'In drainage_main, gw_num1 is :', gw_num1
write(80,*) 'In drainage_main, h_out1 is :', h_out1

open(3030, file='0input_mhele.txt')
do i=1, size(mhele)
   read(3030, *) mhele(i)
end do
close(3030)

!=======================
do i = 1, 2
   xq(2*i-1) = qin(1) ! initialize xq
   xq(2*i) = h_out1(1)+1. ! underwater 1.0 m
   xqold(2*i-1) = qin(1) ! initialize xqold
   xqold(2*i) = h_out1(1)+1.
end do
!=======================
!do z=1, size(qin1)
do z=1, gw_num1
   qx1=qin1(z)
!====================
   if (h_out1(z)+1.0 > di(1)) then
      h_out = h_out1(z)+1.0
   else
      h_out = di(1)
   end if
!====================
   write(80,*) '==='
   write(80,*) 'In drainage_main loop, now is step z = :', z
   write(80,*) '==='
```

```
    write(80,*) 'In drainage_main, qx1 is :', qx1
    write(80,*) 'In drainage_main, h_out is :', h_out

    call newt(xq, num_fv)
    do i=1, num_fv
       xqold(i) = xq(i)
    end do
    write(21,11) xq

    flux2(1)=(xq(2)-di(1)-1.0-mhele(1))*da*mhele(2)/dt ! 1.1 m digging

    write(80,*) 'In drainage_main, flux2 is :', flux2
    write(80,*) '==='

end do

11 format(1x,<num_fv>f12.4)
!===============end===============

deallocate(qin)
deallocate(f,xq,xqold)
deallocate(AA,A,R,RR,bb,b,ffnew,fi,ffi,ssf,sf)
deallocate(LL,di,soo,mann,drop)
deallocate(qin_new,qin1)

end subroutine drainage1
end module mod_main
```

```
module mod_intrpl
use mod_par_drainage
implicit none
contains
subroutine intrpl(qin,nt_s,m2,qin1)
integer :: i,j,nt_s,m2
real(8) :: qin(m2), qin1(num)

do i=1,m2-1
   do j=1,nt_s
      qin_new(j,i)=(j-1)*(qin(i+1)-qin(i))/nt_s+qin(i)
   end do
end do

qin1=reshape(qin_new,(/num/))
qin1(num)=qin(m2)

end subroutine intrpl
end module mod_intrpl
```

```
module mod_funcv
use mod_par_drainage
implicit none
contains

function funcv(num_fv, xq)
integer :: num_fv, i, j, ns
real(8) :: funcv(num_fv), xq(num_fv)
real(8) :: b_slot=0.001
logical :: flag_old

num_slot=0 ! defined in the mod_para

if (flag_cir==.false.) then
do i = 1, num_p
   do j = 1, 2
      if (xq(4*i+2*j-4)>0.999*di(i)) then ! surcharged flow
         num_slot=num_slot+1
         bb(i,j)=b_slot
         AA(i,j)=di(i)**2+(xq(4*i+2*j-4)-di(i))*b_slot
         !RR(i,j)=(di(i)**2+(xq(4*i+2*j-4)-di(i))*b_slot)/(3*di(i))
         RR(i,j)=AA(i,j)/(4*di(i)+2.*(xq(4*i+2*j-4)-di(i))) !works
         b(i,j)=b_slot
         A(i,j)=di(i)**2+(xqold(4*i+2*j-4)-di(i))*b_slot
         !R(i,j)=(di(i)**2+(xqold(4*i+2*j-4)-di(i))*b_slot)/(3*di(i))
         R(i,j)=A(i,j)/(4*di(i)+2.*(xqold(4*i+2*j-4)-di(i))) !works
      else ! open channel flow
         AA(i,j)=di(i)*xq(4*i+2*j-4)
         RR(i,j)=di(i)*xq(4*i+2*j-4)/(di(i)+2.*xq(4*i+2*j-4))
         bb(i,j)=di(i)
         A(i,j)=di(i)*xqold(4*i+2*j-4)
         R(i,j)=di(i)*xqold(4*i+2*j-4)/(di(i)+2.*xqold(4*i+2*j-4))
         b(i,j)=di(i)
      end if
   end do
end do

else

do i = 1, num_p
```

```
   do j = 1, 2 !ori
!    do j = 1, ns ! n means there are n nodes in this pipe
       if (xq(4*i+2*j-4)>0.999*di(i)) then
          bb(i,j)=b_slot
          ffnew(i,j)=2.*acos(1.-2.*.91) !this is a const when surcharged
          !RR(i,j)=di(i)/4.*(1-sin(ffnew(i,j))/ffnew(i,j))
          AA(i,j)=3.1416*(di(i)/2.)**2.+(xq(4*i+2*j-4)-di(i))*bb(i,j)
          RR(i,j)=AA(i,j)/(3.1416*di(i)+2.*(xq(4*i+2*j-4)-di(i))) !works
          b(i,j)=b_slot
          !R(i,j)=di(i)/4.*(1-sin(ffnew(i,j))/ffnew(i,j))
          A(i,j)=3.1416*(di(i)/2.)**2.+(xqold(4*i+2*j-4)-di(i))*b(i,j)
          R(i,j)=A(i,j)/(3.1416*di(i)+2.*(xqold(4*i+2*j-4)-di(i))) !works
       else if (xq(4*i+2*j-4)<0.999*di(i)) then
          if (xq(4*i+2*j-4)>=0.91*di(i)) then
             ffnew(i,j)=2.*acos(1.-2.*.91)
             ffi(i,j)=2.*acos(1-2.*abs(xq(4*i+2*j-4))/di(i))
             !RR(i,j)=di(i)/4.*(1-sin(ffnew(i,j))/ffnew(i,j))
             AA(i,j)=di(i)**2./8.*(ffi(i,j)-sin(ffi(i,j)))
             bb(i,j)=di(i)*sin(ffi(i,j)/2.)
             RR(i,j)=di(i)/4.*(1-sin(ffi(i,j))/ffi(i,j))
             fi(i,j)=2.*acos(1-2.*abs(xqold(4*i+2*j-4))/di(i))
             !R(i,j)=di(i)/4.*(1-sin(ffnew(i,j))/ffnew(i,j))
             A(i,j)=di(i)**2./8.*(fi(i,j)-sin(fi(i,j)))
             b(i,j)=di(i)*sin(fi(i,j)/2.)
             R(i,j)=di(i)/4.*(1-sin(fi(i,j))/fi(i,j))
          else
             ffi(i,j)=2.*acos(1-2.*abs(xq(4*i+2*j-4))/di(i))
             AA(i,j)=di(i)**2./8.*(ffi(i,j)-sin(ffi(i,j)))
             bb(i,j)=di(i)*sin(ffi(i,j)/2.)
             RR(i,j)=di(i)/4.*(1-sin(ffi(i,j))/ffi(i,j))
             fi(i,j)=2.*acos(1-2.*abs(xqold(4*i+2*j-4))/di(i))
             A(i,j)=di(i)**2./8.*(fi(i,j)-sin(fi(i,j)))
             b(i,j)=di(i)*sin(fi(i,j)/2.)
             R(i,j)=di(i)/4.*(1-sin(fi(i,j))/fi(i,j))
          end if
       end if
   end do
end do

end if
```

```
do i=1, num_p
   ssf(i)=(mann(i)**2.*abs(xq(4*i-3)/2.+xq(4*i-1)/2.)*(xq(4*i-3)/2.+xq(4*i-1)/2.))&
/((AA(i,1)/2.+AA(i,2)/2.)**2.*((AA(i,1)+AA(i,2))/(bb(i,1)+bb(i,2)))**(4./3.))

   sf(i)=(mann(i)**2.*abs(xqold(4*i-3)/2.+xqold(4*i-1)/2.)*(xqold(4*i-3)/2.+&
xqold(4*i-1)/2.))/((A(i,1)/2.+A(i,2)/2.)**2.*((A(i,1)+A(i,2))/(b(i,1)+b(i,2)))**(4./3.))
end do
!=========eq.===========
sigma=1.
f(1)=xq(1)-qx1

!if (h_out>di(1)) then
   f(2)=xq(4)-h_out
!else
!    f(2)=xq(3)**(2./3)*bb(num_p,2)**(1./3.)-9.81**(1./3.)*AA(num_p,2)
!end if

f(3)=(AA(1,2)+AA(1,1)-A(1,2)-A(1,1))*&
LL(1)/(2.*dt)+0.55*(xq(3)-xq(1))+0.45*(xqold(3)-xqold(1)) ! continuity eq.

f(4)=sigma*((xq(3)+xq(1)-xqold(3)-xqold(1))*LL(1)/(2.*dt)+&
0.55*(xq(3)**2/AA(1,2)-xq(1)**2/AA(1,1))&
+0.45*(xqold(3)**2/A(1,2)-xqold(1)**2/A(1,1)))+g*(0.55*(AA(1,1)+&
AA(1,2))/2.+0.45*(A(1,1)+A(1,2))/2.)&
*(0.55*(xq(4)-xq(2))+0.45*(xqold(4)-xqold(2))+0.55*LL(1)*ssf(1)+&
0.45*LL(1)*sf(1) –0.55*LL(1)*so-0.45*LL(1)*so) ! momentum eq.

if (num_p>=2) then
   do i=2, num_p ! 4
      f(2*i+2)=(AA(i,2)+AA(i,1)-A(i,2)-A(i,1))*LL(i)/(2.*dt)+&
0.55*(xq(4*i-1)-xq(4*i-3))+0.45*(xqold(4*i-1)-xqold(4*i-3))
      f(2*i+3)=sigma*((xq(4*i-1)+xq(4*i-3)-xqold(4*i-1)-&
xqold(4*i-3))*LL(i)/(2.*dt)+0.55*(xq(4*i-1)**2/AA(i,2)-xq(4*i-3)**2/AA(i,1))&
+0.45*(xqold(4*i-1)**2/A(i,2)-xqold(4*i-3)**2/A(i,1)))+&
g*(0.55*(AA(i,1)+AA(i,2))/2.+0.45*(A(i,1)+A(i,2))/2.)&
*(0.55*(xq(4*i)-xq(4*i-2))+0.45*(xqold(4*i)-xqold(4*i-2))+&
0.55*LL(i)*ssf(i)+0.45*LL(i)*sf(i) -0.55*LL(i)*so-0.45*LL(i)*so)
   end do
end if
```

```
funcv=f

write(80,*) 'In funcv, h_out is :', h_out
end function funcv
end module mod_funcv
```

```
!~~~~~~~~~~~~~~~~~~~~~~~~~~~~~~~~~~~~~~~~~~~~~~~~~~~~~~~~~~~~
!finite difference approximation to the Jacobian matrix, df
!Gaussian Elimination to solve df*delta_x=-fvec(x)
!newton raphson iteration to solve the water depth x
!x(k+1)=x(k)+delta_x(k)
!in the future, line search or back tracking may be considered
!to find the proper step for each iteration step
!so that the convergence will be more global
!CODED BY LIU FEI
!2018.04.02
!~~~~~~~~~~~~~~~~~~~~~~~~~~~~~~~~~~~~~~~~~~~~~~~~~~~~~~~~~~~~
module mod_newton

use mod_funcv
implicit none

contains
subroutine newt(xx,n)
integer :: n, maxits=500
integer :: its
integer :: i,j
real(8) :: sum
real(8) :: df(n,n),d
real(8) :: xx(n),fvec(n),delta_x(n)
real(8), parameter :: tolf2=1.e-4
real(8), parameter :: tolf=0.0001

its=1
fvec=1.

do while (its<maxits .and. (maxval(abs(fvec))>tolf))
   fvec=funcv(n,xx)
   write(71,*) 'funcv(xq) is '
   write(71,131) fvec

   call fdjac(n,xx,df) !compute df, the jacobian matrix
   write(71,*) 'When Iteration = ', its
   write(71,*) 'Jacobian matrix is '
   write(71,11) df
11 format(<n>f20.8)
```

```
   call linear(df,fvec,n,xx,delta_x) ! original
131 format(<n>f20.8)
   xx=xx+delta_x
   its=its+1

13 format(<n>f20.8)

end do

!close(51)

!write(*,*) 'its is ', its

end subroutine newt

subroutine linear(df,fvec,t,xx,delta_x)
integer :: i,j,k,imax,t
real(8) :: max,n
real(8) :: df(t,t),a(t,t+1),m(t,t),x(t),fvec(t),xx(t),delta_x(t)

fvec=-1*funcv(t,xx)

do i=1,t
   do j=1,t
      a(i,j)=df(i,j)
   end do
end do
do i=1,t
   a(i,t+1)=fvec(i)
end do

do k=1,t-1
   max=abs(a(k,k))
   imax=k
   do i=k+1,t
      if (abs(a(i,k))>max) then
         max=abs(a(i,k))
         imax=i
      end if
```

```
    end do
    do j=k,t+1
        m(k,j)=a(k,j)
        a(k,j)=a(imax,j)
        a(imax,j)=m(k,j)
    end do
    do i=k+1,t
        m(i,k)=a(i,k)/a(k,k)
        do j=k+1,t+1
            a(i,j)=a(i,j)-m(i,k)*a(k,j)
        end do
    end do
end do

x(t)=a(t,t+1)/a(t,t)

do k=t-1,1,-1
    n=0
    do j=t,k+1,-1
        n=n+a(k,j)*x(j)
    end do
    x(k)=(a(k,t+1)-n)/a(k,k)
end do
delta_x=x

end subroutine linear

subroutine fdjac(n,x,df)
integer :: n,i,j
real(8) :: x(n)
real(8) :: df(n,n),xh(n,n),xv(n)
real(8), parameter :: eps = 1.0e-4
real(8) :: h

h=eps
do j=1,n
    xh(:,j) = x
end do
do i=1,n
    do j=1,n
```

```
      if (i==j) then
         xh(i,j)=x(i)+h
      end if
   end do
end do

do j=1,n
   xv=xh(:,j)
   df(:,j)=(funcv(n,xv)-funcv(n,x))/h
end do

end subroutine fdjac

function fmin(n,xx)
integer :: n,i
real(8) :: fmin,xx(n),sum,fvec3(n)
fvec3=funcv(n,xx)
sum=0.
do i=1,n
   sum=sum+fvec3(i)**2
end do
fmin=0.5*sum
end function fmin

end module mod_newton
```

Note: The Python code below is the hybrid method for wind and reanalysis data.

```
"""
This code is created by LIU
parameter:
1.band width
2.increment distance
e.g., band width is always 25 km, but each time (not typhoon step), expand the 25 km band
the increment, the ring is becoming large but the width does not change.
"""
import numpy as np
nele=np.loadtxt('../nele_xy.txt')
xc=np.loadtxt('../track_x1.txt')
yc=np.loadtxt('../track_y1.txt')
####################
flag_1=False
if flag_1:
    dis=[]
    for i in range(len(xc)):
#    for i in range(2):
        dis.append([])
        for j in range(len(nele)):
            dis[i].append(np.sqrt((nele[j][0]-xc[i])**2+(nele[j][1]-yc[i])**2))
    dis1=[]
    for i in range(len(nele)):
        dis1.append([])
        for j in range(len(xc)):
            dis1[i].append(dis[j][i])
    print(len(dis1))
    print(len(dis1[0]))
    np.savetxt('../distance_to_typhoon.txt',dis1,fmt='%12.6f')
####################
n1=325
dis=np.loadtxt('../distance_to_typhoon.txt')
#dis=dis1
era_u=np.loadtxt('../blend_code/1_hour_x_y_U.out') # x y u 477
era_v=np.loadtxt('../blend_code/1_hour_x_y_V.out') # x y v 477
myers=np.loadtxt('../../wind8506_0.85/wind_nele_325.out') # 0.85_ori 2 325 325
myers_u,myers_v=[],[]
for i in range(len(myers)):
```

```
#    myers_u.append(myers[i][182:543]) # for 2 542 542 => u: 361
#    myers_v.append(myers[i][724:1085]) # for 2 542 542 => v: 361
    myers_u.append(myers[i][2:n1+2]) #     for 2 362 => u: 362,no xy
    myers_v.append(myers[i][n1+2:n1*2+2]) # for 2 362 => v: 362, no xy
#print(len(era_u)) # 61905
#print(len(era_u[0])) # 237
#print(len(myers_u)) # 61905
#print(len(myers_u[0])) # 235
era_uv,myers_uv=[],[]
for i in range(len(era_u)): #61905
    era_uv.append([])
    myers_uv.append([])
    for j in range(325): # 237-2
        era_uv[i].append(np.sqrt((era_u[i][j+2+150])**2+(era_v[i][j+2+150])**2))
        myers_uv[i].append(np.sqrt((myers_u[i][j])**2+(myers_v[i][j])**2))
#print(len(era_uv)) # 61905
#print(len(era_uv[0])) # 235
#print(len(myers_uv)) # 61905
#print(len(myers_uv[0])) # 235

"""use below"""
rs=1000000
unit=5000 # 100 km
inc=5000 # 5 km
d=[]
for k in range(n1): # n1 is the total timestep
    d.append([])
#    for j in range(int(rs/unit)): # for each step, there will be so many bands
    for j in range(int((rs-unit)/inc+1)): # for each step, there will be so many bands
        d[k].append([])
        for i in range(len(nele)):
            if ((j*inc+0)<=dis[i][k]<=(j*inc+unit)):
                d[k][j].append(abs(era_uv[i][k]-myers_uv[i][k]))

dd=[]
for k in range(n1):
    dd.append([])
    for j in range(int(int((rs-unit)/inc+1))):
        if (len(d[k][j])==0):
            dd[k].append(0)
```

```
        else:
            dd[k].append(sum(d[k][j])/len(d[k][j]))

fol='./'
np.savetxt(fol+'z_method3_ave_dd'+str(int(unit/1000))+'km_'+str(int(inc/1000))+'km.txt',dd,fmt='%12.6f'
)
# 325 rows * 20 cols, 1 row means 1 time step from 1st line to last, 1 col means from #inner ring to
500km ring

min_dis,min_num=[],[]
for i in range(len(dd)):
    min_dis.append(min(dd[i]))
    min_num.append(dd[i].index(min(dd[i])))

np.savetxt(fol+'z_method3_min_numdd'+str(int(unit/1000))+'km_'+str(int(inc/1000))+'km.txt',min_num,f
mt='%12.6f')
np.savetxt(fol+'z_method3_min_disdd'+str(int(unit/1000))+'km_'+str(int(inc/1000))+'km.txt',min_dis,fmt
='%12.6f')

num=min_num
blend_u,blend_v=[],[]
for k in range(n1):
    blend_u.append([])
    blend_v.append([])
    for i in range(len(nele)):
        if (dis[i][k]>(num[k]*inc+unit) or num[k]==0):
            blend_u[k].append(era_u[i][k+2+150])
            blend_v[k].append(era_v[i][k+2+150])
        elif (dis[i][k]<=num[k]*inc):
            blend_u[k].append(myers_u[i][k])
            blend_v[k].append(myers_v[i][k])
        else:
            blend_u[k].append((dis[i][k]-num[k]*inc)/unit*era_u[i][k+2+150]+(num[k]*inc+unit-dis[i][k])/un
it*myers_u[i][k])
            blend_v[k].append((dis[i][k]-num[k]*inc)/unit*era_v[i][k+2+150]+(num[k]*inc+unit-dis[i][k])/un
it*myers_v[i][k])

#print(len(blend_u)) # 235
#print(len(blend_u[0])) # 61905
"""change shape to 61905 * 235"""
```

```
blend_u1,blend_v1=[],[]
for i in range(len(nele)):
    blend_u1.append([])
    blend_v1.append([])
    for j in range(n1):
        blend_u1[i].append(blend_u[j][i])
        blend_v1[i].append(blend_v[j][i])
#print(len(blend_u1)) # 61905
#print(len(blend_u1[0])) # 235

blend_uv=[]
for i in range(len(blend_u1)):
    blend_uv.append([])
    for j in range(1):
        blend_uv[i]=np.append(blend_u1[i], blend_v1[i])
xy_blend_uv=[]
for i in range(len(blend_u1)):
    xy_blend_uv.append([])
    for j in range(1):
        xy_blend_uv[i]=np.append(nele[i], blend_uv[i])
print(len(xy_blend_uv)) # 61905
print(len(xy_blend_uv[0])) # 472
np.savetxt('wind_nele_blend_method3_band'+str(int(unit/1000))+'km.out',xy_blend_uv,fmt='%12.6f')
```